# Solid-Solid Recuperation to Improve the Energy Efficiency of Tunnel Kilns

**Dissertation**

zur Erlangung des akademischen Grades

**Doktoringenieur**
**(Dr.-Ing.)**

vorgelegt von:    M. Sc. Ping Meng
geb. am:          06.09.1979
in:               Beijing / China

genehmigt durch die Fakultät für Verfahrens- und Systemtechnik
der Otto-von-Guericke-Universität Magdeburg

Gutachter und Betreuer:

     Prof. Dr.-Ing. Eckehard Specht, Universität Magdeburg

Gutachter:

     Prof. Dr.-Ing. Gerd Walter, TU Bergakademie Freiberg

     Dr.-Ing. Anne Tretau, Institut für Ziegelforschung Essen

Vorsitzender der Prüfungskommission:

     Prof. Dr.-Ing. Dominique Thévenin, Universität Magdeburg

eingereicht am:              01.11.2010
Promotionskolloquium am:     21.02.2011

# Schriftliche Erklärung

Ich erkläre hiermit, dass ich die vorliegende Arbeit ohne unzulässige Hilfe Dritter und ohne Benutzung anderer als der angegebenen Hilfsmittel angefertigt habe; die aus fremden Quellen direkt oder indirekt übernommenen Gedanken sind als solche kenntlich gemacht.

Insbesondere habe ich nicht die Hilfe einer kommerziellen Promotionsberatung in Anspruch genommen. Dritte haben von mir weder unmittelbar noch mittelbar geldwerte Leistungen für Arbeiten erhalten, die im Zusammenhang mit dem Inhalt der vorgelegten Dissertation stehen.

Die Arbeit wurde bisher weder im Inland noch im Ausland in gleicher oder ähnlicher Form als Dissertation eingereicht und ist als Ganzes auch noch nicht veröffentlicht.

Magdeburg, den 01.11.2010

Ping Meng

# Acknowledgments

# Abstract

With the continuous increase of energy price in today's life, it is of high importance to invent a novel process for the tunnel kiln. In this work, counter-travelling tunnel kilns with ventilators have been introduced, which work with higher energy efficiencies compared to regular kilns. The necessary calculations and preliminary investigations have also been reported.

The concept of a counter-travelling tunnel kiln was further developed and optimized. With this kiln type, kiln cars move in the two tracks in opposite directions through the central separated channel. Middle ventilators are used to keep the kiln gas recirculating between both kiln sides. Thus, the heat from the hot ware can be transferred to the cold ware on both sides of the kiln. To describe this complicated process of solid-solid-recuperation, a simplified mathematical model with analytical equations was built first; a standard clinker brick without holes were taken as an example. The principle effects and process mechanism were clearly shown with the model. The influence of all kinds of variables, such as temperature, brick piles' height, gap thickness of brick piles etc., were investigated. It was evident that the electrical ventilator power is strongly dependent on the gap thickness of the brick piles, and the ventilator power would be minimal at a gap thickness of around 10-20 mm. Meanwhile, an energy balance of the whole kiln process was done, including the sum of fossil and primary electrical energy, illustrating the optimum temperature difference between the hot and cold side.

Computational fluid dynamics (CFD) was used to study the gas recirculation in the cross section. 2D and 3D simulations were carried out with the commercial software package FLUENT 6.3. 2D simulations for the internal horizontal ventilator were carried out at first to investigate the flow pressure drop by the turn over and inlet/outlet. Later, 2D simulations were carried out for vertical ventilator as well, where homogenous flow optimization was performed and then the influence of the ventilator geometry for the total pressure drop of the gas recirculation was investigated. The optimum operational conditions for the high heat transfer with low pressure drop in the cross section were determined. In addition to the 2D simulations, 3D simulations were performed for investigation of the ventilator pressure drop and the gas recirculation in the firing zone. The gas velocity inside each gap in the cross section and the gas velocity along the kiln length were revealed.

Then, the simplified model was verified with an extended model by modifying the assumptions of the first by an unsteady state model. The transient temperature changes both for the solid and the gas were shown. The temperature difference inside the solid was also investigated. It was revealed that the temperature difference between the top and bottom of the brick pile was less than 10 K, where as between the core and surface is around 64 K. A comparison of the simplified and transient models was carried out. It was evident that the simplified model can explain the process relatively accurately, and the results obtained from the simplified model are reliable.

Furthermore, simulations for roof tiles were carried out, illustrating optimum gap thickness. It was shown that the principle effects and process mechanism are the same as those for the clinker bricks. The energy consumption of the flue gas, the driving out, the heat loss from the kiln wall, and the primary energy of the ventilators were determined.

As this study demonstrated, because of the solid-solid-recuperation, the energy consumption of this counter-travelling kiln is only approximately 40% of that of conventional brick tunnel kiln. The most obvious energy-saving term is that from the flue gas. This is the effect that by the solid-solid-recuperation process the ballast gas by the solid-gas-recuperation process is avoided. Therefore, the aim of this research project is fully achieved.

**Key words:** Ceramic firing, Tunnel kiln, Energy saving

# Zusammenfassung

Auf Grund stetig steigender Energiepreise und durch den Vergleich der aktuellen Energieeffizienz des Tunnelofenprozesses mit anderen Öfen, gewinnt die langfristige Einführung von alternativen Brennprozessen mehr und mehr an Bedeutung. Als ersten und wichtigsten Schritt wurden in dieser Arbeit die für die Einführung des neuen Brennofenprozesses notwendigen Berechnungen und Voruntersuchungen durchgeführt.

Das Konzept des Gegenlauftunnelofens wurde weiterentwickelt und optimiert. Bei diesem Ofentyp bewegen sich die Ofenwagen auf zwei Linien entgegengesetzt durch den mittig getrennten Tunnel. Mittels eines Gebläses wird die Umluftströmung zwischen den beiden Tunnelseiten realisiert. Dadurch wird Wärme von dem heißen Gut an das kalte Gut übertragen und umgekehrt. Zur Beschreibung des komplizierten Prozesses der Solid-Solid-Rekuperation wurde zunächst ein vereinfachtes mathematisches Modell mit analytischen Gleichungen erstellt. Als Beispiel wurde ein üblicher Ziegelstein verwendet. Die prinzipiellen Effekte und der Prozessmechanismus wurden mit diesem Modell eindeutig gezeigt. Der Einfluss aller möglichen Variablen, wie z. B. Temperatur, Höhe des Ziegelstapels sowie die Spaltbreite, wurde untersucht. Es gab Anzeichen dafür, dass die Leistung des elektrischen Ventilators stark von der Spaltbreite abhängt. Der minimale Wert der Ventilatorleistung ergab sich, wenn die Spaltbreiten zwischen 10-20 mm lagen. Des Weiteren wurde eine Energiebilanz für den gesamten Prozess im Ofen erstellt. Aus der Summe aus der Brennstoffenergie und der auf die Primärenergie bezogenen Ventilatorleistung, wurde die optimale Temperatur zwischen der heißen und kalten Seite des Ziegelstapels aufgezeigt.

Da experimentelle Untersuchungen nicht möglich waren, wurde ein CFD-Programmsystem verwendet, um die Umluftströmung im Querschnitt zu bestimmen. 2D-und 3D-Simulationen wurden mit dem kommerziellen Software-Paket FLUENT 6.3 durchgeführt. 2D-Simulation für den Ventilator wurde zunächst erstellt, um den Druckverlust der Strömung bei der Umlenkung sowie am Ein- und Austritt eines Spaltes zu untersuchen. Es folgte eine 2D-Simulation für Ventilatoren mit senkrechter Antriebswelle. Dabei wurde eine homogene Strömungsoptimierung durchgeführt und der Einfluss der Geometrie des Ventilators für den gesamten Druckabfall der Umluftströmung untersucht. Die optimalen Betriebsbedingungen für eine hohe Wärmeübertragung mit geringem Druckabfall im Querschnitt wurden bestimmt. Weiterhin wurden 3D-Simulationen zur Untersuchung des Druckverlustes des Ventilators und der Umluftströmung in der Brennzone durchgeführt. Die Gasgeschwindigkeitsverteilungen in den Spalten des Querschnitts der Ziegelstapel und in Ofenlängsrichtung wurden aufgezeigt.

In einem nächsten Schritt wurde das vereinfachte Modell mit einem erweiterten Modell verifiziert. Die Annahmen des vereinfachten Modells wurden durch ein instationäres Modell modifiziert. Die instationären Temperaturveränderungen sowohl für den Feststoff als auch für das Gas wurden dargestellt. Die Temperaturdifferenz innerhalb des Feststoffes wurde ebenfalls untersucht. Es zeigte sich, dass die Feststofftemperaturdifferenz zwischen dem oberen und unteren Ende eines Ziegelstapels weniger als 10 K beträgt, während zwischen Kern und Oberfläche eine Temperaturdifferenz von rund 64 K vorlag. Ein Vergleich der Ergebnisse des vereinfachten Modells und dem instationären Modell wurde durchgeführt. Dabei wurde deutlich, dass das vereinfachte Modell den Prozess relativ genau erklärt, und die erzielten Ergebnisse zuverlässig sind.

Darüber hinaus wurde die Simulation für Dachziegel durchgeführt. Die optimale Spaltdicke wurde dargestellt. Es konnte gezeigt werden, dass die prinzipiellen Effekte und der Prozessmechanismus annähernd die gleichen sind wie für Klinker. Für die Energieverbräuche hinsichtlich Abgas-, Ausfahr- und Wandverlust sowie Ventilatorleistung bezogen auf Primärenergie wurden die minimalen Werte bestimmt.

Wie diese Studie gezeigt hat, beträgt der Energieverbrauch des Gegenlauftunnelofens auf Grund der Solid-Solid-Rekuperation nur etwa 40% des herkömmlichen Ziegeltunnelofens. Die meiste Energieeinsparung ergab sich aus dem Abgas. Bei den Solid-Solid-Rekuperation-Prozessen wird der Wärmeballast des Abgases, welcher bei den Solid-Gas-Rekuperation-Prozessen entsteht, vermieden. Diese Energieeinsparung kann durchaus als bedeutend angesehen werden und somit wurde das Ziel des Forschungsprojektes vollständig erreicht.

**Schlagwörter:** keramischer Brennen, Tunnelofen, Energieeinsparung

# Table of content

# List of Tables

# List of Figures

# Nomenclature

| | | |
|---|---|---|
| $A$ | $m^2$ | Surface area |
| $b$ | m | Brick width |
| $B$ | m | Kiln width |
| $c$ | J/(kg·k) | Specific heat capacity |
| $c_p$ | J/(kg·k) | Specific heat capacity at constant pressure |
| $d_h$ | m | Hydraulic diameter |
| $d_o$ | m | Burner diameter |
| $D$ | m | Diameter |
| $E$ | MJ/kg | Specific energy |
| $F$ | N | external body force |
| $h_u$ | J/kg | Fuel enthalpy |
| $H$ | m | Height |
| $\dot{H}$ | W | Enthalpy flow |
| $J$ | mol/(m²·s) | Diffusion flux |
| $L$ | m | Length |
| $L$ | $kg_L/kg_f$ | Air demand |
| $\dot{M}$ | kg/s | Mass flow |
| $n$ | - | Number of brick piles |
| $n$ | - | Exponent index |
| $P_{el}$ | W | Electrical power |
| $P^*_{el}$ | W/m | Electrical power per length |
| $\Delta p_v$ | Pa | Pressure drop |
| $\dot{q}$ | $W/m^2$ | Heat flux |
| $\dot{Q}$ | W | Heat flow |
| $R$ | m | Radius |
| $s$ | m | Gap thickness |
| $S_m$ | $kg/m^3$ | Mass change |
| $t$ | s | Time |
| $T$ | K | Absolute temperature |
| $\dot{V}$ | $m^3/s$ | Volumetric flow |
| $w$ | m/s | velocity |
| $W_R$ | J | Friction work |
| $X,Y,Z$ | m | Local coordinates |

**Greek letters**

| | | |
|---|---|---|
| $\alpha$ | W/(m$^2$·K) | Heat transfer coefficient |
| $\beta$ | K$^{-1}$ | Thermal expansion coefficient |
| $\varepsilon$ | - | Turbulence dissipation rate |
| $\eta$ | - | Efficiency |
| $\vartheta$ | °C | Temperature |
| $\Delta\vartheta$ | K | Temperature difference |
| $\kappa$ | - | Turbulence kinetic energy |
| $\lambda$ | W/(m·K) | Thermal conductivity |
| $\lambda$ | - | Flow friction factor |
| $\lambda$ | - | Access air number |
| $\mu$ | Pa·s | Dynamic viscosity |
| $\nu$ | m$^2$/s | Kinematic viscosity |
| $\xi$ | - | Pressure drop coefficient |
| $\rho$ | kg/m$^3$ | Density |
| $\tau$ | N/m$^2$ | Stress |
| $\chi$ | - | Transient factor |

**Subscripts:**

| | |
|---|---|
| $b$ | Bottom |
| $conv.$ | Convective |
| $eff.$ | Effective |
| $el$ | Electrical |
| $f$ | Fuel |
| $g$ | Gas |
| $is.$ | Isentropic |
| $k$ | Kiln |
| $lam.$ | Laminar |
| $L$ | Air |
| $m$ | Mean |
| $s$ | Solid |
| $t$ | Top |
| $turb.$ | Turbulent |
| $T$ | Transportation medium |
| $ws.$ | Wall surface |
| $W$ | Kiln wall |

**Dimensionless numbers:**

| | |
|---|---|
| *Bi* | Biot number |
| *Nu* | Nusselt number |
| *Pr* | Prandtl number |
| *Re* | Reynolds number |
| *St* | Stanton number |

# 1. Introduction

## 1.1 Ceramic and its raw material

Ceramic products are widely used in daily life and industries. Generally, the term "ceramics," or ceramic products, is used to describe the inorganic materials, possibly with some organic content, which are made up of non-metallic compounds and made permanent by the firing process. In addition to clay based materials, today ceramics include a multitude of products with a small fraction of clay or none at all. Ceramics can be glazed or unglazed, porous or vitrified.

### 1.1.1 Ceramic

Historically, the ceramic can be classified into two groups: "coarse or construction", and "fine or traditional and industrial ceramics", according to the production multiple stages firing processes or the inside equivalent particle diameters.

Nowadays, based on the manufacture of ceramic products, the major ceramic sectors are defined as follows [1]:

• Bricks and roof tiles
• Wall and floor tiles
• Table- and ornamental ware (household ceramics)
• Refractory products
• Sanitary ware
• Technical ceramics
• Vitrified clay pipes
• Expanded clay aggregates
• Inorganic bonded abrasives.

In this dissertation, the energy consumption for the first sector, "bricks and roof tiles," is investigated as an example. Herein, the production process of block pavers and roof tiles with a new production process will be investigated respectively, to illustrate the energy saving for this new production process. The energy consumption and energy saving of these two products with the new process will be compared with the traditional tunnel kiln.

## 1.1.2 Raw material

Common clay minerals (plastic clay) are hydrated aluminium silicates that have resulted from the weathering of rocks; there are two structural units involved in most clay mineral lattices. One is the 'silica sheet' formed by tetrahedron tetrahedra consisting of a $Si^{4+}$ surrounded by four oxygen octahedra in which an $Al^{3+}$ ion is surrounded by six hydroxyl groups. These octahedral sheets condense with silica sheets to form the clay minerals.

There are a large number of mineral species called clay minerals, but the most important are kaolinite, $Al_2O_3 \cdot 2SiO_2 \cdot 2H_2O$, montmorillonite, $Al_2O_3 \cdot 4SiO_2 \cdot H_2O$ and halloysite, $Al_2O_3 \cdot 2SiO_2 \cdot 3H_2O$, illite, $K_2O \cdot 3Al_2O_3 \cdot 6SiO_2 \cdot 2H_2O$, and bentonite, $Al_2O_3 \cdot 4SiO_2 \cdot 5H_2O$.

The kaolinite group includes the dioctahedral minerals kaolinite, dickite, nacrite, and halloysite, and the trioctahedral minerals antigorite, chamosite, chrysotile, and cronstedite. The primary structural unit of this group is a layer composed of one octahedral sheet condensed with one tetrahedral sheet. In the dioctahedral minerals, the octahedral site are occupied by aluminum; in the trioctahedral minerals, these sites are occupied by magnesium and iron. Kaolinite and halloysite are single-layer structures. Although dickite and nacrite have the same basic structure, the stacking sequence of layers is different in these minerals [1]. Kaolinite, dickite, and nacrite occur as plates; halloysite, which can have a single layer of water between its sheets, occurs in a tubular form.

Formulas (or bodies) of clay-based ceramics may consist of one single clay or more clays, mixed with mineral modifiers, so-called non-plastics, such as powdered quartz and feldspar.

## 1.1.3 General ceramic production

The main steps in the manufacturing of ceramic products are largely dependent on the materials used and the final product. Fig. 1.1 schematically shows the typical process and possible or necessary supply and disposal facilities. This process is made up of the following steps: mining/quarrying of materials and transport to the ceramic plant, storage of the raw materials, preparation of the raw materials, shaping, drying, surface treatment, firing and subsequent treatment.
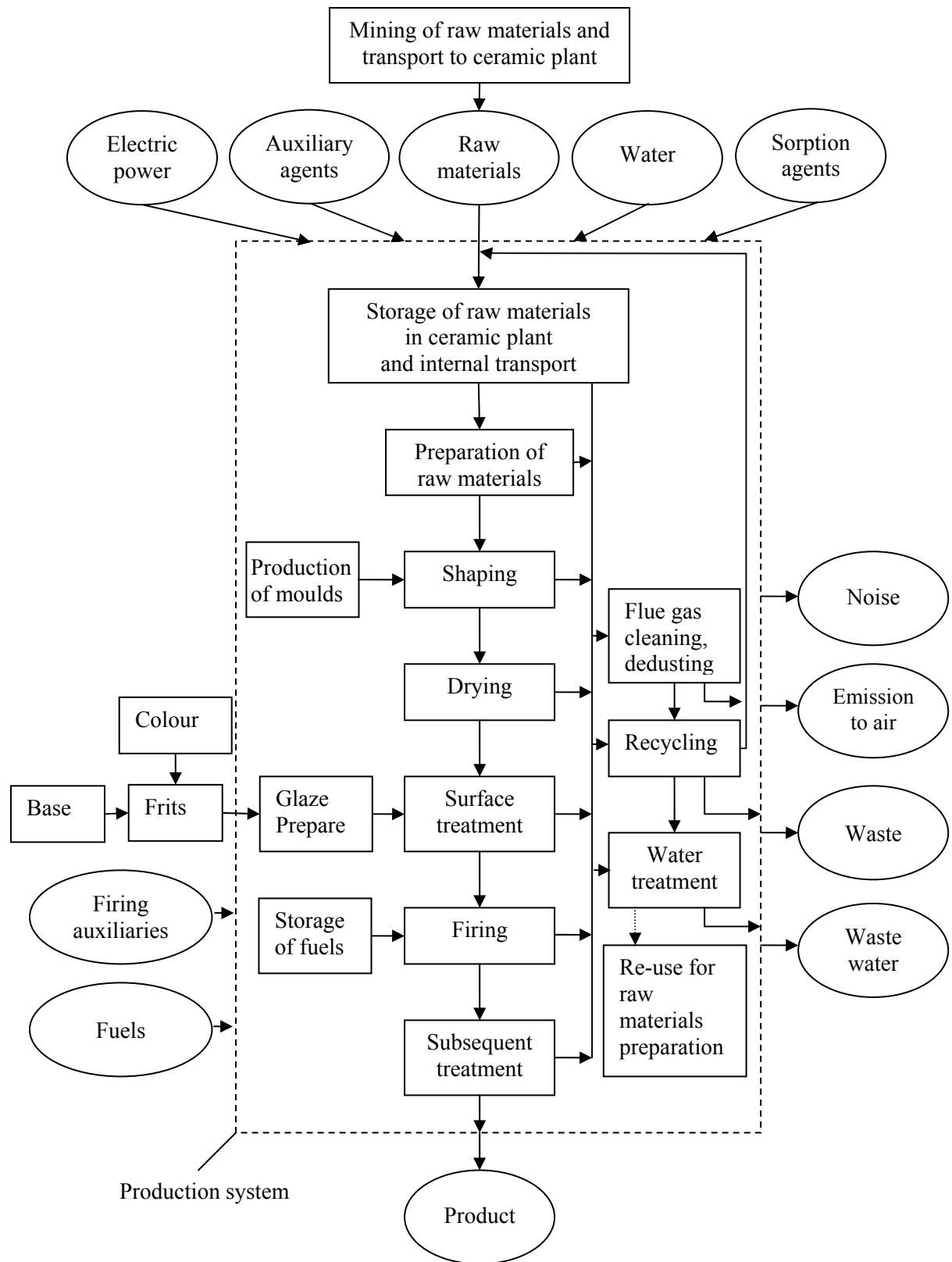
Figure 1.1: General production process for ceramic products [1]

# 1.1.4 Firing Process

Firing is a key process in the manufacture of ceramics, as it controls many important properties of the finished products. These include mechanical strength, abrasion resistance, dimensional stability, resistance to water and chemicals, and fire resistance.

When the clay-based ceramic products are fired in a kiln, all moisture is driven off at temperatures between 100 and 200°C. If organic matter and iron pyrites are present, oxidation takes place at temperatures between about 300 and 500°C. Water combined within the structure of clay minerals ('crystal water') is usually released at temperatures between 500 and 650°C, whilst carbonates such as calcite and dolomite dissociate with the release of carbon dioxide in the temperature range of 750 to 950°C.

- $CaMg(CO_3)_2 \rightarrow CaO+MgO+2CO_2\uparrow$
- $CaCO_3 \rightarrow CaO+CO_2\uparrow$

The most important changes relating to the development of ceramic properties involve the breakdown of the lattice structure of the original clay minerals, followed by the formation of new crystalline compounds and glassy phases. The temperature at which vitrification (glass formation) takes place varies according to the mineralogy of the clay. Vitrification usually commences at about 900°C and is completed by about 1050°C (for many brick clay) or about 1100°C in the case of more refractory fireclays.

During the vitrification stage of ceramic firing, many non-clay minerals such as quartz, oxides or iron, lime compounds and alkalis (oxides of sodium and postassium) become incorporated in the fire body. Some sintering and solid solution occurs, and eutectic reactions take place at the interface of mineral grains and melt phases.

Non-clay products, such as some refractory products, also depend on sintering, vitrification or recrystallization stages, but in most cases much higher temperatures are required to achieve the desired properties. Fig. 1.2 shows the range of industrial maturing temperatures for different products groups [2].
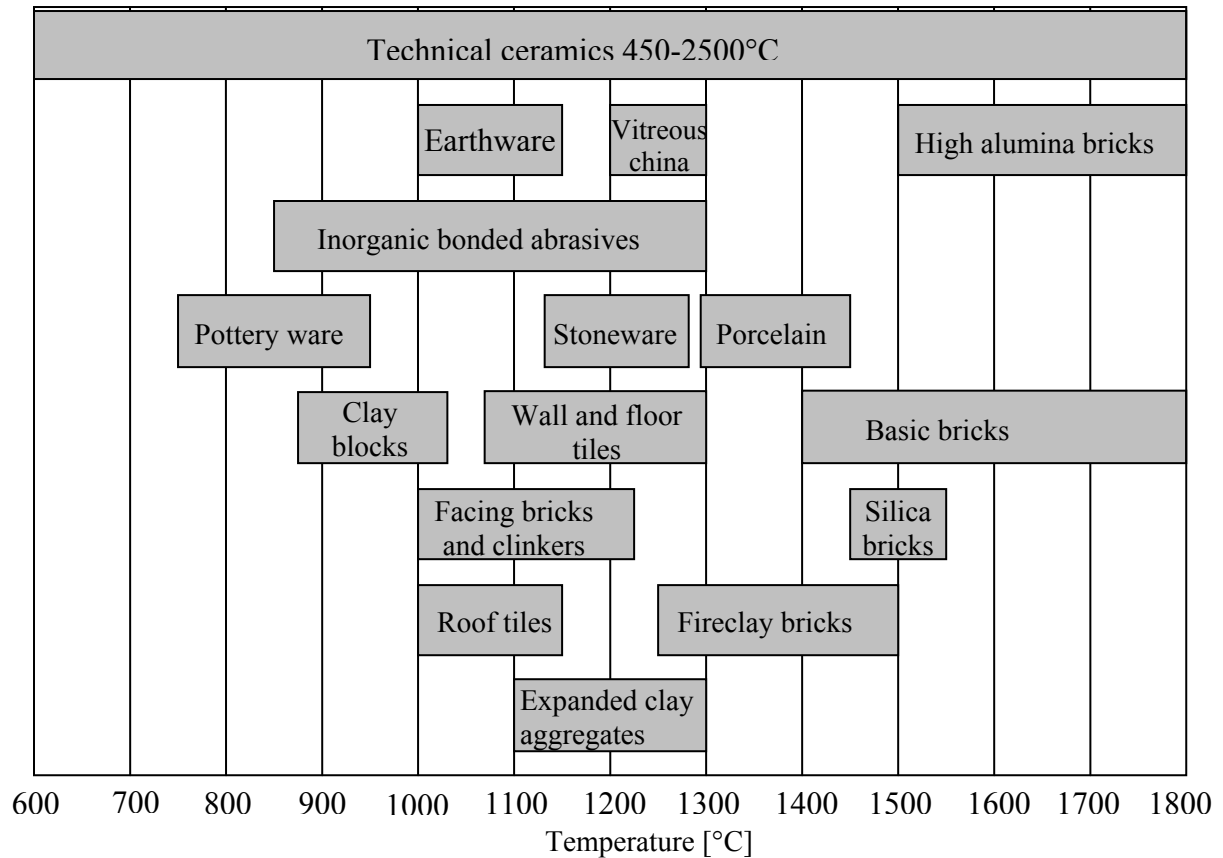
Figure 1.2:    Ranges of firing temperatures for different product groups [2]

The temperatures necessary for the firing process are mainly created by burning natural gas and fuel oil. In some cases, solid fuels, biogas/biomass and electric power are also used for heat generation.

## 1.2  Ceramic production equipments

Ceramic is one of the oldest materials used by human beings. The production of bricks can be traced back to the beginning of 5000 BC [3], with so called field firing, which means to fire the bricks under the open heaven. The brick stack shown is Fig. 1.3 shows this production process. It is not only the oldest but also the longest used process of brick production, as it is still used in various developing countries in Africa, Asian and South America, as well as in some European countries.

Figure 1.3:    Brick stack shortly before completion [4]

As it can be seen, the stack consists of a large upwardly tapered brick pile, which depending on the stack dimension is composed of three thousand to three million pieces of brick, the maximum height of which is 4 m. Recently larger stacks have been utilized in countries such as South Africa [5]. Until about 1800, the fuel of this production process, depending on local availability, consisted of peat, all kinds of wood, sticks, straw, reeds, olive seeds, and dried manure, which is still used in India today. From 1800 on, coal and brown coal in a size of 0.3 to 1.0 cm were used as fuel.

## 1.2.1 Kilns for ceramic production

The range of kiln types for ceramic production from ancient times to now is very large. If it is investigated more in depth, not only do the kiln types differ, but there are also many variants within each kiln type. If the classification of the kiln type in the present literature is investigated, the intensive facts about the development of the kiln can be observed.

Generally, there are two types of kilns to produce ceramics: periodic kilns and continuous kilns [3]. Within these classifications there are still more sub-classifications for each type. While it is impossible to enumerate all kilns, here some of the most important kilns are discussed as examples.

**Periodic kilns**

- Shuttle kiln

The shuttle kiln, one of the typical periodic kilns, is like a chamber, as shown in Fig. 1.4. It is suitable for firing sanitary ware, metal, table ware, roof tiles, insulators, and advanced technical ceramics. It offers flexibility when the ceramic body composition is altered frequently, and these advantages outweigh their somewhat lower energy efficiency.

6

Figure 1.4      Front view of shuttle kiln [6]

The cross section of shuttle kiln is shown in the Fig. 1.5. It illustrates that fuel is supplied from the both sides of the kiln. The ware to be fired is brought into the kiln area on a shuttle car. During the firing process, the kiln chamber is sealed, and then subjected to a defined firing cycle. Flue gas goes out from the top of the kiln chamber.
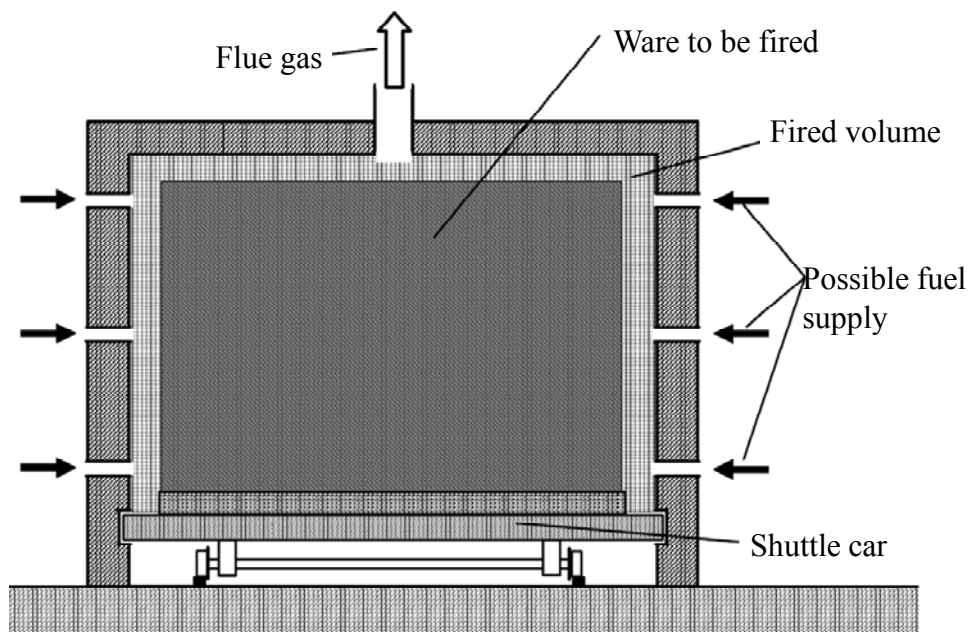


Figure 1.5:     Cross section of shuttle kiln [1]

**Continuous kilns**

- Ring kiln

A great milestone for ceramic production came from the invention of the ring kiln, designed by Friedrich Hoffmann. With Hoffman's ring kiln, it became possible for the first

time to continuously operate the mass to be fired in the kiln. The outside appearance of this kiln is shown in Fig. 1.6.



Figure 1.6: Outside appearance of a Hoffmann Kiln [7]

The Hoffmann Kiln is a series of batch process kilns. It consists of a main fire passage surrounded on each side by several small rooms. The inside construction of the kiln is shown in Fig. 1.7. Each room contains a pallet of bricks. In the main fire passage, there is a "fire wagon" that holds a fire that burns continuously. Each room is fired for a specific time, until the bricks are vitrified properly, and thereafter the fire wagon is rolled to the next room to be fired.



Figure 1.7: Scale model of Hoffmann kiln [7]

Each room is connected to the next room by a passageway carrying hot gases from the fire. In this way, the hottest gases are directed into the room that is currently being fired. Then the gases pass into the adjacent room that is scheduled to be fired next, thereby preheating the bricks. As the gases pass through the kiln circuit, they gradually cool as they transfer heat to the brick as it is preheated and dried. This is essentially a counter-current heat exchanger, which makes for a very efficient use of heat and fuel. This efficiency is a principle advantage of the Hoffmann kiln, and is one of the reasons for its original development and continued use throughout history.

8

In addition to the inner opening to the fire passage, each room also has an outside door, through which recently-fired brick is removed, and replaced with wet brick to be dried and then fired in the next firing cycle. Any fuel may be used in a Hoffmann kilns, including gasoline, natural gas, heavy petroleum and wood fuel.

- Roller hearth kiln

The roller hearth kiln is a prefabricated continuous kiln, whose hearth is formed by a motor driven roller. The goods shall be loaded on refractory plates or batts in case they are not suitable to be loaded on the rollers directly. The goods to be fired are automatically conveyed from the kiln entrance to the exit on the roller way. Fig. 1.8 shows this process. Because nothing beside the goods and refractory plates pass through the kiln, this type of kiln's thermal efficiency is superior to other types. Also considerably short firing cycle is another feature of this type of kiln.
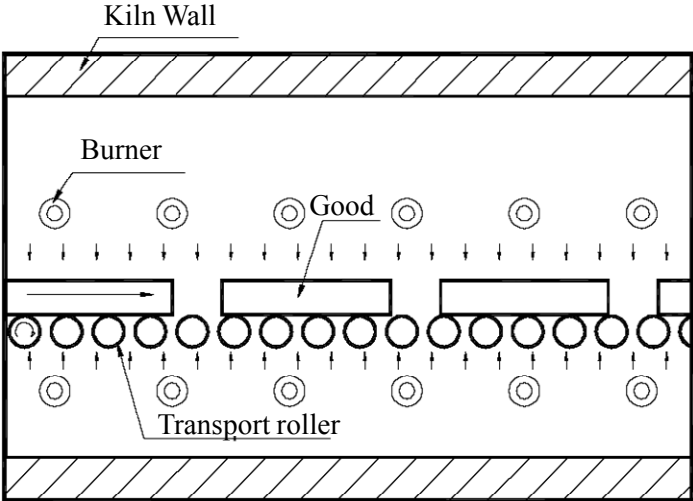


Figure 1.8:      Schematic diagram of roller kiln [8]

Roller kilns are now almost universally used for wall and floor tile production, and firing schedules have been reduced to less than 40 minutes [3]. Tiles travel over driven rollers, and the heat required for firing is provided by natural gas-air burners located at the sides of the kiln. The main heat transmission mechanisms are convection and radiation, and as the kilns are non-muffled, the heat transmission coefficients are raised, reducing the firing cycle and energy consumption. Roller hearth kilns are also sometimes used for the production of clay roof tiles, vitrified clay pipes, sanitary ware and tableware. Fig. 1.9 shows the roller kiln with the transported good.
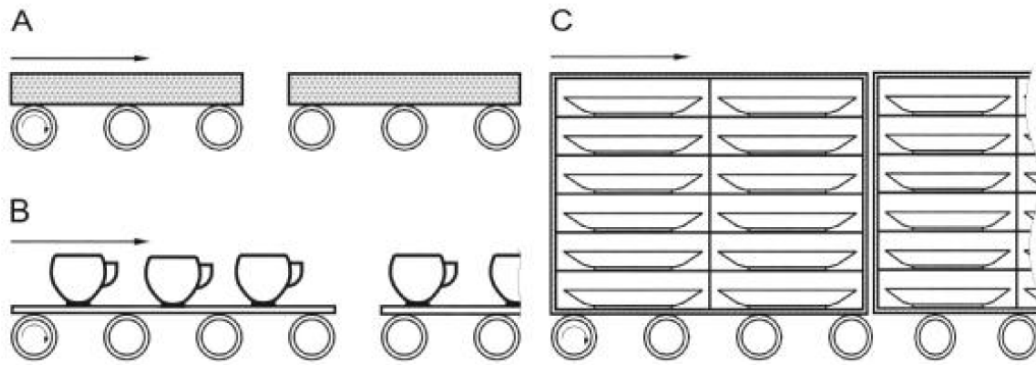
Figure 1.9:    Roller hearth kiln with transported good [8]

## 1.2.2 Tunnel kiln

From 1947, the tunnel kiln gradually replaced the ring kiln. In 2000, the tunnel kiln was the most popular and commonly used kiln in Germany. The technical data of the tunnel kiln largely varies. A tunnel kiln is a long kiln, which looks like a tunnel and is made of refractory and heat insulated construction materials. Inside the kiln, there are kiln cars to transport the green wares and the final products.

During the operation of the tunnel kiln, the preheated green wares are loaded on the kiln car. They enter into the kiln with the kiln car from one side of the kiln, then after the increase in temperature and undergoing of the sintering, the green wares become products and move out of the kiln from the other side. After the removal of all the products, the empty kiln car will go the other side of the kiln, to begin the next production cycle. This process is shown in Fig. 1.10 and 1.11.
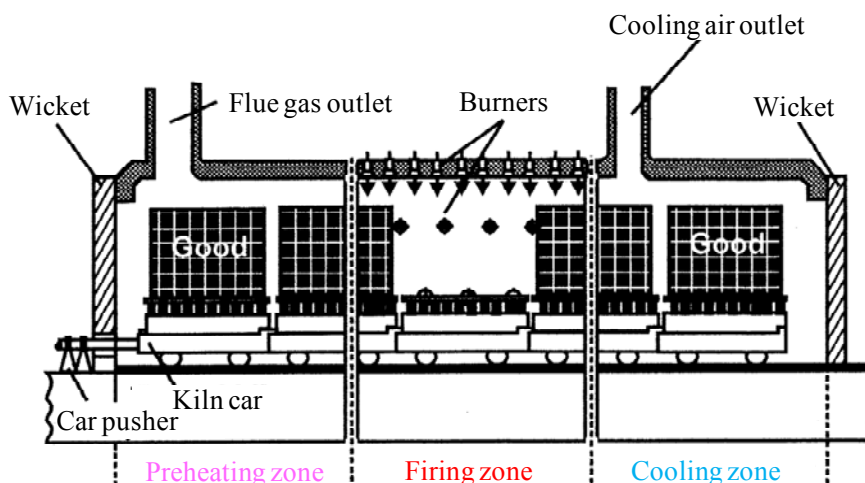


Figure 1.10:    Schematic diagram of tunnel kiln
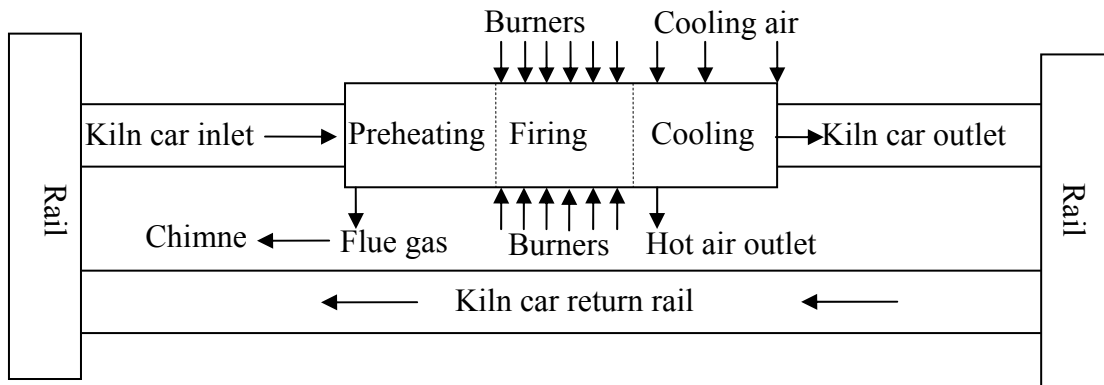
Figure 1.11:    Schematic diagram of the whole tunnel kiln system and its working process

The solid and gas temperature profile and flow direction are shown in Fig. 1.12. It illustrates that in the preheating and firing zone, the heat from the high temperature flue gas preheats the green ware; therefore the green ware temperature increases and the flue gas temperature decreases, which is a counter-current heat exchanger with solid-gas-recuperation. While in the cooling zone as the low temperature cooling air cools the fired product, the solid temperature decreases and cooling air temperature increases. Here again is a counter-current heat exchanger with solid-gas-recuperation. The high temperature cooling air will be used, later, for the drying system.
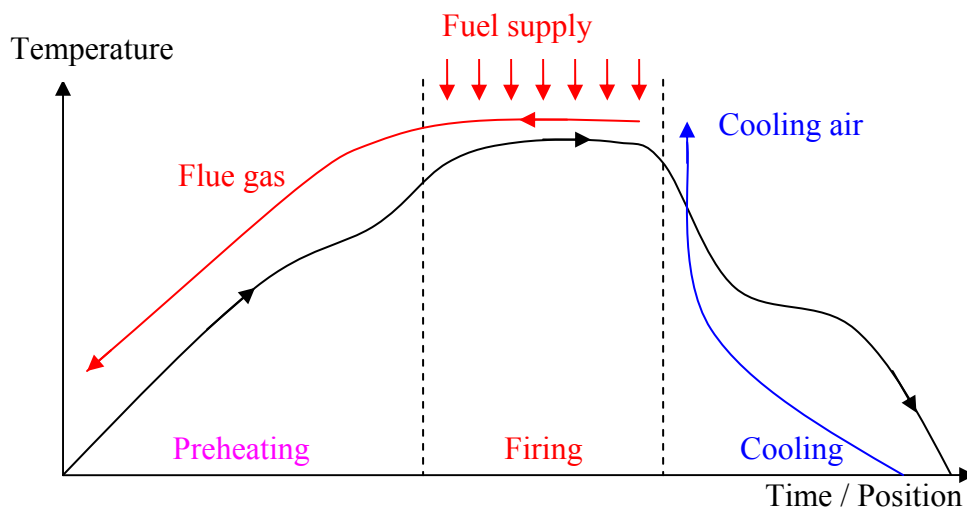


Figure 1.12:    Temperature profile and flow direction of goods and gas

As shown above, a tunnel kiln consists of a series of one after another connected counter-current heat exchangers with solid-gas-recuperation.  That is to say, the solid on the kiln cars moves continually in the opposite direction of the gas flow in the kiln. In Fig. 1.12, the arrows show the flow direction of the goods and gas.

11

## 1.2.3 Development history of tunnel kiln

The principle advantages of tunnel kilns were so credible that the basic idea of it has always be in use. For about a century from 1840, there were only some individual experiments for introducing the tunnel kiln into the brick manufacturing industry, It was first implemented in industry in 1947, and from then on spread very quickly and generally. At that time, the tunnel kiln system was characterized by two parallelly arranged combustion chambers. At the sides of the chambers, four pairs of atomising burners are installed opposing each other, as shown in Fig. 1.13. Until 1964, around 150 of this kind of side-fired tunnel kilns were built [3].
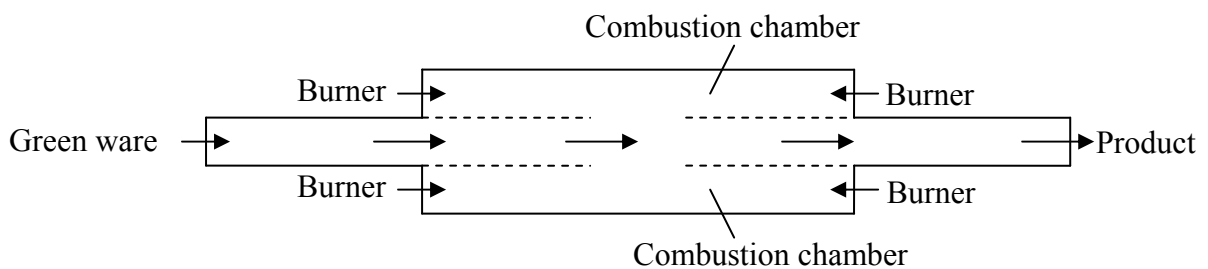


Figure 1.13:   Schematic diagram of side-fired tunnel kiln

The quick implementation and development of the tunnel kiln after 1950 were driven by multiple reasons: A lot of the ring kilns built in 1900 needed to be replaced, partly because of their natural lifespan, but also partly because they could not guarantee the firing of consistently high quality bricks. It was also difficult for find workers who were willing to work in the hot and dirty ring kilns.

The kiln width of side-fired kilns was limited, because if the kiln very wide, the temperature between the wall and middle of the kiln could not be homogenous. A milestone happened in 1953, when a top-fired tunnel kiln was built. It was made possible by installing the burners from the top of the modified ring kiln. This top-fired kiln made it possible to build the kiln with a wider width and enough performance for the economical throughput.

In 1957, the first tunnel kiln with a suspended ceiling was built, thus supporting the basic equipment for tunnel kilns and allowing wider firing channels and correspondingly larger throughputs.
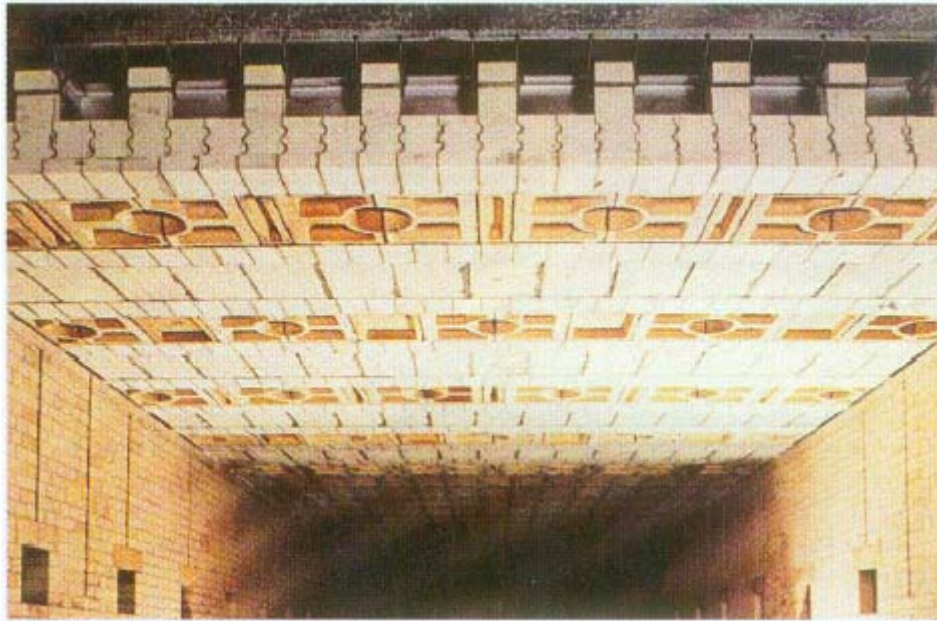
Figure 1.14: Tunnel kiln with flat suspended ceiling [3]

In 1959, a tunnel kiln for roof tiles was built. The characteristics of coal-fired kiln were kiln furniture arranged on the tunnel car, in which roof tiles were inserted, the firing velocity with high excess air and depression to 100 mm $H_2O$, and the flue gas transportation through the transverse floor channels.

In 1964, there were over 200 tunnel kilns and around 25 companies working on tunnel kiln construction in West Germany. Until 1992, the five biggest German tunnel kiln companies had built around 1250 tunnel kilns domestically and abroad [3].

## 1.2.4 Modern tunnel kiln

Unlike the old tunnel kiln, in which the burners are only installed in the firing zone, in the new tunnel kiln, comprehensive burners are available in the preheating zone and it is similar to the kiln operation in the steel industry. Although the cooling zone directly connected with the firing zone is a constructive part of the tunnel kiln, it is further separated by the process. In this zone, the heated cooling air will be extracted out of the kiln process. In the old tunnel kiln, only a small part of the cooling air was extracted.  In both cases air is the counter-current heat transfer medium. Therefore, a tunnel kiln is a Solid-Gas-Recuperator.

Comparison between

-the current normal tunnel kiln process with fuel fired preheating zone and external cooling zone

and

- the original tunnel kiln with counter-flow heat exchange in the preheating and cooling zone and the use of the cooling air as hot process air
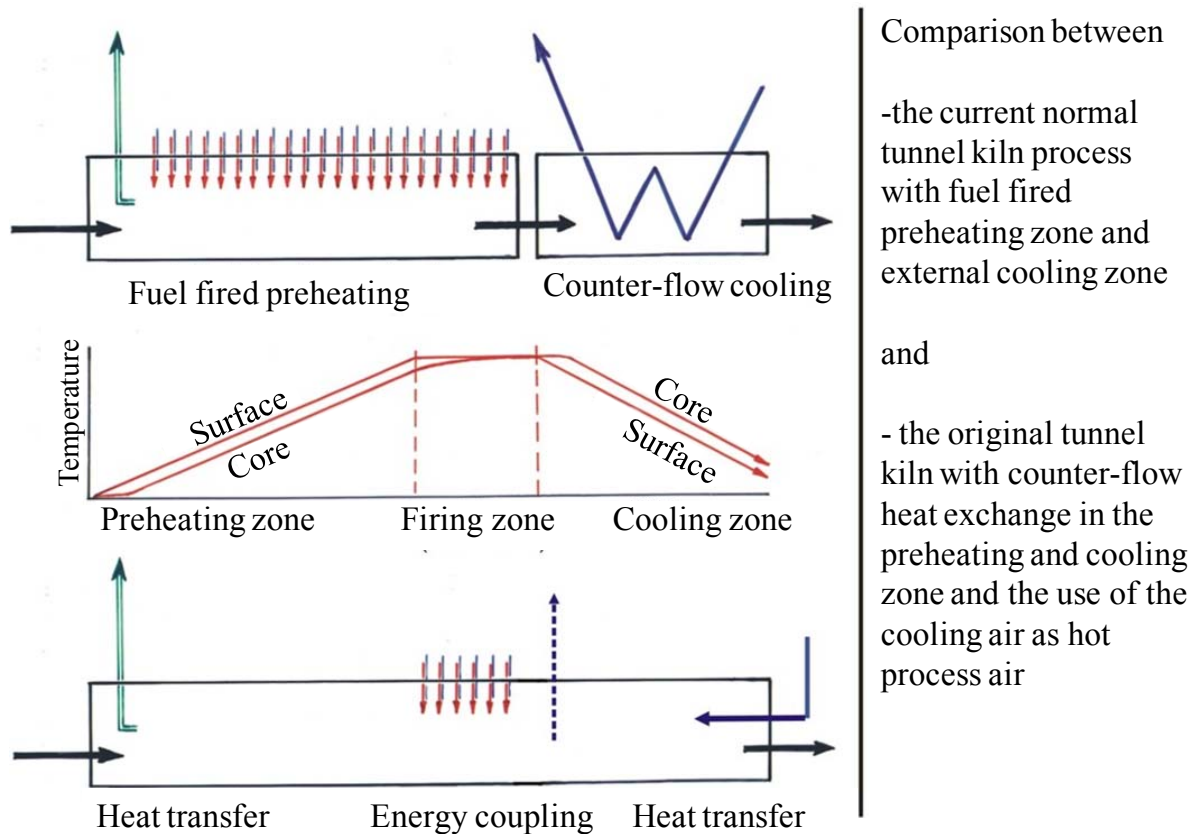
Figure 1.15:    Tunnel kiln in brick industry as coupled unit of fuel fired kiln with connected counter-current cooler and as simple series of counter-current heat transfer with the enclosed, fuel fired firing zone

# 1.3  Common problems of tunnel kiln

At first sight, the advantages of a gas-solid counter flow kiln (the traditional tunnel kiln) can be seen:  it has large capacity flows (namely all or many product surfaces around air flow) direct used for the convective heat transfer. Thus, it seems that no additional heat exchange mechanism needs to be developed, such as the solid-solid-counter flow kiln.

But in fact, in a normal tunnel kiln, the air flow due to the straight-line or the buoyancy effects (convection) must be compulsorily controlled; for example, adjust the vertical layer disturbed transverse movements and turbulences, if the above described disadvantages need to be avoided. In the normal tunnel kiln, in order to achieve a uniform heating and cooling, independent on position, various tools such as hot and cold air nozzles, high-velocity burners and high-temperature circulations are also used. This means meanwhile, that for heat exchange in a gas-solid counter flow kiln, a forced convection also must be used, if high performance and uniform product quality over the cross section are desired. Thus, the apparent advantage of the normal tunnel kiln disappeared, when compared to the counter travelling kiln with forced circulation.

## 1.3.1 Energy consumption and efficiency of tunnel kiln

The principle use of energy within the industry is for the process of transforming clay into a durable form suitable for all types of construction. The energy consumption depends on the raw material, the manufacturing process, and the product type, in addition to the type of firing techniques employed. Although a particular firing process may be more energy efficient, it may not be suitable for the specific product.

Large variations are found in the specific energy consumption within Europe, depending on differences in construction and product types used. Each type of product has a specific energy consumption pattern due to the firing process. Table 1.1 shows the operation data and energy requirement for tunnel kiln for bricks and roof tiles.

Table 1.1:     Operation data and energy requirement of tunnel kilns [1]

| Tunnel kilns | Unit | Facing bricks and clay pavers | Clay blocks | Roof tiles |
|---|---|---|---|---|
| Throughput | t/h | 1-15 | 3-15 | 3-6 |
| Kiln length | m | 35-160 | 60-120 | 80-140 |
| Cross section | $m^2$ | 1.3-6.0 | 4-12 | 4-10 |
| Setting density | $kg/m^3$ | 650-1500 | 350-500 | 200-400 |
| Firing temperature | °C | 1000-1300 | 900-1050 | 1000-1150 |
| Specific energy requirement (drying + firing) | kJ/kg | 1600-3000 | 1000-2500[*) ] | 1600-3500 |
| Flue gas volumetric flow | $m^3/h$ | 5000-20000 | 10000-50000 | 10000-40000 |
| Flue gas temperature | °C | 100-230 | 100-300 | 170-200 |

[*) ] Including heat content of the pore-forming agent

Focusing on brick production, the theoretical energy requirement is only the energy necessary for water evaporation, which is 620 kJ/kg brick, and theoretically, the energy requirement for the brick sintering is 0 kJ/kg brick. Comparing with the production process of other products with different kiln processes, the energy efficiency of tunnel kiln is relatively low. Fig. 1.16 shows the theoretical energy requirement and the real energy requirement for different products. It can be seen that for brick production with a tunnel kiln, the difference between the theoretical and the real energy requirement is higher than in the other production processes. This tells that there is a high potential to improve the tunnel kiln process.
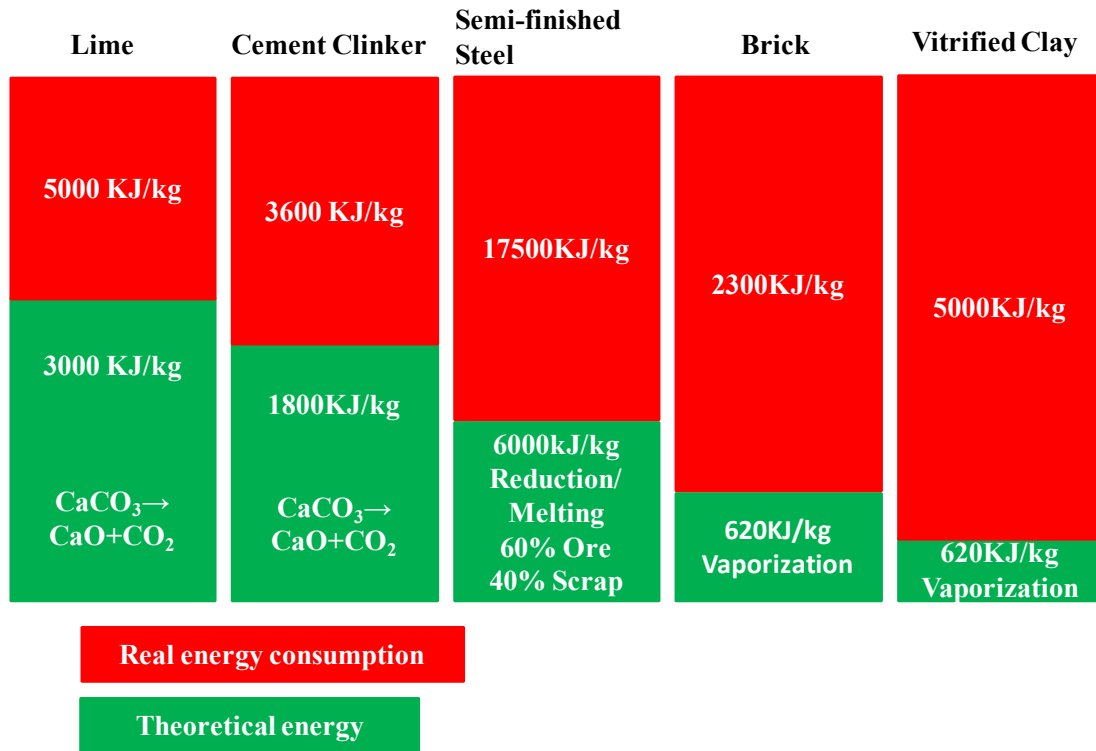
Figure 1.16:   Theoretical and real energy consumption for different products

Firing is the most energy intensive step for the brick production process. Therefore, the energy efficiency of firing has received a great deal of attention. The most important present research to improve the kiln energy efficiency is: waste heat recovery and control systems [9]; reduced thermal mass of kiln cars and furniture [10]; lightweight construction [11]; fast firing and roller kilns [12,13]; high-speed burners [10]; substitution of low-cost fuels [14] and so on.

## 1.3.2 Disadvantages of tunnel kiln

As discussed above, tunnel kilns consist of a series of one after another connected counter-current heat exchangers and therefore they have a principally lower energy consumption due to the obtained heat recovery. However, comparing to the other production processes, the tunnel kiln process has a relatively low energy efficiency. There is a big potential to improve the tunnel kiln process.

The main disadvantage of the tunnel kiln is that only one of the exchanged mass flows becomes useful, while the other - that is to say the air or kiln gas - only produces a ballast mass. Therefore, the air flow in the tunnel kiln plays the role of both counter-current energy carrier and heat transfer medium.

Historically, air is used as a heat transfer medium in the tunnel kiln, but it has various disadvantages:

- The extraction of at least part of the cooling air is necessary. If all of the cooling air was retained in the kiln, along with the combustion gas from the burners, installed in the preheating and firing zone, the capacity flow ratio between the kiln gas and the counter flowing brick piles would increase strongly. This would lead to high flue gas temperatures and volumes. The necessity of the burners installed in the preheating zone results in the high difference of gas temperature and composition between the top and bottom of the pile, especially in position near the top of high piles. These differences can be equalized by the impulse flow of the high-velocity burner in the firing zone. In the operation of a "modern" tunnel kiln, the necessary cooling air extraction leads to the issue of "kiln-dryer combination" [15]. Even in an older tunnel, cooling air extraction is also essential. In those cases, only a small part of the cooling air is extracted; the majority of cooling air is as large as the combustion gas flow coming into the firing zone.

- The flue gas as a heat transfer ballast mass is extracted relatively cold. It contains unburned carbon oxide [16]. The contained sulphur oxides can only be cleaned up at great expense. By extraction of flue gas in the hot kiln area, gas clean up would not be necessary, as all components would be completely burned. Sulphur oxides (as well as hydrogen fluoride found often in brick factory flue gas) bind easily with lime in hot conditions [17].

- The local volumetric flow of the air (exactly: its capacity flow rate to the mass flow of bricks, so called L/Z-ratio) must be so oriented, that the supposed course of the firing curve can be realized. This is especially important for the cooling zone, as there is no possibility to adjust the firing curve (in this case the cooling curve) through the operation of the burners. Fig. 1.17 shows the effect of the flow capacity ratio on the shape of the firing curve. In most cases, a capacitive flow ratio is close to one in both the preheating and cooling zones.

Temperature curve for flue gas and green ware during **preheating** in counter-flow for different throughput flow ratio L/Z

Temperature curve for cooling air and bricks during **cooling** in counter-flow for different throughput flow ratio L/Z
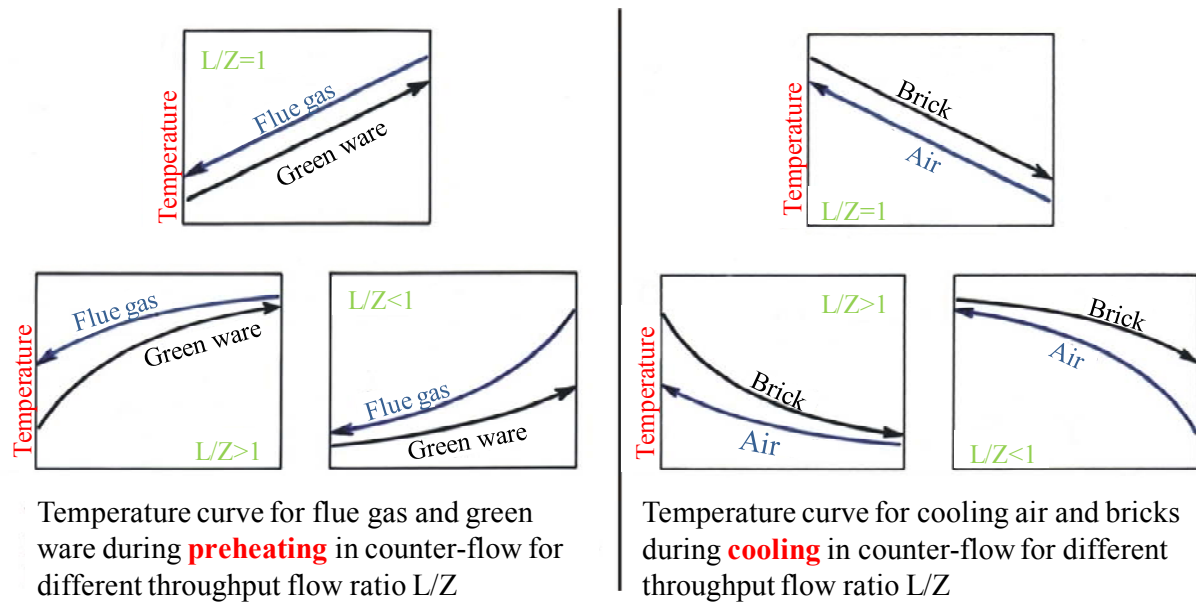
Figure 1.17:   Effects of different capacity flow ratio for the configuration of the firing curves in preheating and cooling zone

The solution to this problem is that the recuperation is not between the product flow and air or flue gas, but between the two counter-travelling product flows [18]. The function of the air and the flue gas in the tunnel kiln is therefore mainly to serve as a heat transfer medium for the two counter travelling solid mass flows, between which heat is transferred. This will be described later.

# 1.4  Counter-travelling tunnel kiln

As discussed above for the brick production process with a traditional tunnel kiln, the real average energy requirement is 2300 kJ/kg of bricks [19, 32]. However theoretically, if the green brick entering into the dryer contains 10% mass moisture [20], the moisture vaporization energy is only 620 kJ/kg of bricks. This means the process efficiency of traditional tunnel kilns is relative low. More energy is used for producing the ballast gas and compensating for the heat loss of the ballast gas transportation from the cooling zone to the dryer. As shown in the process of modern tunnel kiln, much energy is used to preheat the green wares in the preheating zone. Therefore, the disadvantages of solid-gas-recuperation of the tunnel kiln should be replaced by a new process, in which solid-solid-recuperation is the main heat transfer mechanism.

## 1.4.1 Riedel counter-travelling kiln

The first idea for a counter-travelling kiln can be traced back to 1880, but the first attempted kiln construction of this kind was in 1974 by the construction company Riedel, driven by the fuel crisis. This company had begun building traditional tunnel kilns in 1952

[21]. It avoids the disadvantages of the tunnel kiln discussed above, which is dependent on solid-gas recuperation. With solid-solid recuperation, the generation of the ballast gas flow is reduced.

A schematic view of the Riedel counter-travelling kiln is shown in Fig. 1.18 [18]; it consists of two parallel channels with counter travelling product masses. The firing zones of the two channels are located at the same position in the middle of the kiln, and the cooling zone of one channel is located beside the preheating zone of the other channel. The higher the brick pile, the greater the cross sectional convection caused by buoyancy. The large brick pile height produces a higher force for the heat transfer between two channels, which can be relatively easily calculated [21] by development of an effective heat transfer coefficient. This coefficient can be used to calculate the enthalpy transport by the heat transfer driven by natural convection from the solid surface and is described by a transient factor [22]. This allows the hot fired products just coming out from the firing zone of one channel to directly transfer its heat to the unfired green products of the other channel, thus preheating up to the firing zone, and cooling through the cooling zone.

| Cooling zone | ← Firing zone ← | Preheating zone | ← |
| Preheating zone → | Firing zone → | Cooling zone | |
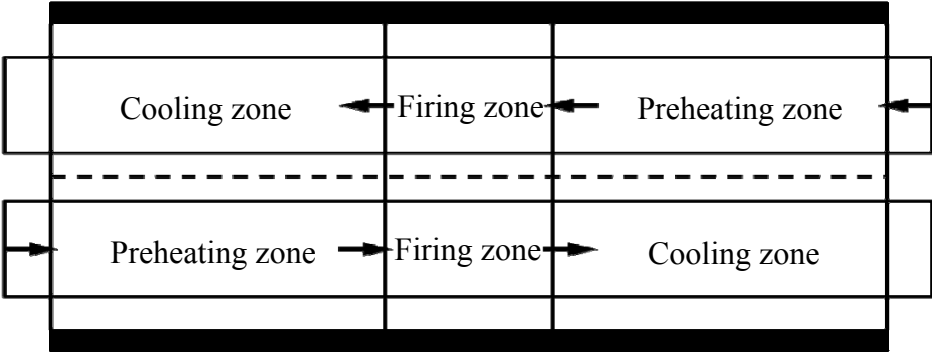
Figure 1.18:    Schematic view of Riedel counter travelling tunnel kiln

The two counter travelling product mass flows form a solid-solid recuperator. In the cross section of both product flows in the kiln channel, recirculated air between both sides take on the function of intermediated-carrier, as shown in Fig. 1.19. It saves heat by absorbing on the hot side and then releases the heat to the cold side. From the viewpoint of the air, there is a regenerative heat exchange depending on the natural convection of the air due to the solid temperature difference on both sides. For the whole process, this is the recuperative heat exchange between the two product flows, but the important thing is to determine the prevailing local heat transfer coefficients.

19
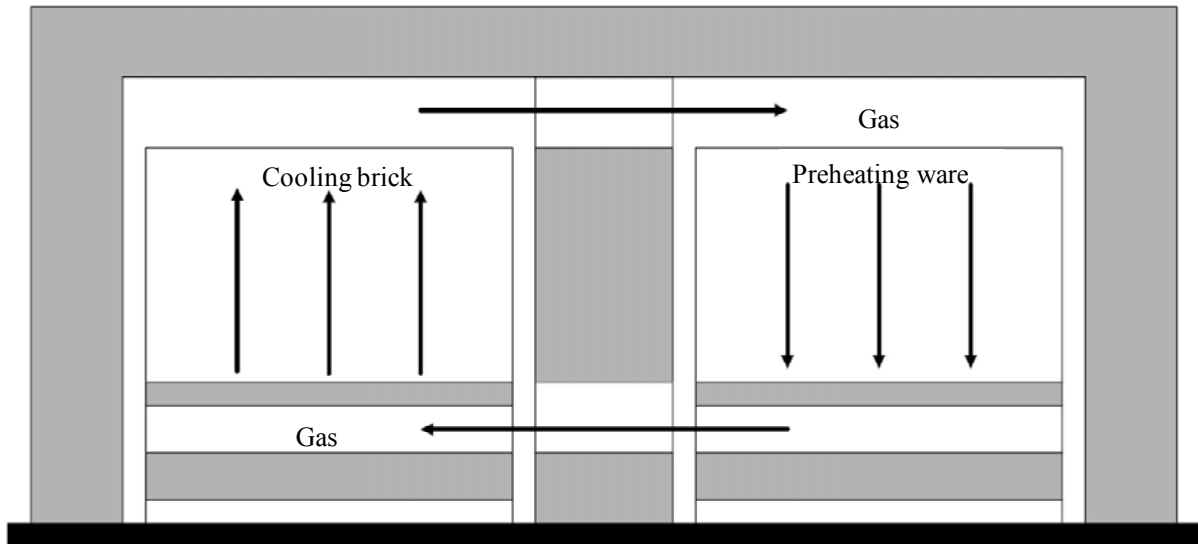
Figure 1.19:   Transverse convection in one cross section through the counter travelling tunnel kiln

A comparison of a Riedel counter-travelling kiln and a conventional tunnel kiln was first carried out in 1979. Under the support of the Federal Ministry of Research and Technology (BMFT) in December 1979, the first Riedel counter-travelling kiln was built and operated until December 1980 as part of a research project. The extensive ranges of measurement data and practical experience were evaluated during 1981. After modifications to the kiln to minimize side effects and improve the process, the new kiln operated again in 1984 and entered into the market in 1985. In 1995 a counter-travelling system was built by the company Riedel at Grechwitz, Germany to fire the different pored hind wall bricks; the Institute of Bricks and Tiles Research Essen (IZF Essen) carried out the extensive measurements and analysis on this system. This study concluded that at that time, while the new system was an alternative process for the conventional tunnel kiln process, there were still some problems to be improved in the Riedel counter-travelling kiln [23].

## 1.4.2 Counter-travelling tunnel kiln with ventilators

As discussed above, there are still some problems in the Riedel counter-travelling tunnel kiln. The main problem comes from the gas recirculation in the cross section. In the Riedel system, the gas recirculation in the cross section is forced by natural convection, which is caused by the solid temperature difference between both channels. This is not steady due to the temperature change of both sides. In order to maintain stable gas recirculation in the cross section, ventilators can be added on the top of the kiln in the preheating and cooling zones. Fig. 1.20 shows this ventilator. The ventilator used here is an example from the company Brackemeier; the ventilator can work under high temperature up to 900°C. With the addition of the ventilator, stable gas recirculation in the cross section can be ensured.
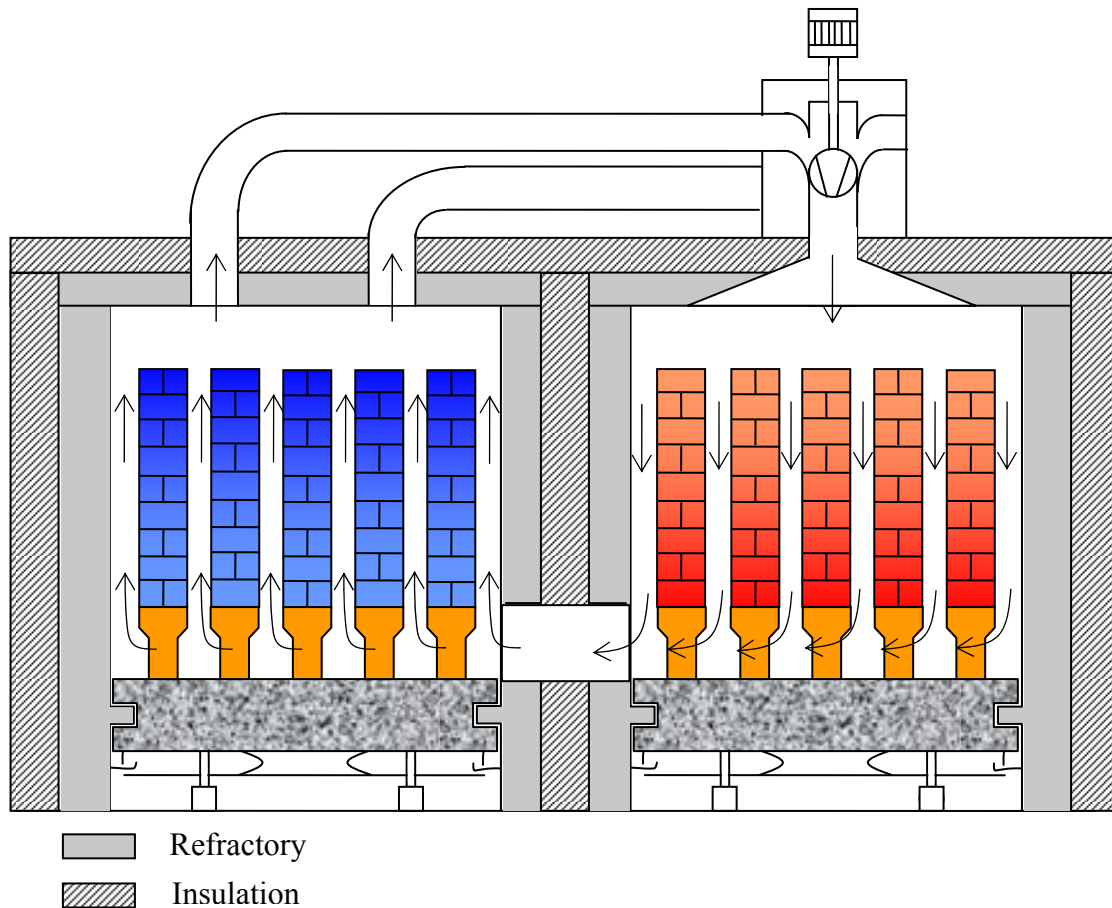
Figure 1.20:    Cross section of counter-travelling tunnel kiln with ventilator

In this counter-travelling tunnel kiln, the heat transfer medium is still air, but the brick piles move in two different transport directions. Ballast air, cooling air extraction and some things corresponding to these are no longer required. Conceivable considerations are flat pile setting, fast firing equipment such as roller kilns or slide construction, very light tunnel kiln cars and others, which are currently also discussed for normal tunnel kilns to increase flexibility and power, and to reduce the energy consumed.

## 1.4.3 Comparison between traditional and counter-travelling tunnel kiln

Fig. 1.21 shows the general principle of counter flowing kilns [24], which includes both conventional tunnel kilns and counter travelling kilns based on the solid-solid recuperation concept. The fundamental difference between the tunnel kiln and the counter-travelling kiln is that in the counter travelling kiln, both mass flows of the counter-current heat exchange act as product mass flows. In the normal tunnel kiln, only one of the mass flows is a product flow, while the other mass flow from the air is a heat capacity flow only. The short connection lines between the temperature curves of the two mass flows show that there is a heat exchange between them.
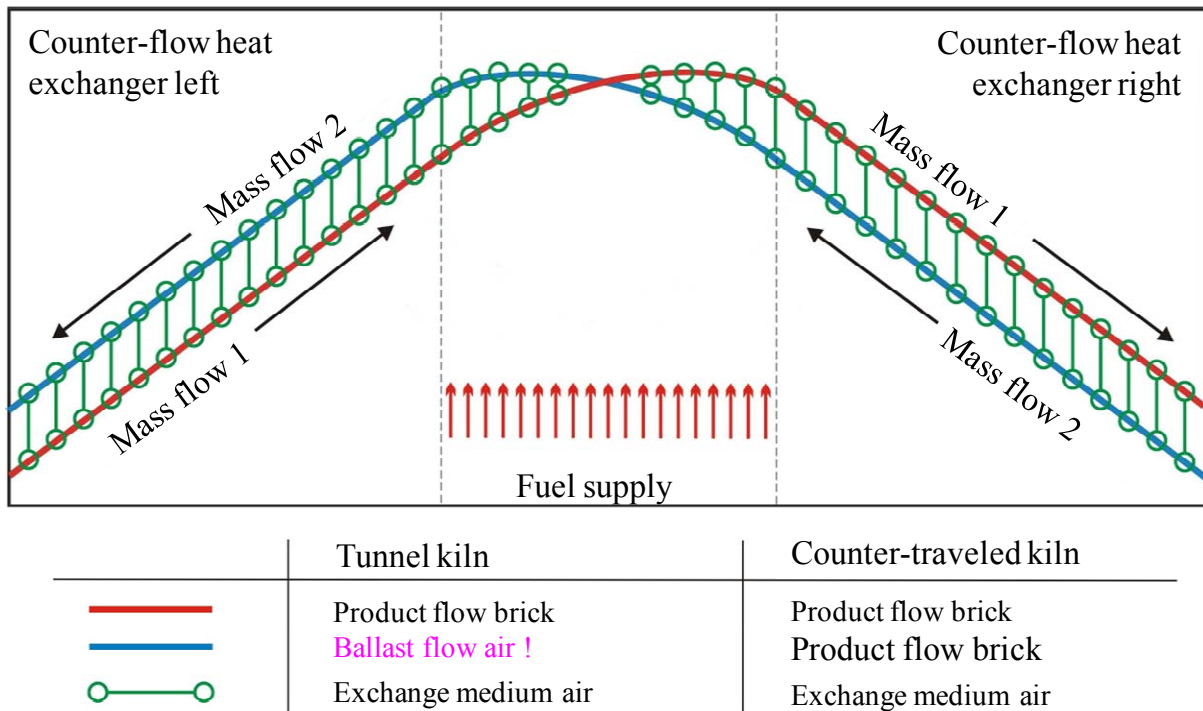
Figure 1.21:    Schematic diagram of counter flow kiln, especially for tunnel kiln and counter travelling kiln

## 1.4.4 Advantages of counter-travelling tunnel kiln

There are also other advantages in a solid-solid counter-flow kiln. These would confront the traditional tunnel kiln and solve all the disadvantages discussed above:

- There is no ballast flow moving through the kiln, but rather product streams moving in the appropriately modified tunnel kiln on an opposite axial.

- There is no flue gas flow released into the environment, whose capacity for a normal tunnel kiln is at least the same as that of the product and whose temperature is very high - it is no longer useful and is in fact contaminated by the flue gas components such as carbonization and sulphur oxides, requiring it to be cleaned up.

- There is also no cooling air extraction, because the cooling, heat-receiving medium here is not the cooling gas, but the product flow moving in the opposite direction, which is heated on the way to the firing zone. This is in fact probably one of the biggest advantages of Solid-Solid recuperation.

- The firing curve configuration of the heating and cooling curves will be approximate symmetrical. However, the heating or cooling speed is adjustable. This can be carried out by increasing or decreasing the heat transfer, for example, through the conveying velocity of hot gas ventilators.

- The flue gases sucked from the firing zone are relatively low in quantity, and they are free of carbonization, and can be cleaned by a low-cost hot desulphurization material if required.

# 1.5 Objective of this work

Due to the pressure from the continuous increases of the energy price, long term introduction of an alternative kiln process is more and more significant. As the first and the most important step to introducing a novel kiln process - a counter-travelling tunnel kiln with ventilators - the necessary calculations and preliminary investigations should be carried out. The primary conditions, which the alternative concepts should fulfill, are those exclusively designed for the bricks and tiles manufacturing in a conventional tunnel kiln: preheating the green ware with adjusted velocity, firing the ware at a constant firing temperature of approximately 1050°C and cooling the fired ware in adjusted velocity. All of these product requirements should be fulfilled. Using convectional tunnel kiln models [22, 25, 26], the mathematical modelling for the solid-solid-recuperation tunnel kiln can be deduced.

The main objectives of this study are listed as follows:

- Building a simplified analytical mathematical model to simulate the cross sectional flow for a counter-travelling tunnel kiln with ventilators. This is based on one standard brick without holes. The influence of all parameters including the gap thickness between bricks in the brick pile, temperature, kiln geometry, throughput, pressure drop and heat transfer are to be investigated. The electrical energy requirement is to be determined.

- Carrying out simulations with a commercial CFD program FLUENT 6.3. This task is to be accomplished in two steps. In the first, 2D simulations are to be carried out to find the pressure drop coefficient of the cross sectional flow and the influence parameters of the ventilator geometry. Then 3D simulations are to be carried out to determinate the pressure drop on the ventilator.

- Verifying the simplified model with numerical calculations. The results of analytical and numerical calculations are to be compared. The transient temperature profiles of both the solid and gas are to be investigated. The temperature profile inside of the solid is also to be determined.

- Analysing the energy balance of the whole kiln. The optimal solid temperature difference between both sides is to be determined. The energy savings and the amortization time for the ventilator investment are to be enumerated.

23

-  Performing the simulation for another product - roof tiles. The effect of a different setting and heat transfer area compared to the standard bricks is to be revealed. The energy savings of roof tiles is to be pointed out.

## 1.6  Summary

The general information on ceramic and ceramic production was presented at the beginning of this chapter. This was followed by the introduction of equipment in ceramic production and a short view of the development of one of the most popular kilns, the tunnel kiln. The process and the state-of-the-art practice and research situation on the Riedel counter-travelling kiln were discussed. Finally, the objectives of this work were enumerated.

# 2. Simplified Mathematical Model

At first, a simplified mathematical model is developed so that the principle process can be described with analytical equations. In order to realize this, the complicated process should be clearly shown and the principle effect of different variables should be illustrated.

## 2.1 Model description

The total model of the kiln is simplified with the description of Fig. 2.1. The recirculation gas in the cold side of the kiln flows from the bottom with temperature $\vartheta_{g,b}$ into the brick gaps. After the gas flows through the gaps, it is cooled down to temperature $\vartheta_{g,t}$ and flows out of the gaps. Then, the gas travels through the ventilators to the other side of the kiln, where the gas temperature remains approximately constant. During flow through the hot brick gaps, the gas temperature is warmed up to $\vartheta_{g,b}$ again.
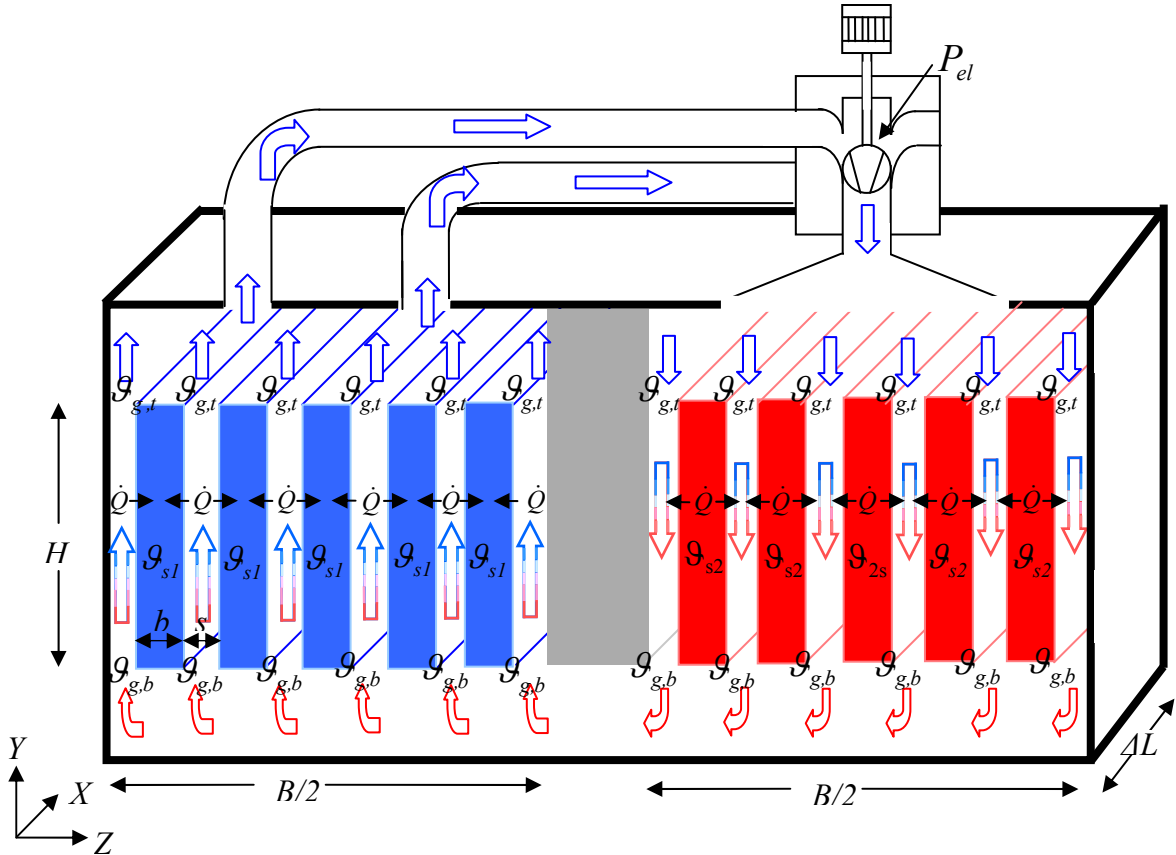


Figure 2.1:     Kiln cross section for the simplified model

The width of the brick gap is $s$, the brick width is $b$ and the brick height is $H$. The width of each kiln part is $B/2$. The length element of the kiln is $\Delta L$. The used coordinate designations are indicated in the figure.

## 2.1.1 Assumptions

Following are the simplifications made for the model:

- The process is assumed to be a steady process; the kiln cars are pushed into the kiln continuously, but not step by step. Thus the temperatures at any cross section remain temporally constant.
- There is no temperature variation along the brick height (*Y*-direction) inside of the bricks, and $\vartheta_{s1}$ and $\vartheta_{s2}$ are the mean temperature of bricks on each side.
- The material properties of the gas are calculated at the mean temperature at the top and bottom of the gap, and are assumed constant.

## 2.1.2 Mathematical equations

An energy balance can be written for each kiln element along the kiln length: in each kiln segment, the transferred heat of the gas through the brick pile gap is equal to the enthalpy change for the bricks along the kiln length.

$$\dot{Q}_g = \dot{H}_s. \tag{2-1}$$

The transferred heat of the gas through brick pile gap is

$$\dot{Q}_g = \dot{M}_g \cdot c_{p,g} \cdot \left( \vartheta_{g,b} - \vartheta_{g,t} \right), \tag{2-2}$$

while the enthalpy change of the bricks along the kiln length is

$$\dot{H}_s = \dot{M}_s \cdot c_s \cdot \frac{d\vartheta_s}{dL}, \tag{2-3}$$

where $\dot{M}_s$ is the mass flow of bricks, which is equal to the throughput of the kiln, $\vartheta_s$ is the mean temperature of the bricks, $c_{p,g}$ and $c_s$ are mean specific heat capacities of the gas and brick respectively. The enthalpy change of the gas is equal to the heat transferred to the brick.

Since the temperature of the brick is assumed to be constant at each position, the temperature change of the gas can be calculated with Newton's capacity model [27]. In each gap on the cold side:

$$\frac{\vartheta_{g,t} - \vartheta_{s1}}{\vartheta_{g,b} - \vartheta_{s1}} = exp\left( -\frac{A \cdot \alpha_{eff.}}{\dot{M}_g \cdot c_{p,g}} \right), \tag{2-4}$$

while on the hot side

$$\frac{\vartheta_{g,b} - \vartheta_{s2}}{\vartheta_{g,t} - \vartheta_{s2}} = exp\left(-\frac{A \cdot \alpha_{eff.}}{\dot{M}_g \cdot c_{p,g}}\right),$$  (2-5)

where

$$A = 2 \cdot H \cdot \Delta L$$  (2-6)

is the heat transfer surface in each gap and $\alpha_{eff.}$ is the effective heat transfer coefficient. Therefore the temperature difference of the gas according to the above equations is

$$\Delta\vartheta_g = \frac{1 - exp\left(-\frac{2 \cdot H \cdot \Delta L \cdot \alpha_{eff.}}{\dot{M}_g \cdot c_{p,g}}\right)}{1 + exp\left(-\frac{2 \cdot H \cdot \Delta L \cdot \alpha_{eff.}}{\dot{M}_g \cdot c_{p,g}}\right)} \cdot (\vartheta_{s2} - \vartheta_{s1}).$$  (2-7)

For this calculation, the mass flow of the gas and the effective heat transfer coefficient are needed and should be determined first. The temperature of the bricks is not constant over the cross section, because of the unsteady cooling and heating, but the temperature appears to have an approximately parabolic profile as illustrated in Fig. 2.2. Thus, the effective heat transfer coefficient includes the convective heat transfer on the surface and heat conduction inside the solid. It is defined as [22]

$$\alpha_{eff.} = \frac{1}{\dfrac{1}{\alpha_{conv.}} + \dfrac{b/2}{\chi \cdot \lambda_s}} .$$  (2-8)

Here $\lambda_s$ is the heat conductivity of the brick and $\chi$ is the transient factor, which dependents on the geometry. For the approximately linear temperature changes of the brick, the values 3, 4, 5 can be taken for the plate, the cylinder and the sphere respectively. Here the value 3 is used for a brick pile as it can be approximated using plate form.
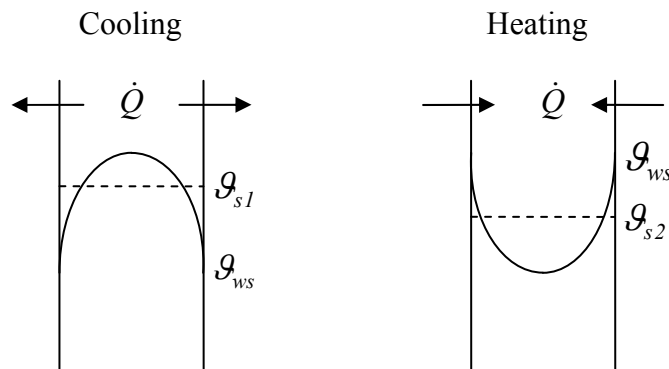


Figure 2.2:     Principle temperature profile in cross section of brick

The convective heat transfer coefficient can be obtained from Nusselt Number *Nu*

$$\alpha_{conv.} = \frac{Nu \cdot \lambda_g}{d_h},$$  (2-9)

where $\lambda_g$ is the mean heat conductivity of the gas and $d_h$ is the hydraulic diameter. The flow between the brick piles can be seen as a rectangular gap. Because the length is relatively much higher than the thickness, the approximation can be used as [28]

$$d_h = 2 \cdot s .$$ (2-10)

For the rectangular gap, the Nusselt functions are [29]:

$$Nu = \sqrt{Nu_{lam.}^2 + Nu_{turb.}^2} ,$$ (2-11)

$$Nu_{Lam.} = \sqrt[3]{3.66^3 + 1.61^3 \cdot Re \cdot Pr \cdot \frac{d_h}{H}} ,$$ (2-12)

$$Nu_{turb.} = 0.0214 \cdot \left( Re^{0.8} - 100 \right) \cdot Pr^{0.4} \cdot \left[ 1 + \left( \frac{d_h}{H} \right)^{0.67} \right] .$$ (2-13)

The Reynolds number is defined as

$$Re = \frac{w_g \cdot d_h}{v_g} ,$$ (2-14)

where $v_g$ is the viscosity of the gas and $w_g$ is the gas velocity inside the gap.

The gas velocity is dependent on the power of the ventilators $P_{el}$ and the pressure drop. They are connected through:

$$P_{el} \cdot \eta_{is} = \dot{V}_g \cdot \Delta p_V$$ (2-15)

Here, $\eta_{is}$ is the efficiency of the ventilators. For the high temperature ventilators used here, the efficiency is usually 0.7.

The total gas volumetric flow depends on the number of brick piles $n$ in the cross section and the length of the kiln segment $\Delta L$:

$$\dot{V}_g = (n + 1) \cdot s \cdot \Delta L \cdot w_g .$$ (2-16)
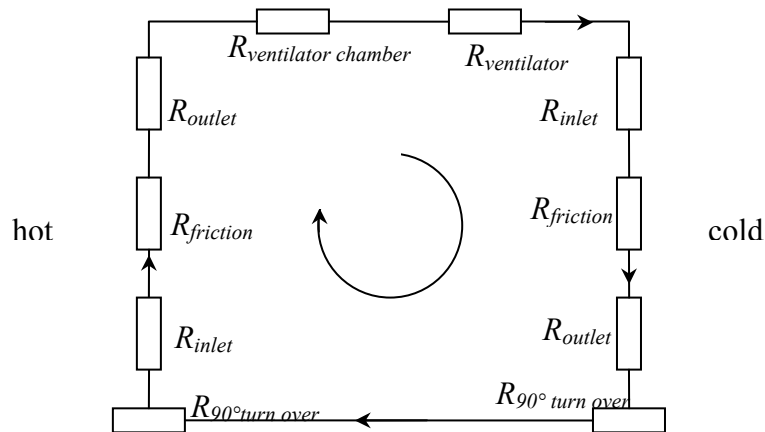


Figure 2.3:    Schematic diagram of the pressure drops in cross section

The gas recirculation pressure drops in the cross section are shown in the Fig. 2.3. After coming out of the ventilator, the gas must flow into the gaps, then after the wall friction, it flows out of the gaps again, undergoing a 90° elbow turn. It then flows to the other side of the kiln, where the gas flows into the gap again, experiences the wall friction, flows out of the gaps again and then must go through the tube to the ventilator. The pressure drop for the flow from one kiln side to the other can be neglected, because here the cross section area is very large and therefore the gas flow velocity is very small. The pressure drops for the total recirculation are therefore as follows

$$\Delta P_v = \frac{1}{2} \cdot \rho_g \cdot w_g^2 \cdot \left[ \left( \xi_1 + \xi_2 + \lambda \cdot \frac{H}{d_h} + \xi_3 + \xi_4 \right)_{left} + \left( \xi_1 + \xi_2 + \lambda \cdot \frac{H}{d_h} + \xi_3 + \xi_4 \right)_{right} + \xi_5 \right] \qquad (2\text{-}17)$$

The pressure drop coefficients of the gas recirculation are displayed in Table 2.1. The values of both fluid turn over and ventilator system were calculated by using commercial CFD package FLUENT 6.3, which will be discussed in a separate chapter.

Table 2.1: Pressure drop coefficient of gas recirculation

| Symbol | Explanation | Left | Right |
|---|---|---|---|
| $\xi_1$ | 90° turn over | 0.1 | 0 |
| $\xi_2$ | inlet | 0.5 | 0.5 |
| $\lambda \cdot \dfrac{H}{d_h}$ | friction in gap | 0.57 | 0.57 |
| $\xi_3$ | outlet | 1 | 1 |
| $\xi_4$ | 90° turn over | 0 | 0.5 |
| $\xi_5$ | ventilator | 9.05 | |

With these equations, the gas velocity inside of the brick pile can be expressed as

$$w_g = \left[ \frac{P_{el} \cdot \eta_{is}}{(n+1) \cdot \rho_g \cdot s \cdot \Delta L \cdot \left( \xi_1 + \xi_2 + \lambda \cdot \frac{H}{d_h} + \xi_3 + \xi_4 + \frac{\xi_5}{2} \right)} \right]^{\frac{1}{3}}. \qquad (2\text{-}18)$$

The material properties for the gas are determined by the mean temperature [27]

$$\overline{\vartheta} = \frac{\vartheta_{g,t} + \vartheta_{g,b}}{2}. \qquad (2\text{-}19)$$

By coupling Eq. (2-4) and (2-5) together, the mean temperature can also be expressed as

$$\overline{\vartheta} = \frac{\vartheta_{s1} + \vartheta_{s2}}{2}. \qquad (2\text{-}20)$$

The temperature dependent material properties can be approximated by the following equations with an error smaller than ± 3% [30]

$$\frac{\rho_g}{\rho_{0,g}} = \left(\frac{T}{T_0}\right)^{-1} ,$$ (2-21a)

$$\frac{c_{p,g}}{c_{p0,g}} = \left(\frac{T}{T_0}\right)^{n_c} ,$$ (2-21b)

$$\frac{\nu_g}{\nu_{0,g}} = \left(\frac{T}{T_0}\right)^{n_\mu+1} ,$$ (2-21c)

$$\frac{\lambda_g}{\lambda_{0,g}} = \left(\frac{T}{T_0}\right)^{n_\lambda}$$ (2-21d)

The exponent indexes for air are compiled in Table 2.2. These values can also be used for the combustion gas.

Table 2.2: Thermo physical material properties of air [30]

| | $\rho_{o,g}$ | $c_{po,g}$ | $n_c$ | $\nu_{o,g}$ | $n_\mu$ | $\lambda_{o,g}$ | $n_\lambda$ |
|---|---|---|---|---|---|---|---|
| **Value** | 1.29 | 1000 | 0.10 | $13.5 \times 10^{-6}$ | 0.67 | 0.025 | 0.76 |
| **Unit** | kg/m$^3$ | J/kg·K | - | m$^2$/s | - | W/m·K | - |

With the equation series explained above, the power of the ventilators can be calculated as functions of geometric parameters and process parameters.

$$P_{el} = f\left(b, n, s, H, \Delta L, \Delta \vartheta_s, \dot{M}_s\right)$$ (2-22)

The geometric parameters are: brick pile width $b$, brick height $H$, number of the brick piles $n$ in each side and gap thickness $s$. And the process parameters are: kiln length $\Delta L$ for one ventilator, temperature difference between both kiln sides $\Delta \vartheta_s$ and the brick throughput $\dot{M}_s$. The effects of these parameters will be discussed in the following sections.

## 2.1.3 Calculation algorithm

The flow chart for the calculation is shown in Fig. 2.4. As shown, the simulation starts at the position when $l = 0$, where the green brick just enters into the kiln. Here the mean gas temperature is calculated first. Different ventilator powers $P_{el}$ are tested to calculate the heat transfer, until the heat transferred from the gas flow through the brick pile gap is equal to the enthalpy needed for the solid in this kiln element $\Delta L$ along the kiln length direction. After that, the next iteration will be continued at the next kiln position, until all the kiln positions are finished.

With the above described model, a series of simulations have been carried out. The influence of all parameters including the gap thickness, temperature, kiln geometry, throughput, the pressure drop, and heat transfer had been investigated. The electrical energy requirement has thereby been determined.
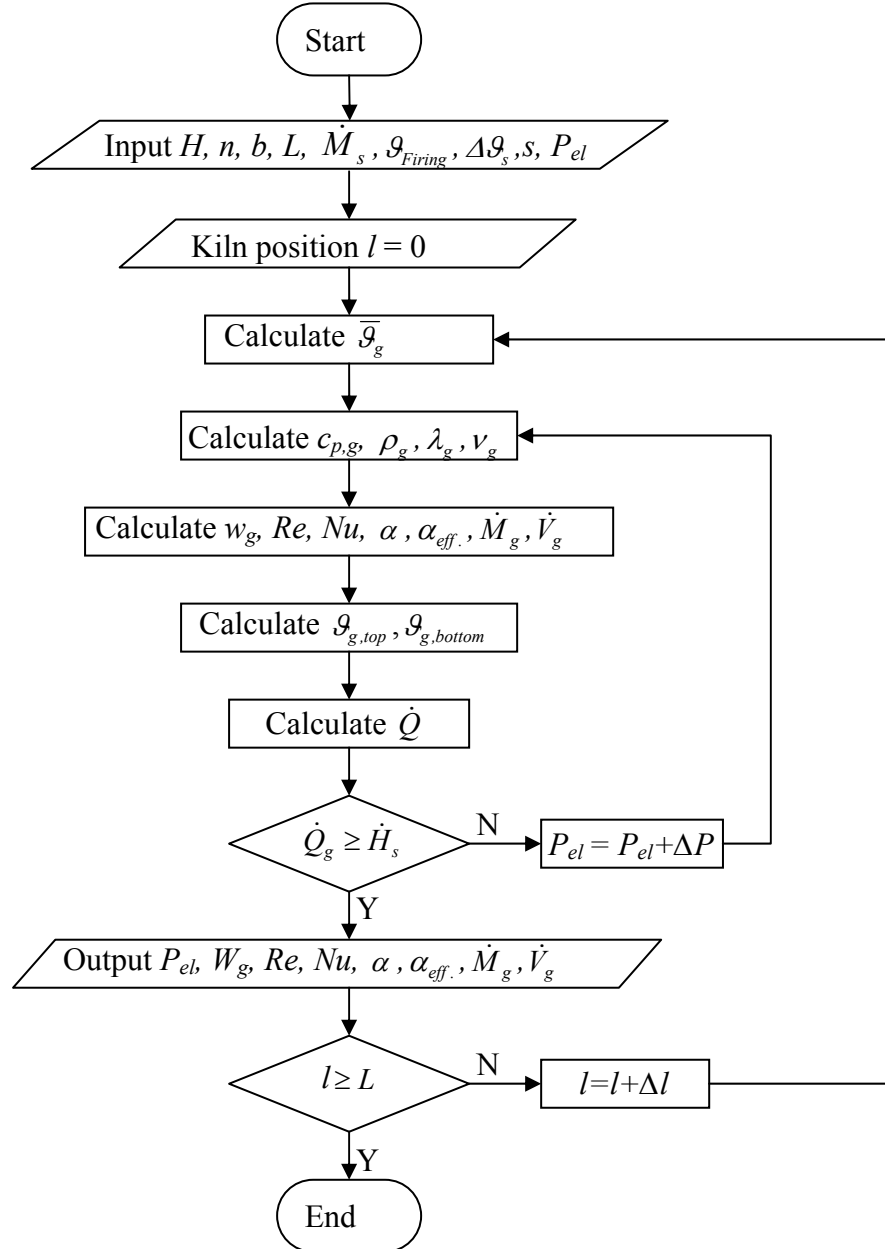


Figure 2.4:     Flow chart for the calculation algorithm

# 2.2  Power of ventilators

## 2.2.1 Reference tunnel kiln

The width of the whole brick pile is dependent on the width of a single brick; Fig. 2.5 shows the brick dimension and the brick pile width with a standard single brick as an example. Here a single standard brick with the dimension of 71x120x240 mm is shown.
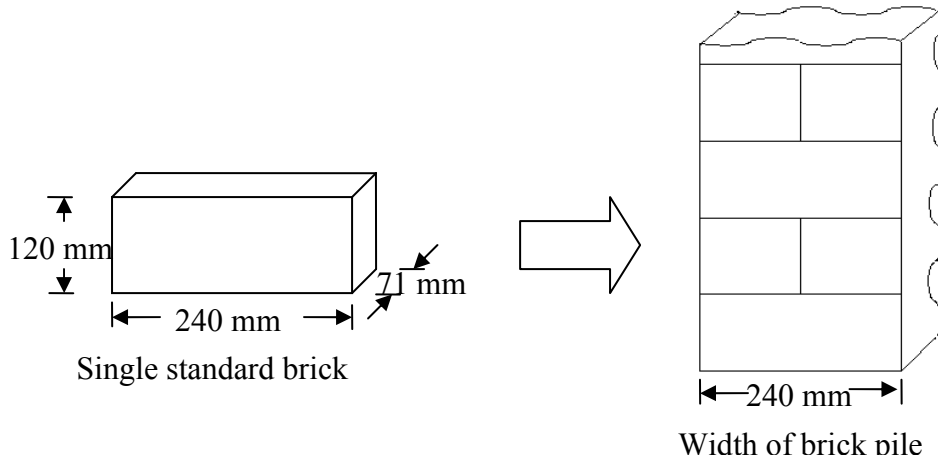
Figure 2.5: Width of whole brick pile and single standard brick

To simulate the effects of the parameters, a typical tunnel kiln is used as a reference. The cross section of this kiln is shown in Fig. 2.6.
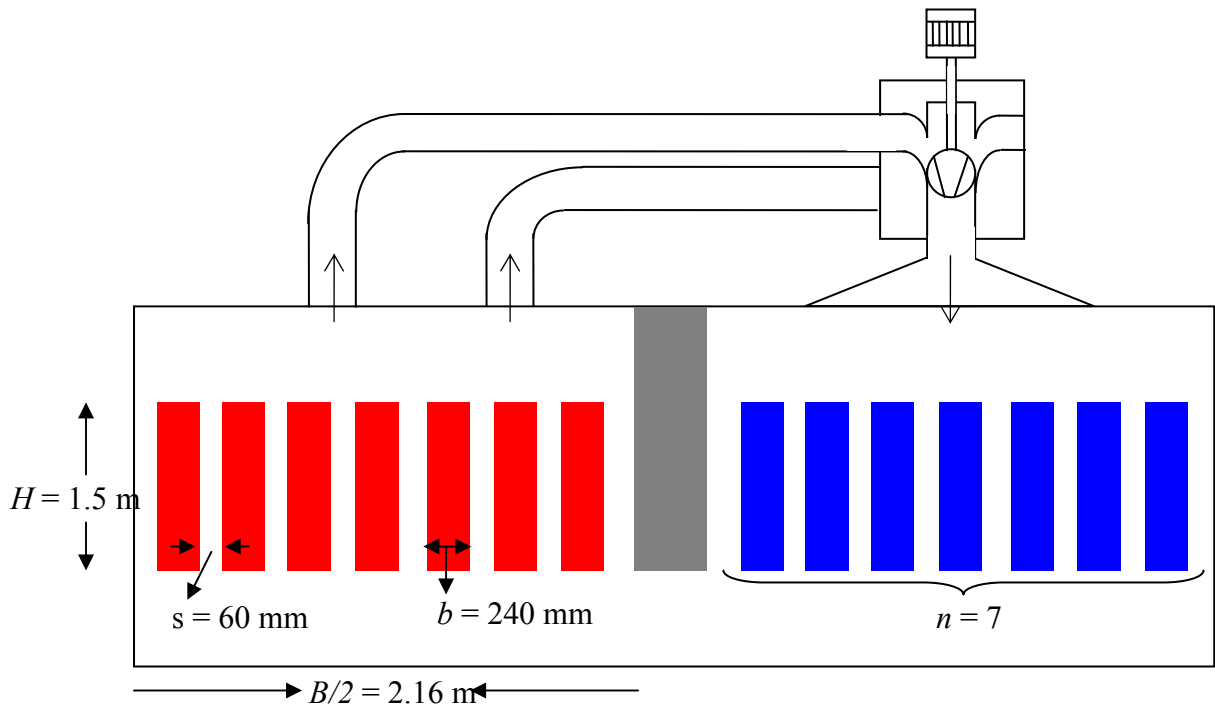


Figure 2.6: Cross section of reference kiln

It can be seen that the height of the brick pile is 1.5 m, the width of the brick pile is 240 mm, the gap thickness between the two brick piles is 60 mm and the number of brick piles per side is 7. Therefore, the kiln width of each part is 2.16 m.

In Fig. 2.7 the length view of reference kiln is shown. The whole length of this kiln is 110 m. It is divided into three parts: preheating and cooling zones are each 50 m in length respectively from either end of the kiln and the remaining 10 m in the middle comprise the firing zone. The firing temperature is 1050°C and the entry temperature is 25°C. The

temperature difference between both sides is 160 K. The brick throughput is 8 t/h. These data are compiled again in Table 2.3.
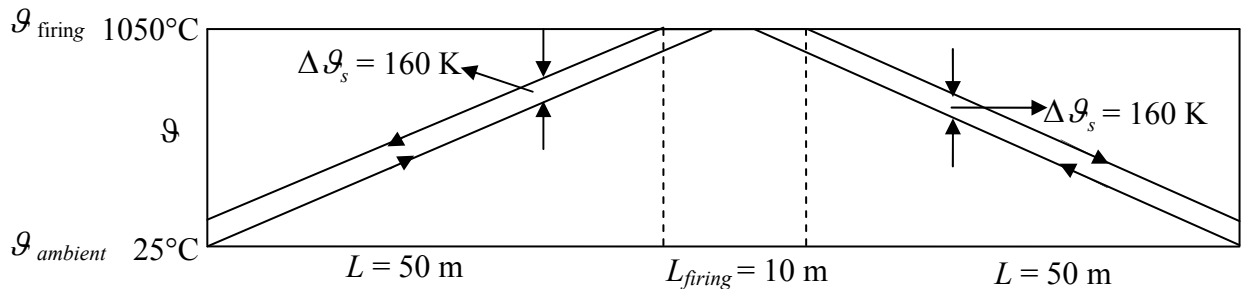


Figure 2.7:    Length view of reference kiln

Table 2.3:    Data of reference kiln

| Symbol | Explanation | Value | Unit |
|---|---|---|---|
| $\dot{M}_s$ | Throughput of brick | 8 | t/h |
| $L$ | Kiln length | 110 | m |
| $b$ | Brick pile width | 0.24 | m |
| $B$ | Kiln width | 4.32 | m |
| $n$ | Number of brick piles | 7 | - |
| $s$ | Gap thickness | 0.06 | m |
| $H$ | Height of the brick pile | 1.5 | m |
| $\Delta\vartheta_s$ | Temperature difference of both sides | 160 | K |

## 2.2.2 Ventilator power per length

First, the ventilator power per length is investigated, because this can determine heat transfer and furthermore the operation mechanism of the kiln. In Fig. 2.8 the dependence of the ventilator power on the brick pile gap thickness is shown, with the gas temperature as a parameter. The curves are principally the same shape. It is shown that in the range from 1 to 2 cm, there is a minimum value, which is expressed by a dashed line. The minimum value is based on the connection between the volumetric flow and pressure drop. When the gap thickness is decreased from very large to small values, the ventilator power decreases. This is the effect of the decrease of the volumetric flow; while it is shown that if the gap further decreases than the optimal value, the ventilator power increases again, this is due to the effect of an increase in the pressure drop of the gas recirculation. The higher the gas temperature, the higher the gas viscosity and lower the gas density, and therefore, a lower enthalpy flow is transported. This must be compensated for with a higher ventilator power.
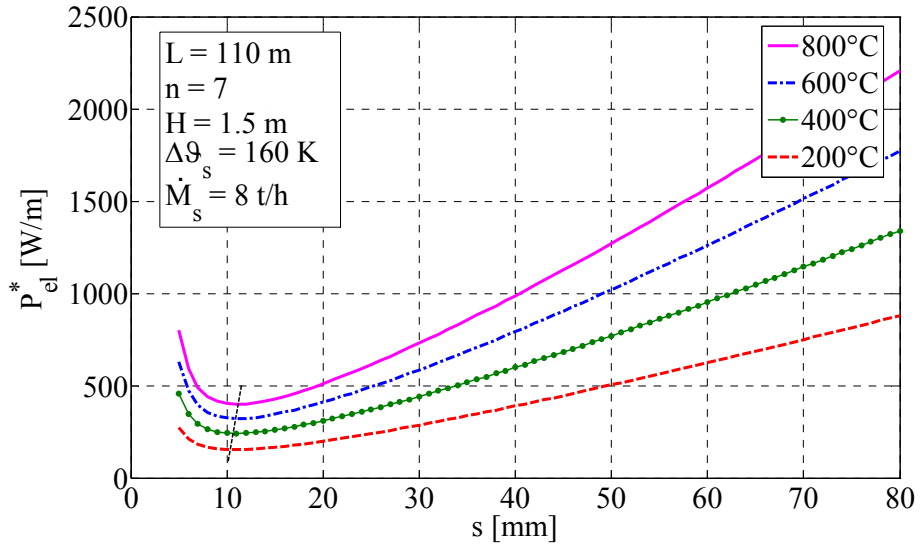
Figure 2.8:     Ventilator power per length at different gap thickness and gas temperatures

In Fig. 2.9 the variation of ventilator power with temperature is shown. A gap thickness of 60 mm represents the typical brick pile setting value, while a gap thickness of 20 mm represents the optimal value. The top scale in the figure shows the kiln length at the appropriate temperature. It can be seen that the ventilator power increases approximately linearly with the temperature.
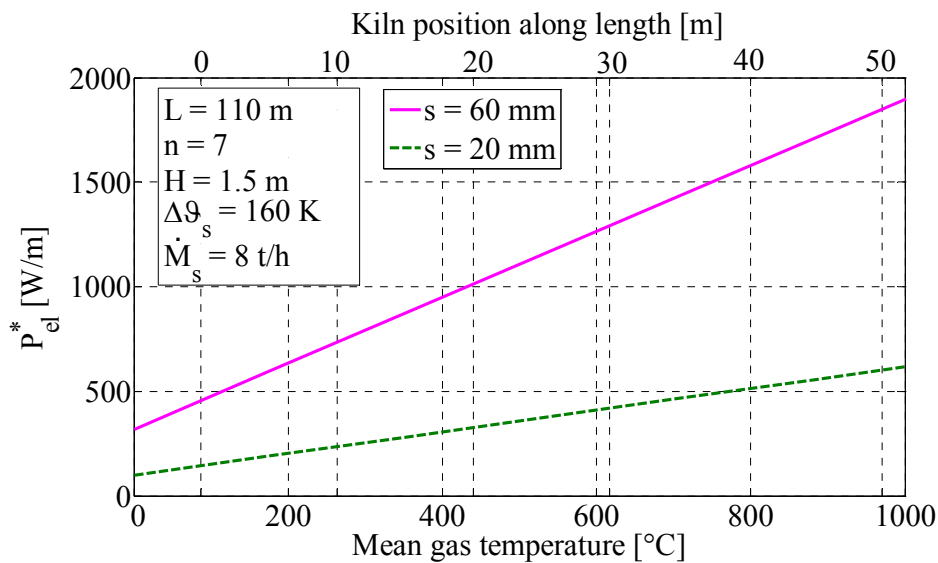


Figure 2.9:     Variation of ventilator power on temperature

The phenomenon of the minimum is further explained through the following. Fig. 2.10 shows the dependence of the gas flow velocity through the gaps on the gap thickness at different temperatures. The gas velocity decreases slowly with the decrease in brick gap thickness until around 10 to 20 mm, where it increases very rapidly. The higher the gas temperature is, the higher the gas velocity inside the gap.
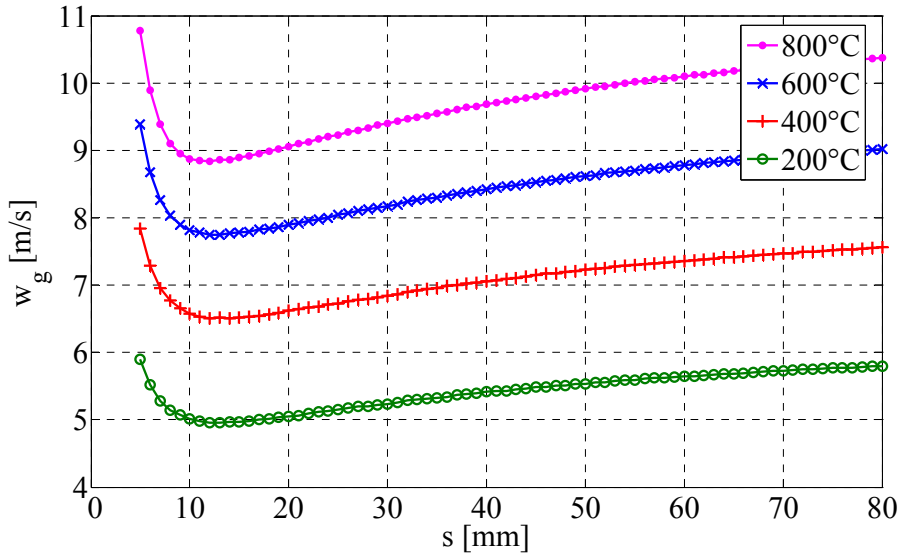
Figure 2.10: Gas velocity in the gap between the brick piles

In Fig. 2.11, the corresponding heat transfer coefficients are shown. Two values are displayed: the value of the pure convective heat transfer α and the effective heat transfer $\alpha_{eff}$, which includes the heat conduction inside the bricks. The values at thicknesses above 20 mm are almost constant. The decrease of the heat transfer coefficient induced by the reduction of the gas velocity is here further kept approximately constant, due to the decrease of the appropriate Nusselt functions Eq. (2-11) to (2-13). By a very small gap thickness, smaller than 20 mm, the heat transfer coefficient increases very fast with the decrease in gap thickness. The reason is that in this region, the gas velocity inside the gap also increases very fast with the decrease of the gap thickness. It also indicates that the influence of the gas temperature for the heat transfer coefficient can be neglected.
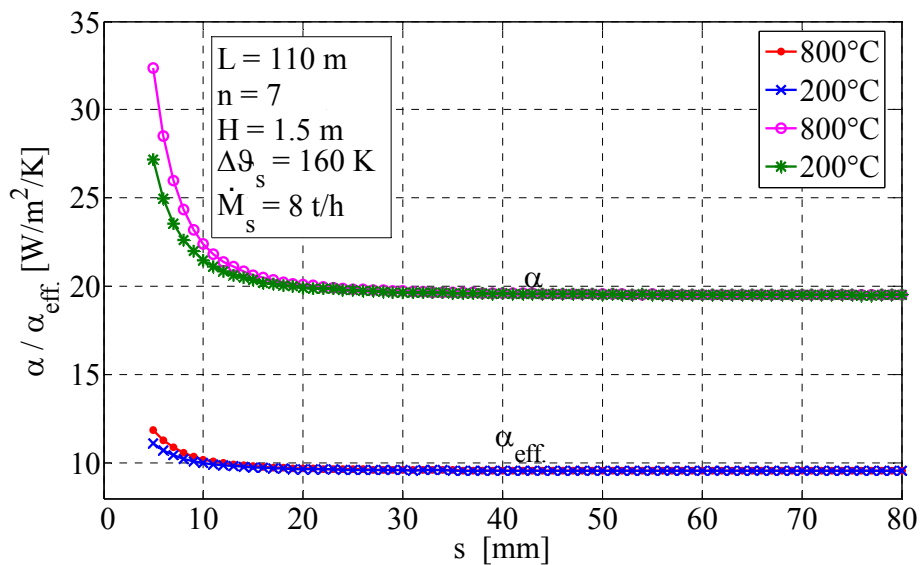


Figure 2.11: Convective and effective heat transfer coefficient in gaps

In Fig. 2.12, the gas temperature difference on the top and bottom of the gap is shown, analogous to those shown before. With the decrease in gap thickness, the temperature difference increases continuously. When the gap thickness is bigger than 20 mm, the temperature difference is smaller than 30 K. It is obviously smaller than the average temperature difference between the bricks of the both kiln sides, which is 160 K. It is also shown that the influence of the gas temperature can be neglected again. Due to this low gas temperature difference, gas recirculation between both kiln sides through natural convecction is impossible. This is not discussed further in detail in this chapter.
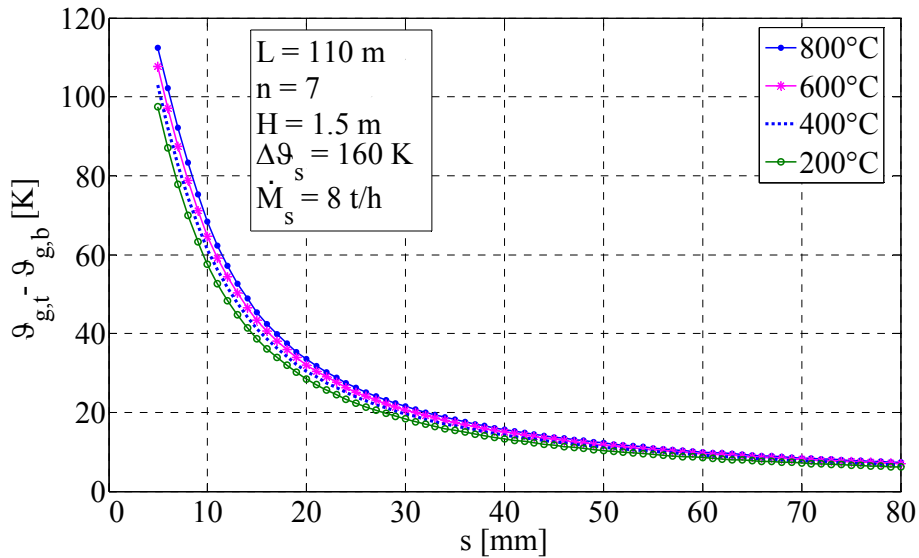


Figure 2.12: Gas temperature difference between top and bottom of the brick pile

In Fig. 3.13, the total pressure drop in the whole cross section recirculation is shown. The change tendency dependent on the gap thickness and the gas temperature is analogous to the change tendency of the gas temperature difference. When the gap thickness is smaller than 20 mm, the pressure drop increases very rapidly with the reduction of the gap thickness.
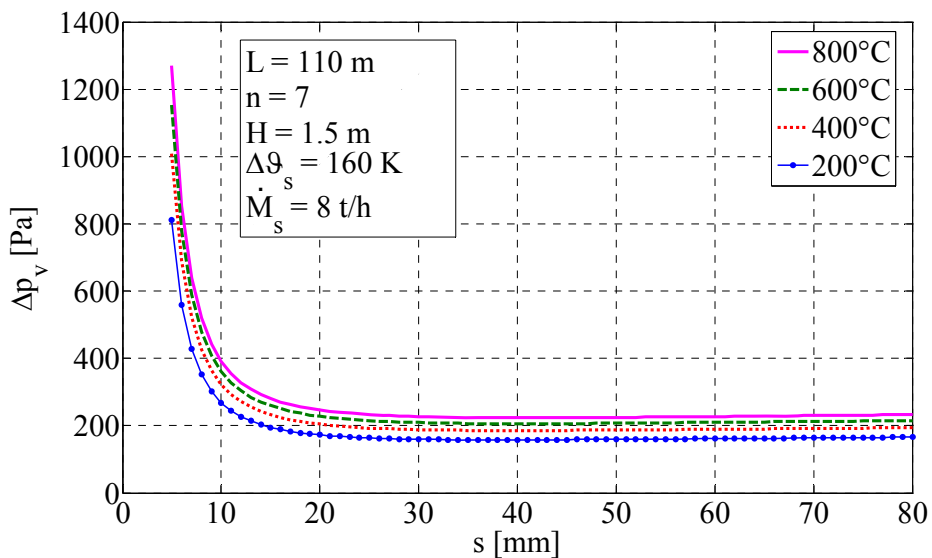


Figure 2.13: Pressure drop in the whole cross section recirculation

36

In Fig. 2.14, the volumetric flow of gas in the cross section between the both kiln sides is shown. The volumetric flows increase almost linearly with the increase in gap thickness. The higher the gas temperature is, the higher the volumetric flow is.
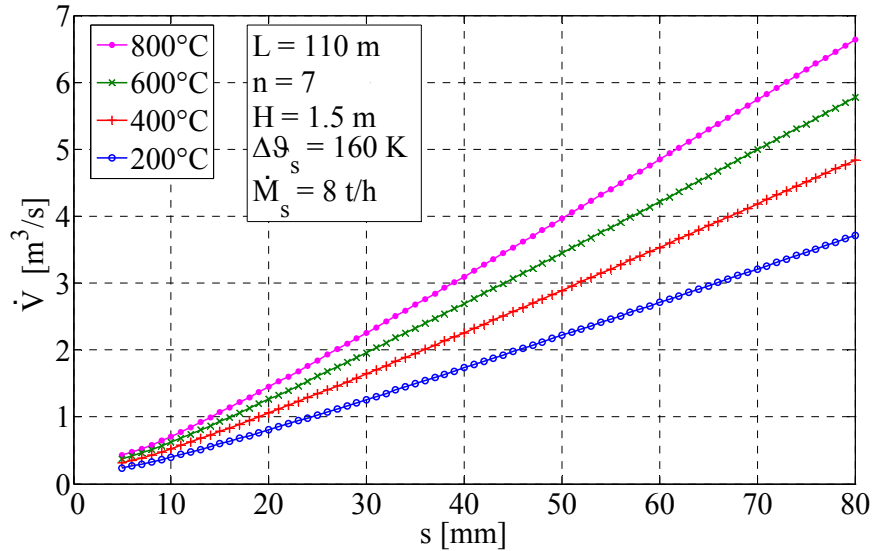


Figure 2.14:    Volumetric flow of the gas in the cross section between the both kiln sides

The power of the ventilator is proportional to the product of the pressure drop and volumetric flow. From the above figures, the following conclusion can be drawn: when the gap thickness is larger than 20 mm, both of the pressure drop and volumetric flow decrease with the reduction in gap thickness, causing the ventilator power to decrease as well. When the gap thickness is smaller than 20 mm, the pressure drop increases rapidly; this leads to an increase in the ventilator power. This is dependent on the gas temperature, because the volumetric flow also depends on gas temperature.

## 2.2.3 Total ventilator power

To evaluate the kiln process, the total ventilator power is very important. Here, the ventilator power per length must be integrated along the kiln length

$$P_{el} = \int_{0}^{L} P_{el}^{*} \cdot dL \,.$$  (2-23)

The dependence of the total ventilator power on the gap thickness is shown in Fig. 2.15. It states that for the entire kiln, the minimum also located in the range between 10 to 20 mm. At the typical gap thickness of 60 mm, the total ventilator power is around 120 kW, while in the minimum range, the value is only one fourth that of the typical gap thickness. Because the electrical power per length for the ventilator increases linearly dependent on the temperature as shown in Fig. 2.9, the total ventilator power can be obtained approximately through

$$P_{el} = P_{el}^{*}(\vartheta_{m}) \cdot L \,,$$  (2-24)

where $\vartheta_m$ is the mean temperature along the kiln length, which is around 500°C.
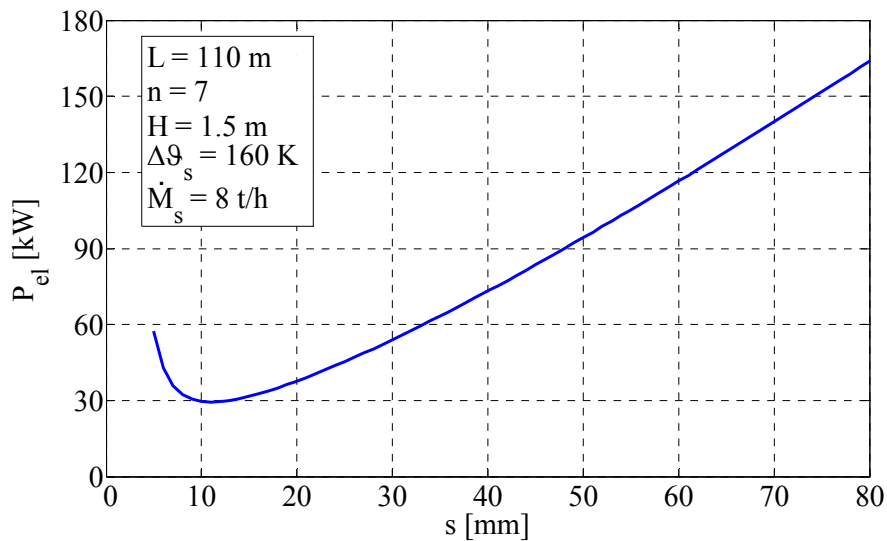


Figure 2.15:    Total ventilator power of the basic kiln

## 2.2.4 Geometry influence

In the following figures, the influence of kiln geometry on the total ventilator power will be investigated. The following parameters will be investigated:  the number of brick piles, the brick piles' height, and the kiln length.

Firstly, the influence of the number of the bricks piles and, as a result, kiln width is investigated. Fig. 2.16 illustrates the total ventilator power dependent on gap thickness for different numbers of brick piles for 6, 7, and 8, respectively. The minimum is located in the range from 10 to 20 mm again. The larger the width is, the lower the ventilator power is. This can be explained in that with the increase of the kiln width, a larger surface area for heat transfer is available.  Therefore, a smaller heat transfer coefficient and thus a lower flow rate are sufficient for the enthalpy transport.
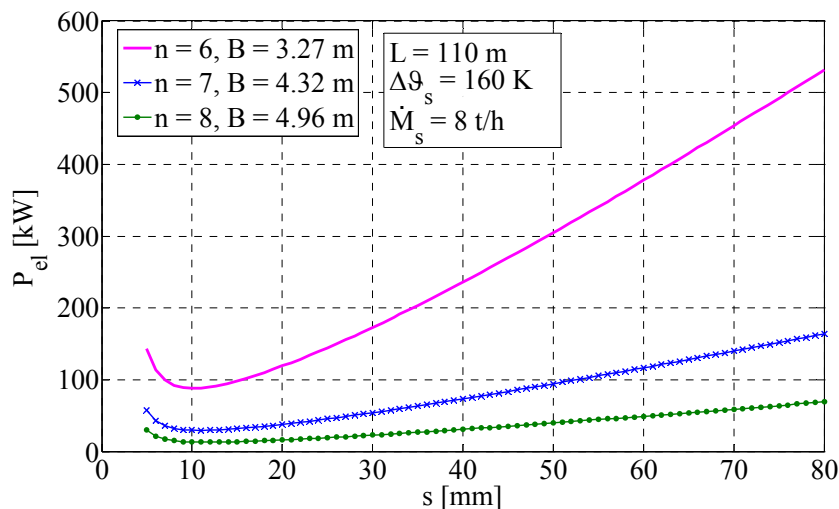


Figure 2.16:    Ventilator power for three different kiln widths

38

In Fig. 2.17 the variation of the total ventilator power on the number of brick piles is shown, again displaying the two characteristic gap thicknesses of 20 and 60 mm. The appropriate kiln width dependent on the number of bricks piles are given on the top scale of the figure. From this figure it can be seen that with the reduction in the number of brick piles, the ventilator power increases exponentially. A reduction of the number of piles from 7 to 6 doubles the ventilator power required. An increase of the brick pile number from 8 to 9 decreases the ventilator power only by a small amount.
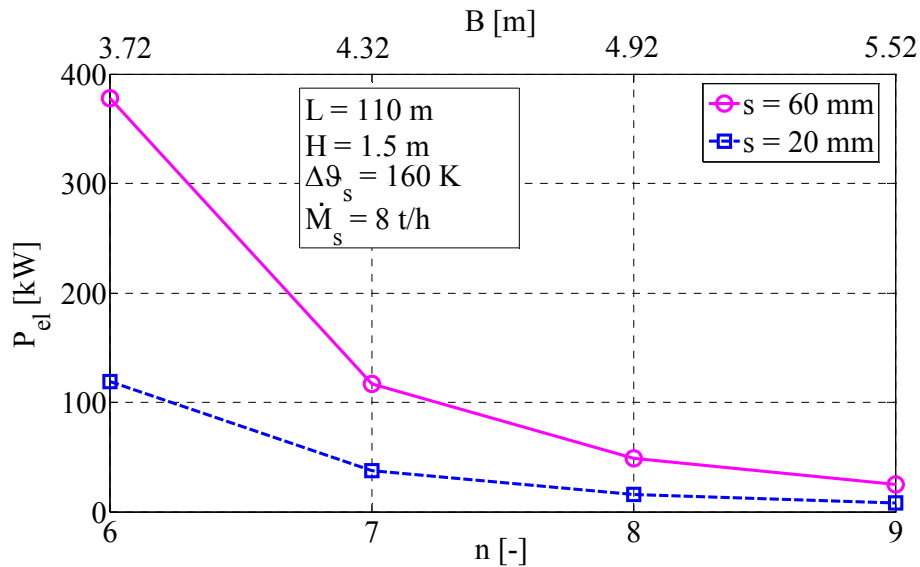
Figure 2.17:   Ventilator power dependent on the numbers of the brick pile

In Fig. 2.18 the total ventilator power is shown for the example brick heights of 1.3 m and 1.5 m. The higher the brick pile is, the lower the ventilator power is. This can be explained again by the increase of the heat transfer area.
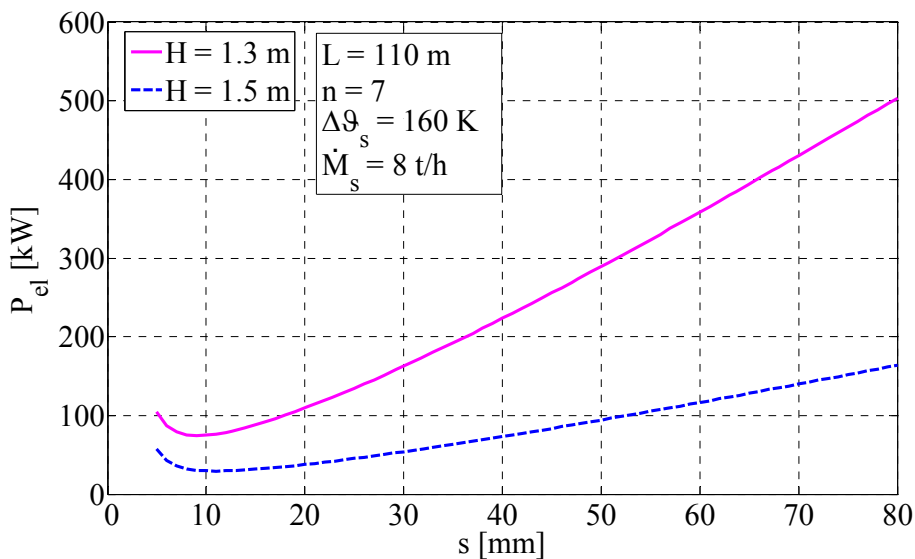
Figure 2.18:   Ventilator power for two different kiln heights

The throughput of the kiln is related to the kiln geometry by

$$\dot{M}_s = \rho_{s,s} \cdot A_k \cdot w_s,$$ (2-25)

where $\rho_{s,s}$ is the setting density of the bricks piles and $w_s$ is the moving velocity of the kiln car. This is the result of the kiln length and the moving time

$$w_s = \frac{L}{t}.$$ (2-26)

The cross sectional area of the kiln is

$$A_k = n \cdot (b+s) \cdot H.$$ (2-27)

Fig. 2.19 compares the ventilator power for different pile numbers and heights, which are selected so that the cross section of the kiln is kept constant. This figure reveals that the ventilator power is independent of both the brick pile number and the brick height, as long as the cross section remains constant. Whether many piles with shorter height or fewer piles with higher heights are set, there is no significant difference in viewpoint of ventilator energy.
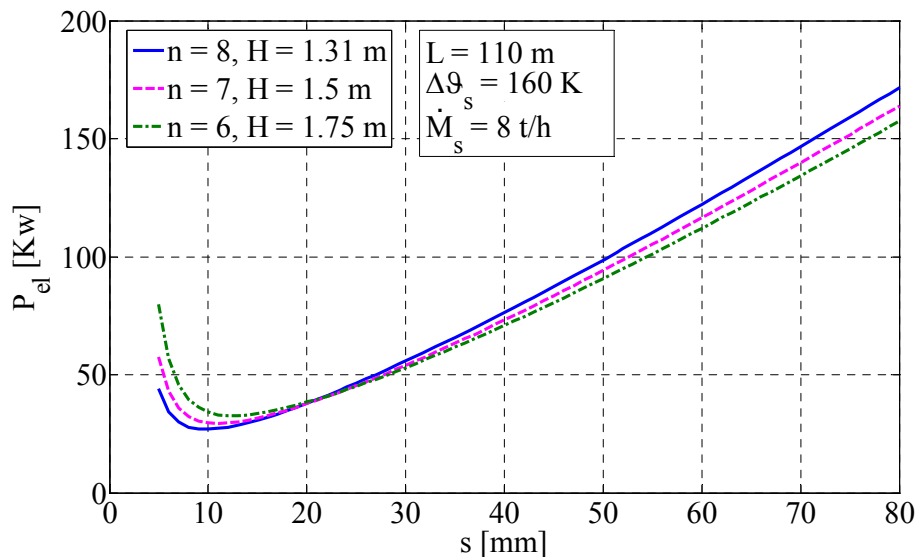


Figure 2.19:   Influence of cross section form on the ventilator power

The influence of the kiln length on the ventilator power is presented in the Fig. 2.20. The throughput is kept constant. The longer the kiln is, the lower the ventilator power is. The reason could be the higher heat transfer surface area in the longer kiln. It shows that the bigger the kiln volume, the smaller the ventilator power required. However, if the total energy consumption is taken into consideration, the heat lost from the kiln wall will increase in the kiln with a larger volume.
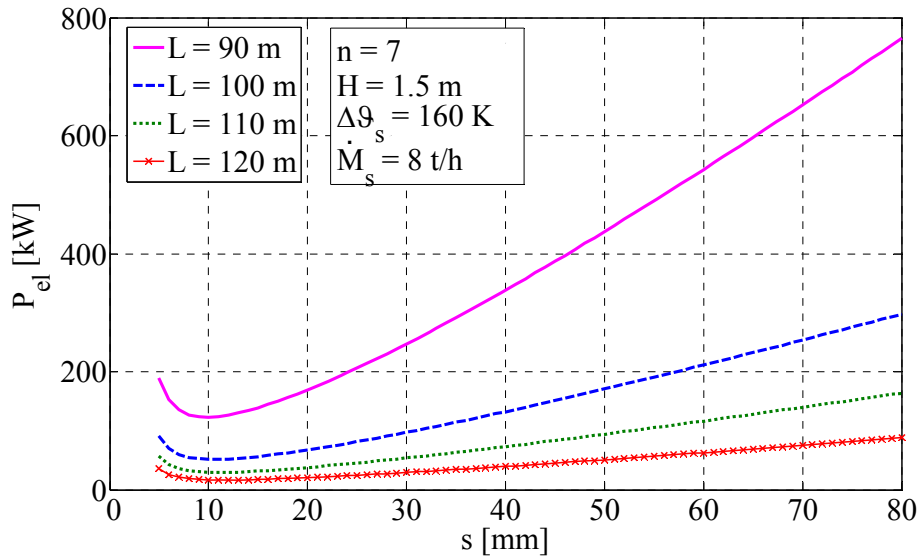
Figure 2.20:    Influence of kiln length on the ventilator power

In Fig. 2.21 the ventilator power for different kiln lengths is illustrated, while the kiln volume is kept constant. The longer the kiln is, the smaller its cross sectional area is, which decreases the number of brick piles. From this figure, it can be seen that the combination of width and length of the kiln have no significant influence, as long as the kiln volume remains the same.
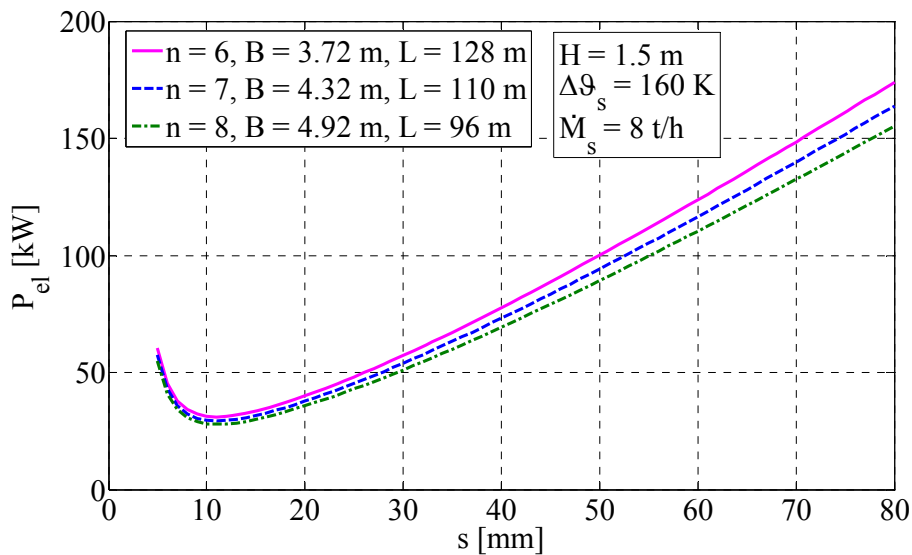


Figure 2.21:    Ventilator power for different kiln length by the same kiln volume

## 2.2.5 Influence of the throughput

In Fig. 3.23 the ventilator power depending on throughput for both the characteristic gap thicknesses are shown. Here it appears that the ventilator power increases exponentially with the increase in throughput. Up to the interpretation case of 8t/h, the increase is still relatively small; after that case the increase becomes very large.
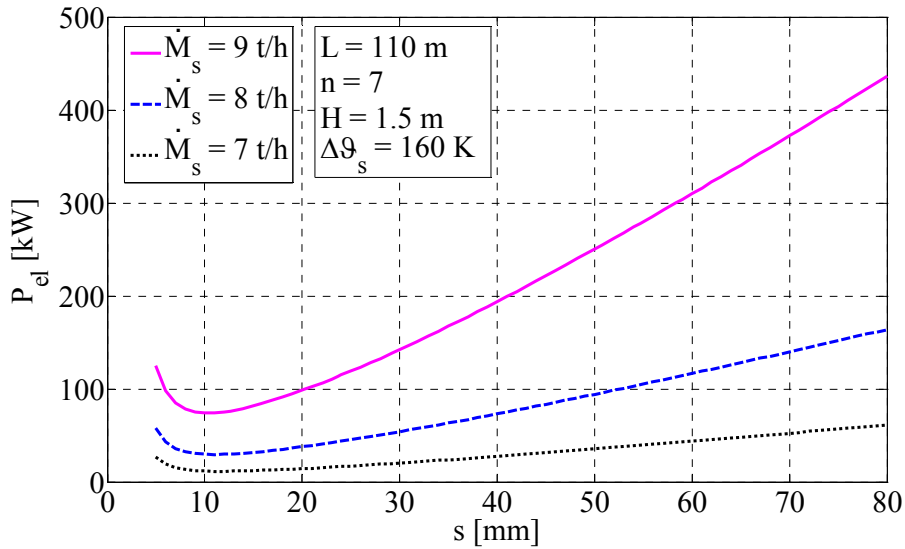
Figure 2.22:    Ventilator power of reference kiln for three different throughputs

In Fig. 3.23 the ventilator power depending on throughput for both the characteristic gap thicknesses are shown. Here it appears that the ventilator power increases exponentially with the increase of the throughput. Up to the interpretation case of 8 t/h, the increase is still relatively small, after that the increase becomes very big.
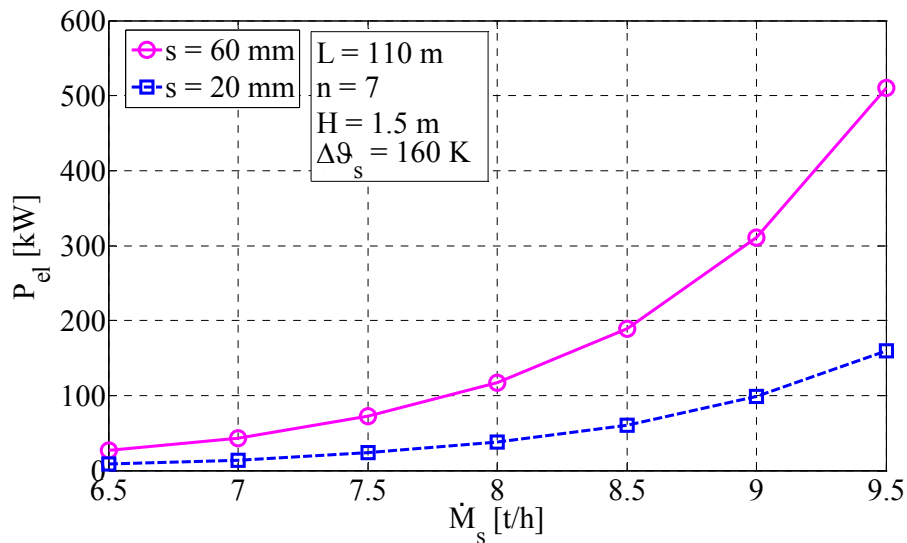


Figure 2.23:    Ventilator power depending on throughput

## 2.2.6 Influence of temperature difference

As the last parameter, the bricks' temperature difference between the both kiln sides $\Delta\vartheta_s$ is investigated.  In Fig. 2.24 the ventilator power dependence on the gap thickness is shown again, with the bricks temperature difference between the both sides $\Delta\vartheta_s$ as parameter. The minimum is located again in the range between 10 to 20 mm. The higher the temperature

difference $\Delta\vartheta_s$ is, the lower the heat transfer volumetric flow required, and therefore the lower the required ventilator power is.
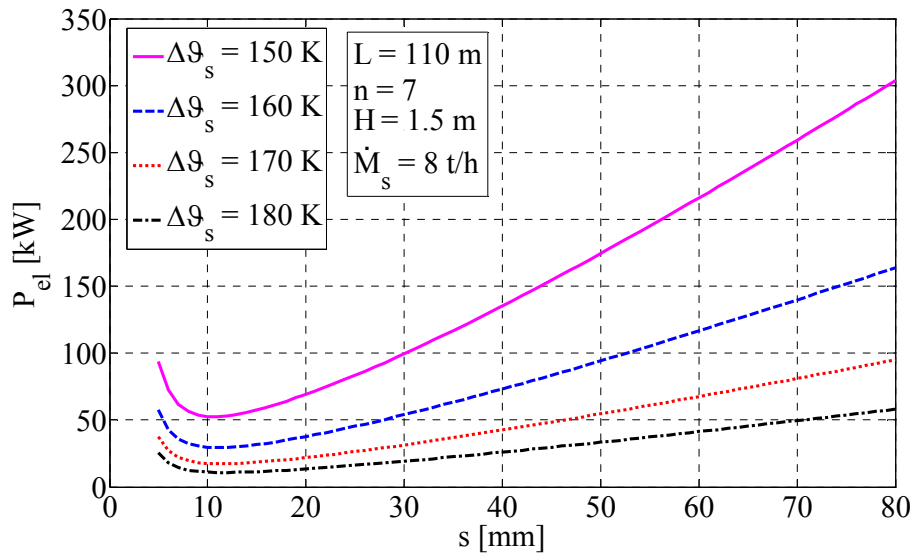


Figure 2.24: Ventilator power for given temperature differences of both kiln sides

# 2.3  Fossil fuel energy consumption

The energy consumption of the fossil fuel is also dependent on the temperature difference of both kiln sides, which will be shown in the following section. In order to determine this energy consumption, the total energy balance of the kiln should be made. The energy flows are shown in Fig. 2.25.
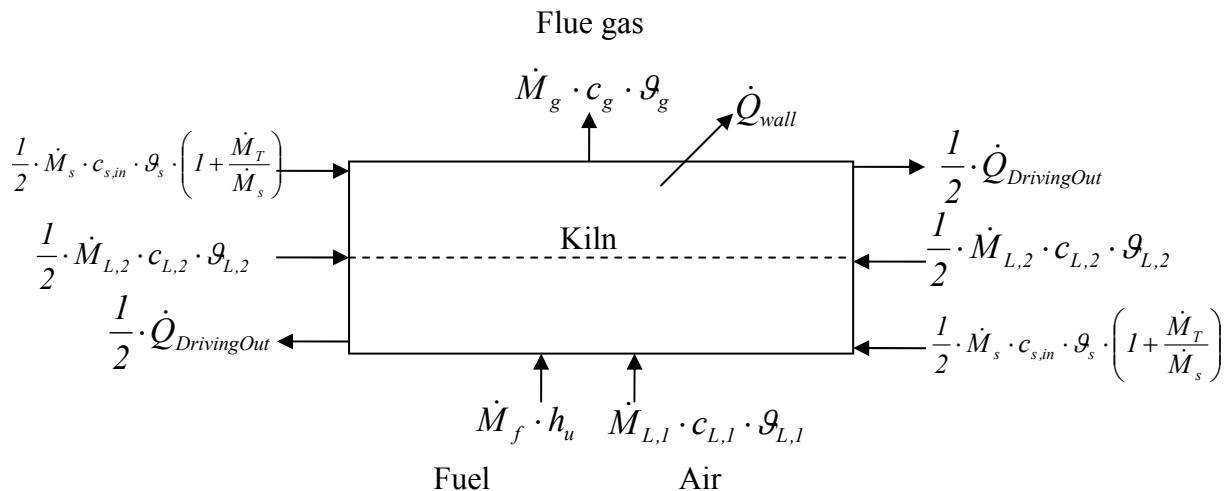


Figure 2.25: Energy flow of the kiln

In the kiln, with the input of the fuel, the energy $\dot{M}_f \cdot h_u$ is provided. At the same time, the air flows are also supplied. Air flow 1 is supplied from the burners for the combustion of the natural gas. Air flow 2 will be supplied in the kiln length direction. These air flows

transfer the rest of the moisture and carbonization gases of the bricks into the firing zone. The portions of these air flows are defined by excess air number $\lambda$

$$\dot{M}_{L1} = \lambda_1 \cdot L \cdot \dot{M}_f , \tag{2-28}$$

$$\dot{M}_{L2} = \lambda_2 \cdot L \cdot \dot{M}_f , \tag{2-29}$$

where $L$ is the stochiometic air demand of the fuel. Air flow 1 can also be preheated by the flue gas. The heat loss of the flue gas is

$$\dot{Q}_g = \dot{M}_g \cdot c_{p,g} \cdot \vartheta_g , \tag{2-30}$$

with $c_{pg}$ defined as the mean specific heat capacity. The mass flow of the flue gas is

$$\dot{M}_g = \left[ 1 + (\lambda_1 + \lambda_2) \cdot L \right] \cdot \dot{M}_f . \tag{2-31}$$

The driving out heat loss from the bricks is

$$\Delta \dot{H}_s = (\dot{M}_s + \dot{M}_T) \cdot c_s \cdot (\vartheta_{s,out} - \vartheta_{s,in}) . \tag{2-32}$$

Here, $\dot{M}_s$ and $\dot{M}_T$ are the mass flow of the brick and kiln cars respectively, $c_s$ is the mean specific heat capacity, and $\vartheta_{s,out}$ and $\vartheta_{s,in}$ are the exit and entrance temperature of the bricks. The temperature of the kiln car is not known. Therefore, the temperatures of the bricks are used to estimate the kiln car temperature. The kiln wall heat loss is $\dot{Q}_W$. Thus, for the energy balance, the following equation is valid

$$\dot{M}_f \cdot h_u + \dot{M}_{L1} \cdot c_L \cdot \vartheta_{L1} + \dot{M}_{L2} \cdot c_L \cdot \vartheta_{L2} = (\dot{M}_s + \dot{M}_T) \cdot c_s \cdot (\vartheta_{s,out} - \vartheta_{s,in}) + \dot{M}_g \cdot c_{p,g} \cdot \vartheta_g + \dot{Q}_W . \tag{2-33}$$

With the above equation, the specific energy consumption of the fuel can be obtained

$$\frac{\dot{M}_f \cdot h_u}{\dot{M}_s} = \frac{(1 + \dot{M}_T / \dot{M}_s) \cdot c_s \cdot (\vartheta_{s,out} - \vartheta_{s,in}) + \dot{Q}_W / \dot{M}_s}{1 + \dfrac{\lambda_1 \cdot L \cdot c_L \cdot \vartheta_{L1}}{h_u} + \dfrac{\lambda_2 \cdot L \cdot c_L \cdot \vartheta_{L2}}{h_u} - \dfrac{\left[ 1 + (\lambda_1 + \lambda_2) \cdot L \right] \cdot c_{p,g} \cdot \vartheta_g}{h_u}} . \tag{2-34}$$

The temperature difference between the entrance and the exit of the bricks must be the same as the temperature difference between both sides of the kiln

$$\vartheta_{s,out} - \vartheta_{s,in} = \vartheta_1 - \vartheta_2 = \Delta \vartheta_s . \tag{2-35}$$

Due to the possibility of flue gas heat recuperation, the energy balance of the whole kiln for three cases is shown; the material properties used for these three cases are shown in Table 2.4.

Table 2.4: Material properties for the energy balance of the whole kiln

| | $\lambda_1$ | $\lambda_2$ | $L$ | $h_u$ | $\vartheta_{L,1}$ | $\vartheta_{L,2}$ | $\vartheta_g$ | $\vartheta_{s,in}$ | $c_{L,1}$ | $c_{L,2}$ | $c_g$ | $c_s$ |
|---|---|---|---|---|---|---|---|---|---|---|---|---|
| | - | - | $\dfrac{kg_L}{kg_f}$ | $\dfrac{MJ}{kg}$ | °C | °C | °C | °C | $\dfrac{kJ}{kg \cdot K}$ | $\dfrac{kJ}{kg \cdot K}$ | $\dfrac{kJ}{kg \cdot K}$ | $\dfrac{J}{kg \cdot K}$ |
| a | 1 | 0.3 | 15 | 45 | 25 | 25 | 500 | 25 | 1.00 | 1.00 | 1.09 | 835 |
| b | | | | | 200 | | 300 | | | | | |
| c | 0.9 | 0.2 | | | 200 | | 300 | | | | | |

44

Natural gas is used as the fuel. The specific heat loss from the kiln wall will be the value from the real production processes:

$$\dot{Q}_W / \dot{M}_s = 0.1 \ MJ/kg. \tag{2-36}$$

The mass flow of the kiln car related to the bricks can be expressed as

$$\dot{M}_T = 0.33 \cdot \dot{M}_s . \tag{2-37}$$

The heat losses for the three cases described in Table 2.4 are illustrated in Fig. 2.26. The driving out heat loss and the flue gas increase linearly with the increase of the temperature difference between both sides $\Delta \vartheta_S$; that is to say that they increase linearly with the increase of the driving out temperature of the brick.

The higher the temperature difference $\Delta \vartheta_S$, the higher the temperature the bricks have when they move out of the kiln. Therefore, the driving out temperature is also high. This contains not only the enthalpy of the brick, but also of the kiln car. According to experience, the driving loss of the kiln car is 1/3 of the brick according to Eq. (2-37). In Fig. 2.26 the specific driving out loss of the brick including the driving out loss of the kiln car and the flue gas loss are shown. The specific driving out loss increases linearly with the increase of the temperature difference.
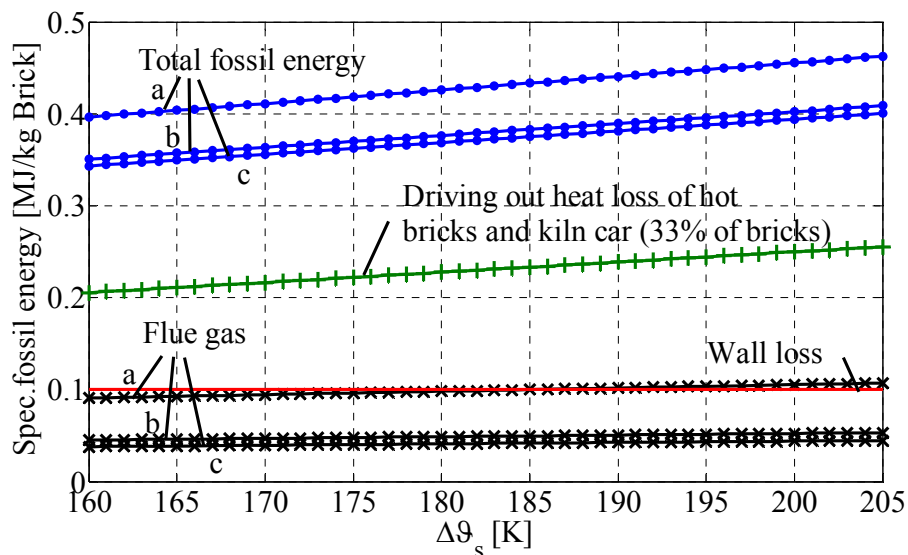


Figure 2.26:   Energy flow of kiln depending on the temperature difference of both sides

On the contrary, the specific ventilator energy decreases exponentially with the increase in temperature difference. As a result, an optimal temperature difference $\Delta \vartheta_S$ should be found, at which the total energy consumption is minimal.

## 2.4  Total energy consumption

The total energy consumption for the kiln process will be investigated. It is the sum of the fossil fuel energy and electrical ventilator energy. For the comparison of these two different energies, the electrical energy of the ventilator must be converted into the primary energy. Specific ventilator power $E_{vent.}$ is found using the efficiency of the power plant $\eta_{el}$

$$E_{vent.} = \frac{P_{el}}{\dot{M}_s} \cdot \frac{1}{\eta_{el}}. \tag{2-38}$$

The general average efficiency of a German power station is around 35% [31]. For economic views, although the cost ratio of the electricity and natural gas must be used as for typical fossil fuel, there is a fluctuation in the free market. Therefore, the consideration of the electricity generation efficiency and furthermore the energy investigation is restricted, because they are only temporally stable. The ratio of electricity and natural gas per kWh is insignificantly higher than the primary energy expenditure by a factor of three.

Fig. 2.27 shows the total specific energy requirement of the kiln dependent on the bricks' temperature difference between both sides $\Delta\vartheta_S$, which is the sum of the fuel energy and the primary energy of the ventilator power. Here the fossil fuel energy is not equal to the primary energy, but the fossil energy efficiency is more than 90% and therefore in this research work, the difference between the fossil energy and primary fossil energy is neglected.
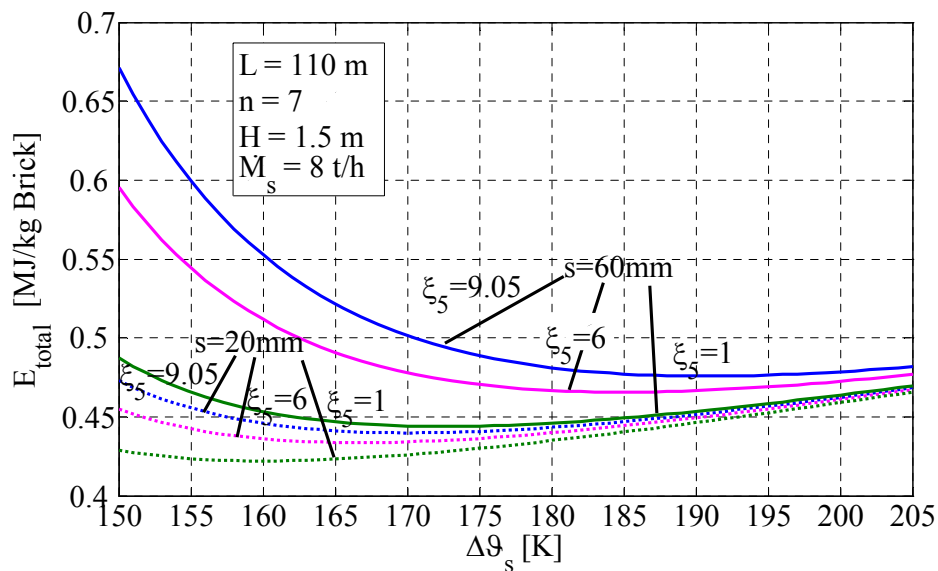


Figure 2.27:    Sum of the fossil energy and primary ventilator power

According to the FLUENT simulations (more details in Chapter 3), the pressure drop coefficient $\xi_5$ of the 3D ventilator is 9.05; however, for the 2D simulation $\xi_5$ is equal to 1.12. This value is strongly dependent on the geometry of the ventilator, and furthermore influences the total energy of the entire process. Here, $\xi_5$ as a parameter from 1-9.05 is displayed. It is shown that there is a minimum value for the total energy when the bricks' temperature

difference between both sides $\Delta\vartheta_S$ is in the range of 160°C to 190°C. The course of the curve within this range is very flat, so the exact adjustment of the temperature difference is not so crucial; this makes the operation of the kiln easier. Compared to the fossil fuel energy, the ventilator power is relatively small.

According to the scientific research, the average specific energy consumption for the clinker bricks in Germany is 2.3 MJ/kg of brick [19, 32]. It consists of 1.05 MJ/kg for the dryer and 1.25 MJ/kg for the kiln process [32]. The total energy consumption shown in Fig. 2.27 reveals that when $\xi_5$ is equal to 9.05, the optimal temperature difference between both sides is 190 K and 175 K for a gap thickness of 60 mm and 20 mm respectively, and the energy consumption for the kiln process with the solid-solid recuperation tunnel kiln is 0.47 MJ/kg and 0.43 MJ/kg respectively. Therefore, the energy savings for the kiln process is 62% and 66% respectively.

# 2.5 Summary

With the simplified model, the new tunnel kiln with solid-solid-recuperation can be already be expressed with relatively good approximations. The ventilator power is strongly dependent on the gap thickness $s$. The minimal ventilator power happens at a gap thickness between 10-20 mm. Such small gap thicknesses cannot be set by the robot in the real industry. Usual setting distances of the brick pile are around 60 mm. At this setting distance, the ventilator power is four times higher.

For the geometrical design, the ventilator power depends only on the volume of the kiln. The larger is the volume, the higher the initial investment cost is, but the ventilator power required is lower. Whether the kiln is built wider, taller, or longer has no influence, so long as the cross sectional area or the volumes remains the same.

The energy consumption of the tunnel kiln is determined by the sum of the primary ventilator energy and fossil fuel energy, both of which are dependent on the bricks' temperature difference between both sides $\Delta\vartheta_S$. The sum of the energies depending on temperature difference between both sides $\Delta\vartheta_S$ is shown with both characteristic gap thicknesses as a parameter. Here it is revealed that for the total energy consumption, there is a minimum for each gap thickness. This is located for a gap thickness of 20 mm at 175 K and for a gap thickness of 60 mm at 190 K. An energy savings of 66% or 62% respectively can be reached for the kiln process.

47

# 3. CFD Simulation

The pressure drop of the gas recirculation must be as small as possible and the recirculation in the cross section must be homogenous. The flow was investigated with one of the CFD software packages: FLUENT. Two dimensional (2D) and three dimensional (3D) simulations were carried out. It should be investigated to what extent the real flow can be approximated with a two dimensional approach, because the flow through an entire kiln with a total length of 100 m should be represented in 2D. However, the ventilators work in a 3D situation, and therefore, 3D simulations were also carried out.

## 3.1 CFD and FLUENT introduction

### 3.1.1 CFD

With the development of computer and information technology, CFD is used more and more in the engineering and aerodynamics field. CFD, which stands for Computational Fluid Dynamics, is a technique to run the "virtual" experiment on a computer for the actual simulation of engineering flow. Its results can predict the behaviors, heat transfer, mass transfer, and chemical reactions of the flow. It provides comprehensive data, which are not easily obtainable from the real experiments, for new designs, product development, troubleshooting, and modification of an engineering process or piece of equipment.

The fundamental mechanism of CFD can be explained as follows: The investigated domain is divided into a large number of finite control volumes. According to the fundamental law of flow mechanics, the flow behaviors of the studied volume taken with its adjacent volumes can be solved through a series of coupled, non-linear partial differential equations. These governing equations are the mass conservation equation and momentum conservation equation, as well as the energy conservation equation if necessary. These equations are not able to be solved analytically for most engineering problems, but it is possible to obtain an approximate computer-based solution.

There are a lot of commercial CFD software packages, including FLUENT, CFX and ANSYS. All of these software packages include three major steps: pre-processor (to define the investigation domain), solver (to solve the coupled, non-linear differential equations) and post-processor (to report the final results).

In this study, only FLUENT was used to simulate the gas flow recirculation in the kiln cross section and the gas flow in the firing zone with combustion. However, comparison with the results from other CFD software is also necessary in the industrial application.

## 3.1.2 FLUENT

Fluent uses CFD codes based on the finite volume method for solving transport equations for mass, momentum and energy conservation. The basic idea of the finite volume method is to satisfy the integral form of the conservation law to some degree of approximation for each of many contiguous control volumes, which cover the research domain. Here the domain is divided into a finite set of computational cells as control volumes, as shown in Fig. 3.1.
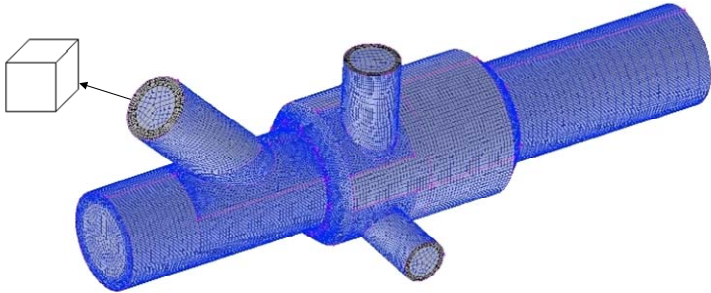


Figure 3.1:     Research domain divided into finite set of control volumes

The control volumes can be divided using triangular or quadrilateral elements for 2D cells; for 3D cells, tetrahedrons, hexahedrons, prisms/wedges and pyramids are used. These cell types are shown in Fig. 3.2. All types of meshes can be adapted in FLUENT, and the type of element used dependents on the geometry of the domain and the simulation cost. The mesh can be generated by GAMBIT, TGrid, or any one of the CAD systems. In this study, the grids are generated by GAMBIT and exported into FLUENT to solve.



Triangle                Ouadrilateral
(a) 2D cell types

Tetrahedron        Hexahedron        Prism / wedge        Pyramid
(a) 3D cell types
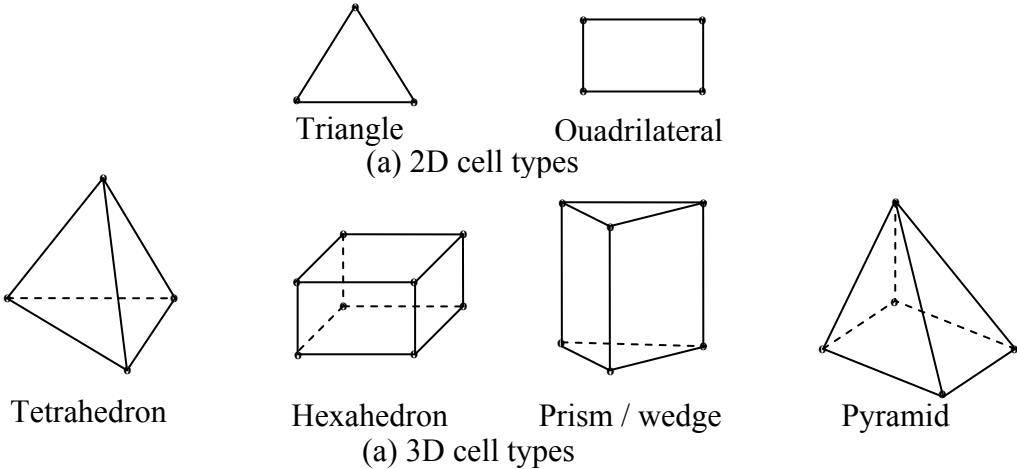
Figure 3.2:     Cell types [33]

49

After importing the geometry and grid, the cells with the use of their adjacent cells will be solved through a set of coupled differentiation equations. The basic equations are stated in the FLUENT 6.3 user's guide. They are:

**Mass conservation equation**

The equation for the conservation of mass, or continuity equation, can be written as follows [33]:

$$\frac{\partial \rho}{\partial t} + \nabla \cdot (\rho \vec{w}) = S_m \quad . \tag{3-1}$$

Eq. (3-1) is the general form of the mass conservation equation and is valid for incompressible as well as compressible flows. The source $S_m$ is the mass added to the continuous phase from the dispersed second phase (e.g., due to vaporization of liquid droplets) and other any user-defined sources.

**Momentum conservation equations**

Conservation of momentum in an inertial (non-accelerating) reference frame is described by the equation [33]:

$$\frac{\partial}{\partial t}(\rho \vec{w}) + \nabla \cdot (\rho \vec{w}\vec{w}) = -\nabla p + \nabla \cdot \overline{\overline{\tau}} + \rho \vec{g} + \vec{F} . \tag{3-2}$$

where p is the static pressure, $\overline{\overline{\tau}}$ is the stress tensor (described below), and $\rho \vec{g}$ and $\vec{F}$ are, respectively, the gravitational body force and external body forces (e.g., that arise from interaction with the dispersed phase). $\vec{F}$ also contains other model-dependent source terms such as porous-media and user-defined sources.

The stress tensor $\overline{\overline{\tau}}$ is given by

$$\overline{\overline{\tau}} = \mu \left[ \left( \nabla \vec{w} + \nabla \vec{w}^T \right) - \frac{2}{3} \nabla \cdot \vec{w} I \right]. \tag{3-3}$$

where $\mu$ is the molecular viscosity, I is the unit tensor, and the second term on the right hand side is the effect of volume dilation.

**Energy conservation equations**

The energy equation can be written in many different forms. FLUENT solves the energy equation in the following form [33]:

$$\frac{\partial}{\partial t}(\rho E) + \nabla \cdot (\vec{w}(\rho E + p)) = \nabla \cdot \left( k_{eff} \nabla T - \sum_j h_j \vec{J}_j + \left( \overline{\overline{\tau}}_{eff} \cdot \vec{w} \right) \right) + S_h . \tag{3-4}$$

50

where $k_{eff}$ is the effective conductivity $k + k_t$, wherein $k_t$ is the turbulent thermal conductivity defined according to the turbulence model being used, and $\vec{J}_j$ is the diffusion flux of species $j$. The first three terms on the right-hand side of Eq. (3-4) represent the energy transfer due to conduction, species diffusion, and viscous dissipation, respectively. $S_h$ includes the heat of chemical reaction, and any other volumetric heat sources defined by the user.

In Eq. (3-4),

$$E = h - \frac{p}{\rho} + \frac{w^2}{2},$$  (3-5)

where the sensible enthalpy $h$ is defined for ideal gases as

$$h = \sum_j Y_j h_j,$$  (3-6)

and for incompressible flows as

$$h = \sum_j Y_j h_j + \frac{p}{\rho}.$$  (3-7)

In Eq. (3-6) and (3-7), $Y_j$ is the mass fraction of species $j$ and

$$h_j = \int_{T_{ref}}^{T} c_{p,j} dT.$$  (3-8)

where $T_{ref}$ is 298.15 K.

**Steps in solving CFD problems with FLUENT**

Generally, the basic procedural steps for solving in FLUENT are as follows [34]:

1. Define the modeling goals.
2. Create the model geometry and grid.
3. Set up the solver and physical models.
4. Compute and monitor the solution.
5. Examine and save the results.
6. Consider revisions to the numerical or physical model parameters, if necessary.

## 3.1.3 FLUENT numerical solvers

FLUENT allows you to choose one of two numerical methods: [33]
- pressure-based solver
- density-based solver

In both methods the velocity field is obtained from the momentum equations. In the density-based approach, the continuity equation is used to obtain the density field, while the pressure

field is determined from the equation of state. On the other hand, in the pressure-based approach, the pressure field is extracted by solving a pressure or pressure correction equation which is obtained by manipulating the continuity and momentum equations.

Using either method, FLUENT will solve the governing integral equations for the conservation of mass and momentum, and, when appropriate, for energy and other scalars such as turbulence and chemical species. In both cases a control-volume-based technique is used.

**Pressure-based solver [33]**

Two pressure-based solver algorithms are available in FLUENT. A segregated algorithm, and a coupled algorithm. These two approaches are discussed in the sections below.

The Pressure-based segregated algorithm

The pressure-based solver uses a solution algorithm in which the governing equations are solved sequentially (i.e., segregated from one another). Since the governing equations are non-linear and coupled, the solution loop must be carried out iteratively in order to obtain a converged numerical solution.

In the segregated algorithm, the individual governing equations are solved one after another for the solution variables. During the solution, each governing equation is decoupled from the other equations. The segregated algorithm is memory-efficient, since the individual equations need only be stored in the memory one at a time. However, the solution convergence is relatively slow, due to so many equations being solved in a decoupled manner.

In the segregated algorithm, each iteration consists of the steps illustrated in Fig. 3.3. and outlined below:
1. Update the fluid properties (e,g, density, viscosity, specific heat) using the turbulent viscosity (diffusivity) of the current solution.
2. Solve the momentum equations, one after another, using the recently updated values for pressure and face mass fluxes.
3. Solve the pressure correction equation using the recently obtained velocity field and the mass-flux.
4. Correct face mass fluxes, pressure, and the velocity field using the pressure correction obtained from Step 3.
5. Solve the equations for additional scalars, if any, such as turbulent quantities, energy, species, and radiation intensity using the current values of the solution variables.
6. Update the source terms arising from the interactions among different phases (e.g., a source term for the carrier phase due to discrete particles).

52

7.  Check for the convergence of the equations.

These steps are continued until the convergence criteria are met.
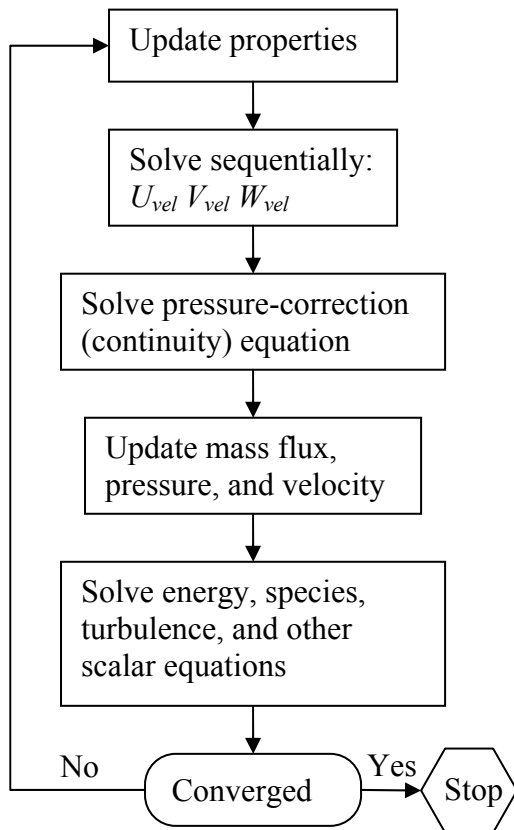
Pressure-based segregated algorithm          Pressure-based coupled algorithm
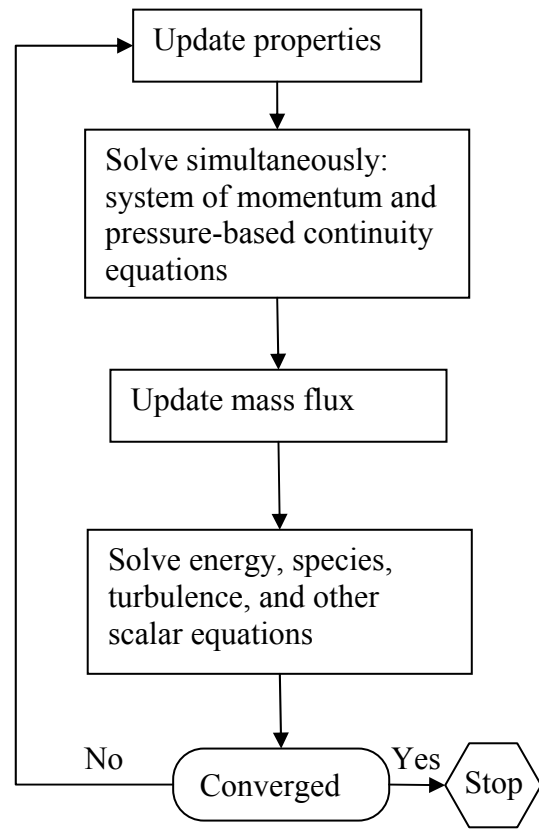


Figure 3.3:      Overview of the pressure-based solution methods

The Pressure-based coupled algorithm

Unlike the segregated algorithm described above, the pressure-based coupled algorithm solves a coupled system of equations comprised of the momentum equations and the pressure-based continuity equation. Thus, in the coupled algorithm, Steps 2 and 3 in the segregated solution algorithm are replaced by a single step in which the coupled system of equations are solved. The remaining equations are solved in a decoupled fashion as in the segregated algorithm.

**Density-based solver [33]**

The density-based solver solves the governing equations of continuity, momentum, and, where appropriate, energy and species transport simultaneously (i.e., coupled together).

Governing equations for additional scalars will be solved afterward and sequentially, that is, segregated from one another and from the coupled set. Since the governing equations are non-linear and coupled, several iterations of the solution loop must be performed before a converged solution is obtained. Each iteration consists of the steps illustrated in Fig. 3.4 and outlined below:

1. Update the fluid properties based on the current solution. (If the calculation has just begun, the fluid properties will be based on the initialized solution.)
2. Solve the continuity, momentum, and (where appropriate) energy and species equations simultaneously.
3. Where appropriate, solve equations for scalars such as turbulence and radiation using the previously updated values of the other variables.
4. When interphase coupling is to be included, update the source terms in the appropriate continuous phase equations with a discrete phase trajectory calculation.
5. Check for the convergence of the equation set.

These steps are continued until the convergence criteria are met.
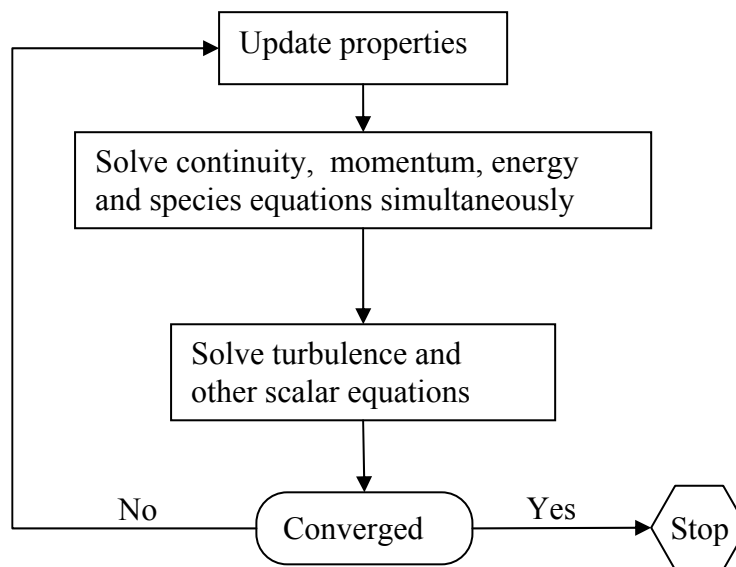
Figure 3.4:     Overview of the density-based solution method

In the density-based solution method, the coupled system of equations (continuity, momentum, energy and species equations if available) can be solved by using either the coupled-explicit formulation or the coupled-implicit formulation.

The manner in which the governing equations are made linear may take an "implicit" or "explicit" form with respect to the dependent variable (or set of variables) of interest.

**Implicit:** For a given variable, the unknown value in each cell is computed using a relation that includes both existing and unknown values from neighboring cells. Therefore, each unknown will appear in more than one equation in the system, and these equations must be solved simultaneously to give the unknown quantities.

**Explicit**: For a given variable, the unknown value in each cell is computed using a relation that includes only existing values. Therefore, each unknown will appear in only one equation in the system, and the equations for the unknown value in each cell can be solved one at a time to give the unknown quantities.

## 3.1.4 Turbulent model

Turbulent flows are characterized by fluctuating velocity fields. These fluctuations mix transported quantities such as momentum, energy, and species concentration, and cause the transported quantities to fluctuate as well. Since these fluctuations can be of small scale and high frequency, they are too computationally expensive to simulate directly in practical engineering calculations. Instead, the instantaneous (exact) governing equations can be time-averaged, ensemble-averaged, or otherwise manipulated to remove the small scales, resulting in a modified set of equations that are computationally less expensive to solve. However, the modified equations contain additional unknown variables, and turbulence models are needed to determine these variables in terms of known quantities [33].

There are a variety of models provided by FLUENT, used according to which governing equations are applied. In this work, the standard $\kappa$-$\varepsilon$ was used for CFD simulation because of its cost-efficiency and reasonable accuracy for a wide class of flows.

The standard $\kappa$-$\varepsilon$ model is by far the most popular and most widely used turbulence model, especially for industrial applications. It is a semi-empirical model based on model transport equations for the turbulent kinetic energy ($\kappa$) and its dissipation rate ($\varepsilon$). The model transport equation $\kappa$ is derived from the exact equation, while the model transport equation for $\varepsilon$ was obtained using physical reasoning and bears little resemblance to its mathematically exact counterpart [33].

The turbulence kinetic energy $\kappa$ and its rate of dissipation $\varepsilon$ are obtained from the following transport equations:

$$\frac{\partial}{\partial t}\left(\rho\kappa\right)+\frac{\partial}{\partial x_i}\left(\rho\kappa w_i\right)=\frac{\partial}{\partial x_j}\left[\left(\mu+\frac{\mu_t}{\sigma_\kappa}\right)\frac{\partial\kappa}{\partial x_j}\right]+G_\kappa+G_b-\rho\varepsilon-ZY_M+S_\kappa \qquad (3\text{-}9)$$

and

$$\frac{\partial}{\partial t}\left(\rho\varepsilon\right)+\frac{\partial}{\partial x_i}\left(\rho\varepsilon w_i\right)=\frac{\partial}{\partial x_j}\left[\left(\mu+\frac{\mu_t}{\sigma_\varepsilon}\right)\frac{\partial\varepsilon}{\partial x_j}\right]+C_{1\varepsilon}\frac{\varepsilon}{\kappa}\left(G_\kappa+C_{3\varepsilon}G_b\right)-C_{2\varepsilon\rho}\frac{\varepsilon^2}{\kappa}+S_\varepsilon \qquad (3\text{-}10)$$

In these equations, $G_\kappa$ represents the generation of turbulent kinetic energy due to the mean velocity gradients; it is defined as

$$G_\kappa = -\rho \overline{w_i' w_j'} \frac{\partial w_j}{\partial x_i} . \tag{3-11}$$

$G_b$ is the generation of turbulent kinetic energy due to buoyancy, and can be calculated by:

$$G_b = \beta g_i \frac{\mu_t}{Pr_t} \frac{\partial T}{\partial x_i} , \tag{3-12}$$

where $Pr_t$ is the turbulent Prandtl number for energy, $g_i$ is the component of the gravitational vector in the $i$th direction, and $\beta$ is the coefficient of thermal expansion, defined as:

$$\beta = -\frac{1}{\rho} \left( \frac{\partial \rho}{\partial T} \right)_p . \tag{3-13}$$

The turbulent (or eddy) viscosity, $\mu_t$, is computed by combining $\kappa$ and $\varepsilon$ as follows

$$\mu_t = \rho C_\mu \frac{\kappa^2}{\varepsilon} , \tag{3-14}$$

where $C_\mu$ is a constant.

The model constants $C_{1\varepsilon}$, $C_{2\varepsilon}$, $C_\mu$, $\sigma_\kappa$, and $\sigma_\varepsilon$ have the following default values [35]:

$C_{1\varepsilon} = 1.44$, $C_{2\varepsilon} = 1.92$, $C_\mu = 0.09$, $\sigma_\kappa = 1.0$, $\sigma_\varepsilon = 1.3$.

These default values have been determined from experiments with air and water for fundamental turbulent shear flows, including homogeneous shear flows and decaying isotropic grid turbulence. They have been found to work fairly well for a wide range of wall-bounded and free shear flows [33]. In this study all of these default values will be used for the simulations.

# 3.2 Two dimension approximation with horizontal internal ventilator

## 3.2.1 Geometry

At first a horizontal arrangement of the ventilator is investigated, which is shown in Fig. 3.5. In this installation, the total pressure drop of the recirculation is very small. However, the ventilator fan comes in contact with the gas, which in the high temperature range meets the firmness problem. The real geometry arrangement and the investigated values for the standard kiln will be described later.
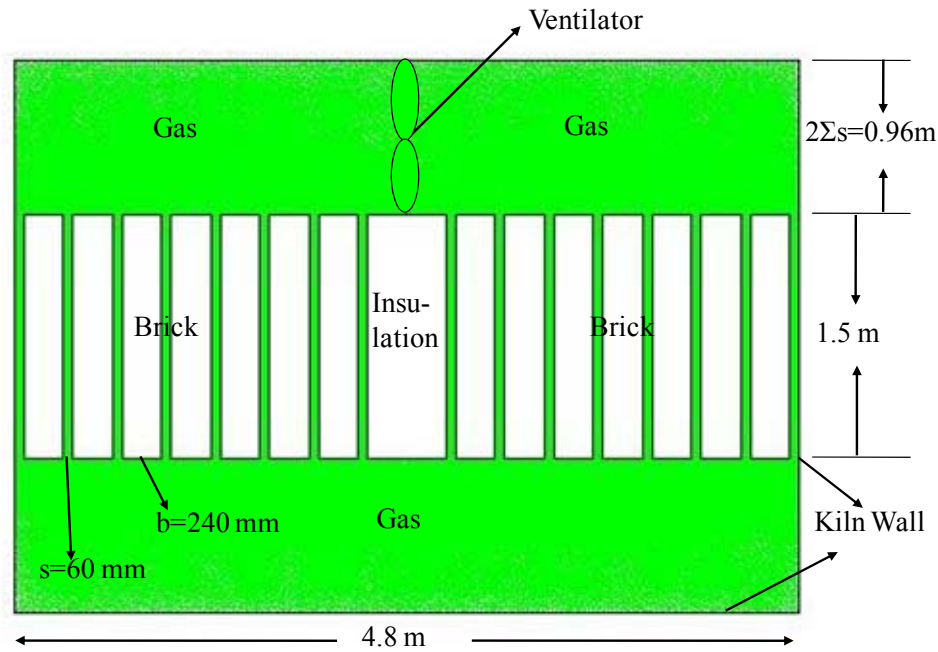
Figure 3.5:    Geometry of the kiln with horizontal ventilator

The kiln width is 4.8 m and there are 7 brick piles; thus there are 8 gaps for the gas recirculation for each side. The gap distance is 60 mm. The brick piles are 240 mm wide and 1.5 m tall. The height of the kiln above and beneath of the brick is 0.96 m, so that the cross sectional area above or underneath the kiln is doubled as the sum area of all gaps. These are the requirements so that the cross sectional flow has a small influence on the flow inside the gap.

## 3.2.2 Grid independent analysis

The flows in the kiln cross section were simulated with FLUENT 6.3. The flow is treated as isothermal, since the temperature difference in the cross section is smaller than 50 K and the heat transfer will not influence the flow. The k-ε-Model was used for the turbulent model simulations.

At first, grid independent analysis was carried out. In the gaps, quadrilateral cells were used, while at the top and bottom of the kiln, triangular cells were used. Eight different sets of grids were built. Fig. 3.6 shows three of the most significantly different grid settings, which cover the inside of the gap. The details about the three different grid settings shown in Fig. 3.6 are listed in Table 3.1.

|  |  |  |
|:---:|:---:|:---:|
| Grid 1 | Grid 2 | Grid 3 |
| Coarsest | Medium | Finest |
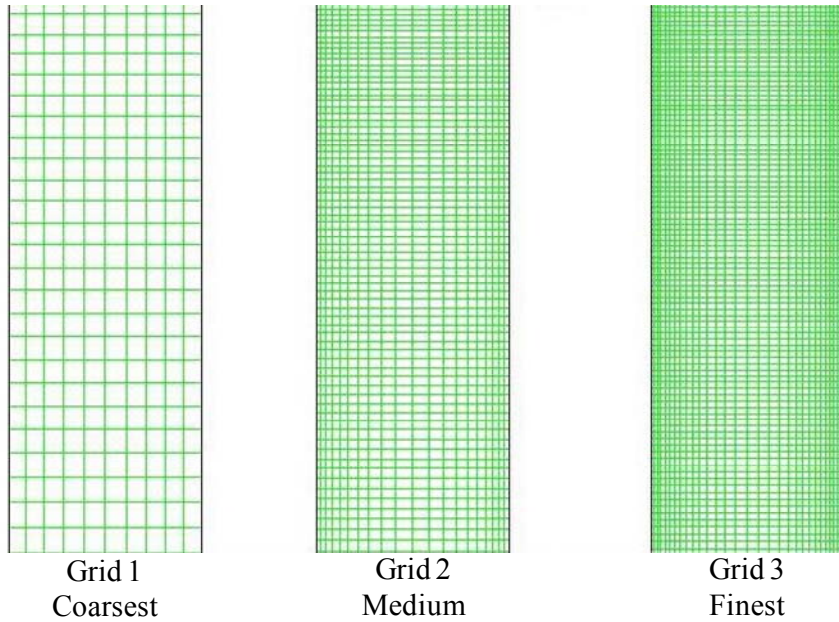
Figure 3.6: Three of the most significant grid settings for inside of the gap

Table 3.1: Details of the three most significant grid settings

| Grid | Growth ratio | Rows | Interval size in [mm] | Cells number |
|:---:|:---:|:---:|:---:|:---:|
| 1 | 1.01 | 10 | 6 | 127830 |
| 2 | 1.15 | 20 | 3 | 364665 |
| 3 | 1.1 | 30 | 2 | 577696 |

The influence of the grid number is described as follows, with consideration of the gas velocity in the gap. As an example, the pressure jump of 50 Pa in the ventilator was defined. In Fig. 3.7, the gas velocity dependence on the grid number is shown for the case of a turbulent model with a k-ε-standard wall function. After the grid number increases to 350 000, the gas velocity remains constant at 8 m/s.
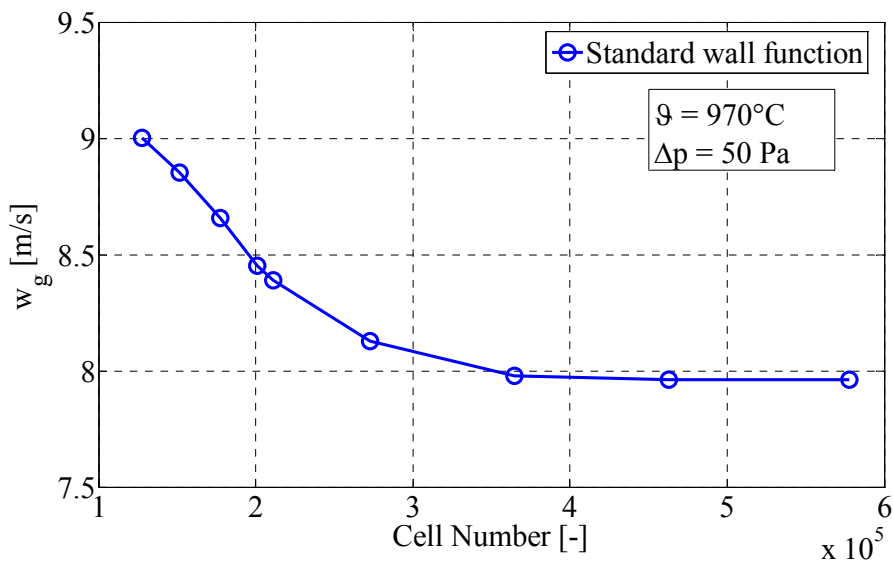


Figure 3.7: Influence of the cell number for the standard wall function

In Fig. 3.8, the gas velocity dependent on the grid number for the case of a turbulent model with a k-ε-enhanced wall function is shown. Here, the velocity also remains constant after the grid number increases to 350 000. However, the dependence of the gas velocity on the grid number is clearly smaller than in the above case. By halving of the grid number, the velocity increases with the enhanced wall function by only 0.04 m/s, while that in the standard wall function increases by 0.6 m/s, more than 10 times that in the enhanced case. Therefore, the enhanced wall function is considered here as the appropriate function and is used in the following simulation. This is rather important, since the enhanced wall function results in a velocity of 9.2 m/s, higher than the velocity of 8.0 m/s in the other case.
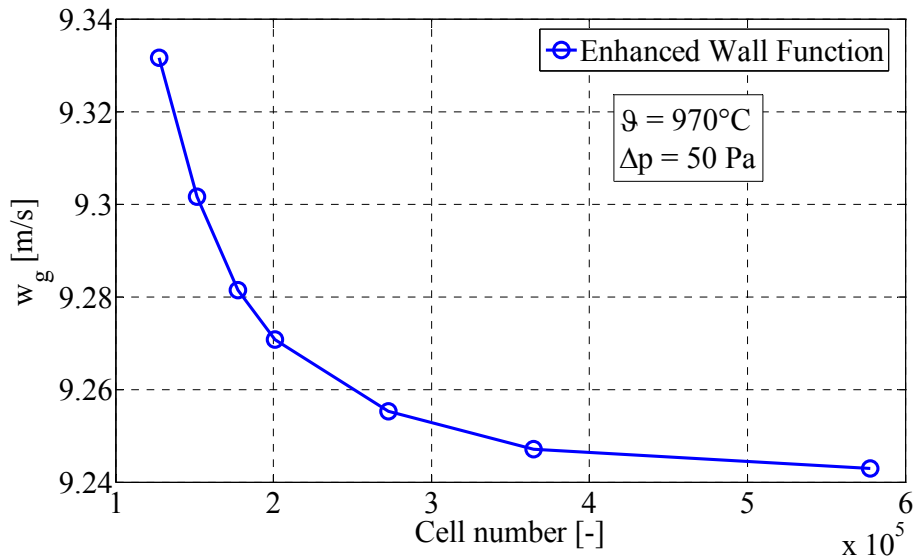


Figure 3.8:     Influence of the cell number for the enhanced wall function

As shown in Fig. 3.8, the cells number influence on the gas velocity becomes very small after a cell number larger than 350 000 when enhanced wall function is used. However, when the enhanced wall function is used in the simulation, Wall $Y$ plus should be checked. Wall $Y$ plus, $Y^+$, is a dimensionless parameter defined by the equation [33]

$$y^+ = \frac{\rho w_\tau y}{\mu},$$  (3-15)

where $y$ is the distance from a point on the wall surface, $\rho$ is the fluid density, $\mu$ is the fluid viscosity, and $w_\tau$ is the friction velocity, which is defined as

$$w_\tau = \sqrt{\tau_w / \rho}.$$  (3-16)

According to the guidelines presented in FLUENT's documentation, the value of $Y^+$ should be smaller than 4-5 when the flow is fully turbulent to insure the accuracy of the simulation [36]. Fig. 3.9 shows the values of $Y^+$ in different grid settings. It can be seen, in the coarsest case (grid 1), $Y^+$ is bigger than 5, while in the other two cases (grid 2 and 3), $Y^+$ is smaller than 5.
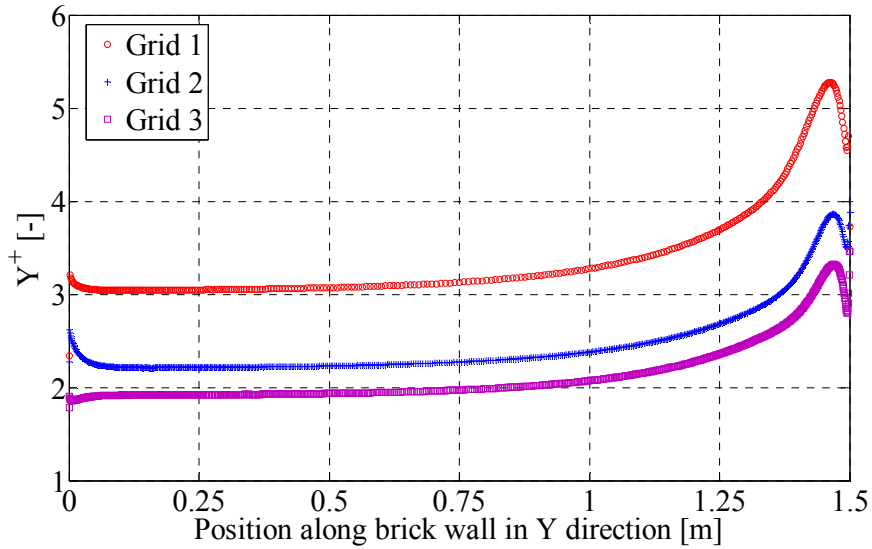
Figure 3.9:     $Y^+$ along the brick wall in each grids setting case

According to the above description, considering simulation accuracy and time, case 2, the medium grid, should be used for the simulation. The details about this grid setting are shown as follows.

The grids in the gap cross section are shown in Fig. 3.10 and 3.11. Inside the gap, quadrilateral cells were used, where the height is constant but the width is decreased as the wall region is approached, since there is high velocity gradient. In total there are 20 cells in the width direction of the gap. For the gap thickness $s = 60$ mm, the cells widths increase from 1.3 mm to 5 mm.
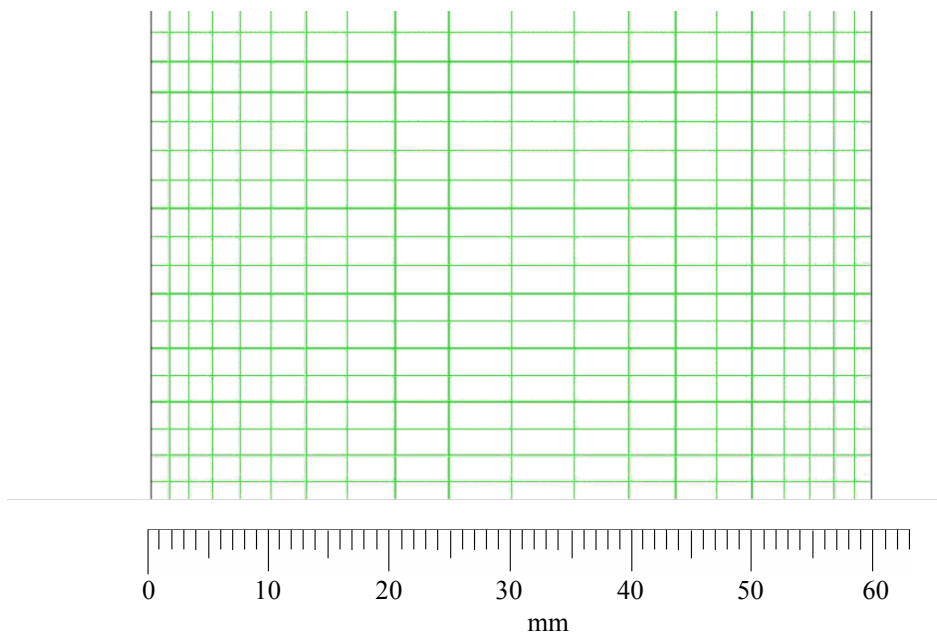


Figure 3.10:    Cells inside the gap with $s = 60$mm

60

Fig. 3.11 shows a gap with thickness $s$ = 20 mm. Similarly to the situation above, there are 20 cells in the gap width direction. Here the cell width is smaller; the cells widths are in the range from 0.8 mm to 1.5 mm.
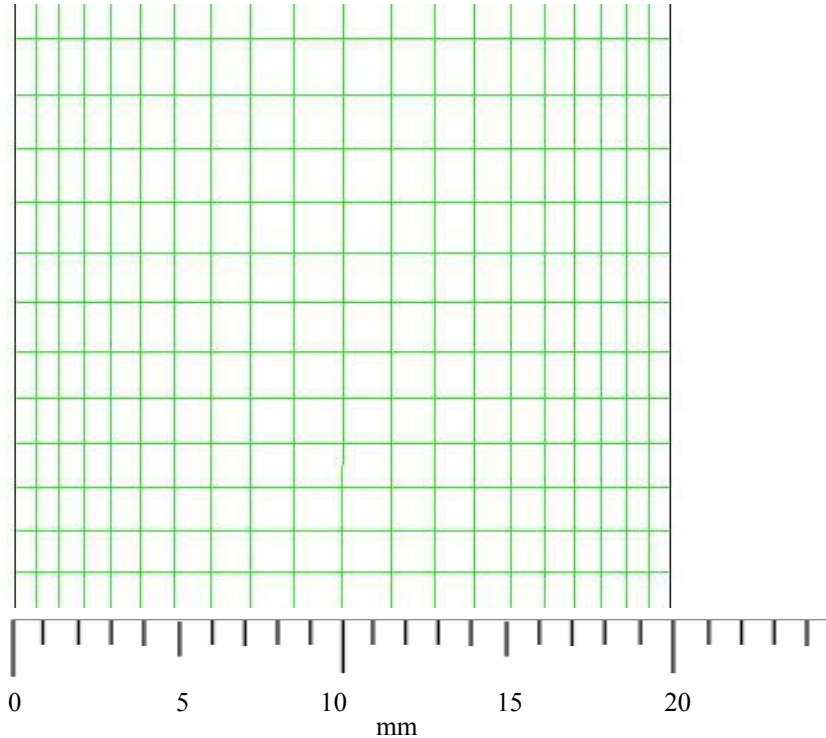


Figure 3.11:   Cells inside the gap with $s$ = 20mm

In the domains above and below the brick piles, triangle cells were used. This is shown in Fig. 3.12
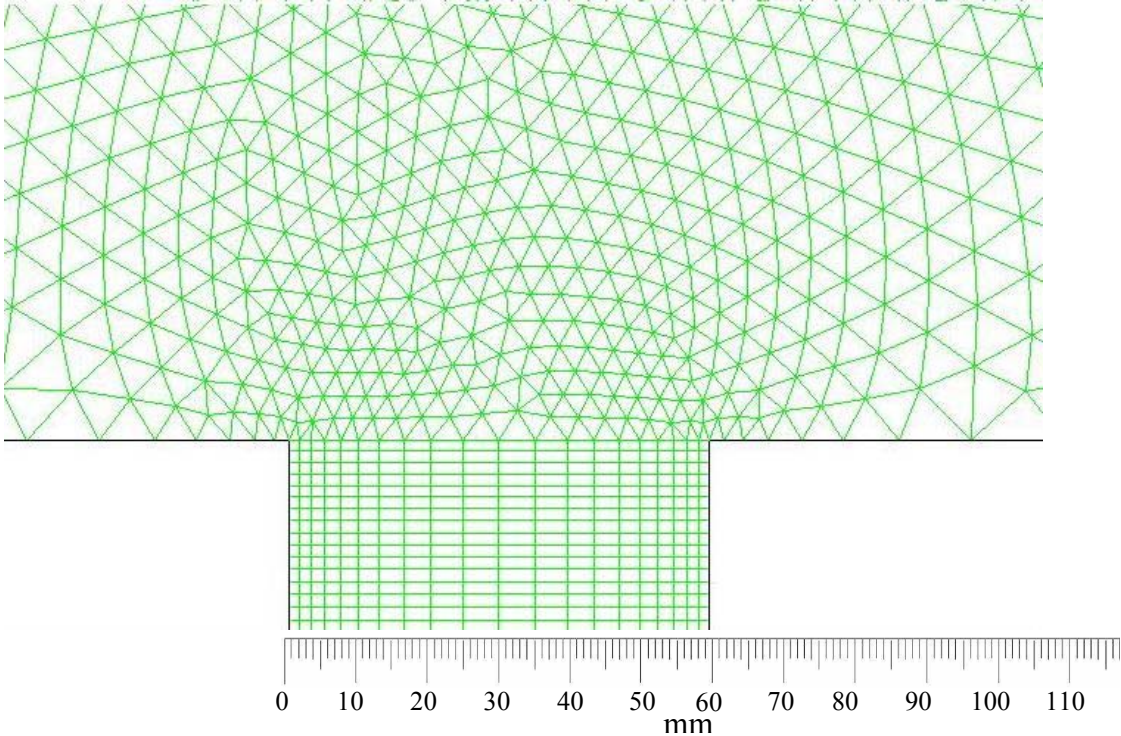


Figure 3.12:   Cells in the kiln cross section in the flow outlet with 60 mm gap

61

Fig. 3.13 and Fig. 3.14 show the grids on top of the kiln when $s = 60$ mm and $s = 20$ mm respectively. It shows that at the inlet and outlet positions of the flow gaps, the grids are fine enough to calculate the pressure drop due to the flow inlet and outlet. It is shows again that, within the gaps, quadrilateral cells were used, while at the top and bottom of the kiln, triangle cells were used. The height of the top or bottom of the kiln is twice of the sum of the entire gap width.
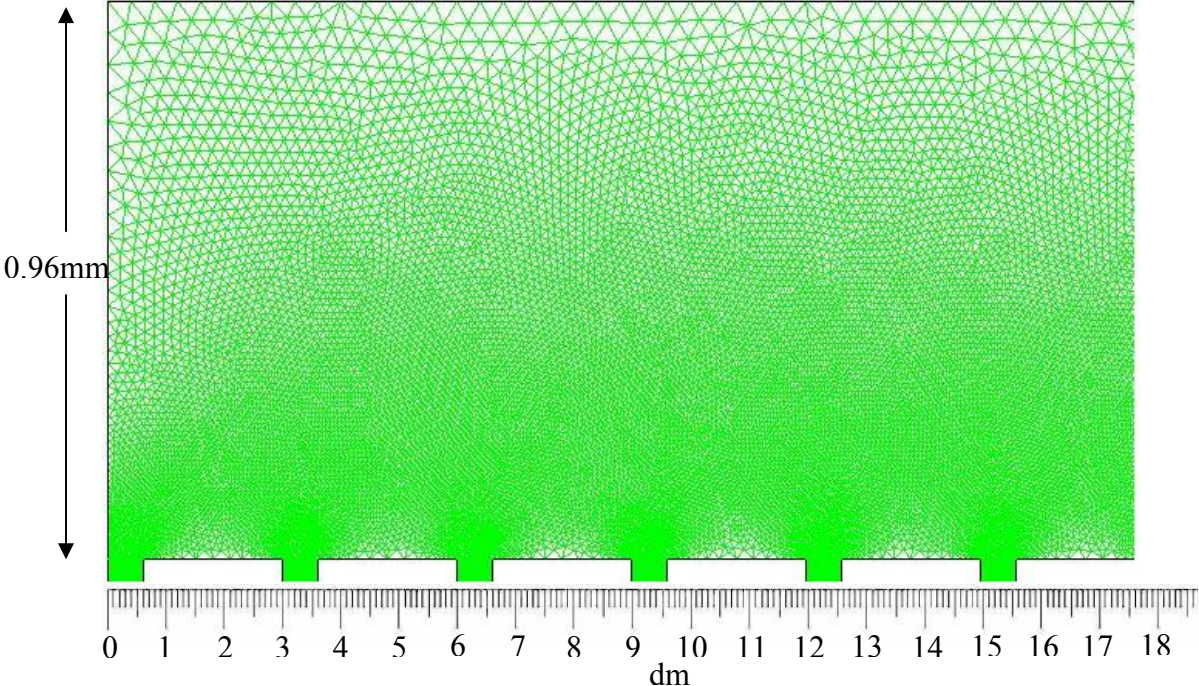


Figure 3.13:    Grids in the kiln cross section with $s = 60$ mm
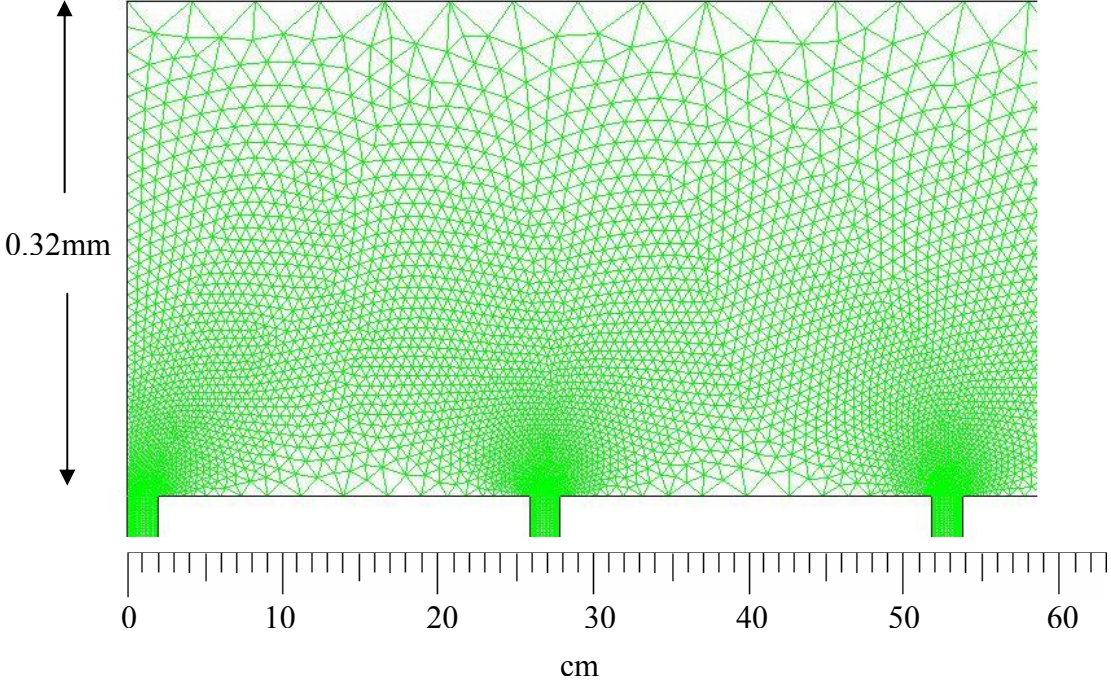


Figure 3.14:    Grids in the kiln cross section with $s = 20$ mm

## 3.2.3 Velocity

In the Fig. 3.15, the velocity vector in the cross section is shown. It indicates a relatively homogenous flow at both sides. The gap thickness s = 60 mm. In the gap, the velocity is around 11 m / s, significantly higher than that in the cross flow between the two kiln parts, which is about 2 m / s.
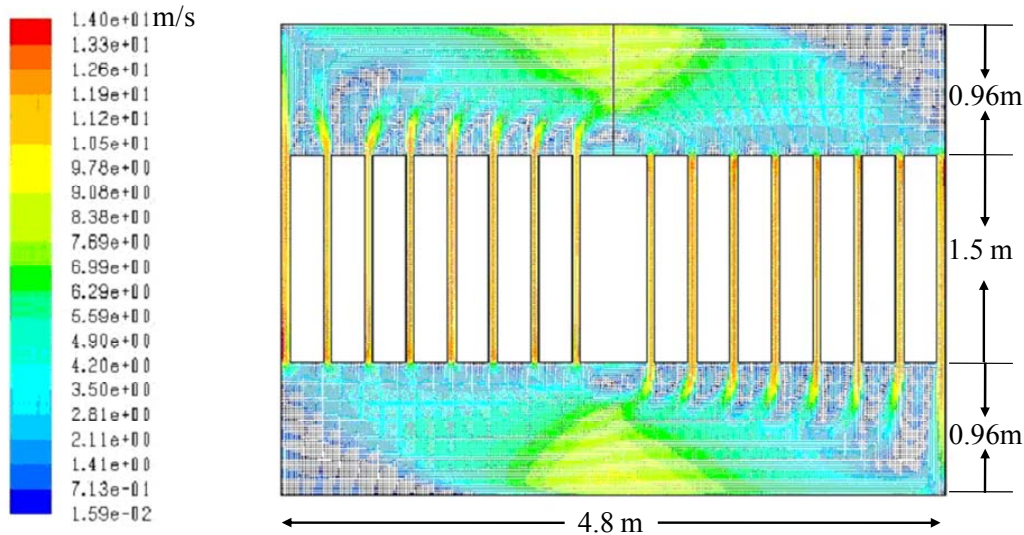


Figure 3.15:    Velocity vector in cross section

In Fig. 3.16, the mean velocity of each gap is shown in the cross section. The absolute velocities on both sides are 11 ± 1 m/s. This deviation of ± 1 m/s can be regarded as relatively low. The flow is very homogenous throughout the cross section. The gas space above and below the bricks is therefore adequate.
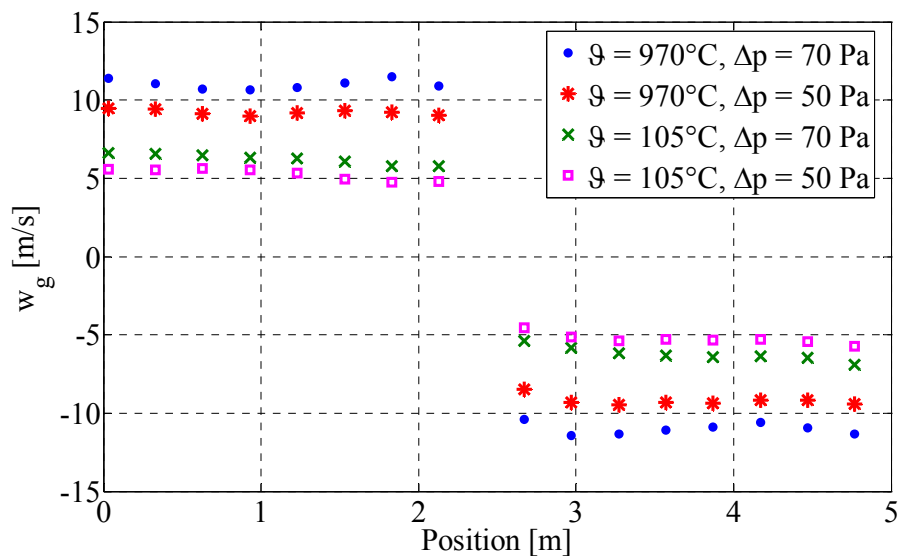


Figure 3.16:    Mean velocities inside of gaps in the cross section

The velocity vectors in the gap are shown in Fig. 3.17. The length of the vectors indicates the velocity in each of the 20 cell. It is clear that the flow is significantly affected by the

roughness of the wall surface. Very close to the wall, gas kinematic blocking reduces the normal fluctuations. However, toward the outer part of the near-wall region, the turbulence is rapidly augmented by the production of turbulent kinetic energy due to the large gradients in mean velocity.
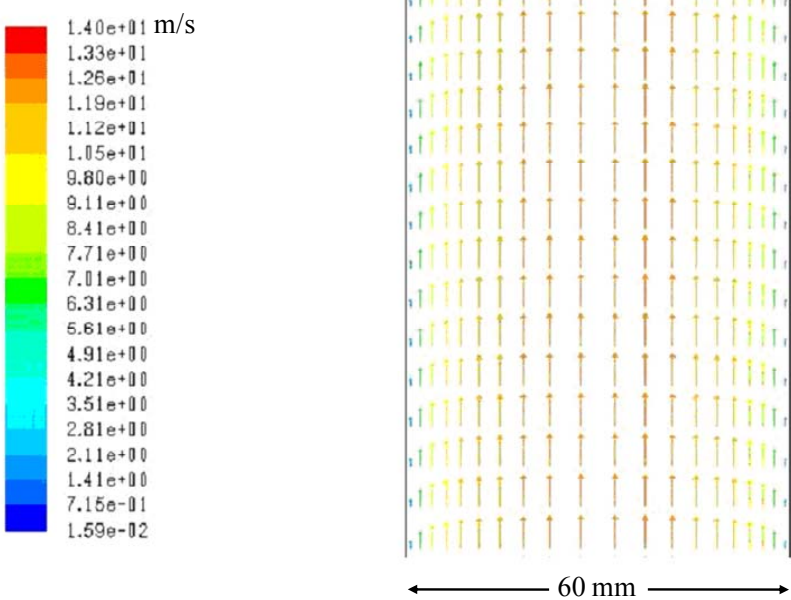


Figure 3.17:    Velocity vectors in gap

The velocity profile in the gap is plotted in Fig. 3.18 and 3.19 for $s = 60$ mm and $s = 20$ mm respectively. Fig. 3.18 clearly shows a typical profile for turbulent flow for the $s = 60$ mm gap. The Reynolds number is 8 000.
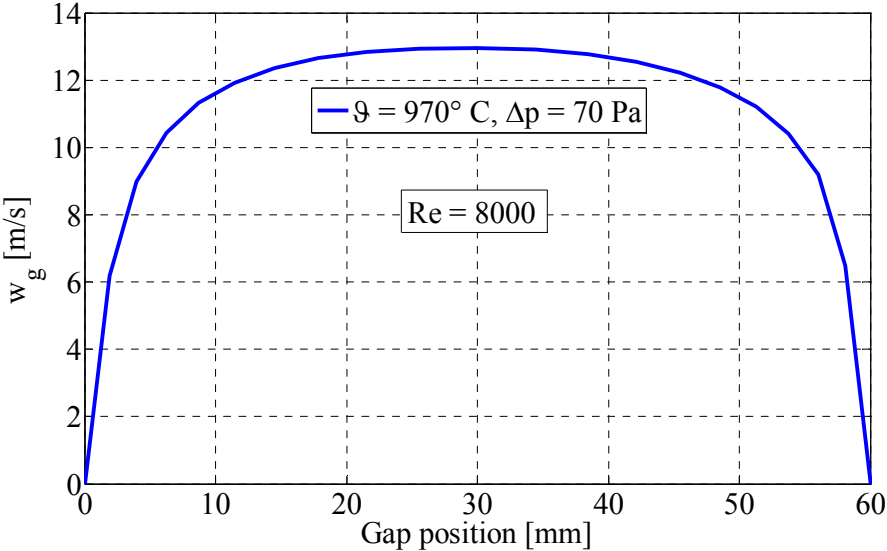


Figure 3.18:    Velocity profile in gap for $s = 60$ mm

Fig. 3.19 shows the velocity profile in the gap with $s = 20$ mm. In this situation, the flow, although turbulent, has a relatively lower Reynolds number, which is 2 400. This can be seen as the transient flow between laminar to turbulent flows.
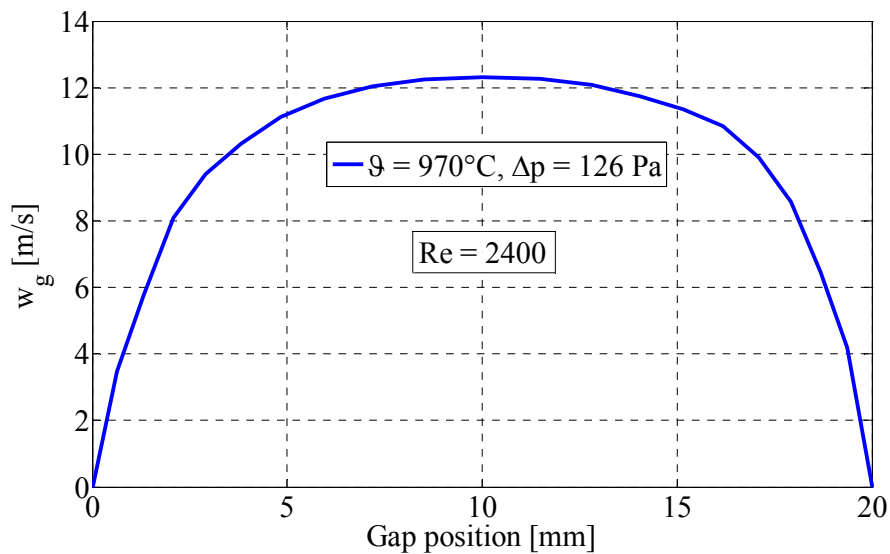


Figure 3.19:    Velocity profile in gap for $s = 20$ mm

## 3.2.4 Pressure drop

As shown in the previous chapter, the pressure drop decides the ventilator power and thus the temperature difference between the two kiln sides. The flow simulation is used, therefore, to identify the pressure drop of the gas recirculation, which is designed by the mathematical model. In Fig. 3.20, the contours of the pressure drop in the cross section are shown. It is evident that the pressure drop is mainly caused by the inlets, outlets, friction and turnover of the flow.
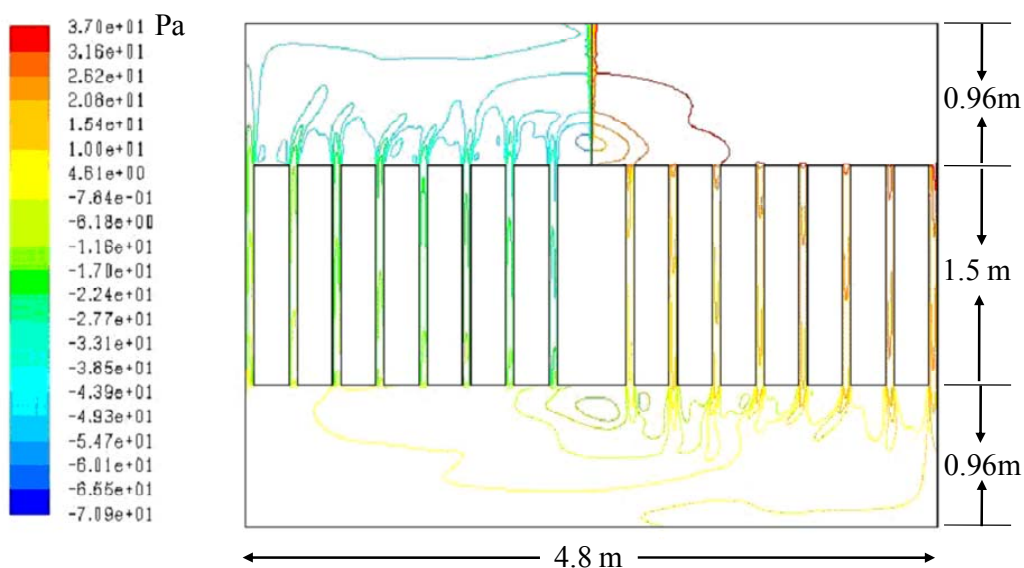


Figure 3.20:    Contour of pressure drop in cross section

In Fig. 3.21, the velocity in the gap as a function of the pressure jump generated by the ventilator is shown. It is evident at every temperature position that the increase in gas velocity inside the gap increases with an increase in ventilator power.
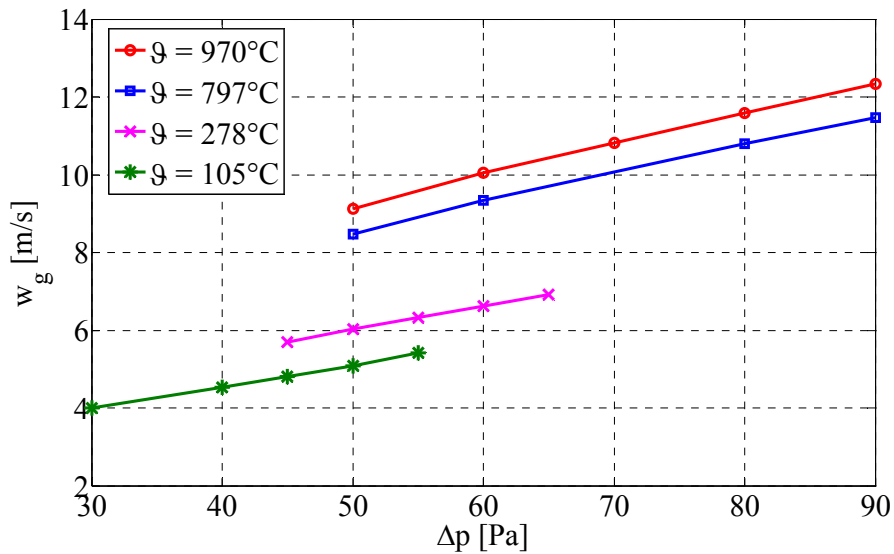


Figure 3.21:    Gas velocity in gap, dependent on the pressure drop

## 3.2.5 Electrical power consumption

According to the Eq. (2-15), in order to calculate the ventilator power, both the pressure drop and volumetric flow are required. The corresponding volumetric flows dependent on the pressure drop are plotted in Fig. 3.22. It can be seen that the corresponding volumetric flow increases with an increase in the pressure drop.
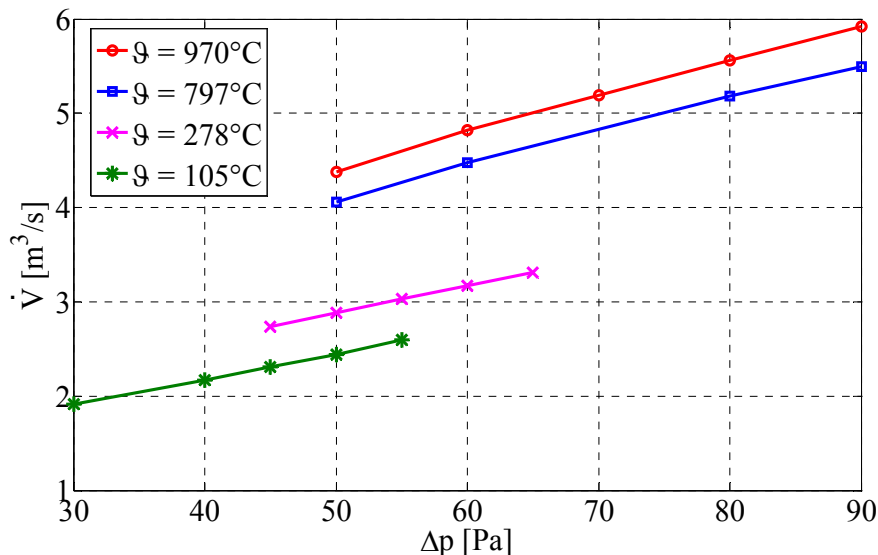


Figure 3.22:    Recirculation volumetric flow in cross section dependent on pressure drop

With the pressure drop and volumetric flow described above, the ventilator power requirement can be calculated according to the Eq. (2-15), and is plotted in Fig. 3.23. It can be seen that the electrical power requirement increases with the increase in temperature linearly,

66

similar to the mechanism described in Fig. 2.9. The values here are smaller than those shown in Fig. 2.9, because here internally arranged ventilators are assumed, and the pressure drops due to the ventilators are not considered. This will be investigated in the following parts.
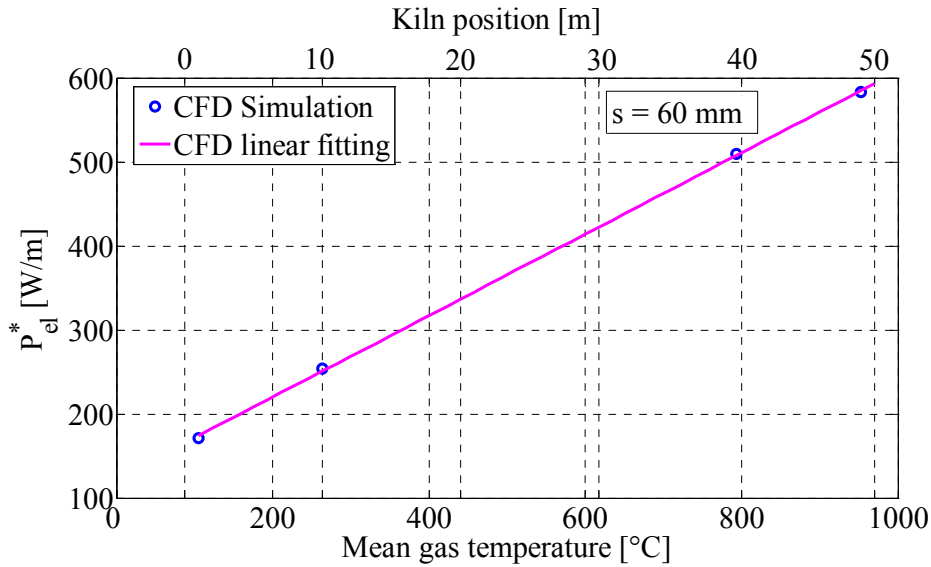


Figure 3.23:    Electrical requirement for the internal arranged ventilators

From these values, the pressure loss coefficient can be determined. These coefficients are summarized in Table 3.2. It is shown that when $s = 60$ mm, all influence factors play a role for the total pressure drop; however when $s = 20$ mm, the wall friction plays the most important role because of the relatively narrow gap thickness.

Table 3.2:    Pressure drop coefficients

| Symbol | Explanation | $s = 60$ mm | | $s = 20$ mm | |
|---|---|---|---|---|---|
| | | Left | Right | Left | Right |
| $\xi_1$ | 90° turn over | 0.1 | 0.1 | 0.1 | 0.1 |
| $\xi_2$ | Inlet | 0.5 | 0.5 | 0.5 | 0.5 |
| $\lambda \cdot \dfrac{H}{d_h}$ | Friction | 0.57 | 0.57 | 2.68 | 2.68 |
| $\xi_3$ | Outlet | 1 | 1 | 1 | 1 |
| $\xi_4$ | 90° turn over | 0.5 | 0.5 | 0.5 | 0.5 |
| | SUM | 5.34 | | 9.56 | |

# 3.3  Two-dimensional Simulation with vertical ventilator

## 3.3.1 Velocity homogenous optimization

A lot of ventilators need a vertical shaft; thus an arrangement looks like the principle figure shown in Fig. 2.1. In Fig. 3.24, the flow vectors for a ventilator from the company

Brackemeier are shown as an example. The flow is sucked out of the left side of the kiln at the top by two pipes, travels through the ventilator and is blown into the right kiln side through the roof from a single pipe.
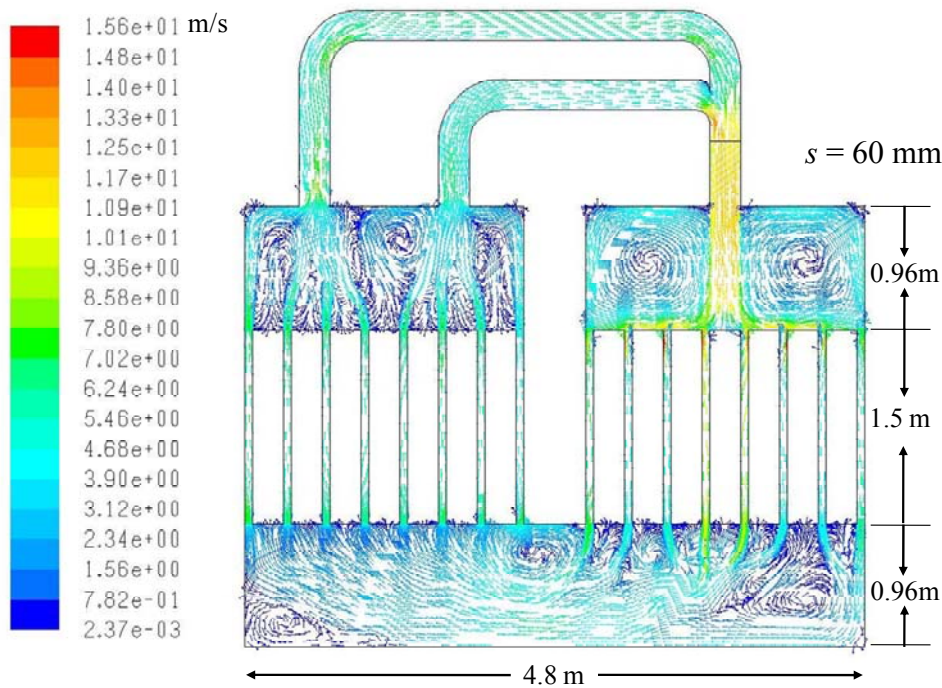


Figure 3.24:   Gas velocity vectors in kiln cross section with a vertical ventilator drive shaft and flat kiln roof s = 60 mm

In Fig. 3.25, the mean velocity in each gap is shown along the kiln width direction. It is evident that there is a relatively homogenous flow in the gaps on the left side of the kiln due to suction. On the right kiln side however, the flow is very uneven. Especially under the impulse of the injector, the velocities in the gap are significantly higher. Therefore, flow optimization should be carried out to make the flow velocity in the cross section as homogenous as possible.
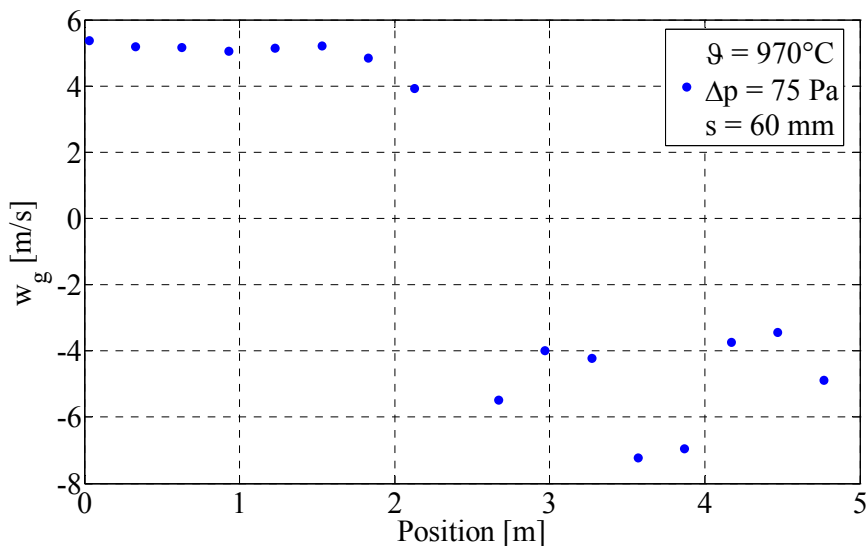


Figure 3.25:   Velocity distribution in gap with flat kiln ceiling

The geometry of the injection must be further improved. Fig. 3.26 shows the flow field in a case where the roof on the injection side is constructed in the form of a funnel. It can be seen that under the funnel-formed roof, there are some swirl flows on the injection side. Again, under the impulse of the injector, the velocities in the gap are significantly higher. This is shown in Fig. 3.25 more clearly.
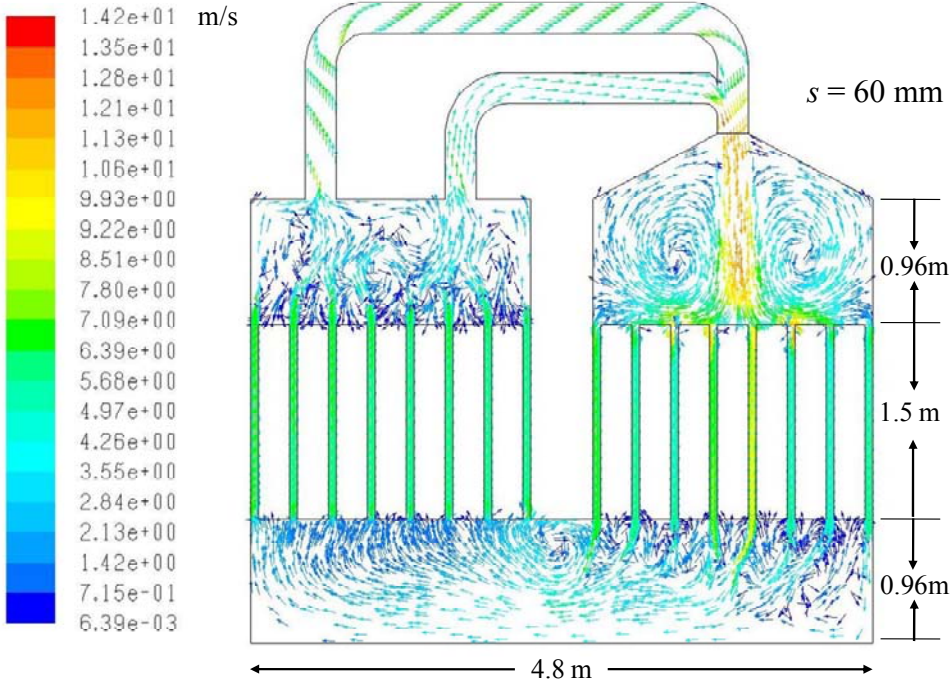


Figure 3.26:    Velocity vectors with funnel-formed roof

The corresponding velocity distribution in the gap is shown in Fig. 3.27. It is evident that the velocity distribution in the right side of the kiln could not be significantly improved with the funnel shaped roof.
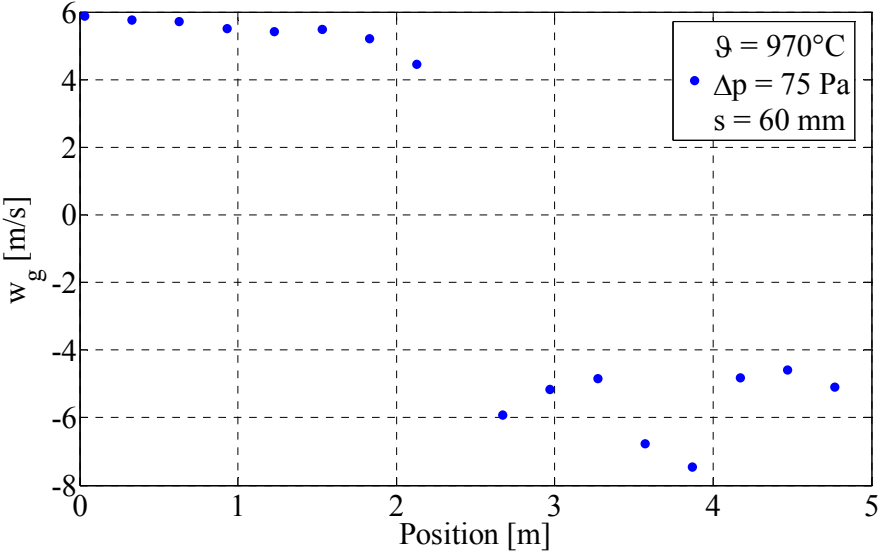


Figure 3.27:    Velocity distribution in kiln cross section with funnel-formed roof

69

In Fig. 3.28, the velocity vectors are shown for the case in which the inflow gas from the roof is distributed into the gaps with distribution plates.
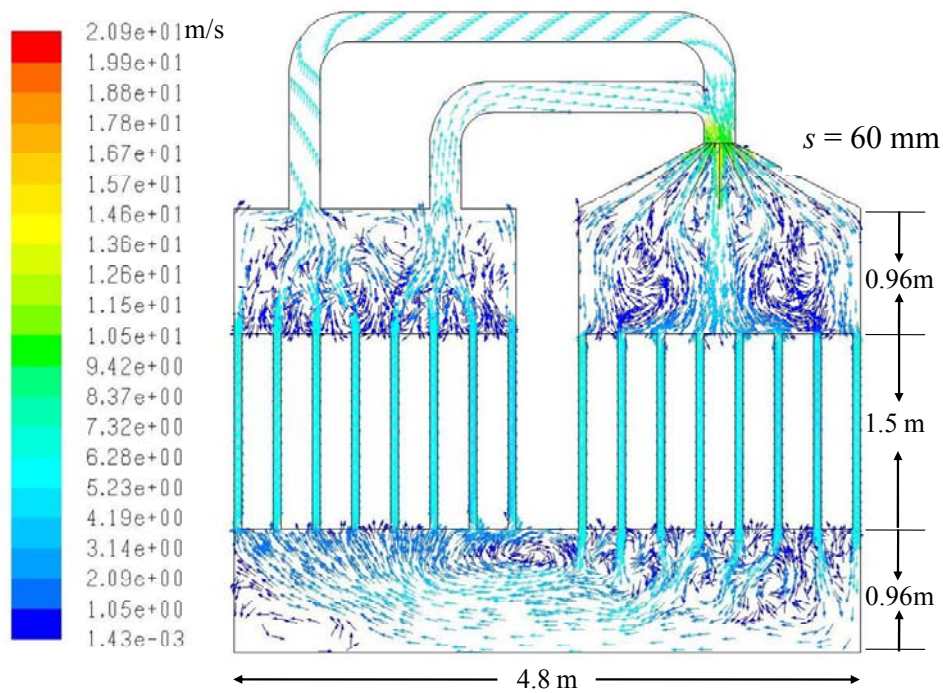


Figure 3.28:    Velocity vectors with distribution plates

In Fig. 3.29 the velocity distribution in the gaps is shown. It illustrates that the velocity in the gaps on the right side of the kiln has become relatively more homogenous than in the first two cases.
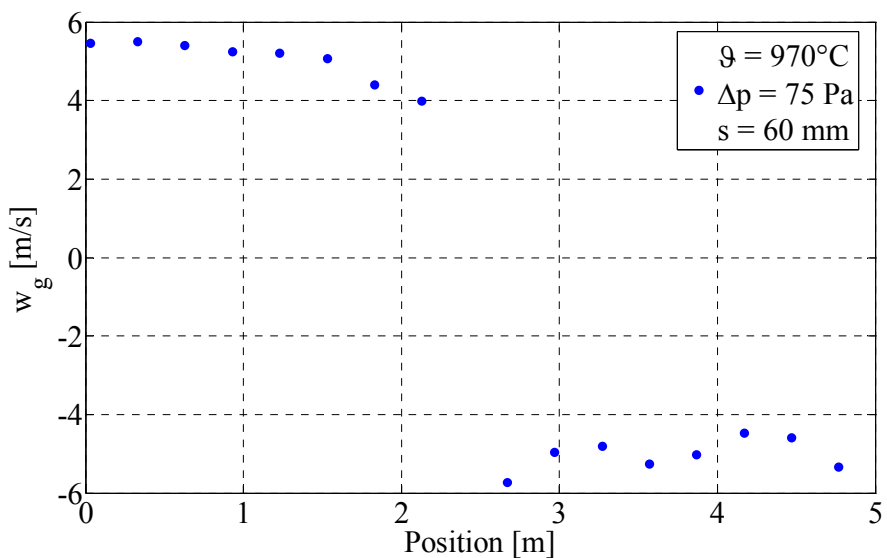


Figure 3.29:    Gas velocity distribution in gap with distribution plates

However, in each of the three cases above, the velocity is relatively uneven in the left kiln side where the suction occurs. The velocity at the position 2 m is 4 m/s, which is significantly

lower than that at position 0 m, where it is 5.5 m/s. The reason is that, the two suction pipes are located in the same cross section position in the 2D simulation, and the pressure drop coefficients are different due to the difference in pipe lengths and elbow bend degree. Therefore, the following modifications to the geometry were created.

In Fig. 3.30, the velocity vector is once more presented for the case, in which the flow is sucked out through only one pipe.
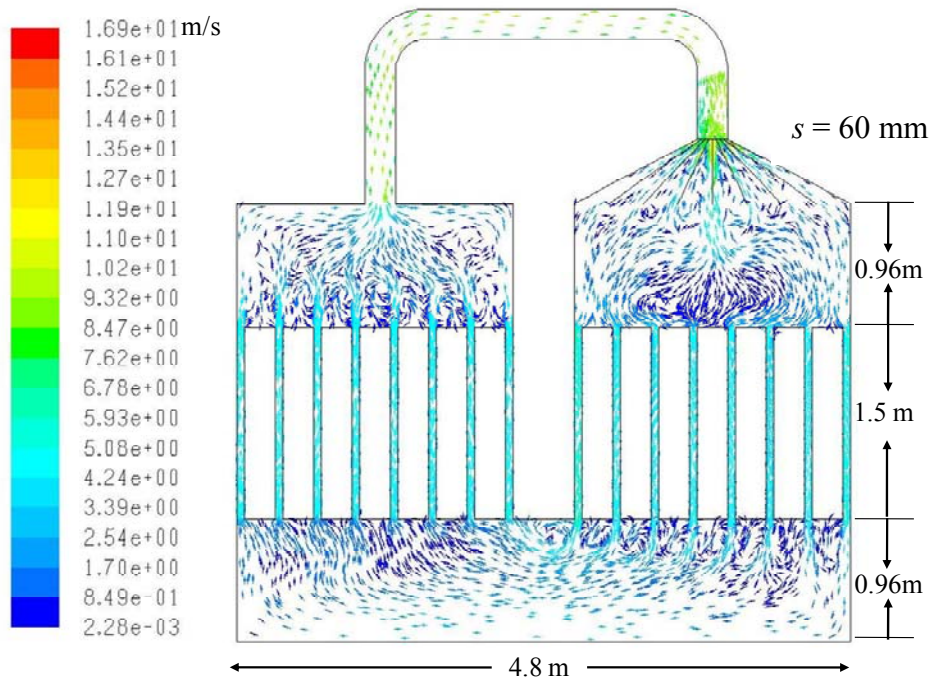


Figure 3.30:   Velocity vectors with only one suction pipe

Fig. 3.31 shows the mean velocity in each gap when the one suction pipe is presented in the 2D simulation. It is evident that on the left side of the kiln, the velocity of each gap is much more homogenous.
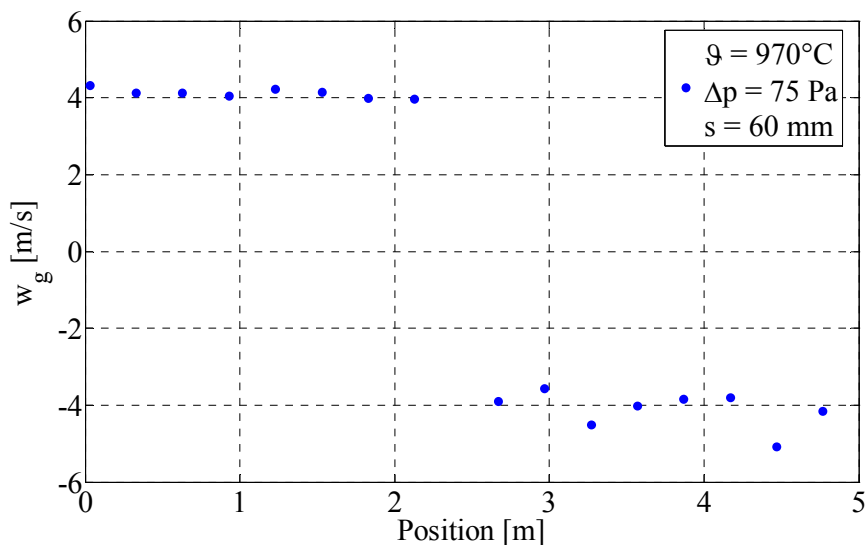


Figure 3.31:   Velocity distribution with only one suction pipe

As it can be seen, the velocity profile becomes significantly more and more homogenous through this flow optimization. However, the velocities are reduced to about 4 m/s. This is due to an increase of flow resistance. Therefore in the following part, ways to reduce the flow resistance are investigated.

## 3.3.2 Pressure drop

The pressure drop of the ventilator system is highly dependent on the diameter $D$ of the pipe and the radius of curvature $R$, as shown in Fig. 3.32. Their influences are investigated as follows.
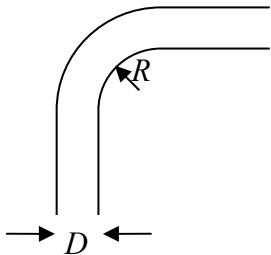


Figure 3.32:    Pipe of the ventilator

In Fig. 3.33, the pressure drop of the recirculation flow as a function of the pipe diameter is shown. On the left ordinate, the value of the pressure drop is indicated; on the right ordinate is the proportion of the pressure drop from the ventilator to the total pressure drop. After a diameter of about 0.5 m, the pressure drop decreases only slightly.
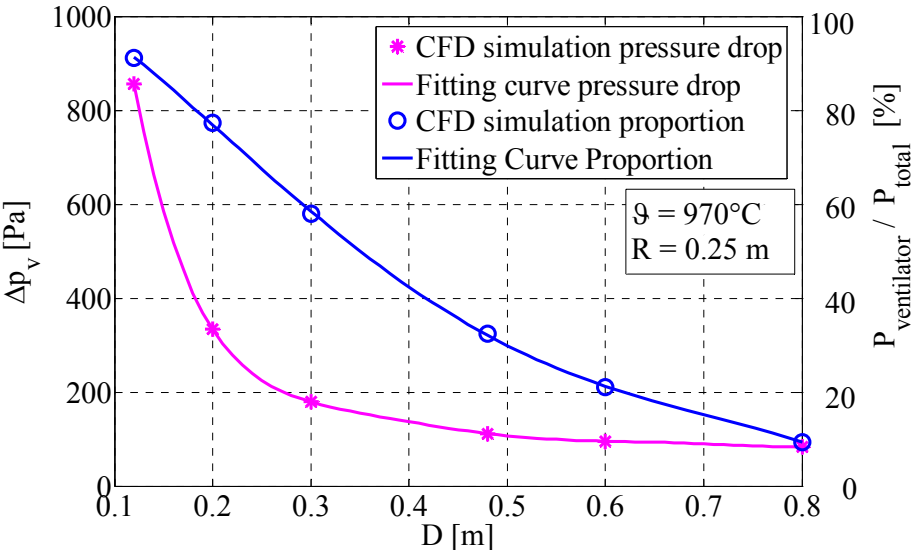


Figure 3.33:    Influence of pipe diameter of ventilator on the pressure drop

In Fig. 3.34 and 3.35, the influence of the curvature radius on the pressure drop is shown. Fig. 3.34 shows the situation when the pipe diameter is 0.24 m, while Fig. 3.35 shows the situation when the pipe diameter is 0.8 m. Both figures show the same phenomenon: the pressure drop decreases at first very fast with the increase of the curvature radius, then the decrease becomes slow, in the medium region, and at last, when the pipe curvature radius increase again, the pressure drop decreases with a higher gradient again. It is also evident that the influence of the curvature radius is relatively smaller than that of the pipe diameter.
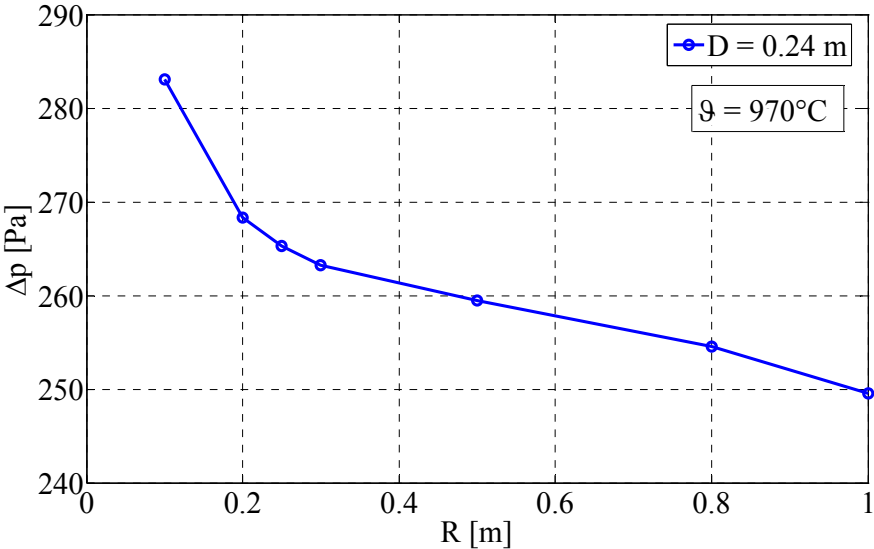


Figure 3.34:  Influence of the curvature radium on the pressure drop with D = 0.24 m
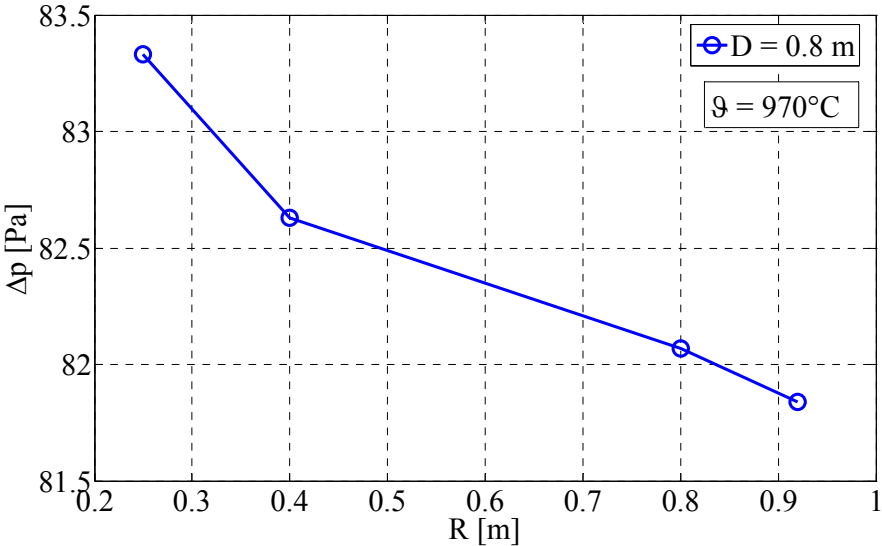


Figure 3.35:  Influence of the curvature radium on the pressure drop with D = 0.8 m

The results above show that both the pipe diameter and the curvature radius should be built as large as possible. However, in the real situation, it is impossible to build them infinitely large. In Fig. 3.36, the velocity vector for the optimal 2D situation is shown for the

geometry, in which the inlets and outlets to the ventilator has a diameter of 0.58 m and a curvature radius of 0.92 m.
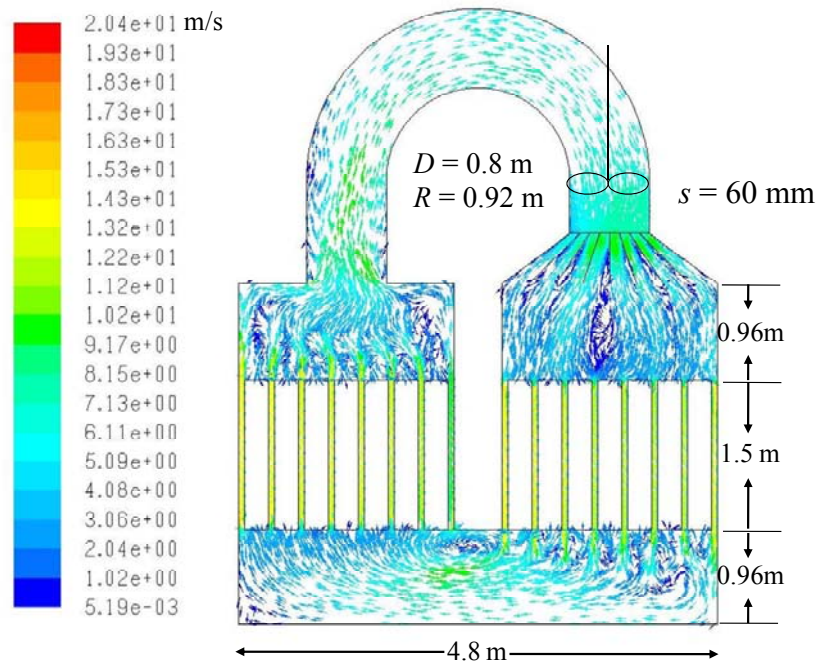


Figure 3.36:    Velocity vector in the optimal 2D situation

In the optimal 2D situation, the pressure drop coefficients for each term are listed in Table 3.3.  It shows that the total of the pressure drop coefficients is therefore 4.742, of which 1.12 (24%) is due to the ventilator.

Table 3.3:       Pressure drop coefficients with 2D optimal vertical ventilator

| Symbol | Explanation | Left | Right |
|--------|-------------|------|-------|
| $\xi_1$ | 90° turn over | 0.1 | 0 |
| $\xi_2$ | Inlet | 0.5 | 0.5 |
| $\lambda \cdot \dfrac{H}{d_h}$ | Friction | 0.57 | 0.57 |
| $\xi_3$ | Outlet | 1 | 1 |
| $\xi_4$ | 90° turn over | 0 | 0.5 |
| | **Sum cross section** | **4.74** | |
| $\xi_5$ | Ventilator | 1.12 | |
| | **Total** | **5.86** | |

## 3.3.3 Electrical power consumption

Like the investigation for the internal ventilator, the electrical power requirements for the optimal vertical ventilator were investigated for different temperatures. Fig. 3.37 shows the results. It is based on the simulation for the gap thickness of 60 mm. Two ventilator geometries are plotted for comparison, one for the internal ventilator and the other for the

vertical ventilator, whose shape is shown in Fig. 3.36. It can be seen that for the whole kiln, the electrical power requirement increases approximately linearly with the increase of the gas temperature, and due to the pressure drop on the vertical ventilator, the electrical power requirement for the vertical ventilator model is higher than that of the internal ventilator.
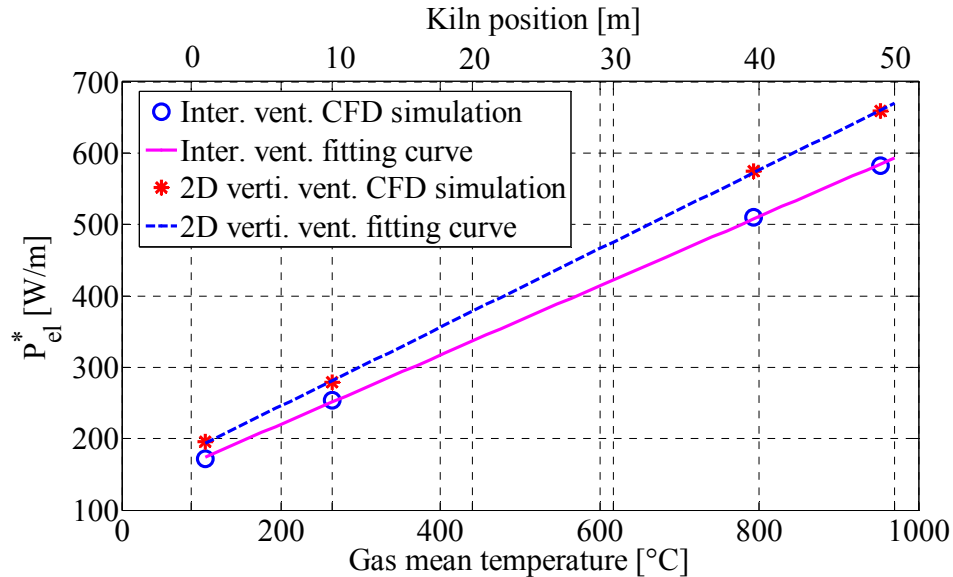


Figure 3.37:   Electrical power requirement for 2D optimal vertical ventilator

# 3.4  Three dimension simulation

The gas flow recirculation was investigated in a three dimension model, which is presented as follows. First, the main differences between the two- and three-dimensional models are compared in Fig. 3.38, they consist mainly of the following two facts:

1. In the 2D model the flow is circulated through one rectangular channel, whose hydraulic diameter is larger; in the 3D model, the flow is circulated through two pipes, whose hydraulic diameters are definitely smaller than that of the 2D model. This results in a difference between pressure drop of the two models.

2. The ventilator power (represented by the pressure jump in the fun function during the simulation) in 2D model works everywhere along kiln length direction (1 m is defaulted by FLUENT), while this power in 3D works only in a pipe cross sectional area. To force the flow recirculation in the whole kiln segment, more ventilator power (e.g. a larger pressure jump of the fun function) is required.
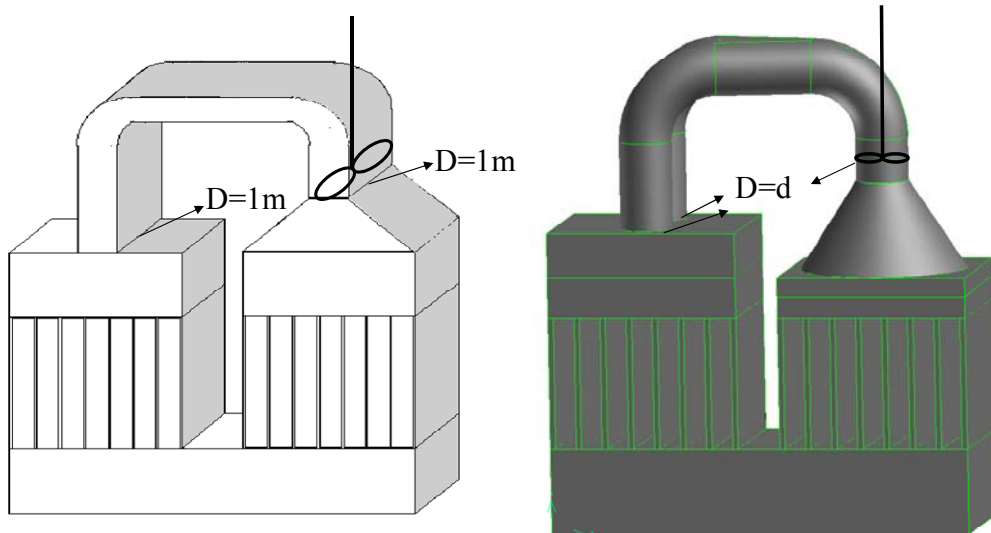
Figure 3.38:    Comparison of two- and three-dimensional models

## 3.4.1 Geometry

As discussed above, a 3D simulation must be carried out. Fig. 3.39 shows the four views of the kiln segment. It illustrates two suction pipes located on the left side of the kiln in the middle along the kiln length direction, and one outlet pipe located in the middle of the right side of the kiln. The considered kiln segment has a length of 2 m, the diameter of the pipe is 0.6 m and the radius of curvature 0.5 m.
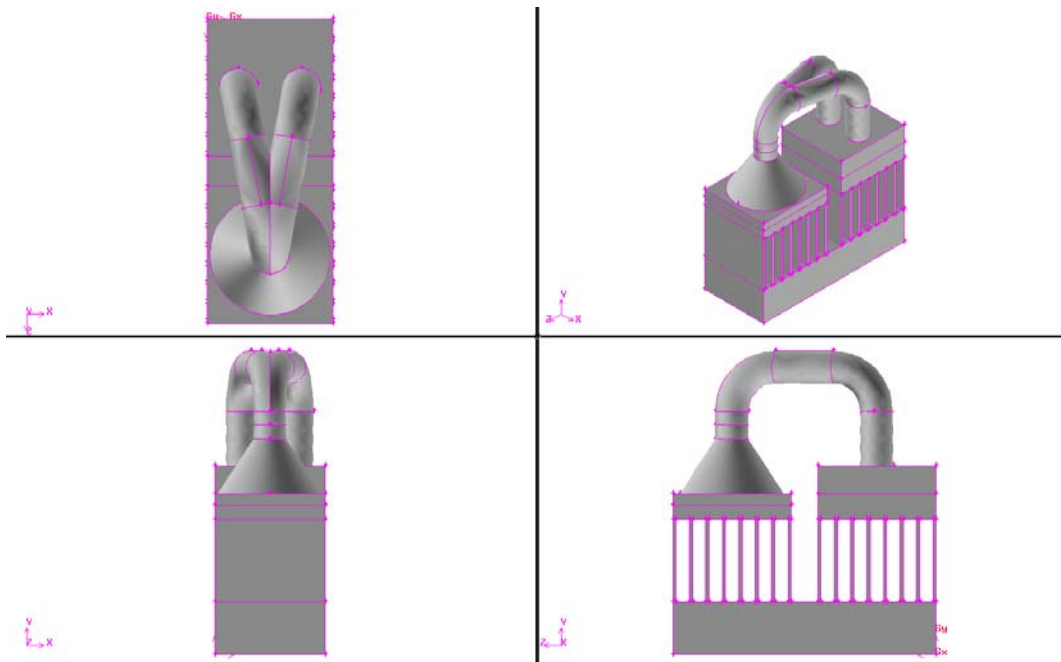


Figure 3.39:    3D-views of kiln segment

As in the simulation of the 2D vertical ventilator, distribution walls are installed under the ventilator to ensure the cross sectional flow is homogenous, which cannot be seen from Fig. 3.39. Instead, it is shown in Fig. 3.40.
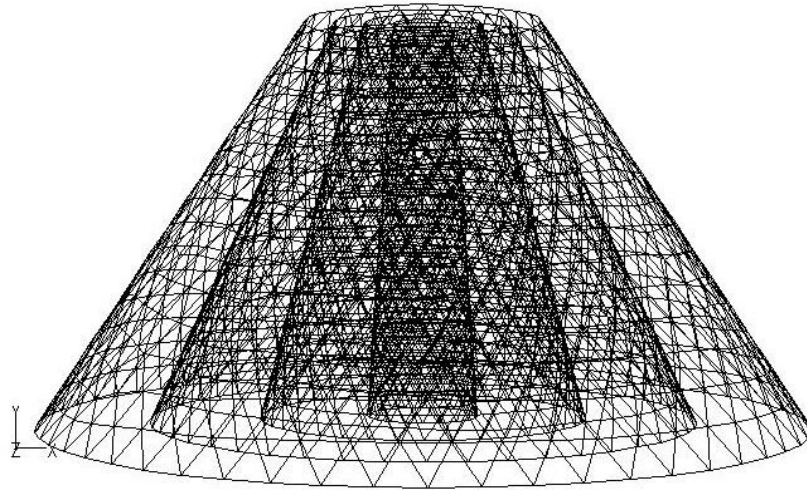
Figure 3.40:    Distribution plates in 3D model

For the 3D simulation, tetrahedral cells were used both inside the gaps and at the top and bottom of the kiln. The use of this shape in the 3D simulation provides both time efficiency and accuracy.  Fig. 3.41 shows the outlet part of the gap. The growth ratio in the gap width direction is 1.2, and the interval size is 7.5 mm.
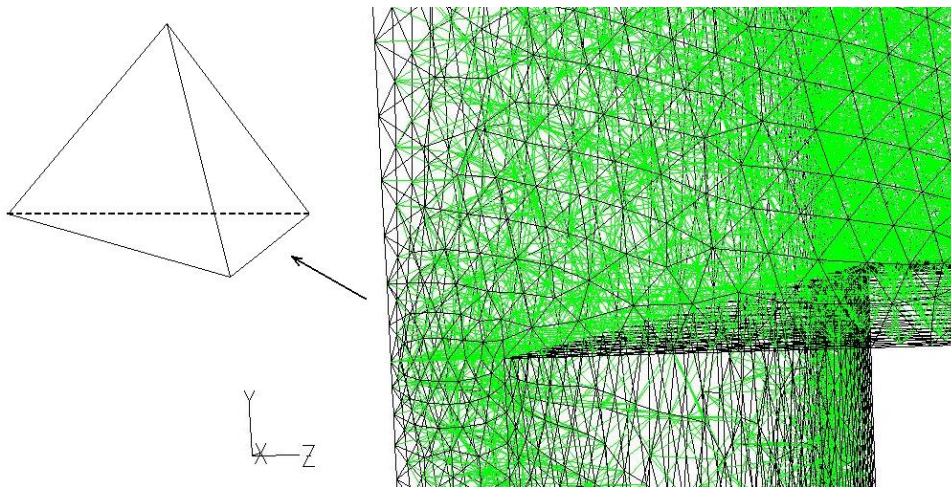


Figure 3.41:    3D cells in the gap outlet position

## 3.4.2 Cross section flow

Fig. 3.42 shows the velocity vector for the middle cross section of the kiln. Like the 2D simulation, it illustrates the flow recirculation in the cross section due to the work of the ventilator. It can be seen that the velocity in the ventilator pipe is much larger, approximately 40 m/s. It also shows the mean velocity inside the gaps is around 11 m/s, while the velocity at the top and bottom of the kiln is approximately 2 m/s.
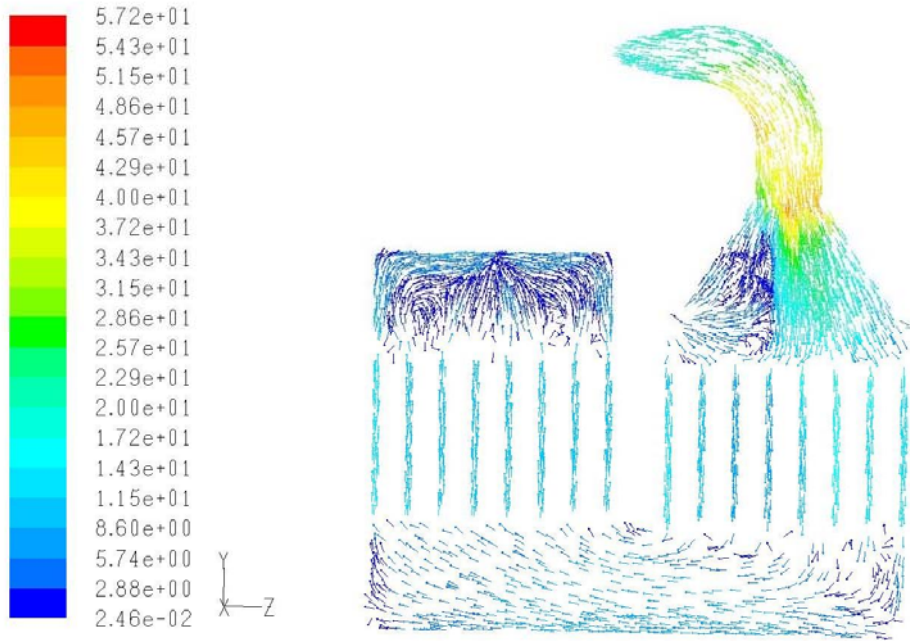
Figure 3.42: Velocity vector in cross section for 3D model

Fig. 3.43 shows the velocity profile inside the gaps. It is clear that the profile is a typical turbulent flow velocity profile. There are some fluctuations on the velocity profile. The reason is that, for 3D simulation, the cells are not fine enough due to the simulation time. It also shows that to reach this velocity, the pressure drop for the 3D model is much larger than that of the 2D internal ventilator, which is shown in Fig. 3.18. For the 2D internal ventilator, the pressure drop is only 126 Pa, while here the pressure drop is 300 Pa.
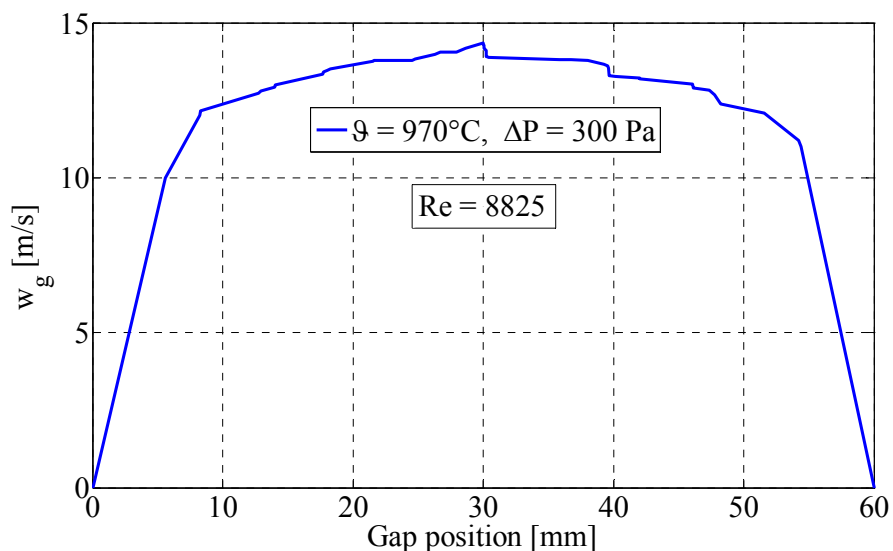


Figure 3.43: Velocity vector in cross section with 3D model

Fig. 3.44 shows the mean velocity of each gap. It can be seen that on the left side under the suction, the velocity for each gap is relative homogenous, while on the right side, due to

78

the impulse of the flow after leaving the ventilator, the velocity on the kiln outer side is higher than that of inner side, despite distribution plates installed under the ventilator. However, this velocity profile is better than that in traditional tunnel kiln. In the traditional tunnel kiln, the so-called wall effect - that almost all the gas flow will go through the gap near to the kiln wall - will be improved by the performance of the ventilator and the gas recirculation in the cross section.
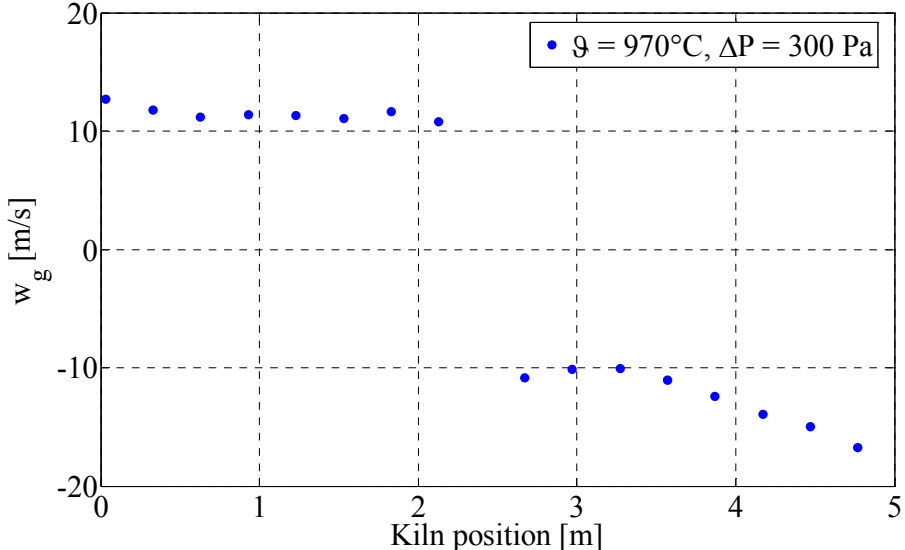


Figure 3.44:    Velocity profile of each gap with 3D model

## 3.4.3 Flow along the kiln length direction

The velocity profiles along the kiln length direction are plotted in Fig. 3.45. It shows the velocity profile in the $X$ direction in four gaps. The red and green lines are on the suction side; the red line is the maximum value, which is the first left point shown in the Fig. 4.44, while the green line is the minimum value, which is the 8th point shown in the same figure. The pink and blue lines are the velocity profiles on the ventilator side; the pink line is the maximum value, which is the sixth point from the right side shown in Fig. 4.44, while the blue line is the minimum value, which is first point shown. It can be seen from Fig. 3.45 that the gas velocity on both sides along the kiln length direction ($X$ direction) are not absolute homogenous. At the middle of the cross section (x = 1 m), the velocity absolute value is higher due to the suction and impulse of the ventilator.  It also shows that on the suction side, the velocity difference between the different gaps is smaller than on the ventilator side. This phenomenon has also been shown in Fig. 3.44. This relatively small derivation in the gas velocity distribution can be accepted, and, when compared to the traditional tunnel kiln, this velocity profile is already much improved.
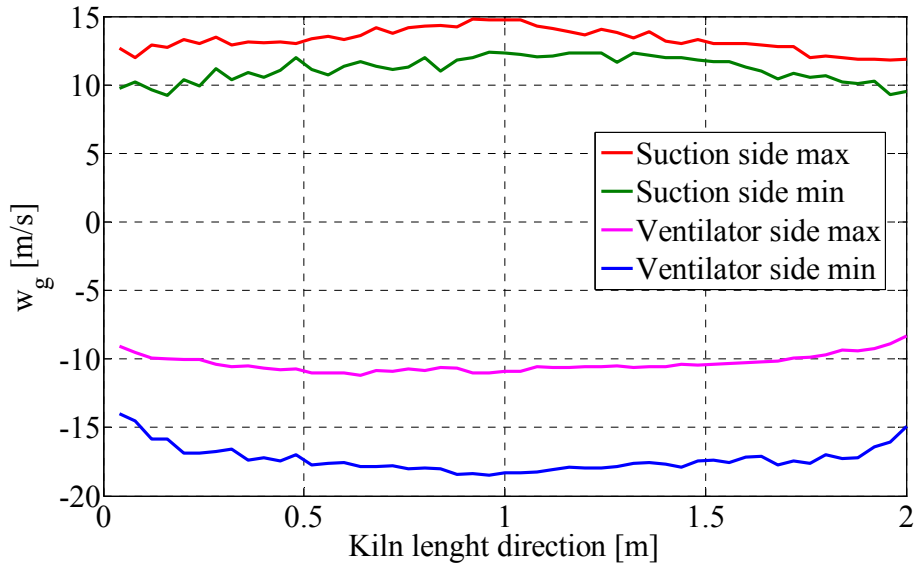
Figure 3.45:  Velocity profile along in the kiln length direction with 3D model

## 3.4.4 Electrical power consumption

The electrical power consumptions for different temperatures are plotted in Fig. 3.46. It shows that for the 3D model, the electrical power consumption also increases with an increase in the gas mean temperature.
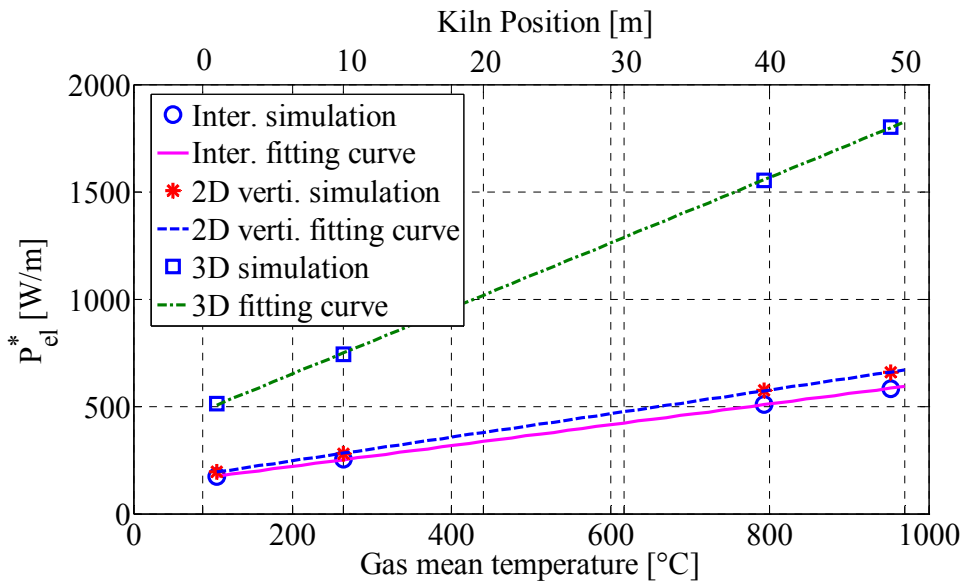


Figure 3.46:  Electrical power requirement for 2D optimal vertical ventilator

For comparison, the electrical power consumptions for the 2D internal ventilator and vertical ventilator are also plotted in Fig. 3.46. As it can be seen, the electrical power consumption for the 3D model is much higher than for the 2D model, due to the model differences discussed at the beginning of section 3.4.

80

The pressure drop coefficients for each term are summarized in table 3.4. It can be seen that the ventilator contributes the most pressure loss for the whole cross section. These values were used in Chapter 2 in the simplified mathematical model.

Table 3.4: Pressure drop coefficients with 3D model

| Symbol | Explanation | Left | Right |
|---|---|---|---|
| | | | |
| $\xi_1$ | 90° turn over | 0.1 | 0 |
| $\xi_2$ | inlet | 0.5 | 0.5 |
| $\lambda \cdot \dfrac{H}{d_h}$ | friction in gap | 0.57 | 0.57 |
| $\xi_3$ | outlet | 1 | 1 |
| $\xi_4$ | 90° turn over | 0 | 0.5 |
| | **Sum cross section** | 4.74 | |
| $\xi_5$ | Ventilator | 9.05 | |
| | **Total** | 13.79 | |

The above discussed results are based on the ventilator geometry shown in Fig. 3.38, whose pipe diameter is 0.6 m and the radius of curvature is 0.5 m. However, in the real situation, a different energy-saving geometry of the ventilator can be installed to change the pressure drop coefficient $\xi_5$ and, furthermore, change the electrical power consumption. Therefore, the sum of the fossil energy and primary ventilator power energy $E_{total}$ is calculated using $\xi_5$ in the range of 1-9.05 as a parameter, as shown in Fig. 2.27.

# 3.5 Firing zone

The above discussed investigations are based on the cooling and preheating zones, in which the gas recirculation in the cross section is generated by the power of the electrical ventilators. In the firing zone, however, the implementation of the ventilators is impossible because of the high temperature, Gas flow recirculation must therefore be generated by the impulse of the burner. Thus, the flow investigation in the firing zone should be carried out.

## 3.5.1 Geometry

In Fig. 3.47 a kiln segment for the firing zone is shown. Here, the gas recirculation is generated by two oppositely installed burners, one located at the top of one kiln side and the other on the bottom of the other side. Two gap thickness are set, $s = 60$ mm and $s = 20$ mm. The gas recirculation in the cross section for different access air numbers and burner diameters was investigated.
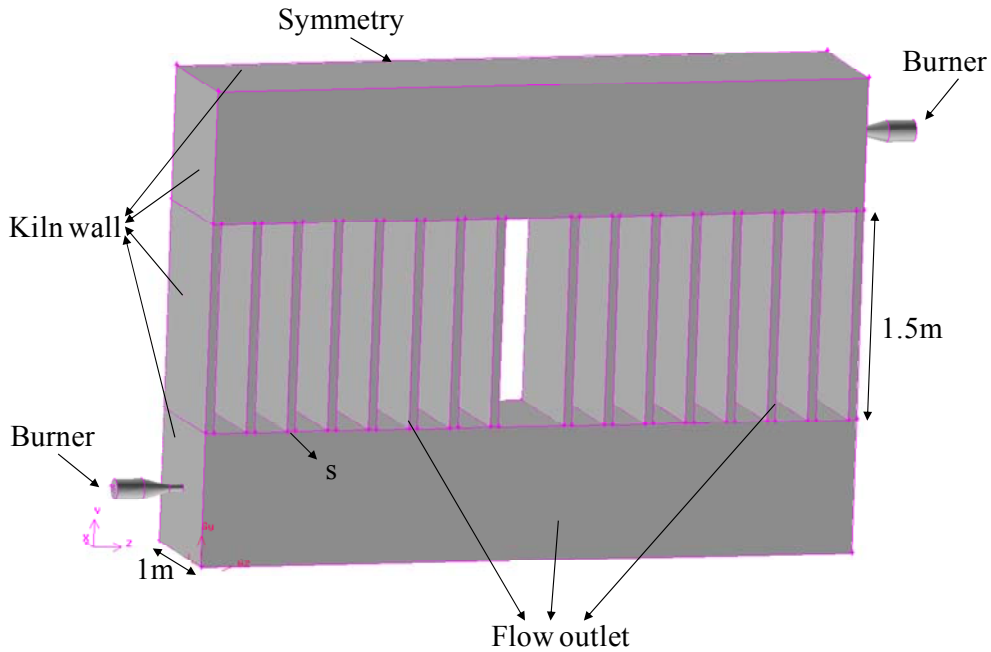
Figure 3.47:    3D model in firing zone

Fig. 3.48 (a) shows the burner in the firing zone in more detail. The burner diameter $d_o$ is shown in the figure. The fuel is supplied from the centre of the burner, and the air from the outer boundary. There is a ring-shaped burner wall to separate the fuel and air, which is shown in Fig. 3.48 (b). This is not a premixed combustion; thus diffusion flame exists in the kiln to fire the green ware.



a) Burner                                            b) Burner wall
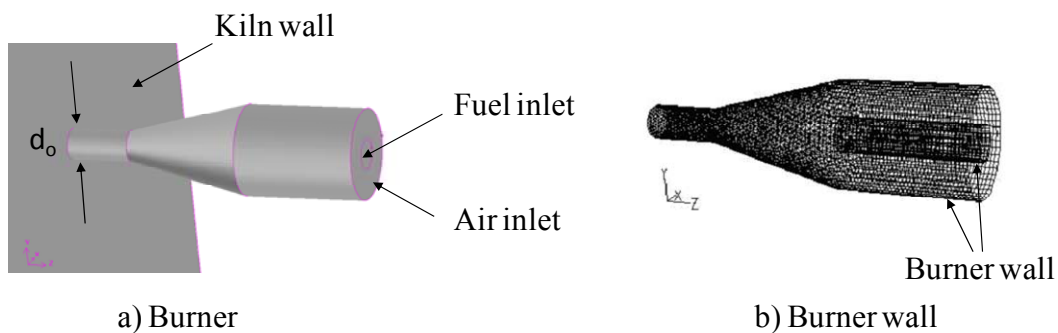
Figure 3.48:    3D burner model

In the firing zone, tetrahedral cells were used both inside the gaps and on the top and bottom of the kiln as in the 3D simulation of the cooling and preheating zones. For the gap width direction of these cells, the growth ratio is 1.2, and the interval size is 7.5 mm. For the burner itself, unstructured cells were used. For the fuel and air inlets, hexahedral cells were used, while for the burner outlet, very fine tetrahedral cells were used to simulate the impulse of the burner outlet into the kiln. These cells are shown in Fig. 3.49.
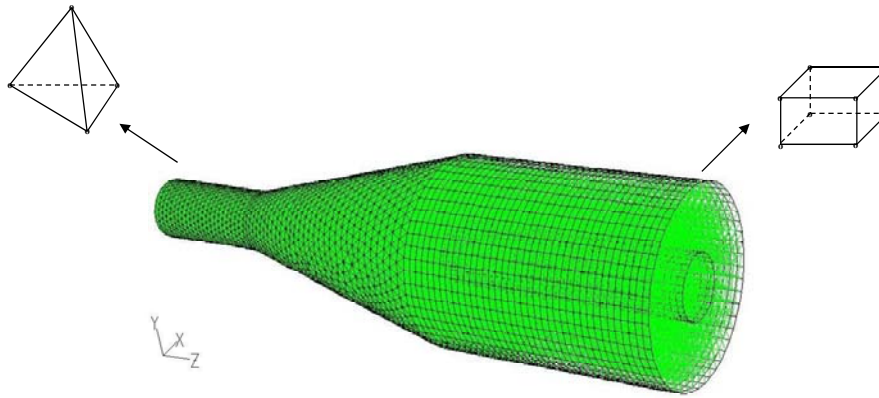
Figure 3.49:    Cells in the burner

With the above described 3D model, simulations in the firing zone were carried out. The fuel is natural gas. The access air number varies from 1-1.3. The burner diameter $d_o$ varies from 20-50 mm. Two gap thicknesses, $s = 60$ mm and $s = 20$ mm, were carried out separately. The burner power was calculated according to the fossil energy requirement illustrated in Fig. 2.26. The firing zone is 10 meter long, and for each meter there are two burners on the top and bottom of both sides. Therefore, there are 20 burners installed in the kiln wall. Thus for each burner, the power is 50.8 kW for $s = 60$mm, and 48.3 kW for $s = 20$ mm.

## 3.5.2 Temperature profile in the cross section

Fig. 3.50 shows the temperature contour of the cross section at x = 0.5 m, located at the middle of the kiln length of the kiln segment. The brick gap thickness is 60 mm; therefore the power of the burner is 50.8 kW. The burner diameter is 50 mm, and the access air number is 1.3. The fuel and air are supplied at ambient temperature from the two burners. It can be seen that the flames are located on the top and bottom of the kiln respectively, with a temperature of about 2000 K. The temperature inside the brick gap is 1300-1400 K.
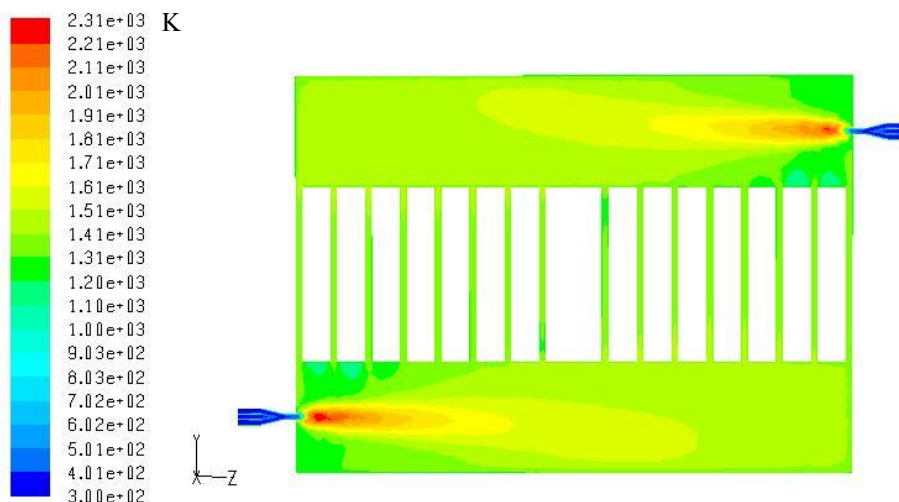


Figure 3.50:    Temperature contour in firing zone

## 3.5.3 Cross section flow

Meanwhile, an investigation for the gas flow in the cross section of the firing zone is carried out to check the gas recirculation. Fig. 3.51 shows the velocity vector of the cross section, located at the middle of the kiln segment at x = 0.5 m. It shows the model with $s = 60$ mm, $d_o = 50$ mm and $\lambda = 1.3$ as an example. It is evident that the gas recirculation in the cross section can be ensured. It can also be seen that the gas on the left gaps flows from the top to the bottom, while the gas on the right gaps flows from the bottom to the top.
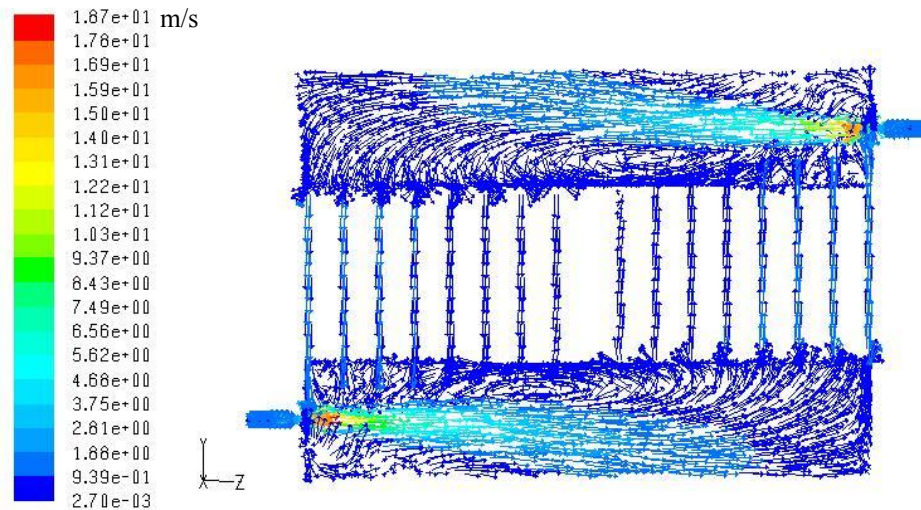


Figure 3.51:    Velocity vector in firing zone

The mean gas velocity for each gas is shown in Fig. 3.52. The horizontal axis represents the kiln position in the cross section, and vertical axis is the mean gas velocity. It shows the simulation results for $s = 60$ mm for different burner diameters between 20-50 mm, while all have an access air number of 1.3. It can be seen that for all burners with different diameters, the gas velocities on the left side are negative and on the right side are positive. Thus it is evident that recirculation in the cross section for each burner diameter can be ensured.
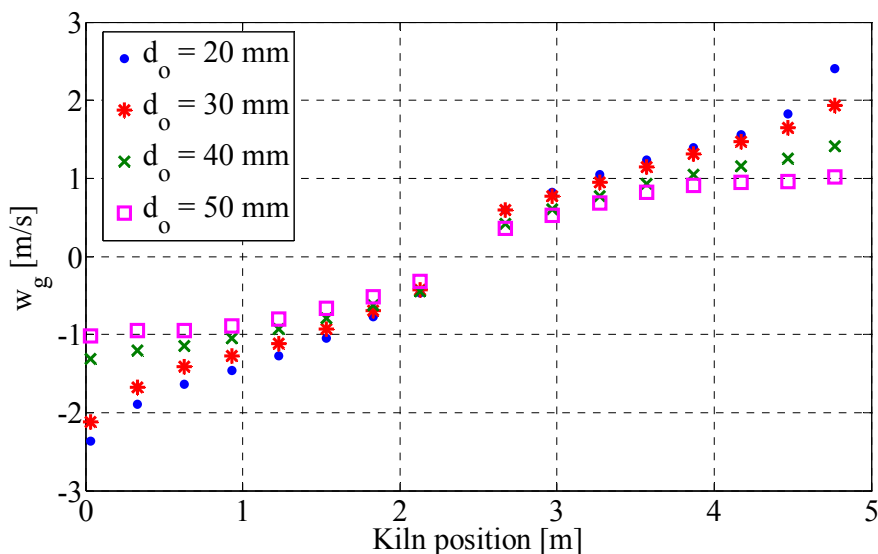


Figure 3.52:    Mean velocity in each gap

84

Fig. 3.51 and 3.52 also demonstrate that the flows through the gaps near the kiln wall are higher than those in the middle of the kiln. The flow is not as homogenous as that in the cooling and preheating zones with ventilators. However, a uniform flow in the firing zone is not as important, since very little heat must be transferred for the sintering occurring here.

## 3.5.4 Flow along the kiln length direction

In Fig. 3.53, the velocity distribution for the simulation with $s = 60$ mm, $d_o = 50$ mm, and $\lambda = 1.3$ along the kiln length direction is shown. It shows two gaps for each side: the gaps with the highest and lowest velocities, which are the gaps near the kiln wall and near the insulation wall. It can be seen that the flow along the kiln length direction is approximately uniform, although the burners are located in the centre of this segment at x = 0.5 m.
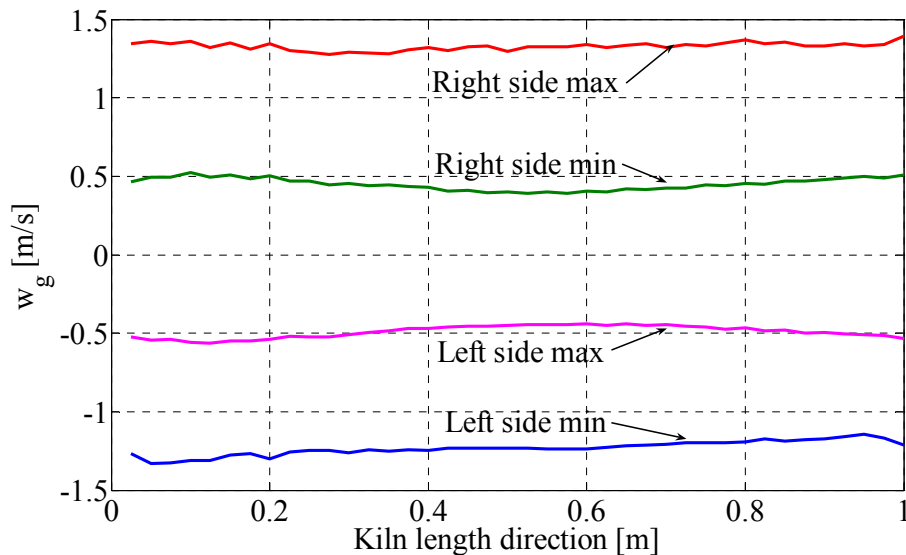


Figure 3.53:   Velocity distribution along kiln length direction

## 3.5.5 Influence of the burner diameter

In Fig. 3.54, the mean velocity in the gaps as a function of the burner diameter is shown. The access air number varies from 1-1.3, and the burner diameter $d_o$ varies from 20 mm-50 mm. Simulations for two gap thickness, $s = 60$ mm and $s = 20$ mm, were carried out separately. As discussed above, the power of the burner is 50.8 kW for $s = 60$mm, and 48.3 kW for $s = 20$ mm.

It can be seen that the larger the burner diameter, the lower the velocity in the gap. This is due to the fact that the bigger the burner diameter, the lower the impulse from the outlet of the burner. For the influence of the access air number, it is evident that the higher the access air number, the higher the gas velocity. This is the result of the relatively higher gas mass flow with the higher access air number.

85
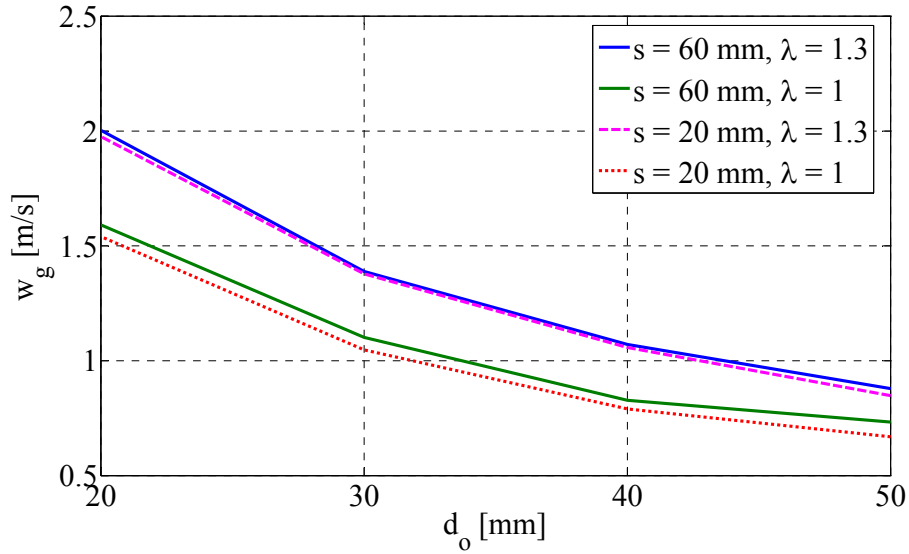
Figure 3.54:    Mean gas velocity in gap dependent on burner diameter

The burner diameter influence on the gas velocity is shown in Fig. 3.54, which shows the mean gas velocity for all gaps. It can be seen that with the decrease in burner diameter, the mean gas velocity in the gaps increases. However, the influence is not the same for every gap. It is bigger for the gaps near to the kiln wall, and smaller for the gaps near to the insulation wall. This phenomenon is clearly illustrated in the Fig. 3.52. Therefore the actual influence on the increase in velocity in the gaps near the kiln wall is larger than the increase in the gaps near the insulation wall.

## 3.5.6 Optimal gap thickness in firing zone

Fig.3.54 has also revealed that in firing zone, the narrower the gap thickness is, the lower the velocity inside the gap is. This effect is influenced by the burner power and the cross sectional gas recirculation.

For the burner power, the smaller the gap thickness is, the lower the fossil energy requirement is, and thus the lower the burner power required. This is explained in Table 3.5.

Table 3.5:       Fossil energy requirement and mass flow inlet for burners

| | Fossil energy requirement $E_{fossil} \left[ \dfrac{MJ_f}{kg_{brick}} \right]$ | Mass flow fuel $\dot{M}_f \left[ \dfrac{kg_f}{s} \right]$ | Mass flow air ($\lambda = 1$) $\dot{M}_L \left[ \dfrac{kg_L}{s} \right]$ |
|---|---|---|---|
| s = 60 mm | 0.4406 | 0.001088 | 0.0163 |
| s = 50 mm | 0.4351 | 0.001074 | 0.0161 |
| s = 40 mm | 0.4296 | 0.001060 | 0.0159 |
| s = 30 mm | 0.4240 | 0.001047 | 0.0157 |
| s = 20 mm | 0.4185 | 0.001033 | 0.0155 |

In Table 5.3, the fuel requirements for thicknesses of 60 mm and 20 mm are taken from Fig. 2.26 at their optimal temperature differences $\Delta\vartheta_s$; for the other gap thickness in the area between 30 mm and 50 mm, the values are obtained by linear interpolation.

For the cross sectional gas recirculation, the narrower the gap thickness, the worse the gas recirculation is. When the gap thickness is very narrow, most of the recirculation gas does not go through the brick gaps but travels in the kiln length direction. This reduces the heat transfer in the cross section. Therefore, the cross sectional gas recirculation conditions for different brick gap thicknesses should also be investigated. For this investigation, the kiln model geometry is described in the section 3.5.1. The values listed in Table 3.5 are for different gap thicknesses between 20 mm and 60 mm. The burner outlet diameter $d_o$ for each case is 50 mm, and the access air number is 1.

Fig. 3.55 shows the total gas mass flow through the gaps, dependent on the gap thickness. Two values are plotted: the gas mass inlet and outlet of the gaps. It can be seen that for both the inlet and outlet, the gas mass flow decreases with a decrease in gap thickness. The reason could be that with the reduction in gap thickness, the majority of the flow travels along the kiln length direction rather than between the cross section. This will lower the heat transfer between the gas and solid. Therefore it is revealed that the larger the brick pile gap thickness, the better the gas recirculation in the cross section.
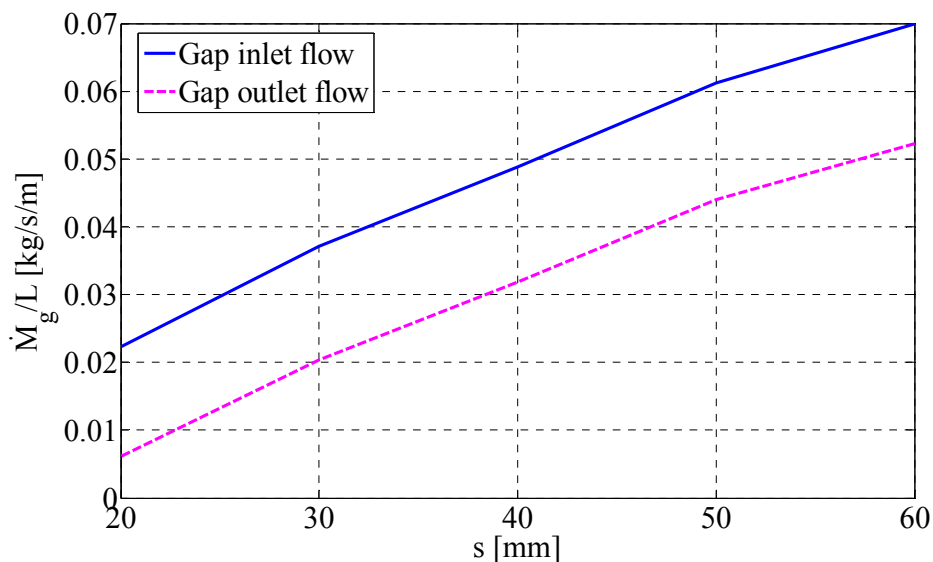


Figure 3.55:   Total gas mass flow through the gaps

However, due to the Nusselt function, the larger the brick pile gap thickness, the worse the heat transfer between the gas and solid will be. Therefore, the heat transfer dependent on gap thickness should also be investigated. This can be carried out by an investigation of the gas temperature difference between the flow inlet and outlet of the gaps. Fig. 3.56 shows these results. It illustrates that the gas temperature difference increases with an increase in gap thickness from 20 mm to 40 mm. After 40 mm, if the gap thickness further increases, the gas

temperature decreases again. The reason is that with the increase in gap thickness, the gas mass flow increases. This is already shown in Fig. 3.55. Therefore, the gas temperature decreases again.
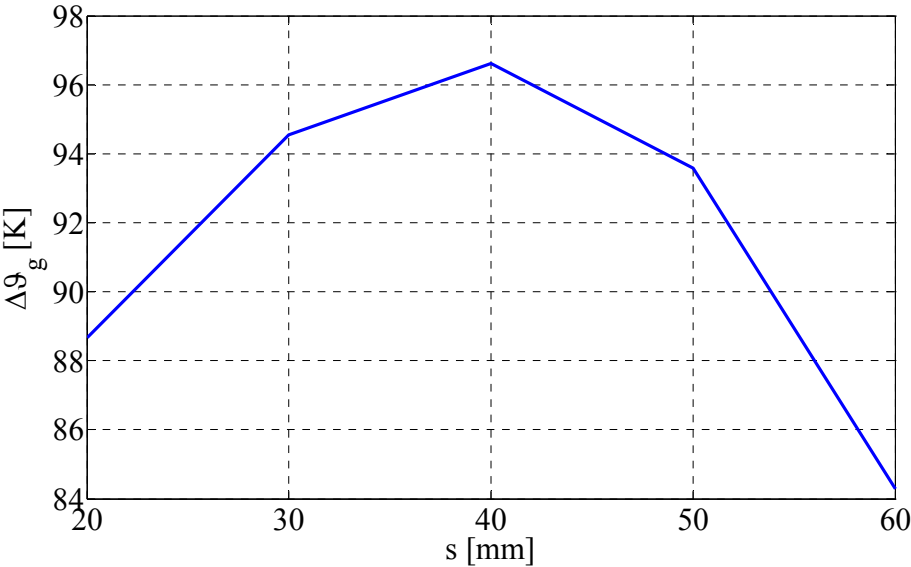
Figure 3.56:    Mean gas temperature difference through the gaps

The transferred heat from the gas to the bricks is shown in Fig. 3.57. This is the value for one kiln side. It is clear that under the double effect of the gas mass flow and the gas temperature difference between the flow inlet and outlet of the gaps, which are already shown in Fig. 3.55 and 3.56, that there is an optimal gap thickness, at which the transferred heat is at its maximum. The optimal gap thickness value in this kiln type is located at 50 mm.
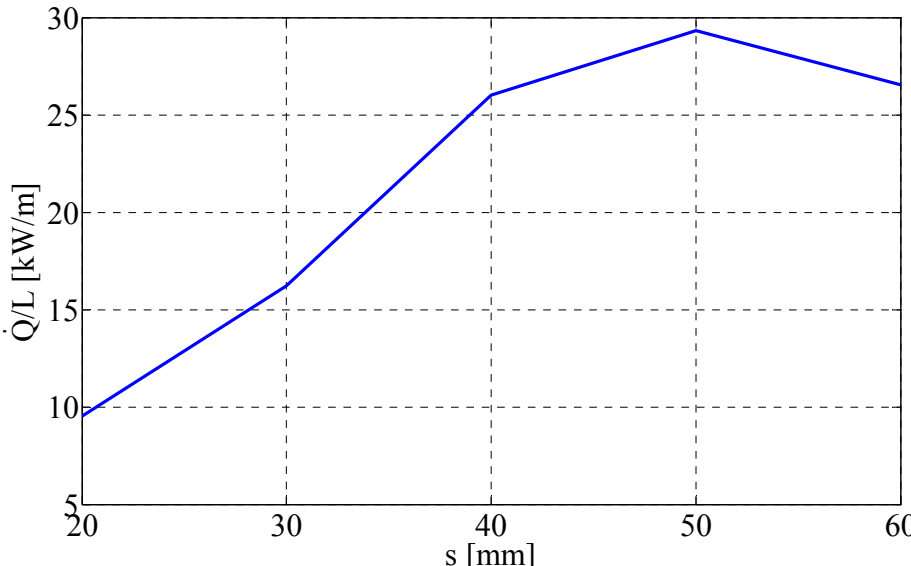
Figure 3.57:    Heat transfer from gas to bricks per side

# 3.6 Summary

CFD simulations with FLUENT 6.3 were performed in this chapter. 2D simulations for the horizontal internal ventilator were firstly carried out. Results showed that the homogenous gas flow in the cross section can be realised with the model of the horizontal internal ventilator. This is important evidence to support the assumption of homogenous gas velocity in the model based simulation in Chapter 2. The pressure drop of the gas recirculation in the cross section was calculated, and furthermore the pressure drop coefficients for the flow turnover were determined.

Then, 2D simulations with a vertical ventilator were performed. The homogenous flow optimization was carried out first. It revealed that the funnel-formed ventilator outlet with distribution walls had the most homogenous gas velocity profile. This simulation was followed by investigating the influence of the ventilator geometry, the diameter of the ventilator pipe, and the radius of the pipe curvature. Finally, on optimal ventilator geometry was enumerated, and the pressure drop and electrical power consumption with this ventilator were determined.

Furthermore, 3D simulations were carried out using one ventilator model as an example. The flow was investigated in the cross sectional direction and along the kiln length direction. It was shown in the suction side that the flow is homogenous, while in the ventilator side, the flow velocity near the kiln wall is higher than that near the insulation wall. Along the kiln length direction, at the middle of the kiln segment, the velocity value is slightly higher due to the suction and impulse of the ventilator. At last, the pressure drop coefficients for each term were listed and these values were used in the model based simulation in the Chapter 2.

Finally, the 3D gas simulations in the firing zone were carried out. It was revealed that gas recirculation in the cross section of the firing zone can be realized. Although with a decrease in burner diameter the mean gas velocity increases, the velocity change dependent on the burner diameter for the gaps near to the insulation wall is very small. The gap thickness influences the gas cross sectional recirculation and heat transfer. An optimal gap thickness of 50 mm is illustrated.

# 4.  Model Verification

The following assumptions were made to simplify the mathematical model described in Chapter 2. They include steady conditions and a uniform temperature of the brick pile. These assumptions are verified in this chapter by a model extension.

## 4.1  Model description

The kiln cars are transported not continuously, but periodically, through the kiln. One car is being pushed into the kiln once the wicket is opened, and simultaneously another car exits. During the transportation of the cars through the kiln, they are stationary most of the time. Transient temperature gradients always exist in the brick after the car is shifted to the next position. Therefore, it is necessary to investigate to what extent the unsteady temperature profile can be approximated by steady conditions.

### 4.1.1 Process description

In Fig. 4.1, the kiln is subdivided into different car segments. Each section has a length of 1 m, and every hour, one car in one channel is driven into the kiln, and all other cars in this channel are moved forward correspondently. So do the cars in the other channel, but in reverse direction.
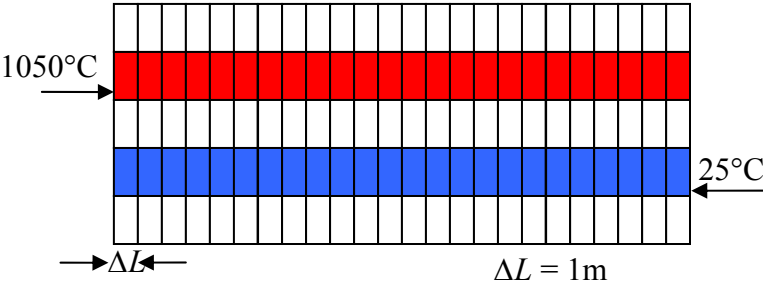


Figure 4.1:     Subdivision of the kiln in car segments

The transient temperature profiles inside the brick piles are qualitatively shown in Fig. 4.2. On the cold (left) side, the temperature increases with the time, and the surface temperature is higher than the core temperature. On the hot (right) side, the temperature decreases accordingly, with a surface temperature lower than the core temperature.
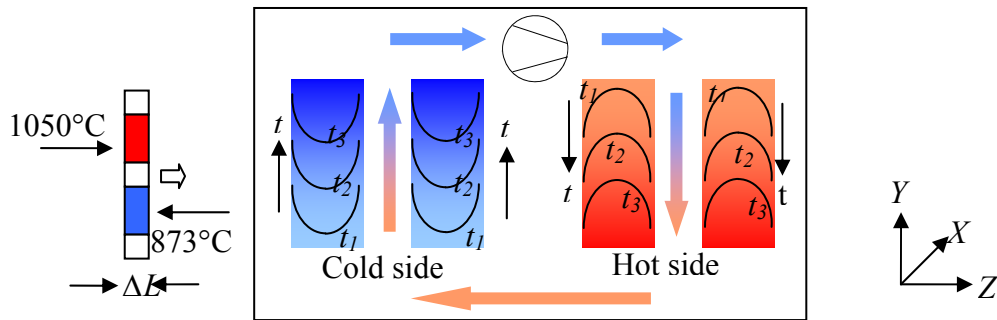
Figure 4.2:    Qualitative transient temperature profile of bricks piles

In Fig. 4.3, the mean temperatures in the cross section of the brick pile as a function of the height $Y$ are shown. In this figure, the hot side is shown on the right and the cold side on the left. The temperature decreases at first approximately linearly with the height. The temperature of the gas lies between the temperatures of the two brick piles. The temperature profiles of the gas in the gap on both sides are almost the same. The temperature profiles of the brick piles move towards each other, that is to say, the temperature difference between the two piles will become smaller and smaller with time.
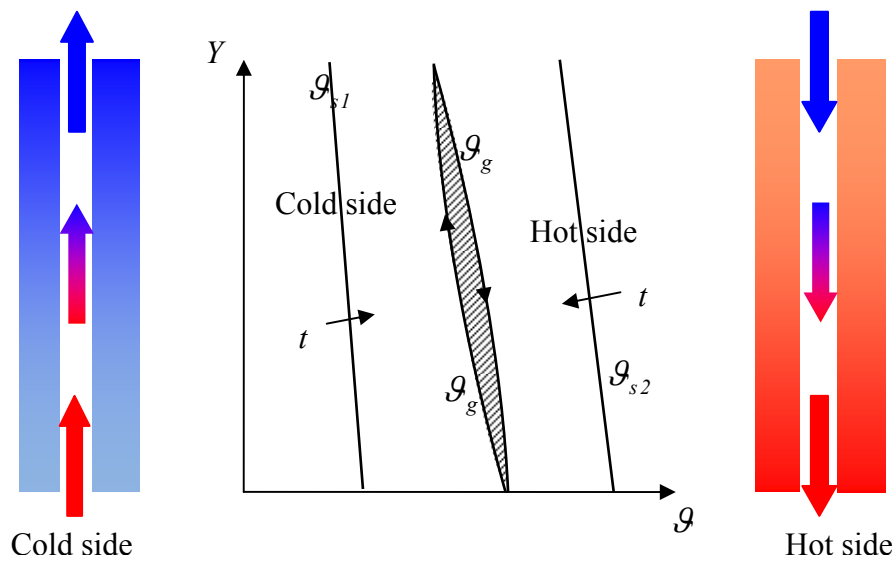


Figure 4.3:    Profile of mean temperature in the cross section of the brick pile dependent on height

## 4.1.2 Algorithm and mathematical equations

For the calculation of the temperatures of the gas and solid, a quasi-transient steady state [37] is assumed. This means that the solid temperature is known at time $t = t_0$ (in the first cross section segment, the solid is just coming out from the firing zone, so that the solid temperature is equal to the firing temperature universally; in other cross section segments, the solid temperature dependent on the height can be taken from the last cross section calculation). Here only a one-dimension problem, the temperature profile along the height direction, will

91

be considered. A very small time step $\Delta t$ is taken, in which the solid temperature during the time from $t = t_o$ to $t = t_o+\Delta t$ is assumed to be constant. With this known solid temperature, the gas temperature dependence on the height, which is also a function of time, from $t = t_o$ to $t = t_o+\Delta t$ can be solved. Then in the time period from $t = t_o+\Delta t$ to $t = t_o+2\cdot\Delta t$, the gas temperature is assumed to be constant. With this gas temperature, the solid temperature dependent on the height can be solved. With this algorithm, the transient temperature changes of both the solid and gas can be simulated. This process is illustrated in Fig. 4.4. When the time step $\Delta t$ is small enough, this process can be treated as a transient state.
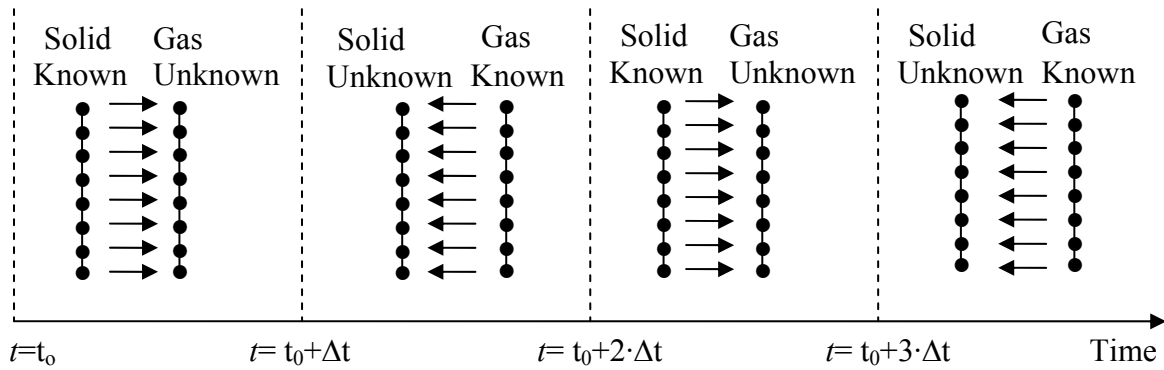


Figure 4.4:    Quasi-transient steady state for gas and solid temperature along the height

The nodes shown in Fig. 4.4 are further illustrated in the 3D view in Fig. 4.5. It represents an infinitesimal element [38] taken from the cross section. Here, only the cold side is shown as an example. The hot side has the same mechanism. The solid element taken out has the width of $b/2$, which is one half of the width of the brick pile $b$, therefore the left surface of the solid element in Fig. 4.4 can be seen as insulation. Analogously, the right surface of the gas can also be seen as such. Here only the temperature dependent on the height is investigated; the temperature profile inside of the cross section will be discussed later. Therefore, the temperature of the solid as well as the gas temperature can be seen as universal in the dimension of $dy$, which are expressed as $\bar{\vartheta}_s$ and $\bar{\vartheta}_g$ respectively.
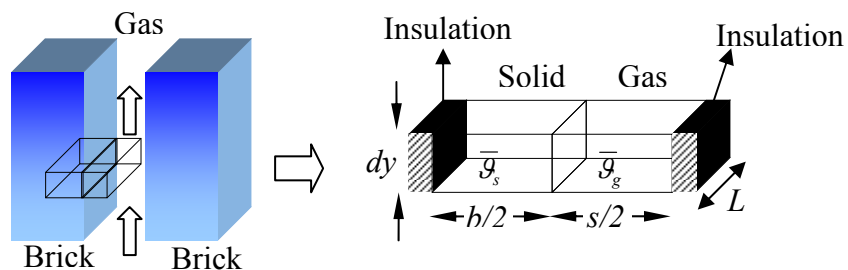


Figure 4.5:    Infinitesimal element to calculate solid and gas temperature

To solve the gas temperature with the solid temperature, an infinitesimal control volume with a height of $dy$ is taken from the gas, on which the energy balance is analyzed. Fig. 4.6 shows this gas control volume.

92
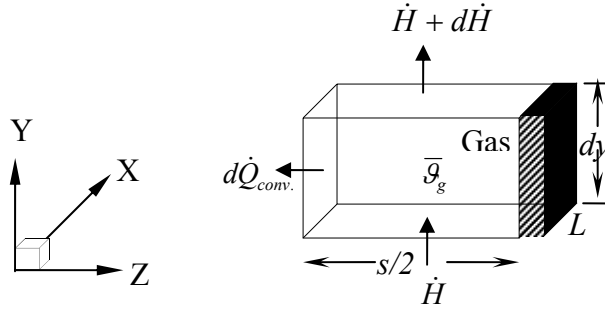
Figure 4.6:    Infinitesimal gas control volume

The inflow gas enthalpy can be expressed as:

$$\dot{H} = \dot{M}_g \cdot c_{p,g} \cdot \overline{\vartheta}_g ,$$  (4-1)

the outflow convection heat between the gas and solid surface can be expressed as:

$$d\dot{Q}_{conv.} = \alpha_{eff.} \cdot dy \cdot L \cdot \left( \overline{\vartheta}_g - \overline{\vartheta}_s \right) ,$$  (4-2)

and the outflow gas enthalpy can be expressed, considering of Taylor-series approximation, as:

$$\dot{H} + d\dot{H} = \dot{M}_g \cdot c_{p,g} \cdot \left( \overline{\vartheta}_g + \frac{d\overline{\vartheta}_g}{dy} \cdot dy + \frac{d^2\overline{\vartheta}_g}{dy^2} \cdot \frac{(dy)^2}{2!} + ... \right) .$$  (4-3)

According to the energy balance of the infinitesimal gas control volume shown in Fig. 4.6, the energy supplied is equal the energy flowing out; mathematically it is expressed as:

$$\alpha_{eff.} \cdot dy \cdot L \cdot \left( \overline{\vartheta}_s - \overline{\vartheta}_g \right) = \dot{M}_g \cdot c_{p,g} \cdot \frac{d\overline{\vartheta}_g}{dy} \cdot dy ,$$  (4-4)

with  $\dot{M}_g = \rho_g \cdot w_g \cdot \frac{s}{2} \cdot L .$  (4-5)

Then, the equation to solve for the gas temperature can be written as:

$$\frac{d\overline{\vartheta}_g}{dy} = \frac{\alpha_{eff.} \cdot \left( \overline{\vartheta}_s - \overline{\vartheta}_g \right)}{\rho_g \cdot w_g \cdot \frac{s}{2} \cdot c_{p,g}} ,$$  (4-6)

with the boundary condition $\overline{\vartheta}_g \big|_{y=0} = \vartheta_{g,0} .$  (4-7)

In the gas boundary condition expressed in Eq. (4-7) $\overline{\vartheta}_g \big|_{y=0} = \vartheta_{g,0}$ , $\vartheta_{g,0}$ ,   the first gas recirculation of the first car segment is assumed to be equal to the ambient temperature or firing temperature. In the other gas recirculation of the first car segment or other car segments, it can be taken from the last iteration. The gas always circulates in the cross section from hot solid to cold solid, and then from cold solid to hot solid again.

For the temperature dependent gas material properties, a non-linear method is used [39]. At the first trial, gas temperatures at each node are assumed to be equal to $\overline{\vartheta}_g \big|_{y=0}$ , and the

material properties are calculated at this temperature. The new gas temperature is then calculated at each node at the end of the first trial. Using this new temperature, the gas material properties for each node can be updated, and a new gas temperature can be further calculated. If the error between the new gas temperature and the gas temperature from the previous trial is smaller than $10^{-6}$, the new gas temperature can be accepted as the actual gas temperature.

The above process can also be used to solve for the solid temperature. Because the problem is a transient problem, the solid temperature strongly depends on the time. The solid temperature will change the heat transfer from the solid to the gas. During the next time step $\Delta t$, the gas temperature can be assumed to be constant, and using the gas temperature, the solid temperature can be estimated.

To solve for the solid temperature using the gas temperature, an infinitesimal finite element of the solid is considered for the analysis of the energy balance. Fig. 4.7 shows this element.
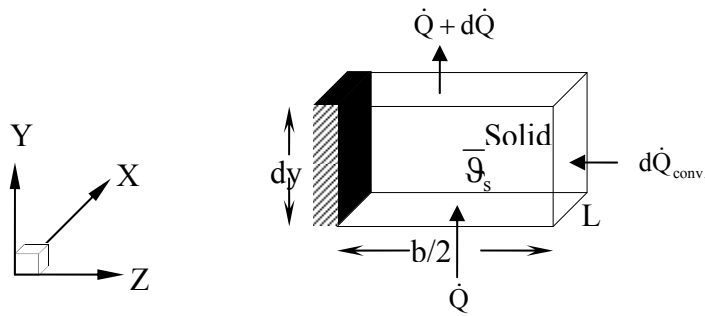


Figure 4.7:    Infinitesimal solid element

Due to the temperature difference in the solid's height direction, there is heat flux from bottom to the top of the solid.  Therefore the heat entering the element is written as:

$$\dot{Q} = \dot{q}_y \cdot \frac{b}{2} \cdot L \ , \tag{4-8}$$

the heat flowing into the element due to the convection is described by:

$$d\dot{Q}_{conv.} = \alpha_{eff.} \cdot \left( \overline{\vartheta}_g - \overline{\vartheta}_s \right) \cdot dy \cdot L , \tag{4-9}$$

and the total heat leaving the element is expressed by:

$$\dot{Q} + d\dot{Q} = \left( \dot{q} + \frac{d\dot{q}_y}{dy} \cdot dy \right) \cdot \frac{b}{2} \cdot L \ . \tag{4-10}$$

For the energy balance on the element, the energy entering minus the energy exiting is equal to the energy stored in the solid; mathematically it can be expressed as:

$$\dot{Q} + d\dot{Q}_{conv.} - \left( \dot{Q} + d\dot{Q} \right) = \rho_s \cdot c_s \cdot dy \cdot L \cdot \frac{b}{2} \cdot \frac{\partial \overline{\vartheta}_s}{\partial t} \ . \tag{4-11}$$

The heat flux due to the temperature difference in the $Y$ direction is:

$$\dot{q}_y = -\lambda_s \cdot \frac{d\overline{\vartheta}_s}{dy}$$

(4-12)

From the above equations, the equation to solve the solid temperature using to gas temperature can be conducted as follows:

$$\frac{\alpha_{eff.} \cdot \left(\overline{\vartheta}_g - \overline{\vartheta}_s\right)}{b/2} - \lambda_s \cdot \frac{\partial^2 \overline{\vartheta}_s}{\partial y^2} = \rho_s \cdot c_s \cdot \frac{\partial \overline{\vartheta}_s}{\partial t}.$$

(4-13)

To solve Eq. (4-13), one initial condition and two boundary equations are needed. The initial condition can be:

$$\overline{\vartheta}_s\big|_{t=0} = \vartheta_{s,0}$$

(4-14)

For the first car segment just coming into the kiln with ambient temperature, there is no temperature difference inside of the solid, so the initial temperature is known. In the other direction the first car segment just coming out from the firing zone, the temperature of the solid is the firing temperature. The initial temperature is also known. For other car segments, the solid initial temperature can be obtained from the previous car segment, which is just moved to the new position.

The boundary conditions are as follows: at the bottom of the solid, the solid is insulated by the basement on the kiln car, so the heat flux is zero here, mathematically expressed by:

$$-\lambda_s \cdot \frac{d\overline{\vartheta}_s}{dy}\bigg|_{y=0} = 0 \ .$$

(4-15)

On the top surface of the solid, a convective heat transfer exists between the solid surface and the gas. Since the fluid velocity in the surface direction at the top of the brick pile is very small, the local heat transfer coefficient is also very small. Thus, the heat flux at the top of the brick can be neglected, expressed as follows:

$$-\lambda_s \cdot \frac{d\overline{\vartheta}_s}{dy}\bigg|_{y=H} \approx 0$$

(4-16)

The model discussed above is the calculation algorithm for the solid and gas temperatures on the cold side, where the heat will be transferred from the gas to the solid. On the hot side where the heat will be transferred from the solid to gas, the calculation algorithm is the same as the above equations.

With the equations described above, the temperature of the solid and gas dependent on the brick pile height and time can be simulated as a function of the ventilator power, gap thickness, temperature difference between the both sides, brick pile number per side, brick pile height, brick production throughput, and so on.

## 4.1.3 Calculation process

The electric ventilator power calculation process is described as follows: for the first calculation, the brick in the hot side is traced. The cold solid inner temperature along the height direction is unknown, and since there is no way to decide the temperature exactly at the first calculation, the desired mean temperature of the cold solid in each kiln position is used, shown in table 4.1. On the hot side, the hot solid coming out from the firing zone is assumed to have the homogenous temperature. During the first calculation, the hot solid will be traced from the firing zone to the kiln exit at the end of the cooling zone, the same path as the flue gas; the hot solid inner temperature profile along the height direction can be obtained from the previous position. Different electrical ventilator powers will produce different hot solid temperatures. The electrical power, that produces a hot solid temperature equal to the desired process temperature, is exactly the electrical power we want. After this calculation, the hot solid temperature profile along the height direction at each position can be obtained. These values will be used in the second calculation. This process is illustrated in Fig. 4.8.
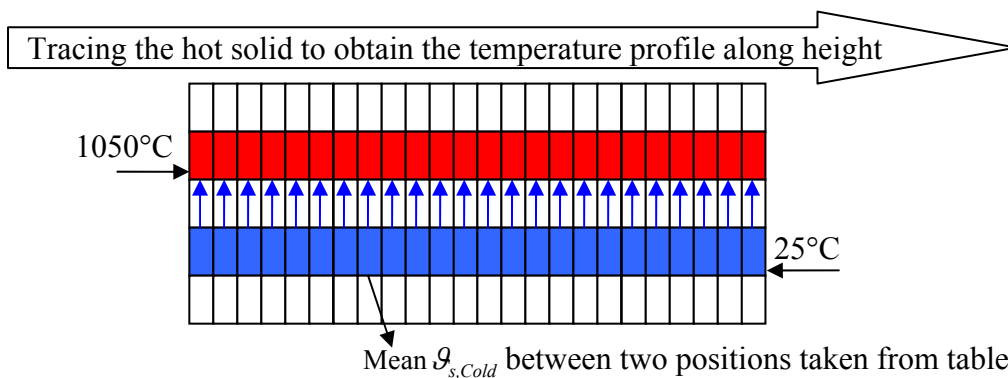


Figure 4.8:     Calculation process for the 1st calculation

Table 4.1:     Mean temperature at each position for $\Delta\vartheta_s = 160$ k along the kiln length

| Position Entrance 0 | Position Firing Zone 0 | Node | Iteration | $\vartheta_{s,hot}$ | $\vartheta_{s,cold}$ | Mean $\vartheta_{s,cold}$ between two positions (used in the 1st calculation) |
|---|---|---|---|---|---|---|
| 50m | 0m | 1 | | 1050 | 890 | |
| | | 2 | 1 | 1032.7 | 872.7 | 881.35 |
| | | 3 | 2 | 1015.4 | 855.4 | 864.05 |
| | | 4 | 3 | 998.1 | 838.1 | 846.75 |
| | | 5 | 4 | 980.8 | 820.8 | 829.45 |
| 45m | 5m | 6 | 5 | 963.5 | 803.5 | 812.15 |
| | | 7 | 6 | 946.2 | 786.2 | 794.85 |
| | | 8 | 7 | 928.9 | 768.9 | 777.55 |
| | | 9 | 8 | 911.6 | 751.6 | 760.25 |
| | | 10 | 9 | 894.3 | 734.3 | 742.95 |

| | | | | | | |
|---|---|---|---|---|---|---|
| 40m | 10m | 11 | 10 | 877 | 717 | 725.65 |
| | | 12 | 11 | 859.7 | 699.7 | 708.35 |
| | | 13 | 12 | 842.4 | 682.4 | 691.05 |
| | | 14 | 13 | 825.1 | 665.1 | 673.75 |
| | | 15 | 14 | 807.8 | 647.8 | 656.45 |
| 35m | 15m | 16 | 15 | 790.5 | 630.5 | 639.15 |
| | | 17 | 16 | 773.2 | 613.2 | 621.85 |
| | | 18 | 17 | 755.9 | 595.9 | 604.55 |
| | | 19 | 18 | 738.6 | 578.6 | 587.25 |
| | | 20 | 19 | 721.3 | 561.3 | 569.95 |
| 30m | 20m | 21 | 20 | 704 | 544 | 552.65 |
| | | 22 | 21 | 686.7 | 526.7 | 535.35 |
| | | 23 | 22 | 669.4 | 509.4 | 518.05 |
| | | 24 | 23 | 652.1 | 492.1 | 500.75 |
| | | 25 | 24 | 634.8 | 474.8 | 483.45 |
| 25m | 25m | 26 | 25 | 617.5 | 457.5 | 466.15 |
| | | 27 | 26 | 600.2 | 440.2 | 448.85 |
| | | 28 | 27 | 582.9 | 422.9 | 431.55 |
| | | 29 | 28 | 565.6 | 405.6 | 414.25 |
| | | 30 | 29 | 548.3 | 388.3 | 396.95 |
| 20m | 30m | 31 | 30 | 531 | 371 | 379.65 |
| | | 32 | 31 | 513.7 | 353.7 | 362.35 |
| | | 33 | 32 | 496.4 | 336.4 | 345.05 |
| | | 34 | 33 | 479.1 | 319.1 | 327.75 |
| | | 35 | 34 | 461.8 | 301.8 | 310.45 |
| 15m | 35m | 36 | 35 | 444.5 | 284.5 | 293.15 |
| | | 37 | 36 | 427.2 | 267.2 | 275.85 |
| | | 38 | 37 | 409.9 | 249.9 | 258.55 |
| | | 39 | 38 | 392.6 | 232.6 | 241.25 |
| | | 40 | 39 | 375.3 | 215.3 | 223.95 |
| 10m | 40m | 41 | 40 | 358 | 198 | 206.65 |
| | | 42 | 41 | 340.7 | 180.7 | 189.35 |
| | | 43 | 42 | 323.4 | 163.4 | 172.05 |
| | | 44 | 43 | 306.1 | 146.1 | 154.75 |
| | | 45 | 44 | 288.8 | 128.8 | 137.45 |
| 5m | 45m | 46 | 45 | 271.5 | 111.5 | 120.15 |
| | | 47 | 46 | 254.2 | 94.2 | 102.85 |
| | | 48 | 47 | 236.9 | 76.9 | 85.55 |
| | | 49 | 48 | 219.6 | 59.6 | 68.25 |
| | | 50 | 49 | 202.3 | 42.3 | 50.95 |
| 0m | 50m | 51 | 50 | 185 | 25 | 33.65 |

In the second calculation, however, the cold solid will be traced from the kiln entrance at the preheating zone to the firing zone, and the gas will be blown from the entrance to the firing zone at the ambient temperature. When the green ware first enters into the kiln, the temperature of the solid is equal to the ambient temperature. When the green ware with ambient temperature meets the hot solid, the hot solid temperature in the appropriate position can be taken from the first calculation. From there the temperature profile of cold solid can be obtained, which can be used to the third calculation. Fig. 4.9 shows this process.

Temperature profile along height taken from the previous calculation

1050°C

25°C

Tracing the cold solid to obtain the temperature profile along height
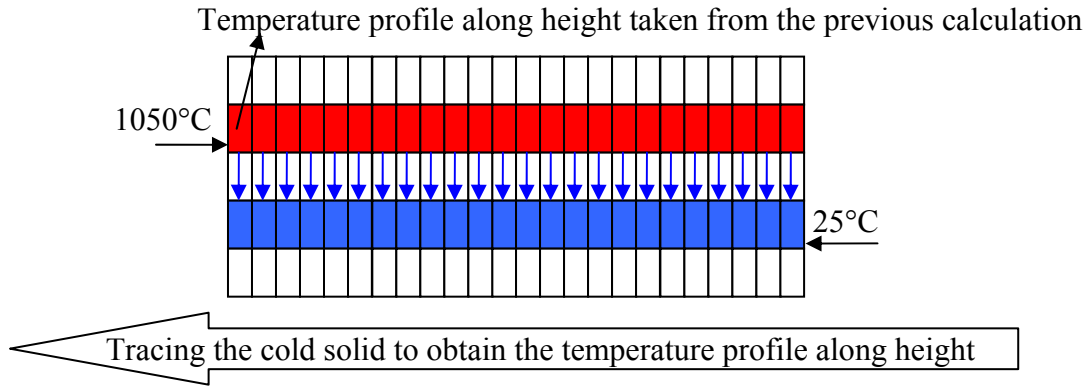
Figure 4.9:    Calculation process for the 2nd calculation

From the third calculation, the temperature profile along the height direction, which is not traced in the current calculation, is always taken from the previous result. Therefore, for each calculation, the result for the solid temperature profile is more and more accurate and will approach the real value. When the result converges, it can be treated as the real value.

The calculation order for each car segment at any time $t = t_0$ can be explained by the following: 1. Determine the hot solid temperature (directly from the firing zone or from the previous calculation for the car segment); 2. Determine the cold solid temperature; 3. Solve for the gas temperature on the cold side according to the cold solid temperature; 4. Solve for the gas temperature on the hot side according to the hot solid temperature. After this, for the next time step $t = t_0+\Delta t$, the calculations will be carried out in the same order, until t is equal to the time required to push the kiln car in the reverse direction to the next position. Then the new kiln car segments will meet each other, and the calculations will start again.

## 4.2  Transient temperature gradients along height

When the mean temperature difference between the both sides is set to 160 K, the temporal initial conditions for the first car segment are:

$$\vartheta_{s,hot}(t=0) = 1050°C \tag{4-17}$$

and

$$\vartheta_{s,cold}(t=0) = 873°C. \tag{4-18}$$

Here is an example considering kiln position, where the kiln car from the firing zone enters into the cooling zone. Meanwhile on the other side, the car with a temperature of 873°C from the preheating zone is pushed forward to the next position near to the firing zone. This value comes from the calculation, which is shown in table 4.1 when the temperature difference of the both kiln sides is 160 K; this value is also shown later in Fig. 4.14.

In Fig. 4.10, the temperature of the gas dependent on the height of the brick piles is shown, with time as a parameter. The gas comes out from the firing zone with a temperature

of 1050°C and flows into the colder pile to preheat the cold brick. Here, the temperature of the gas cools in the first round (t = 0) to 1028°C, decreasing by 22 K. On the way through the hot brick piles, the gas temperature increases back to 1032°C. After 2.3 seconds, the gas is cooled in the cold pile from 1032°C to 1012°C, a decrease of 20 K; the temperature change is thus smaller than in the first round. After each time step, the temperature change is smaller than the previous time step. After 14.3 seconds, the gas temperature decreases from 990°C to 976°C; only a decrease of 14 K has been observed.
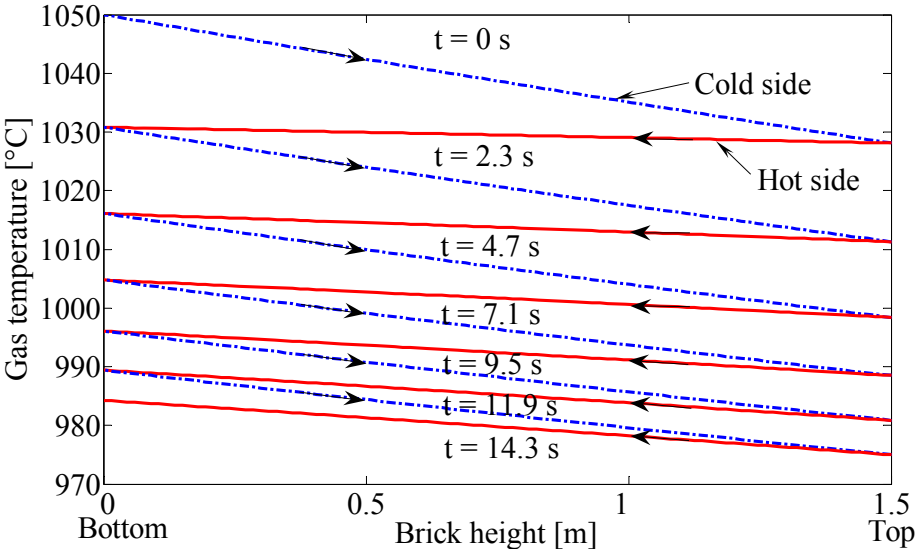


Figure 4.10:  Temperature profile of gas dependence on height for short time

In Fig. 4.11 the temperature profiles of the gas dependent on the pile height at a time of 145 seconds and at one hour are shown, for both the cold and hot sides. It is evident, that already after about 2 minutes (145 s), steady conditions can be used on both sides.
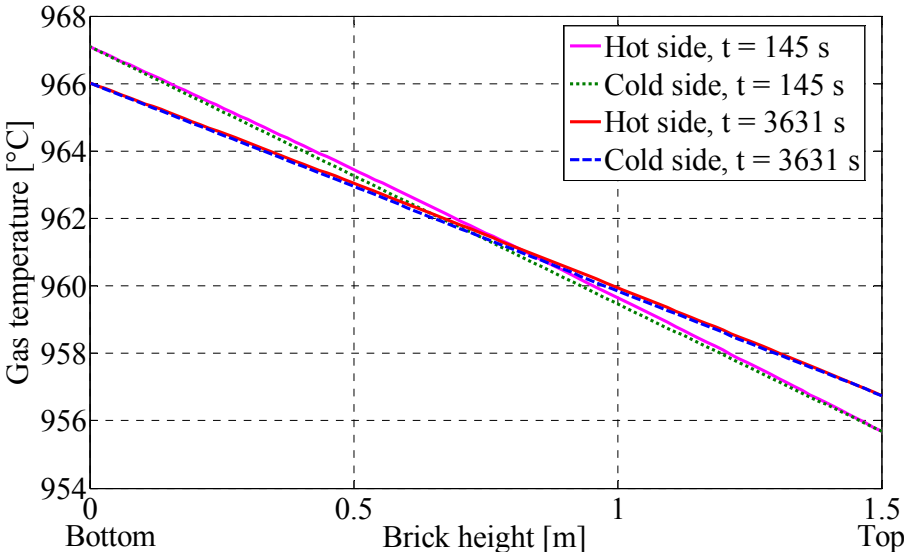


Figure 4.11:  Temperature profile of gas dependence on height at different time

The change in gas temperature as a function of time is shown in Fig. 4.12. It is evident that after about 1 minute, the gas temperature at the bottom of the brick pile decreases linearly with time and that at the top of the brick pile increases linearly.
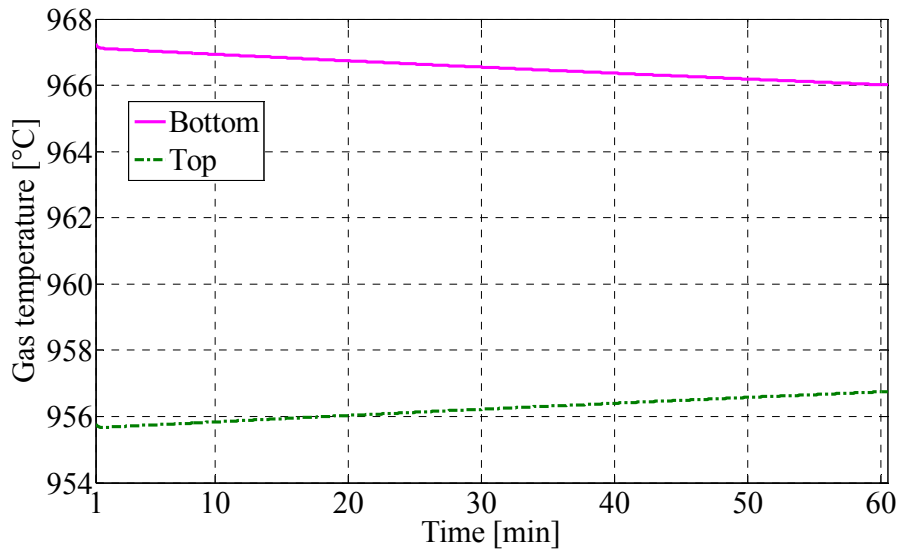


Figure 4.12:   Gas temperature at top and bottom of the brick dependent on time

The gas temperatures at the top and bottom of the brick piles are shown above. The temperature difference between the bottom and top is plotted in Fig. 4.13. It reveals that during the first minute, there is a short thermal start-up, which results in a rapid decrease in the temperature difference from 22 K to 11.5 K; thereafter the temperature difference decreases linearly during one hour from 11.5 K to 9.5 K.
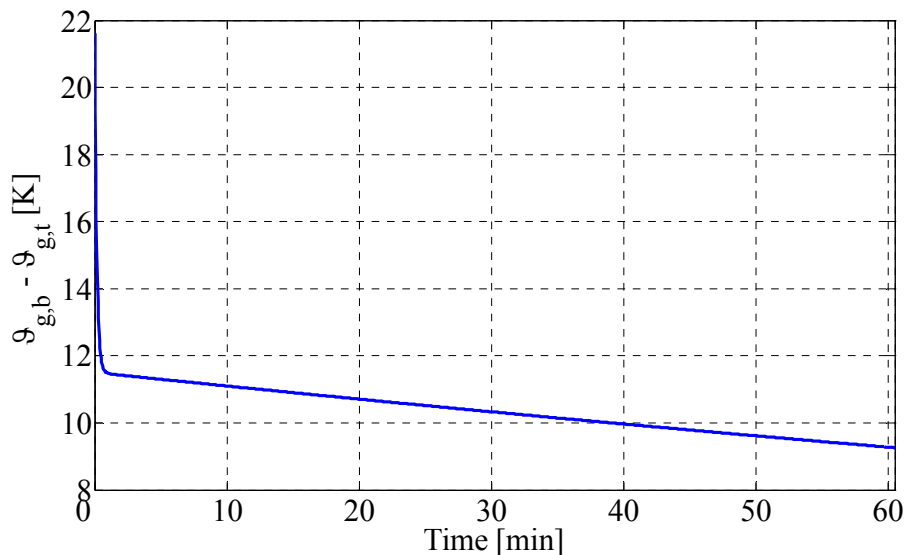


Figure 4.13:   Gas temperature difference between the bottom and top of the brick pile dependent on the time

Meanwhile, the mean temperature of the solid on both sides and the gas temperature at the bottom and top of the gap are shown in Fig. 4.14 as a function of time. After about 60

minutes, the car is driven to another position, so that this process will occur again periodically. In Fig. 4.14, the first kiln segment from the firing zone is shown. The temperature decrease of the hot bricks and the increase of the cold bricks are linear. The bricks coming out from firing zone are cooled by about 15 K from 1050°C to 1035°C, while the bricks on the other kiln side are heated by 15 K from 875°C to 890°C. The temperature difference between the two brick piles thus changes from an initial 175 K to 145 K. Therefore, the transferred heat flux decreases with time, which is also indicated with the decrease in the gas temperature difference between the bottom and top positions. As a consequence, in the mathematical model from Chapter 2, the used temperature difference between both sides must be considered as the mean value during the staying period of the kiln car. The mean value is located at the half period of time - in this example, 160 K after 30 minutes - since the temperature gradients are linear. It can also be seen that for the gas, after the thermal start-up, the temperature on the bottom decreases linearly and on the top increases linearly. The details about temperature change for the gas have already been illustrated in Fig. 4.12.
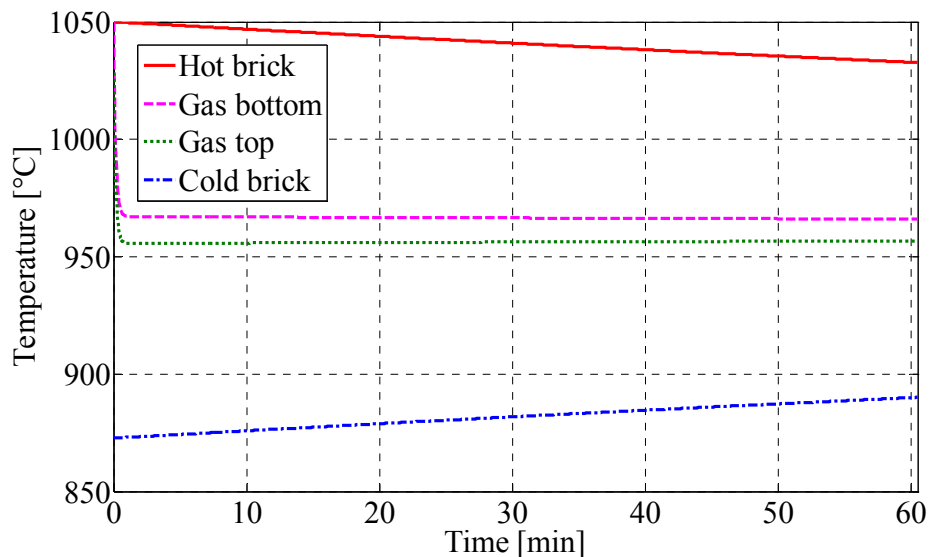


Figure 4.14:   Temporal change of the mean temperature of the brick and gas on both sides

The temperature differences of the solid between the bottom and top of the brick pile are also investigated. They are plotted separately for the brick on the cold and hot sides in Fig. 4.15 as a function of kiln position along the length direction. For comparison, the gas temperature difference between the bottom and top is also plotted.

101
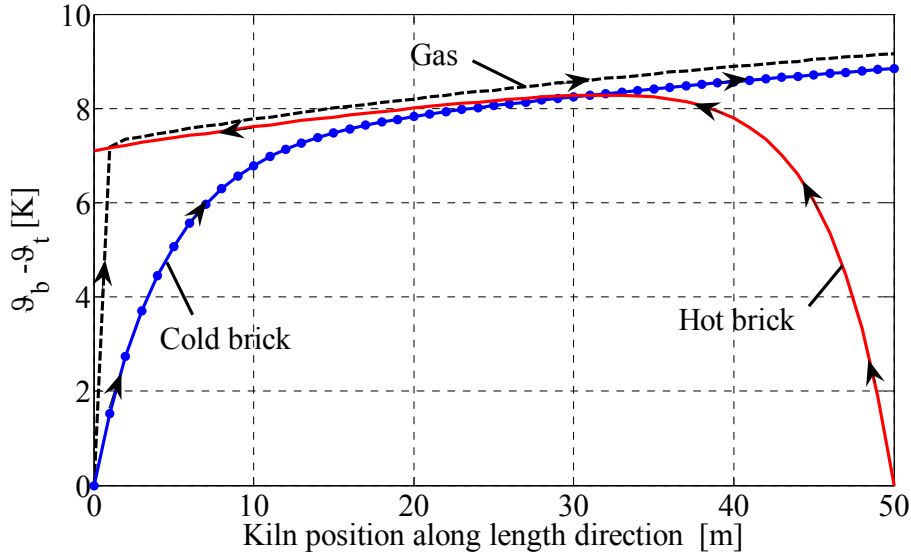
Figure 4.15: Temperature difference between bottom and top of the brick piles for both sides, dependent on the kiln position along the length direction

As it can be seen from Fig. 4.15, the bricks on the cold side enter with an ambient temperature. Therefore, the temperature difference at this position is not available. Thereafter the temperature difference increases to 9 K until they enter into the firing zone at 50 m. The initial increase is progressive until about 20 m, where it becomes nearly linear. The hot brick appears reversed, entering with a uniform temperature of 1050°C from the firing zone at 50 m into the cooling zone. The temperature difference increases again from 0 K to a maximum of 8 K after travelling 20 m at a kiln position of 30 m, and then decreases slightly. For comparison, the difference of the gas temperature along the pile height is also shown. The maximal temperature difference of the gas has approximately the same value as that of the solid. It can be concluded that the temperature difference along the pile height direction is relatively low.

## 4.3 Temperature difference in brick cross section

As shown in the previous section, the temperature of the brick changes linearly with time. In this case, according to the thermal start-up, there is a transient temperature profile during the time when the kiln car is just pushed into a new position. In this part, the temperature difference in the cross section, i.e. the temperature difference between the brick core and surface, is investigated.

According to the analytical solution of the Fourier differentiation equation, the temperature difference between the surface and the core is

$$\vartheta_{surface} - \vartheta_{core} = \Delta\vartheta_{CrossSection} = \frac{1}{2} \cdot \frac{w \cdot \rho_g \cdot c_s}{\lambda_s} \cdot \left(\frac{s}{2}\right)^2 . \tag{4-19}$$

Herein $\rho_s, c_s, \lambda_s$ mean density, specific heat capacity and thermal conductivity of the bricks respectively, $s$ is the thickness of brick pile and $w$ is the heating rate. It can be expressed as

$$w = \frac{\Delta \vartheta_x}{\Delta t}. \tag{4-20}$$

The values used are $\rho_s$ = 1600 kg/m³, $c_s$ = 835 J/kg/K, $\lambda_s$ = 0.75 W/m/K and $s$ = 240 mm. The resultant temperature difference is:

$$\Delta \vartheta_{CrossSection} = 64 \text{ K}. \tag{4-21}$$

This temperature difference is therefore significantly larger than that along the height of the brick pile.

The transient temperature in the cross section is investigated as follows: when the bricks are coming out from the firing zone, they have a uniform temperature of 1050°C. The transient cooling was calculated with the Fourier differentiation equation

$$\rho_s \cdot c_s \cdot \frac{\partial \vartheta_s}{\partial t} = \lambda_s \cdot \frac{\partial^2 \vartheta_s}{\partial z^2}. \tag{4-22}$$

The boundary condition is the convective heat transfer on the surface:

$$-\lambda_s \cdot \frac{\partial \vartheta_s}{\partial z}\bigg|_{z=s/2} = \alpha \cdot \left(\vartheta_{s(z=s/2)} - \vartheta_g\right). \tag{4-23}$$

The corresponding temperature profiles at different times are plotted in Fig. 4.16. After one hour the surface is cooled to 1033°C, while the core still remains almost unchanged at 1048°C.
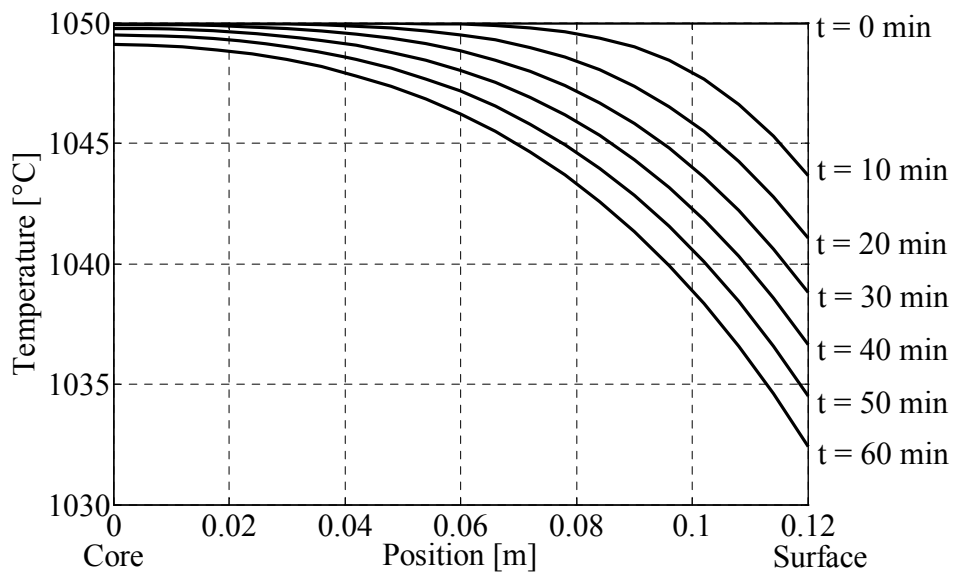


Figure 4.16:   Temperature profile in cross section after driving out from firing zone

Next the temperature difference in cross section along the kiln length is investigated. In the first hour, the temperature profile inside the bricks pile is shown in Fig. 4.16. After one hour, the temperature of the surface and the core of the brick piles are plotted a function of the kiln length position in Fig. 4.17. It is evident that the temperatures both in the core and on surface change linearly after a kiln length of about 15 m.
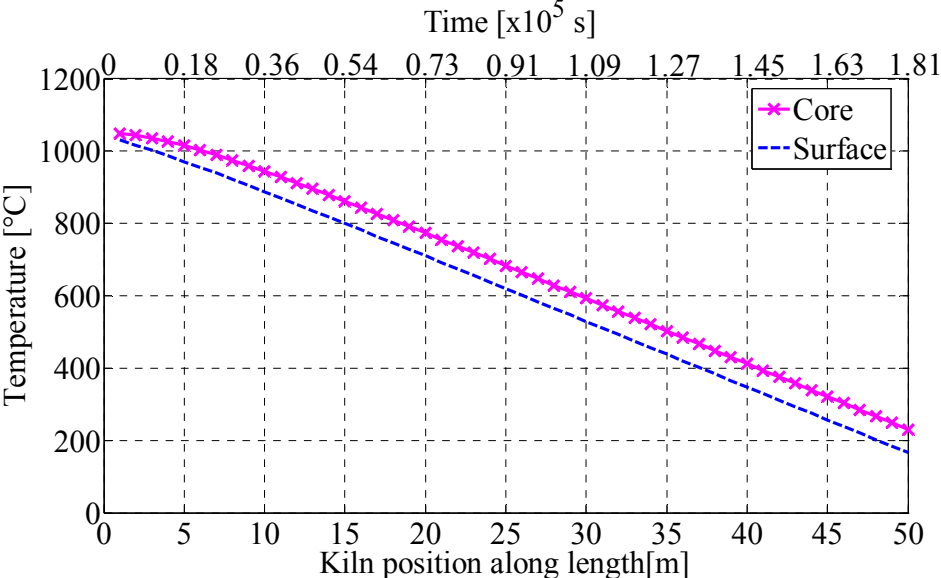


Figure 4.17:    Temperature of core and surface of brick along the kiln length

In Fig. 4.18, the temperature difference between the core and the surface is shown as a function of the kiln length. This increases continuously, starting at the outlet from the firing zone and at around 20 meters is closer to the asymptotic value of 64 K, which was previously calculated analytically. There the temperature difference in cross section leaving the furnace is the greatest.
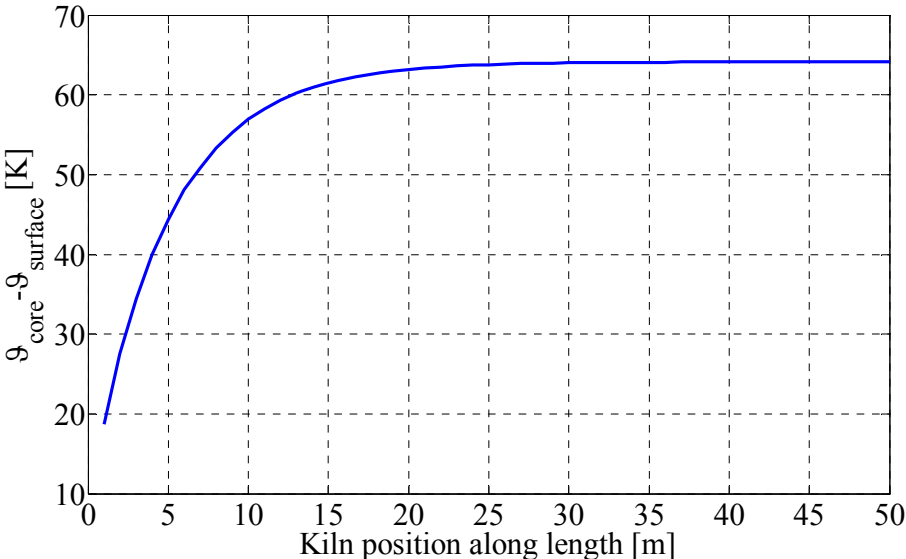


Figure 4.18:    Temperature difference of the bricks in cross section along kiln length

The driving out temperature of the brick is meaningful in the calculation of the driving out loss. The temperature profile in the brick pile cross section at the end of the kiln is plotted in Fig. 4.19. The shape of the curve is parabolic and the temperature difference between the core and surface is 64 K.
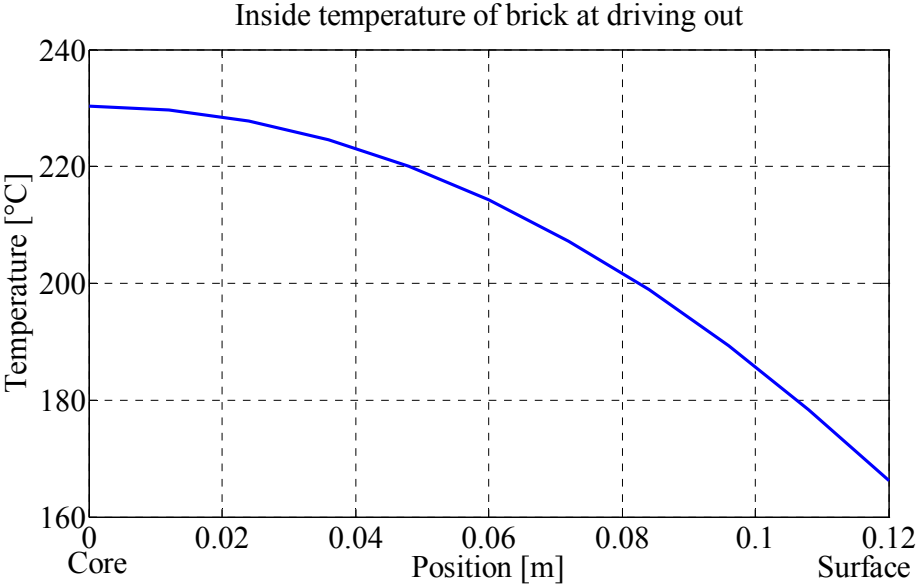


Figure 4.19:    Temperature profile in brick cross section by leaving the kiln

# 4.4 Influence of natural convection

In the previous models, it was assumed that flow is only generated by the ventilators; natural convection was excluded. Therefore, the occurrence of natural convection is investigated as follows. In order to investigate the natural convection, the flow direction should be reversed, so that the natural convection flow can be generated from the points 1, 2, 3, and 4, as shown in Fig. 4.20. To realize this gas flow direction, the ventilator should work in the reverse direction. As it is shown, unlike the model described above, the top temperature is higher than the bottom temperature for both the gas and bricks.
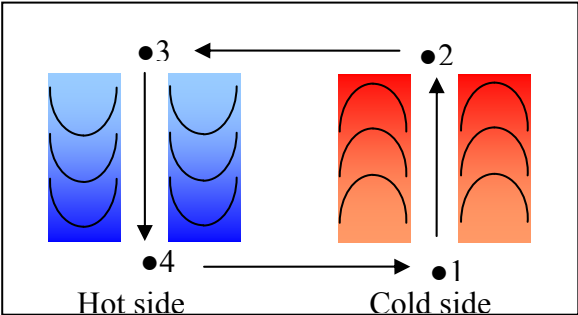


Figure 4.20:    Kiln cross section with reference points for flow

The recirculation gas flow follows the first law of thermodynamics [40]

105

$$d\,\frac{w_g^{\;2}}{2} + dgH + \frac{dp}{\rho} + dW_R = 0\,.\tag{4-24}$$

The sum of the kinetic energy, potential energy, work from the volume change, and work due to friction is zero, since no technical work is done. These differential equations must be integrated over the reference points. These principles are shown in Fig. 4.20. The corresponding temperatures and densities are shown qualitatively in Fig. 4.21. During to the process from point 1 to point 2, the gas is warmed through the hot bricks. Therefore, the density decreases with the brick height. During the process from point 2 to point 3, gas flows from one kiln side to the other side; the gas temperature does not change, and thus neither does the gas density. When the gas flows through the cold brick piles from point 3 to point 4, it is cooled again to the original value and the density is also increases accordingly.
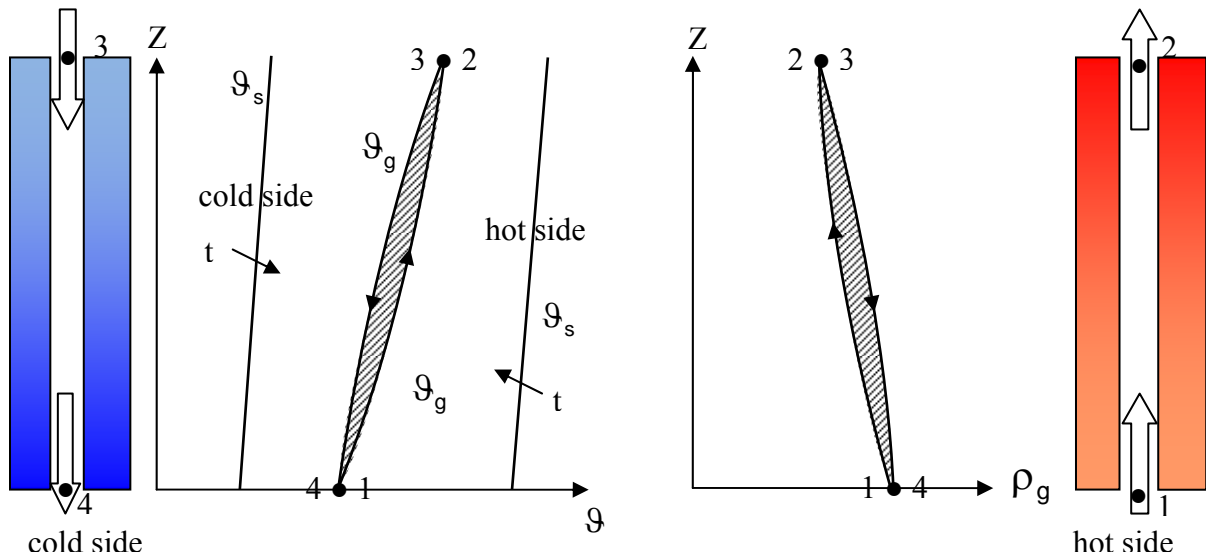


Figure 4.21:    Qualitative temperature and density profiles along the kiln height

For the closed state changes, the ring integral is used for the above differential equations:

$$\oint \frac{dw_g^{\;2}}{2} + g \cdot \oint \frac{dp}{\rho} + \oint W_R = 0\,.\tag{4-25}$$

The closed integral for the velocity and pressure are zero as shown in the following equations:

$$\oint \frac{dw_g^{\;2}}{2} = 0\tag{4-26}$$

and

$$\oint \frac{dp}{\rho} = 0\,.\tag{4-27}$$

The frictional work can be replaced by the frictional pressure drop:

$$\rho \cdot \oint dW_R = \Delta p_v\,.\tag{4-28}$$

Therefore, it can be obtained

$$\Delta p_v = g \cdot \oint \rho \cdot dZ\,.\tag{4-29}$$

This closed integral is proportional to the surface area between the two curves in the $\rho, H$ - diagram in Fig. 4.21. The larger this area is, the higher the driving force necessary to overcome the frictional pressure drop and consequently the stronger is the natural convection flow.

In Fig. 4.22 the temperature profile of the gas over the height of the brick pile is shown, for both the cold and hot sides. The left figure shows a low temperature at the kiln inlet and the right figure shows the high temperature near the firing zone. The corresponding gas density curves are shown in Fig. 4.23
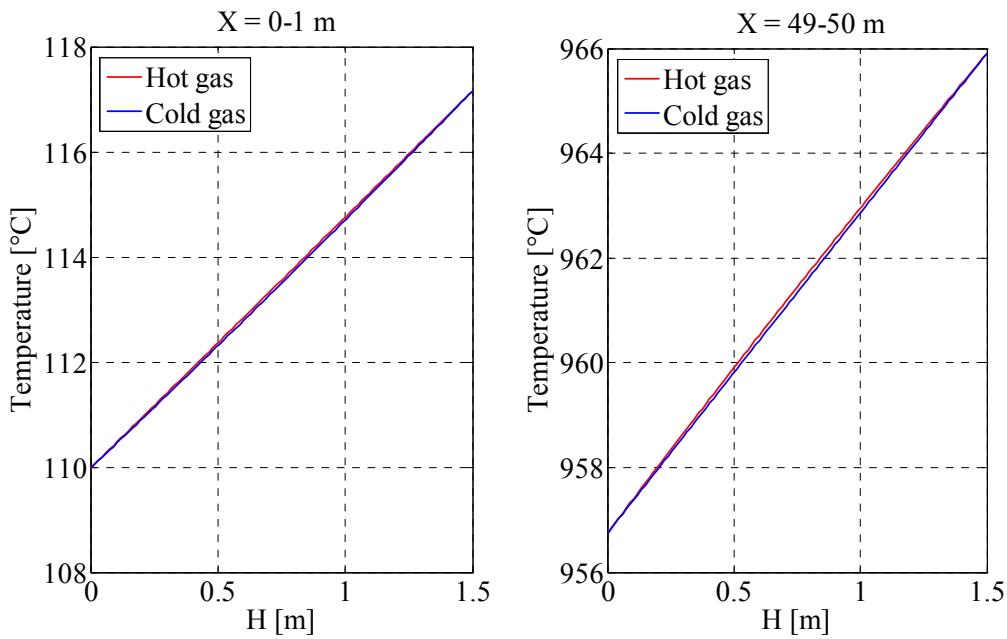


Figure 4.22: Profile of gas temperature over brick height
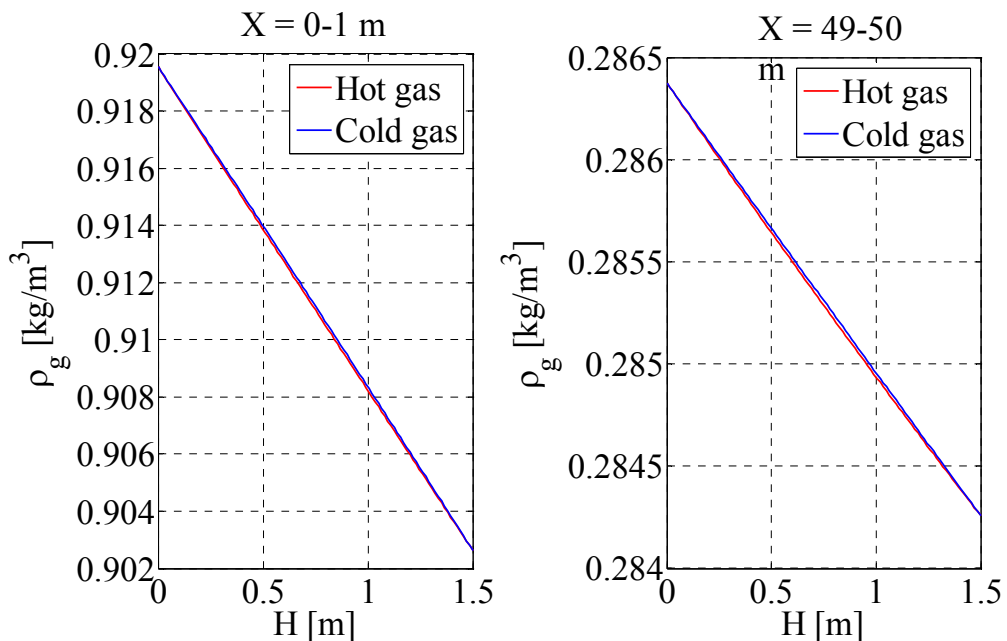


Figure 4.23: Profile of gas density over the brick height

The temperature and density change approximately linearly over the height. Therefore the curves for both kiln sides are almost same. As a consequence, the area under the closed integral is near zero. Thus, there is virtually no force for the natural convection flow. The pressure drop due to natural convection is more than four orders of magnitude smaller than the pressure drop generated by the ventilator.

Gas recirculation by natural convection is extremely small if the brick piles on both sides of the kiln have nearly same temperature profile. This was the fundamental flaw during the development of the "Riedel's counter-travel tunnel kiln" in 1952, in which the gas recirculation between the two kiln sides was expected to be forced only by natural convection. The effect, that between two walls with about the same temperature distribution there is no natural recirculation flow, was already known for over 50 years in the technique of heating, ventilation and air conditioning. In such spaces, only a very unstable flow can be formed. So Riedel's counter-travel tunnel kiln could not work properly and therefore this kiln concept was not continuously pursued. However, with ventilators, sufficient gas recirculation can be generated with which the heat transfer between the two kiln sides can be ensured. Nowadays, high temperature ventilators with a sufficiently high efficiency are available.

Fig. 4.24 shows a natural convection flow in a production hall with an industrial kiln. The incoming air flow at the height $Y_1$ is heated by the kiln, and flows to the height at $Y_2$ with temperature of $\vartheta_2$. This flow then continues with a constant temperature to the roof and from there flows into the environment. There the air is cooled again to the original temperature. The temperatures and the corresponding densities of the four state points are qualitatively shown in the figure. It can be seen from this case that the closed integral $\Delta p_v = g \cdot \oint \rho \cdot dh$ (areas) has a very large value. In these halls, therefore a strong natural convection flow occurs.
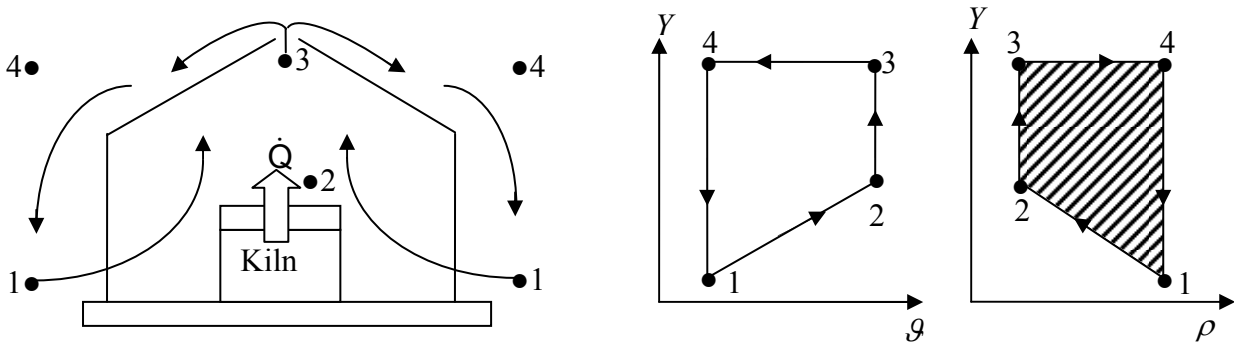


Figure 4.24:   Natural convection flow and surface area of the closed integral in a production hall with a kiln

## 4.5  Model comparison

A model comparison should be carried out to check to what extend the simplified model can correctly express the process. Fig. 4.25 shows the gas velocity inside the gaps along the kiln length direction. It illustrates the result of the transient condition and the steady condition with the simplified model. It shows that the difference between the two models can be neglected.
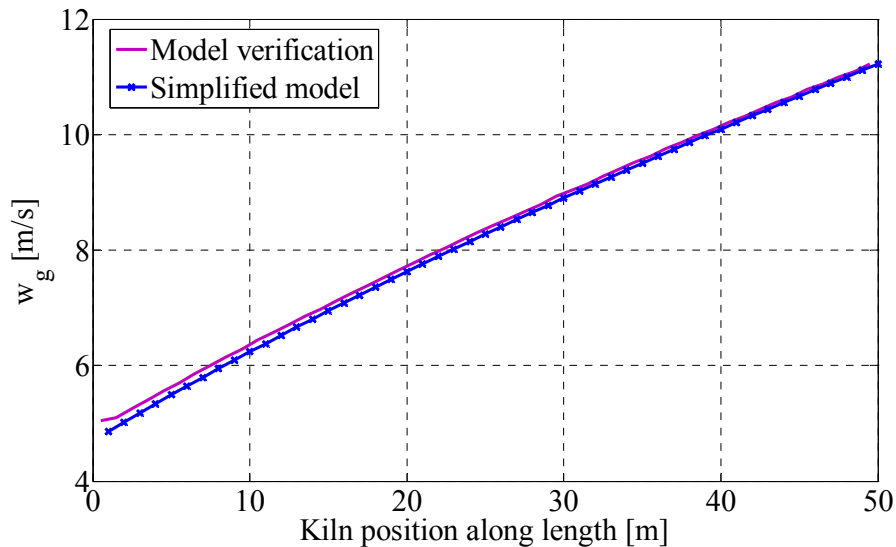


Figure 4.25:    Gas velocity in steady and transient conditions

Furthermore, the mass flows of gas through the gap are investigated for the two models, which are shown in Fig. 4.26. Again it depends on kiln position along the length and the results from the two models are plotted together for comparison. The simulation results for mass flow also show almost the same results for the two models as in the previous study on velocity.
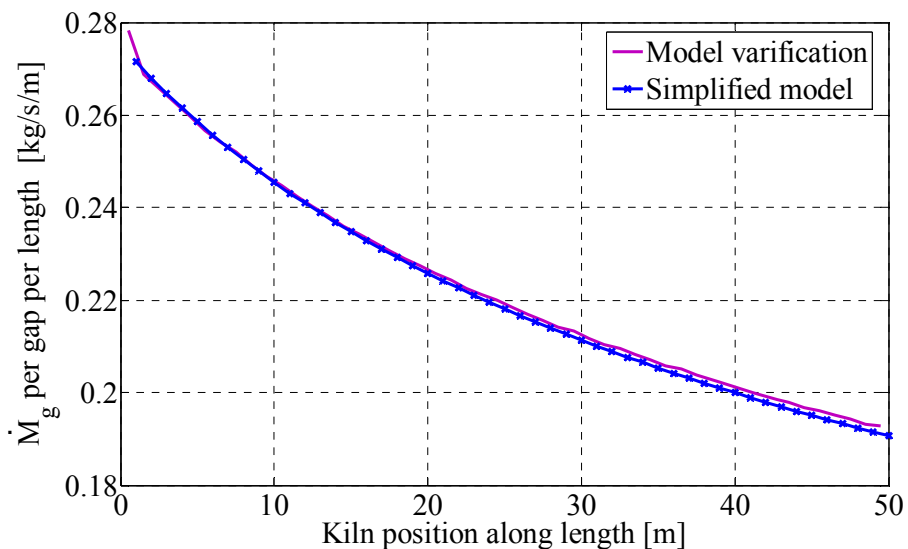


Figure 4.26:    Gas mass flow in steady and transient conditions

Fig.4.27 shows the simulation results for Reynolds numbers inside the gaps for the models of the transient condition and the steady condition for comparison. Again, the difference between them can be neglected.
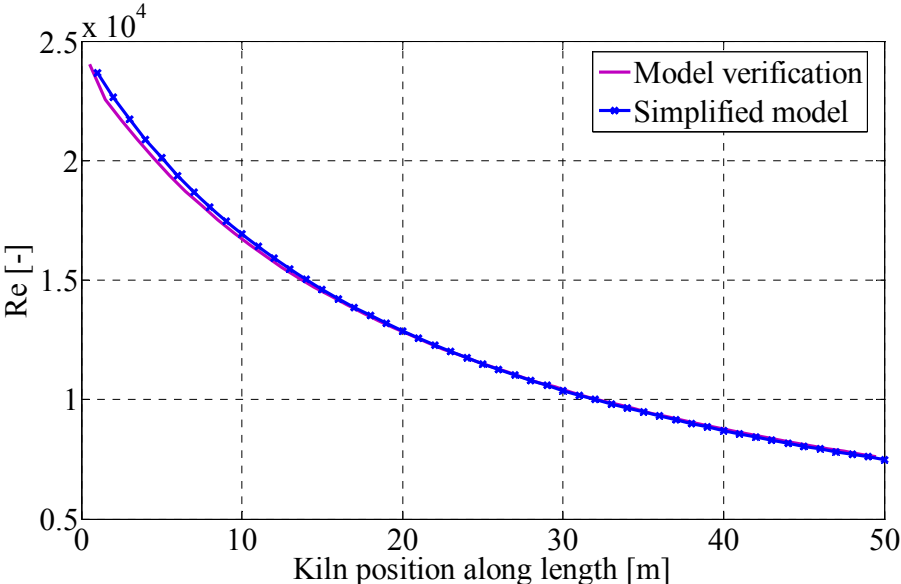


Figure 4.27:    Gas Reynolds number in steady and transient conditions

Finally, a comparison of the two models for the specific ventilator power is shown over the kiln length in Fig. 4.28. It illustrates the result of the transient condition and the steady condition with the simplified model. The difference between them is negligible.
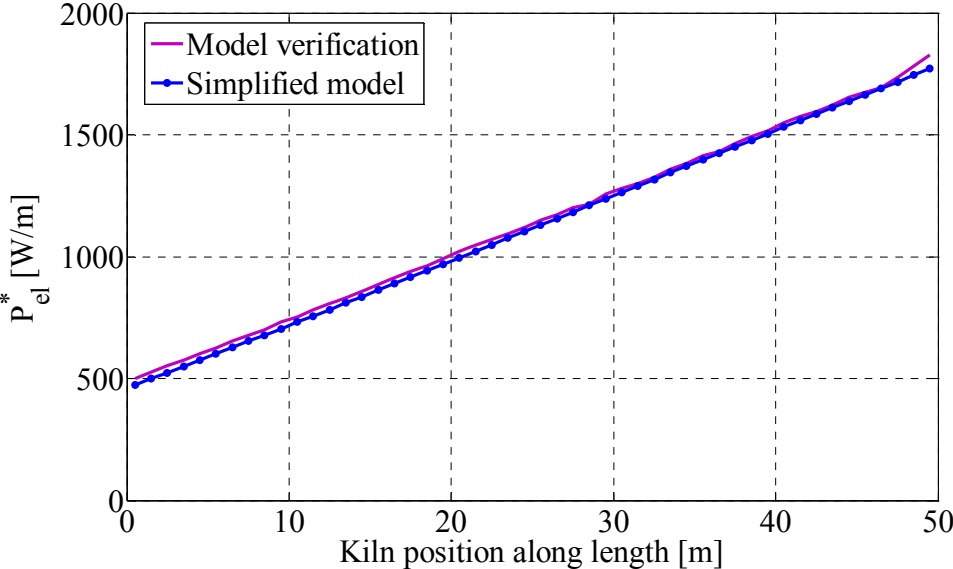


Figure 4.28:    Specific ventilator power in steady and transient conditions

The above discussed figures reveal that the differences between the simplified model and the transient model can be neglected. Although there are some assumptions for the simplified model, e.g. the inside solid temperature is uniform and the process is operated under steady condition, the simplified model can be implemented to express the real process.

## 4.6 Summary

In this chapter, the model described in Chapter 2 was verified with an extended model. The assumptions of the simplified model were modified with an unsteady state model.

At the beginning of this chapter, this transient model was explained. It described the periodical step by step transportation process of the kiln car, and mathematical equations and algorithm were introduced to solve the problems.

It continued by showing the simulation results for the temperature difference between the bottom and top of the brick pile, showing both solid and gas temperature differences. It illustrated that the temperature difference between the bottom and top is less than 10 K both for the solid and gas. It was evident that the temperature difference along the height is relatively small.

Then, the solid temperature difference in the cross section direction was discussed. The results of analytical equations and numerical simulations were shown. Both showed that the solid inner temperature difference in the cross section direction is 64 K. This difference is relatively large compared to the solid temperature difference along the height of the brick pile.

Meanwhile, the effect of natural convection was also discussed. It was shown that the natural convection forced by the gas temperature difference played a very small role in this kiln, so small that it can be neglected. This was shown to be the fundamental flaw of Riedel's system and proved that there is no necessity to consider the natural convection both in the simplified and transient models.

Finally, the results from the two models were compared. The comparisons showed that the difference in results obtained from the two models could be neglected. It was shown that the simplified model can explain the process relatively accurately, and the results obtained from the simplified model are reliable.

# 5. Simulation for Roof Tiles

As discussed in Chapter 1, there are different kinds of ceramic products. That explained above is a standard clinker brick, only one example of ceramic products. In order to investigate the energy saving of the counter-travelling tunnel kiln, the production process for other products should also be investigated.

The tile industry is one of the most significant ceramic sectors. In 1992, it accounted for about 60% of the total annual sales revenue in Europe [9]. The tile industry is characterized by high energy consumption, accounting for about 75% of the total consumption by the ceramics sector [9]. The energy costs make up between 10 and 45% of the production costs [41]; this percentage is significantly higher than for the other ceramic products. Thus, the investigation of energy saving production for the tiles is meaningful for the whole ceramic industry. Here the production process for roof tiles is investigated as another example.

## 5.1 Tiles settings on the kiln cars

Similarly to other ceramic products, roof tiles are produced with tunnel kilns. They have a similar production process to that of bricks, which is already explained in Fig. 1.1. The firing temperature for the roof tiles is 1000-1150°C, which is not very different from the firing temperature of clinker bricks. However, how the roof tiles are set in the kiln car is different from that of bricks and is shown in Fig. 5.1 and 5.2.



Figure 5.1:    Horizontal setting for roof tiles in kiln car with kiln furniture [3]

Figure 5.2:     Vertical setting for the roof tiles on the kiln car with kiln furniture [3]

For the horizontal tile setting shown in Fig 5.1, the gas flow is along the kiln length direction, therefore making it impossible to form gas recirculation in the cross section with the new kiln concept; for the vertical tile setting as shown in Fig. 5.2, there are plenty of vertical gaps between the tiles in the cross section, making it possible to form gas recirculation in the cross section. Therefore, for the new solid-solid recuperation kiln process, tiles are set vertically.

As shown in Fig. 5.1 and 5.2, there is some kiln furniture installed on the kiln car to ensure the stability for the tiles, unlike in brick production. This kiln furniture moves together with the kiln car, and therefore changes temperature with the tiles along the kiln length direction. Due to the relatively large mass of the kiln furniture, their enthalpy change along the kiln position cannot be neglected. When the energy calculations for roof tiles are carried out, the kiln furniture should be taken into consideration.

Another difference in tile production is the width of the solid and the gap thickness in the cross section. For brick production, the solid width is the total width of the brick piles, which is equal to 240 mm for standard bricks as explained in Fig. 2.5, and the gap thickness in practice is around 60 mm due to the automatic setting. For the roof tiles, however, the width of solid is the single tile thickness, which is around 16-20 mm. Due to the use of a robot for setting, the gap thickness between the two tiles is smaller, around 10 mm. This setting process is shown in Fig. 5.3.
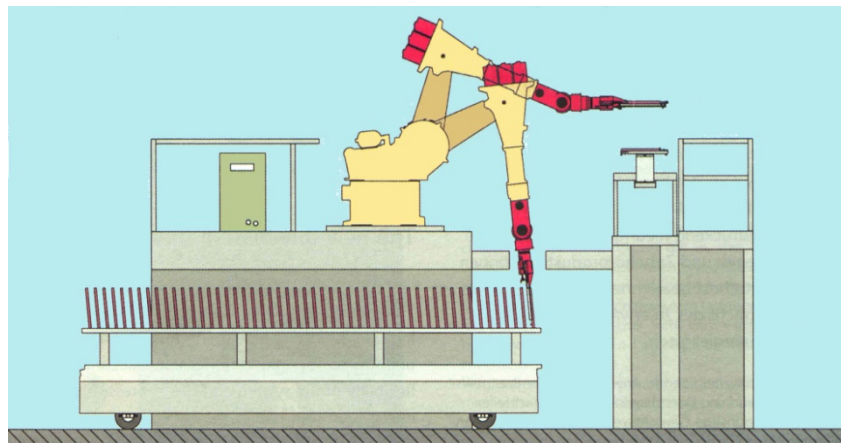


Figure 5.3:     Tiles setting process with robot

113

The two main differences for the roof tiles discussed above lead to different heat transfer results than the clinker bricks. Therefore, it is meaningful to investigate the energy requirement for the roof tiles with the new kiln concept and to compare the results with the brick production process. As an example, the roof tile dimension of 27x40x1.6 cm is used.

# 5.2 Model description

As it has been proved, the simplified model described in Chapter 2 can explain the new kiln process with solid-solid recuperation relatively accurately, and the results obtained from the simplified model are reliable. Therefore, this model will be used for the production process for roof tiles.

## 5.2.1 Model modifications

Three modifications are used to adjust the model for the tile setting in the kiln, which varies from the setting of the bricks.

The first modification is the enthalpy change of the kiln furniture along the kiln length. This enthalpy is obtained from the convective heat transfer between the kiln furniture and the recirculation gas. Here it is assumed the thermal mass of the kiln furniture is the same as the tiles. By adding the mass of the kiln furniture to the mass of the tiles, the enthalpy change of the kiln furniture can accurately be considered.

The second modification is the heat transfer surface area. In the kiln with bricks, it was assumed the bricks were continuously loaded along the kiln length, since the brick piles are loaded on the kiln car and the distance between two kiln cars is relatively small compared to the kiln car length. However, in the kiln with tiles, the single tile pieces are set discontinuously, and the distance between the two tiles cannot be neglected as shown in Fig. 5.4. Therefore, when Eq. (2-6) is used to calculate the heat transfer surface for each gap, a parameter of 70% is added for deleting the spaces, which do not belong to the heat transfer surface along the kiln length. Therefore, Eq. (2-6) can be modified as

$$A = 2 \cdot H \cdot \Delta L \cdot 70\% .$$ (5-1)
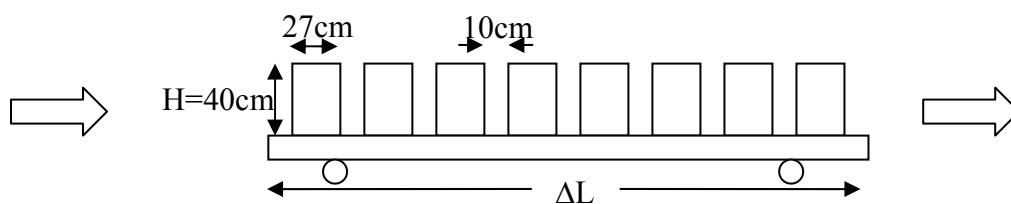


Figure 5.4:     Discontinuous tile setting on the kiln car

The third modification pertains to the pressure drop from the perforated plates, which support the tiles on the kiln car. There are holes on the plates, so that the recirculation gas can flow through the plates. Fig. 5.5 shows these plates with different hole arrangements.
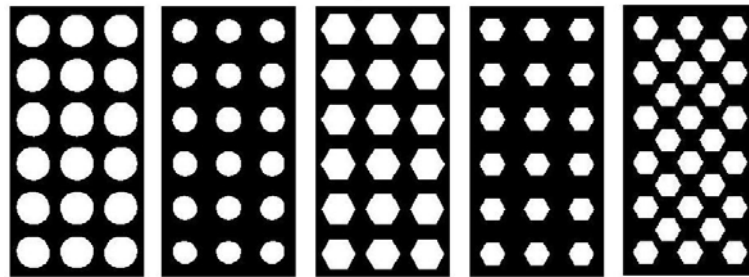


Figure 5.5:     Perforated plates in different hole arrangements

In order to calculate the gas pressure drop for the cross sectional gas recirculation, Eq. (2-17) can be modified by adding a factor of $\xi_6$, which is the pressure drop coefficient of the perforated plates. Therefore the gas pressure drop can be calculated by

$$\Delta P_v = \frac{1}{2} \cdot \rho_g \cdot w_g^2 \cdot \left[ \left( \xi_1 + \xi_2 + \lambda \cdot \frac{H}{d_h} + \xi_3 + \xi_4 \right)_{left} + \left( \xi_1 + \xi_2 + \lambda \cdot \frac{H}{d_h} + \xi_3 + \xi_4 \right)_{right} + \xi_5 + \xi_6 \right]. \quad (5\text{-}2)$$

The value of $\xi_6$ varies from the shape and arrangement of the holes. This will be investigated by the CFD package FLUENT 6.3.

## 5.2.2 Operation data of the kiln

Firstly, the technical data for the roof tile kiln should be determined. In the traditional tunnel kiln process, both the kiln dimension and throughput for the roof tiles are smaller than that for the brick. The cross section for the counter-travelling kiln process for roof tiles, with the roof tile dimensions of 27x40x1.6 cm, is expressed in Fig. 5.6.
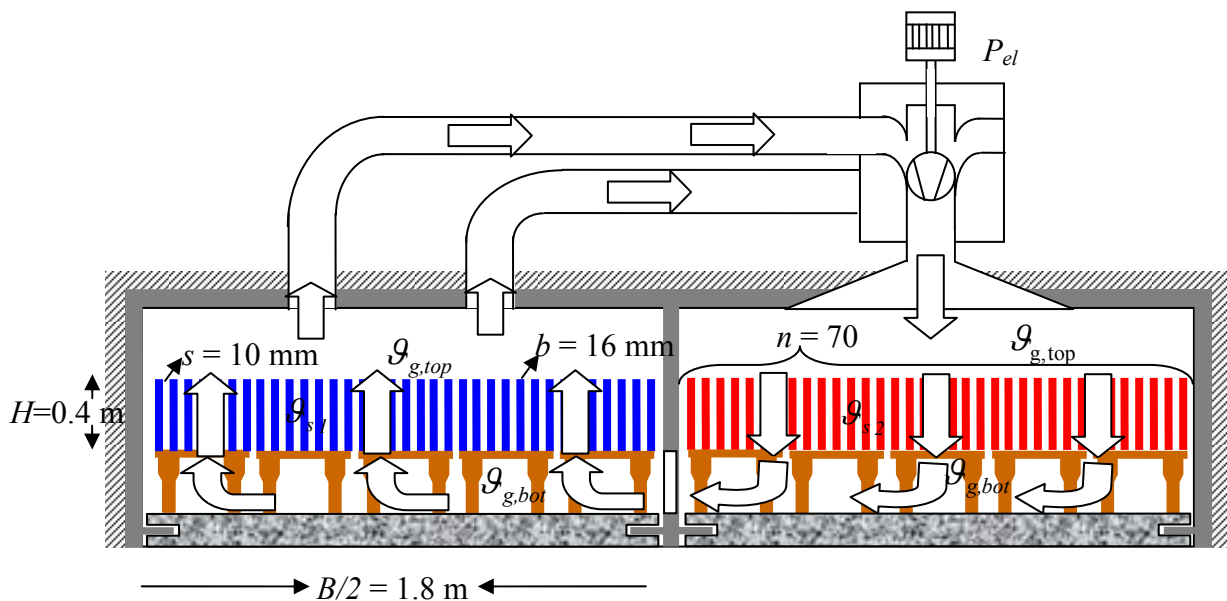


Figure 5.6:     Cross section of kiln for roof tiles

As seen from Fig. 5.6, there are two sides in the kiln cross section, one for hot and cold tiles respectively. The height of the tiles is 0.4 m, the thickness of the tile is 16 mm, the gap thickness between two tiles is 10 mm and the number of tiles is 70 for each side. Therefore, the kiln width on each side is around 1.8 m. The kiln has a total length of 80 m, which is shown in Fig. 5.7 as a length view of the kiln.
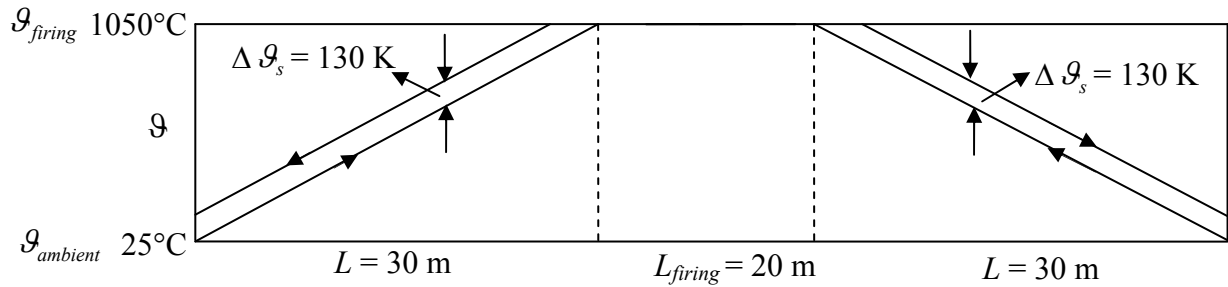


Figure 5.7:     Length view of the tile kiln

The length view of the tile kiln shown in Fig. 5.7 illustrates that the entire length of this kiln is 80 m. Like the kiln for the bricks, this kiln is also divided into three parts. Preheating and cooling zones in each are 30 m long respectively on both sides of the kiln from the entrance and the remaining 20 m in the middle is the firing zone. The firing temperature for the roof tiles is 1050°C and the entry temperature is 25°C. The temperature difference between both sides is 130 K. The tile throughput is 6 t/h. These data are assembled together in Table 5.1.

Table 5.1:     Operation data of tile kiln

| Symbol | Explanation | Value | Unit |
|--------|-------------|-------|------|
| $\dot{M}_s$ | Throughput of tile | 6 | t/h |
| $L$ | Kiln length | 80 | m |
| $b$ | Tile thickness | 0.016 | m |
| $B$ | Kiln width | 2.16 | m |
| $n$ | Number of tiles per side | 70 | - |
| $s$ | Gap thickness | 0.01 | m |
| $H$ | Height of the tile pile | 0.4 | m |
| $\Delta\vartheta_s$ | Temperature difference of both sides | 130 | K |

# 5.3 Pressure drop of perforated plates

According to the Eq. (5-2), the pressure drop coefficient $\xi_6$ due to the perforated plates should be investigated in order to determinate the total pressure drop for the gas recirculation. This research will be carried out with the CFD package FLUENT 6.3. One of the plates is

116

shown in Fig. 5.8 as an example. The dimensions of the plate are as follows: a breadth of 0.6 m, a height of 0.05 m, and a length of 0.3 m. It is installed on the kiln car according to the coordinates shown in Fig. 5.8.
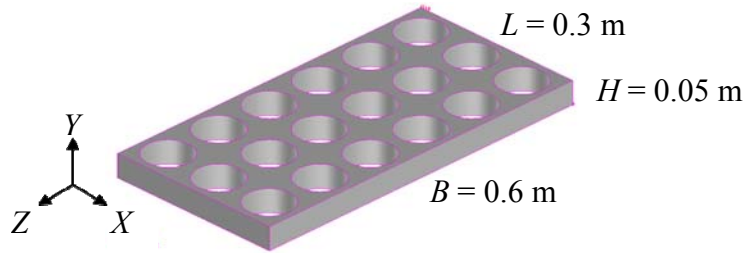


Figure 5.8:     Perforated plate

Since different hole arrangements are possible, different plates should be investigated. This will be explained in the next section.

## 5.3.1 Description of simulation domain

In order to calculate the flow's pressure drop through the plate, a domain is set, shown in Fig. 5.9. Here, a rectangular tube is assumed with the width of 0.6 m and height of 0.3 m. These values are the same as the plate width B and length L shown in Fig. 5.8. In the middle of the tube, there is a plate. The thickness of the plate is 0.05 m, which is equal to the height H shown in Fig. 5.8.
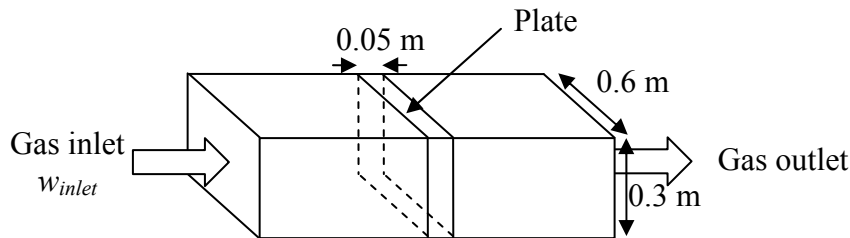


Figure 5.9:     Simulation domain

During the simulation, different hole shapes and holes arrangements are utilized on the plate. The pressure drop $\Delta p_v$ between the two sides of the plate, which depends on the gas inlet velocity, can be calculated. Then, with the local pressure loss equation

$$\Delta p_v = \frac{1}{2} \cdot \rho_g \cdot w_{inlet}^2 \cdot \xi_6 ,$$ (5-3)

the pressure drop $\xi_6$ based on inlet gas velocity, which is expressed by $\xi_6(w_{inlet})$, can be obtained.

## 5.3.2 Simulation results for the pressure drop coefficient

Simulations were carried out for different plates with different hole shapes and hole arrangements, as shown in Fig. 5.5. For each plate form, simulations for two different gas

117

temperatures, 500°C and 1000°C, as well as 3 different gas inlet velocities for each gas temperature, were carried out. Fig. 5.10 shows some of the simulation results.
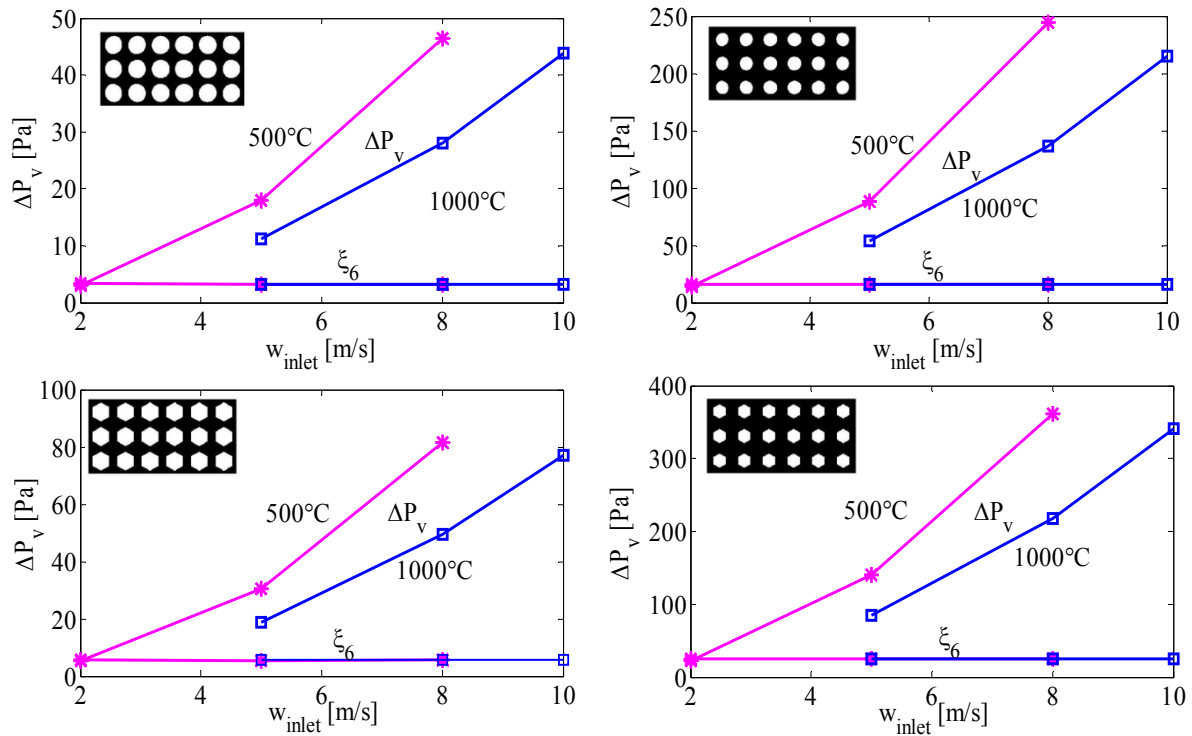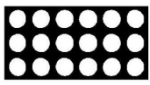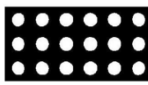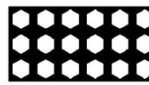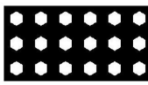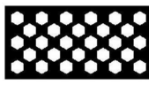


Figure 5.10:     Pressure drop dependent on inlet velocity

As it can be seen from the above figures that for each plate form at each temperature, the pressure drop through the plate increases with the increase in gas inlet velocity. However, the pressure coefficient $\xi_6(w_{inlet})$ is independent of the gas inlet velocity and gas temperature.

Nevertheless, this $\xi_6(w_{inlet})$ cannot be used in Eq. (5-2), because in this equation the pressure drop $\xi_6$ is based on the gas velocity inside of tiles gap, which is expressed by $\xi_6(w_{gap})$. Therefore, $\xi_6(w_{inlet})$ should be transferred into $\xi_6(w_{gap})$ according to the connection between the gas velocity at the gas inlet and that inside the gap. This can be realized by calculating the different flow cross section. Table 5.2 shows the results.

Table 5.2:     Pressure drop coefficients

| | Round hole $R = 0.04$m | Round hole $R = 0.03$m | Prism hole $R = 0.04$m | Prism hole $R = 0.03$m | Prism hole $R = 0.03$m |
|---|---|---|---|---|---|
| |  |  |  |  |  |
| $\xi_6(w_{inlet})$ | 3.237 | 15.718 | 5.609 | 24.903 | 8.152 |
| $\xi_6(w_{gap})$ | 0.36 | 1.746 | 0.623 | 2.767 | 0.906 |

The investigations above show that the pressure drop coefficients for the perforated plates are geometry dependent. The coefficient varies from 0.36 to 2.767 according to different hole shapes and arrangements. The exact value in the real production process cannot be predicted. Therefore, in the following energy requirement calculation, $\xi_6 = 1$ is taken as a standard value, and the influence of $\xi_6$ on the energy consumption will be also investigated.

# 5.4 Energy consumption

With the simplified model described in Chapter 2 and the model modifications for roof tile kilns described above, a series of calculations for the roof tiles production were carried out. As described in Fig. 2.27, the geometry dependent ventilator pressure drop coefficient $\xi_5$ influences the electrical power. Here, $\xi_5 = 9.05$ is used for the simulation, which is the same value as in the brick kiln, allowing the results to be compared with that of brick production.

## 5.4.1 Ventilator power per length

Firstly, as in the investigation for brick production, the ventilator power requirement per length is investigated. The ventilator power per length, dependent on the tile gap thickness at different temperatures, is plotted in Fig. 5.11.
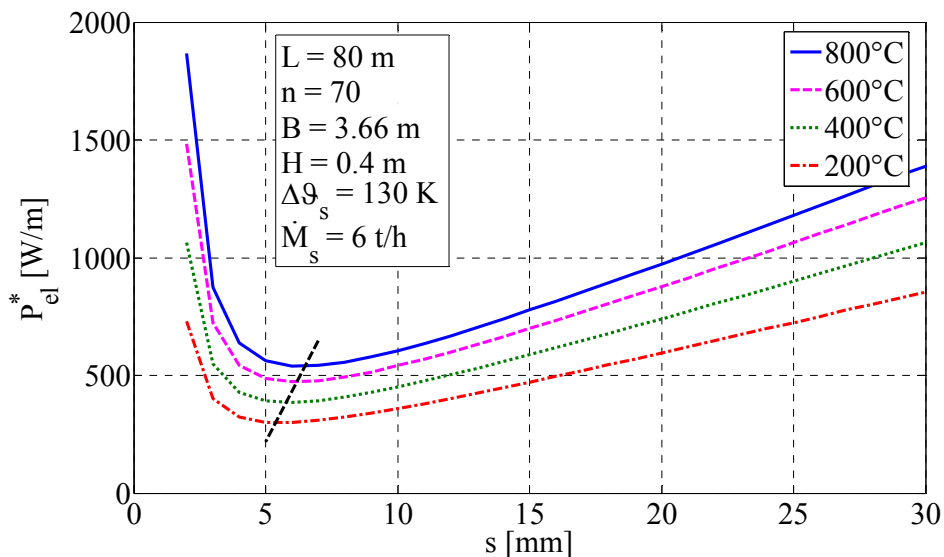


Figure 5.11:   Ventilator power per length dependent on gap thickness

As shown, these curves have the same basic shape. They indicate, as in the brick production process, that there is a minimum value, due to the double effect of the pressure drop and volumetric flow. However, the minimum range is smaller than that in brick production, around 6-7 mm, which is plotted with a dash line. In real industry, the gap

thickness for tiles is 10 mm. It can also be seen that the higher the gas temperature, the higher the ventilator power. This phenomenon has the same mechanism as that of brick production.

Comparing to the ventilator power of brick production shown in Fig. 2.8 and tile production shown in Fig. 5.11, it can be seen at $s = 10$ mm that the electrical power is almost the same for both production processes, but the solid temperature difference of both sides is different. For bricks, the solid temperature difference between both sides is 160 K, while that of the roof tiles is only 130 K. This phenomenon reveals that the electrical energy requirement for the roof tiles is smaller than that for the bricks. The reason could be that the heat transfer of the roof tile kiln is better than that of the brick kiln. This can be explained by the higher effective heat transfer coefficient $\alpha_{eff}$, and the higher total heat transfer surface area $A_{total}$ in the cross section, according to the definition of the Stanton number $St$

$$St = \frac{\alpha_{eff.} \cdot A_{total}}{\dot{M}_s \cdot c_s}, \tag{5-4}$$

where $\alpha_{eff.}$ is the effective heat transfer coefficient, which is defined by the Eq. (2-8), and $A_{total}$ is the total heat transfer surface area in the cross section; it can be expressed as

$$A_{total} = A \cdot n, \tag{5-5}$$

where $A$ is the heat transfer surface of one gap and $n$ is the number of the tiles in the cross section.

For the tile production, because the solid width $b$ is only 16 mm whereas for brick production the solid width is 240 mm, the conductive heat flux from the surface to the core inside the solid becomes smaller; therefore effective heat transfer coefficient $\alpha_{eff.}$ for the tile becomes much higher. Meanwhile, the number of the tiles $n$ is 70 per side, which is 10 times of the number of brick piles, thus the total heat transfer surface area $A_{total}$ is higher than that of bricks. The higher the increase in the effective heat transfer coefficient $\alpha_{eff.}$ and the total heat transfer surface area $A_{total}$ is, the higher the Stanton number $St$ for the tile kiln will be, and therefore the convective heat transfer in the roof tile kiln is better than the brick kiln.

In Fig. 5.12, the variation of ventilator power dependent on temperature is shown. The gap thickness 10 mm represents the practical setting value, while the gap thickness 7 mm represents the optimal value. It can be seen that unlike the results in the brick production process, where the electrical power per length increases approximately linearly with the increase in gas temperature, that although the electrical ventilator power increases with temperature due to the influence of the gas viscosity and density, this increase is not linear. In the low temperature range, the electrical power increases faster with the change in temperature, while in the high temperature range, this increase becomes lower.
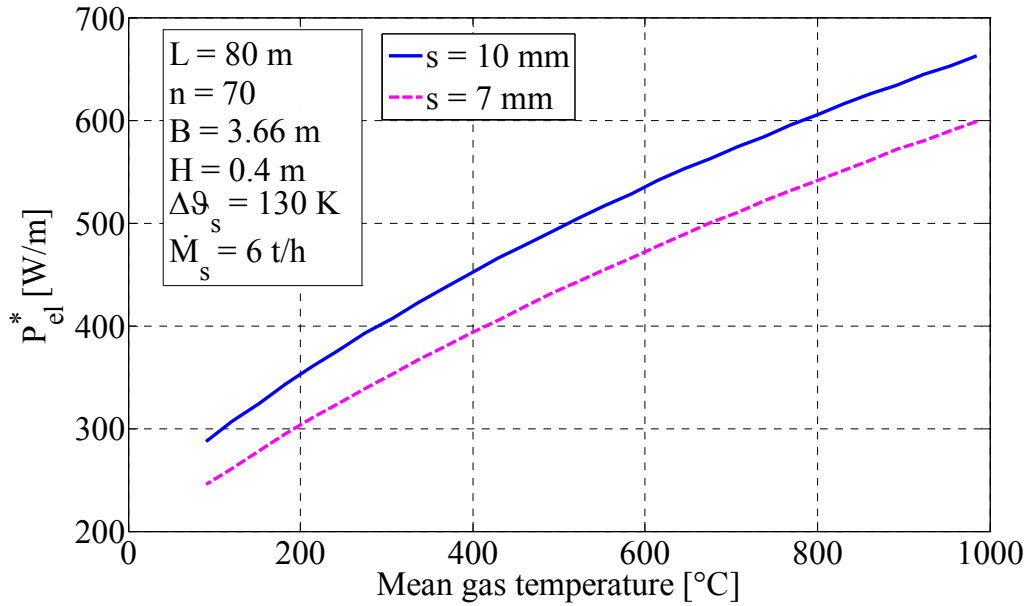
Figure 5.12:   The variation of ventilator power on temperature

Figure 5.13 shows the total pressure drop due to the gas recirculation in the cross section, dependent on gap thickness, with gas temperature as a parameter. It can be seen that when the gap thickness is smaller than 5 mm, the pressure drop increases very rapidly with the decrease of the gap thickness; when the gap is larger than 10 mm, the pressure drop remains constant. The temperature has a small influence on the pressure drop. The higher the temperature, the higher the pressure drop is. It also reveals that the pressure drop in the tile kiln is smaller than that in the brick kiln shown in Fig. 2.13. The reason could be the relative lower gas velocity in the gaps due to the higher heat transfer and the shorter height of the tiles, which decreases the flow friction inside the gap.
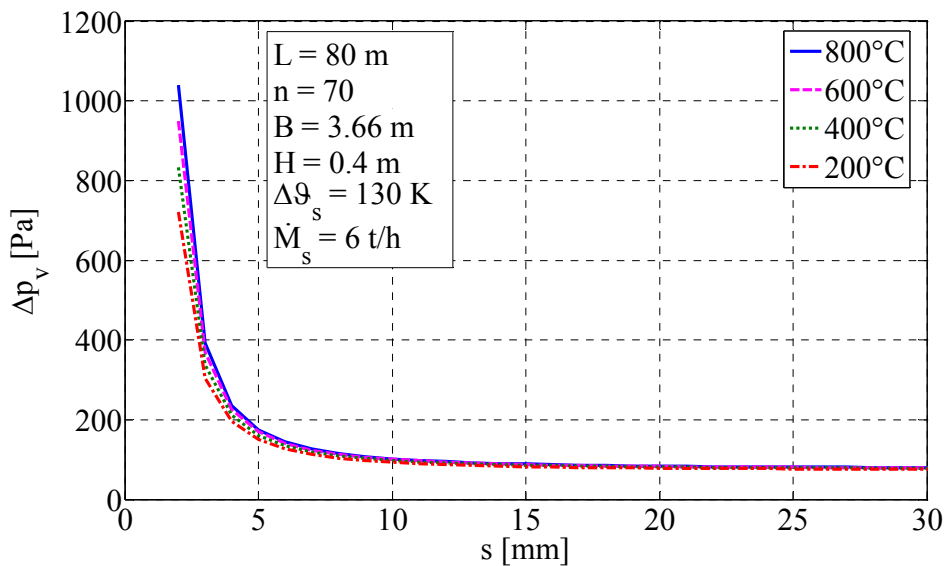


Figure 5.13:   Pressure drop in the cross section recirculation

Figure 5.14 shows the volumetric flow of the gas in the cross section between both sides. Like the phenomenon in the brick kiln, the volumetric flow increase approximately linearly with the increase in gap thickness. Because of the effect of the gas density, the higher the gas temperature is, the higher the volumetric flow will be. Compared with the volumetric flow of the brick kiln shown in Fig. 2.14, the total volumetric flow of tile kiln is higher. This is the effect of an increase in the number of gaps, with a total of 71 gaps per side.
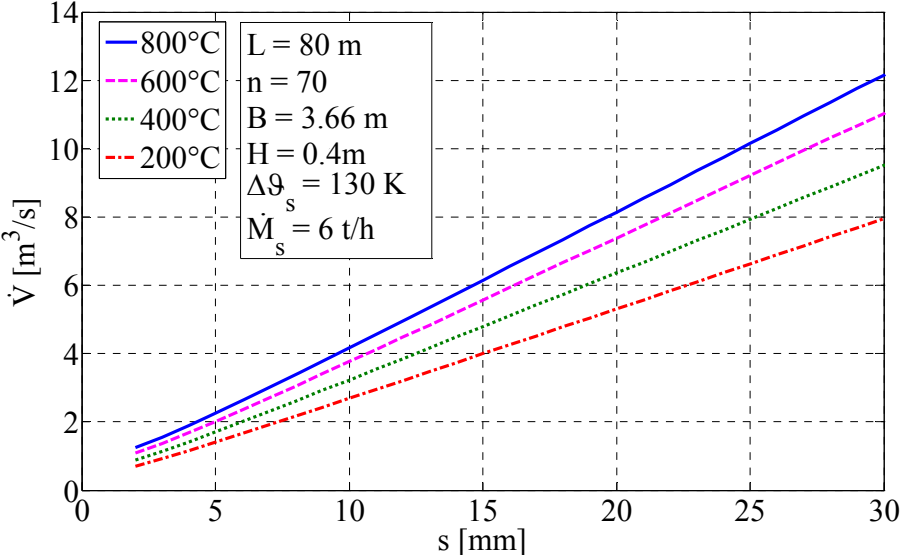


Figure 5.14:   Volumetric flow of the gas in the cross section between the both kiln sides

The results discussed above for the pressure drop and volumetric flow both lead to the phenomenon of a minimum in the electrical power requirement shown in Fig. 5.11.

## 5.4.2 Heat transfer

Fig. 5.15 shows the gas velocity dependent on the gap thickness, with gas temperature as a parameter. It illustrates that when the thickness is very small, the velocity increases very quickly with a decrease in gap thickness; once the gap increases to more than 15 mm, the gas velocity inside the gap remains constant with additional increases in gap thickness. It can also be seen that the gas velocity increases with an increase in gas temperature. This is further plotted in Fig. 5.16.
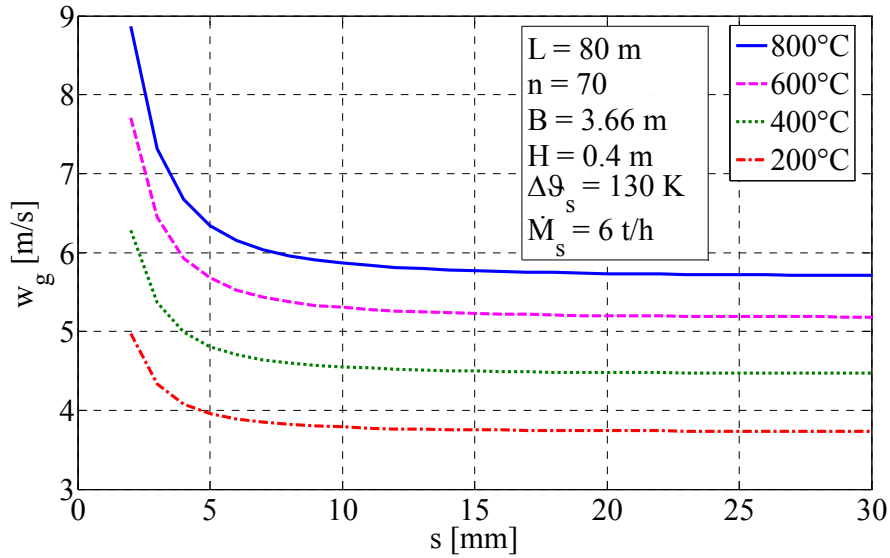
Figure 5.15:    Gas velocity dependent on the gap thickness

Fig. 5.16 shows the gas velocity inside the gaps, dependent on the temperature. This relationship is plotted for a gap thickness of 10 mm. It can be seen that the gas velocity increases with an increase in gas temperature.
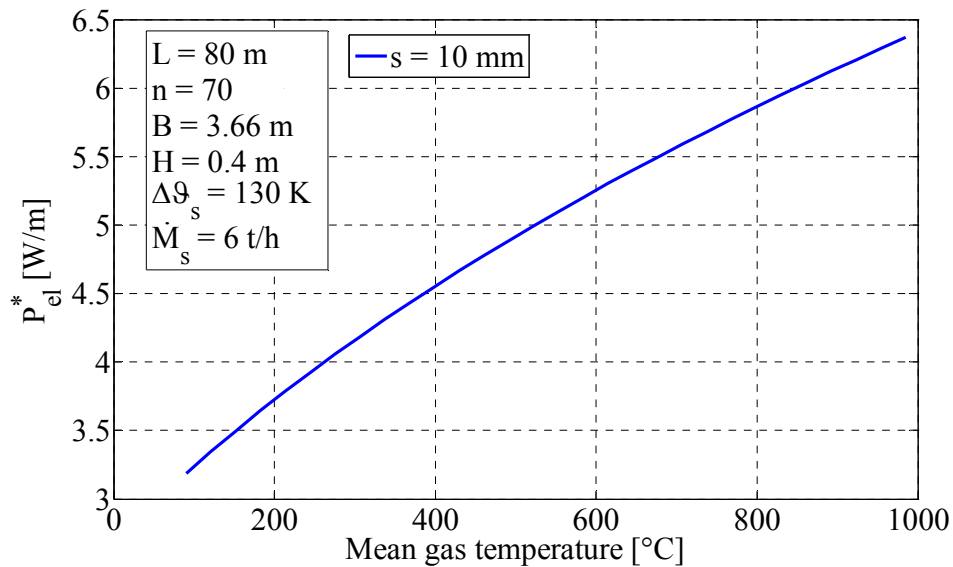


Figure 5.16:    Variation of velocity on temperature

In Fig. 5.17, the heat transfer coefficients dependent on the gap thickness are shown, with the gas mean temperature as a parameter. Similar to the investigation for the brick kiln, two values are shown, the pure heat transfer coefficient and the effective heat transfer coefficient representing the heat conduction inside of the tile bodies. It can be seen that when the gap thickness is smaller than 10 mm, the heat transfer coefficients increase rapidly with a decrease in gap thickness, due to the increase in gas velocity inside of the gaps, as shown in Fig. 5.15.

123

When the gap thickness is larger than this value, the heat transfer coefficients are kept constant.
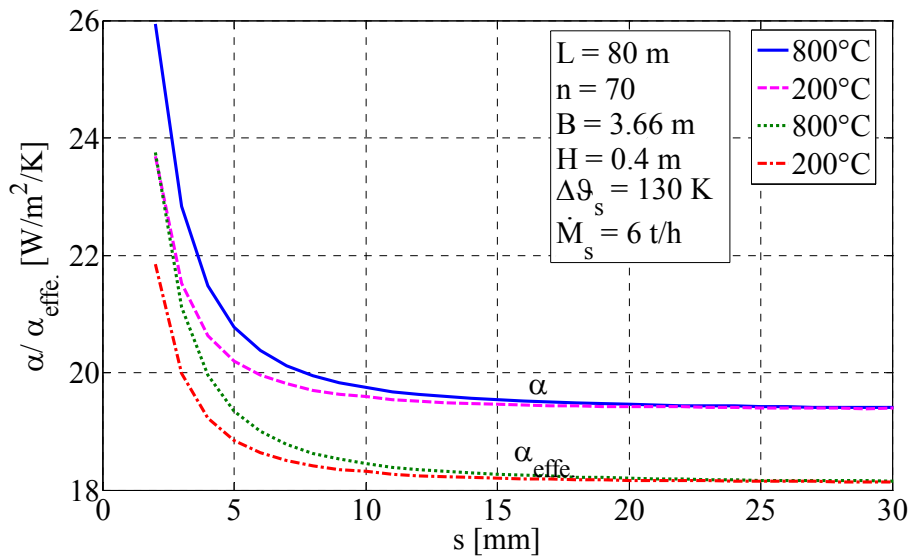


Figure 5.17:    Convective and effective heat transfer coefficients

The difference between the convective and effective heat transfer coefficients in the roof tile kiln shown in Fig. 5.17 is smaller than that in the brick kiln, which is shown in Fig. 2.11. This indicates the heat conduction inside the solid is smaller for tiles than for brick piles. This can be further investigated by the Biot number $Bi$, which is defined as

$$Bi = \frac{\alpha \cdot b/2}{\lambda_s},$$
(5-6)

where $\alpha$ is the convective heat transfer coefficient, $b$ is the thickness of the solid and $\lambda_s$ is the solid conductivity. The $Bi$ for the reference bricks kiln is 3.2, while for the tile kiln it is only 0.21. This value indicates that when compared to the brick process, the solid inner temperature difference in the cross section direction is very small for the tile process. Therefore, the difference between the convective and effective heat transfer coefficients is relative small.

Figure 5.18 shows the gas temperature difference between the bottom and top of the gap, dependent on gap thickness, with gas temperature as a parameter. It can be seen that when the gap thickness is smaller than 10 mm, the gas temperature difference increases rapidly with the decrease in gap thickness; when the gap thickness increases from 20 mm up to 30 mm, the gap temperature difference decreases very slowly. When the gap thickness is 10 mm, which is the utilized value in the production, the gas temperature difference between the bottom and top is 20-30 K. This value is higher than in the brick kiln, due to the smaller gap thickness. In Fig 2.12, it is shown that if the gap thickness for the brick kiln was 10 mm, the temperature difference between the bottom and top of the bricks would be 60 K.
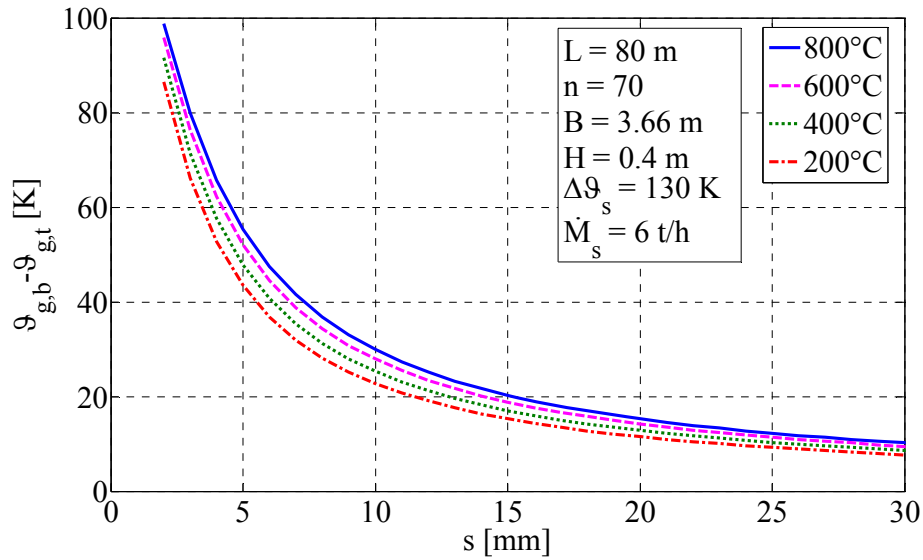
Figure 5.18:    Gas temperature difference between bottom and top of the gap

## 5.4.3 Total and specific ventilator power

Fig. 5.19 shows the total ventilator power for the entire kiln through the integration of the electrical power per length along the kiln length. It is dependent on the tile gap thickness. Five cases are plotted to show the influence of the different parameters. It can be seen that for each case, there is theoretically an optimal gap thickness, approximately 6-7 mm. When the kiln geometry remains constant but the temperature difference between the both sides changes, the higher the temperature difference, the lower the total electrical power requirement. When the kiln geometry changes, but the kiln volume remains constant, the total electrical power requirement does not change as much.
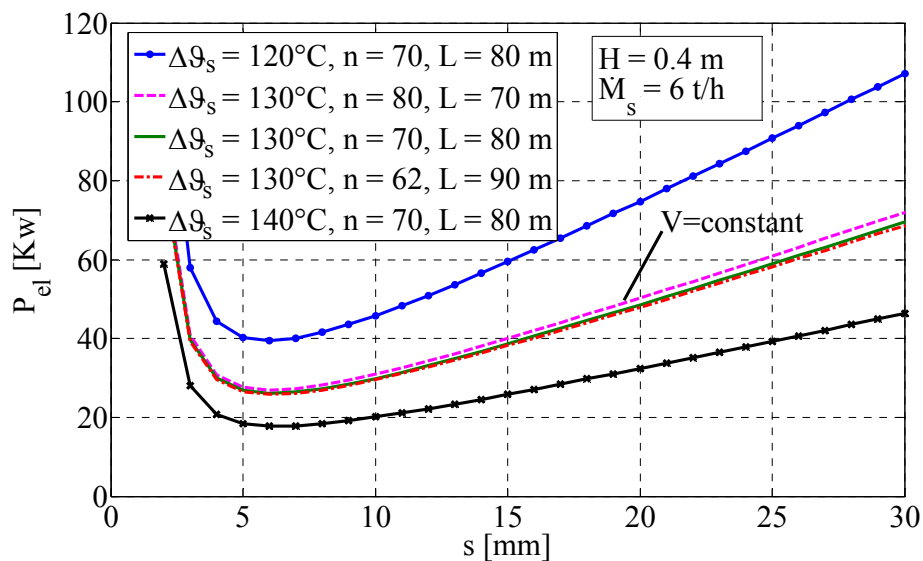


Figure 5.19:    Total ventilator power for the tiles kiln

125

Next, the specific ventilator power is determined. The specific ventilator power is calculated as before through Eq. (2-38) with the use of the primary electrical energy. As discussed before, the temperature difference between both sides influences the electrical energy requirement. The higher the solid temperature difference between both sides, the less electrical energy required. Therefore, the specific primary electrical energy requirement is plotted as a function of the solid temperature difference. This is shown in Fig. 5.20. The two situations shown are for gap thicknesses of 7 mm and 10 mm respectively. From this figure, it can be seen that with a decrease in the temperature difference between both sides $\Delta\vartheta_s$, the ventilator power increases exponentially. A reduction in $\Delta\vartheta_s$ from 130 K to 120 K almost doubles the ventilator power. An increase of the temperature difference from 150 K to 160 K decreases the ventilator power only slightly.
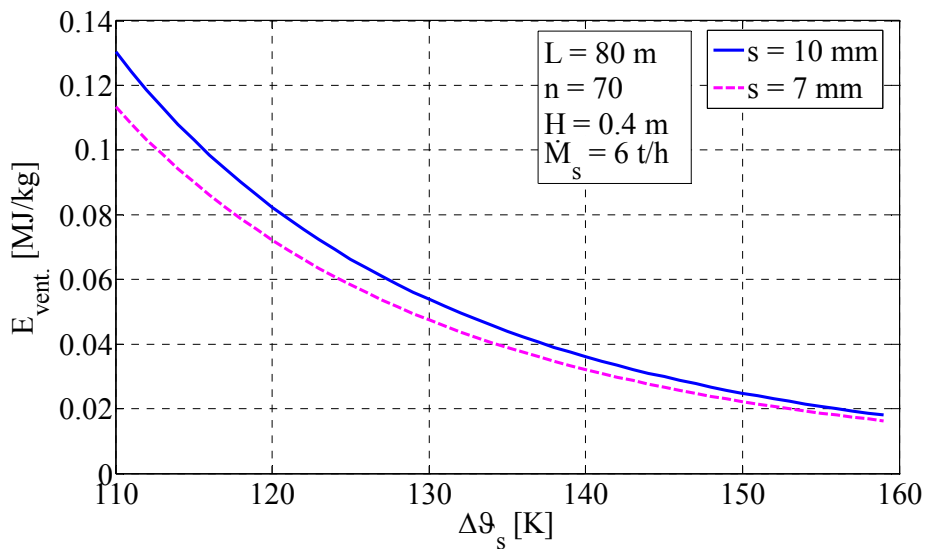


Figure 5.20:    Specific primary ventilator power

## 5.4.4 Fossil energy requirement

As described above, the higher the solid temperature difference between both sides $\Delta\vartheta_s$, the lower the electrical energy requirement is. However, the higher the solid temperature difference between both sides $\Delta\vartheta_s$ is, the higher the driving out temperature of the tiles and kiln furniture will be, thus resulting in higher the flue gas lose and fossil energy consumption. These calculations were carried out with the kiln energy balance described in Fig. 2.25 and Eq. (2-28) through (2-35). The mass flow of the kiln furniture is the same as the tiles' mass flow

$$\dot{M}_T = \dot{M}_s . \tag{5-7}$$

The variations in the driving out energy, flue gas, and total fossil energy depending on the solid temperature difference between both sides $\Delta\vartheta_s$ are shown in Fig. 5.21. Here, the insulation loss from the kiln wall is held constant at 0.1 MJ/kg, and the flue gas temperature $\vartheta_g$ in Eq. (2-34) is 500°C. It can be seen that both the flue gas lose and driving out energy

126

increase linearly with an increase in $\Delta\vartheta_s$. The total fossil energy consists of the driving out energy, the energy lost through flue gas, and the energy lost through the kiln wall and therefore also increases linearly with an increase in the solid temperature difference.
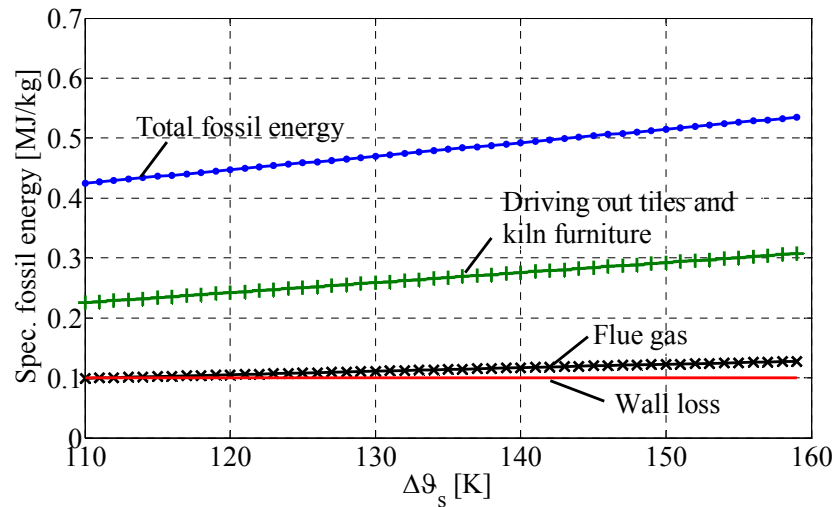


Figure 5.21:    Energy flow of kiln depending on the temperature difference of both sides

## 5.4.5 Total energy requirement

As described above, with an increase in the solid temperature difference $\Delta\vartheta_s$, the specific electrical energy decreases but the fossil energy requirement increases. Therefore, the total specific energy, which is the sum of the primary electrical energy and the fossil energy, should be determined. Fig. 5.22 shows this result. It is the sum of Fig. 5.20 and Fig. 5.21. For the primary electrical energy, $E_{vent}$, and the total energy, $E_{total}$, two curves are shown for gap thicknesses of 7 mm and 10 mm, which are the minimum value and the utilized value respectively. The graph indicates that the difference between the two tiles settings is not so big. From Fig. 5.22, it can be seen that there is a minimal value for the total energy, occurring at a temperature difference of 130 K.
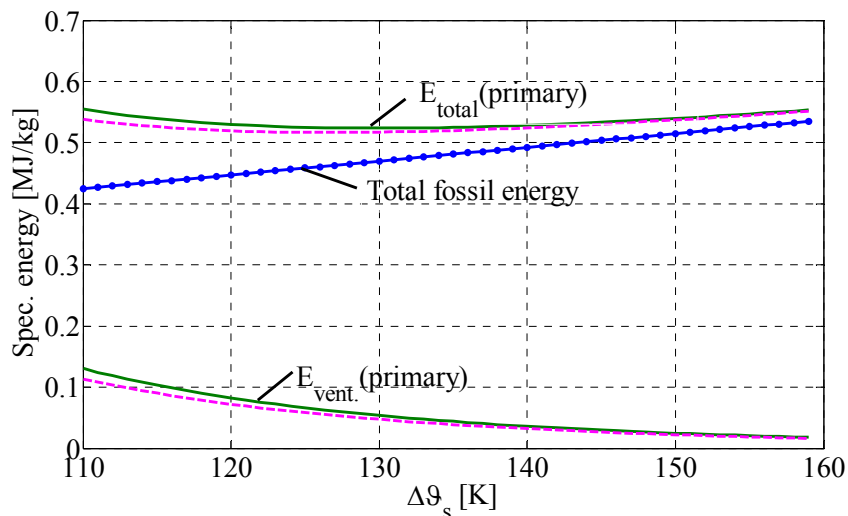


Figure 5.22:    Specific energy depending on the temperature difference of both sides

127

This result reveals that the heat transfer in the tile kiln is better than that in the brick kiln. Although there is plenty of kiln furniture to support the stability of the tiles, and the mass of the kiln furniture is too large to neglected, the energy requirement of the tile kiln is smaller.

According to scientific research, the average energy consumption for roof tiles in Germany is 2.15 MJ/kg of tiles [32]. It consists of 0.82 MJ/kg for the dryer and 1.25 MJ/kg for the kiln process [32]. The total energy consumption shown in Fig. 5.22 illustrates that with the solid-solid recuperation tunnel kiln, when the temperature difference between both sides is 130 K, the energy consumption is 0.53 MJ/kg. This is an energy saving of 60% for the kiln process.

# 5.5 Other influences on energy consumption

Besides the reference kiln discussed in the previous sections, there are other kilns utilized for roof tile production, which have other parameters. The influences of the other parameters on the energy consumption and energy savings are discussed as follows.

## 5.5.1 Influence of the thermal mass of kiln furniture

As already discussed above, a lot of measures for increasing energy efficiency during the firing process have already been carried out; the reduction of thermal mass of kiln cars and furniture [9] is one of them. Here the influence of the thermal mass of the kiln furniture on the solid-solid-recuperation tunnel kiln in tile production is further investigated.

Presently, the thermal mass of the kiln furniture is approximately the same as that of the tiles in the tunnel kiln for tile production. When the thermal mass of the kiln furniture is lighter, the mass ratio between the kiln furniture and tiles can reach a value of 0.5. Fig. 5.23 reveals the influence of the mass ratio on the driving out energy and total energy consumption. It shows that when the thermal mass ratio decrease from 1 to 0.5, the driving out energy from the tiles decreases slightly due to the decrease in the optimal $\varDelta\vartheta_s$ (shown in Fig. 5.24). The driving out energy from the kiln furniture decreases from the same value as the tiles to half the value of the tiles. The total energy consumption decreases from around 0.53 to 0.39 MJ/kg.
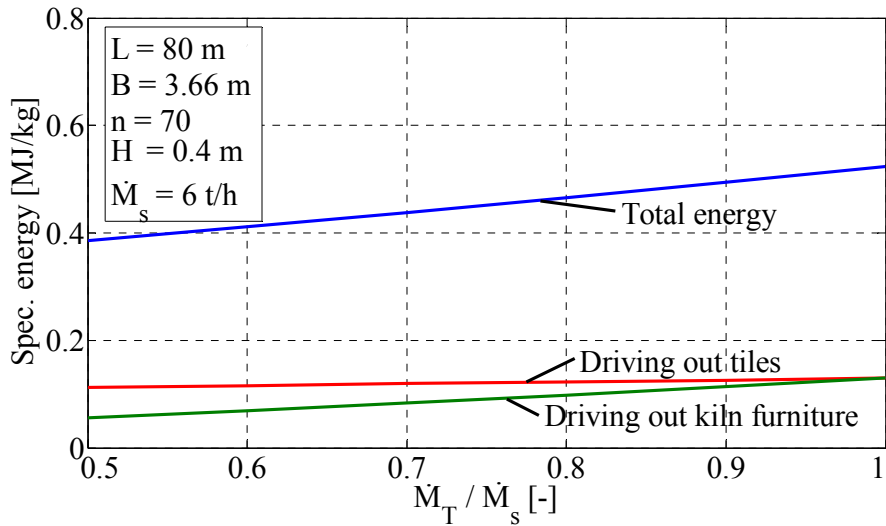
Figure 5.23: Influence of kiln furniture thermal mass on the energy

Fig. 5.24 shows the change in the optimal $\Delta\vartheta_s$ and the energy savings from the kiln process. These saving values are based on the energy consumption of a traditional kiln of 1.34 MJ/kg described in [32]. It can be seen that when the mass ratio between the kiln furniture and tiles decrease from 1 to 0.5, the optimal $\Delta\vartheta_s$ decrease from 130 K to 110 K, and the energy savings compared to the traditional tunnel kiln process increases from 60% to 70%.
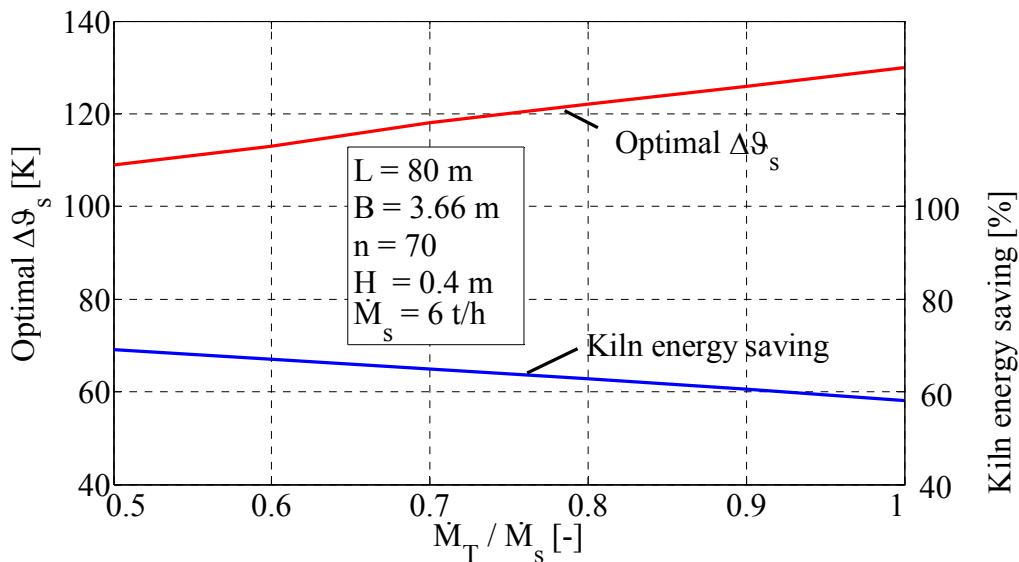


Figure 5.24: Influence of kiln furniture thermal mass on the optimal temperature difference and kiln energy saving

## 5.5.2 Influence of the tile layers

An increase in the tile layers can also increase the energy efficiency, due to the increase of the heat transfer surface and the decrease of the thermal mass of the kiln furniture. Fig. 5.6

shows the cross section for a single layer of tile. However, two layers of tile can be loaded on the kiln car, which is shown on the right land side in Fig. 5.2. Therefore a two layer tile production process should also be investigated.

For the two layer tile setting in the solid-solid-recuperation tunnel kiln, the following modifications for the model are made. The height of the tiles increases from 0.4m to 0.8m, the thermal mass ratio between the kiln furniture and tiles decreases to the half value, and the pressure drop increases due to the increase in friction inside the gaps, as well as the flow outlet and inlet pressure loss. Fig. 5.25 shows the result. It can be seen that $\Delta\vartheta_s$ is 72-80 K, which is lower than that for the single layer tile setting, where $\Delta\vartheta_s$ is 110-130K, as shown in Fig. 5.25. The energy savings in the double layer kiln process is 74-77%, which is higher than in the single layer setting, where the energy saving is 60-70%.
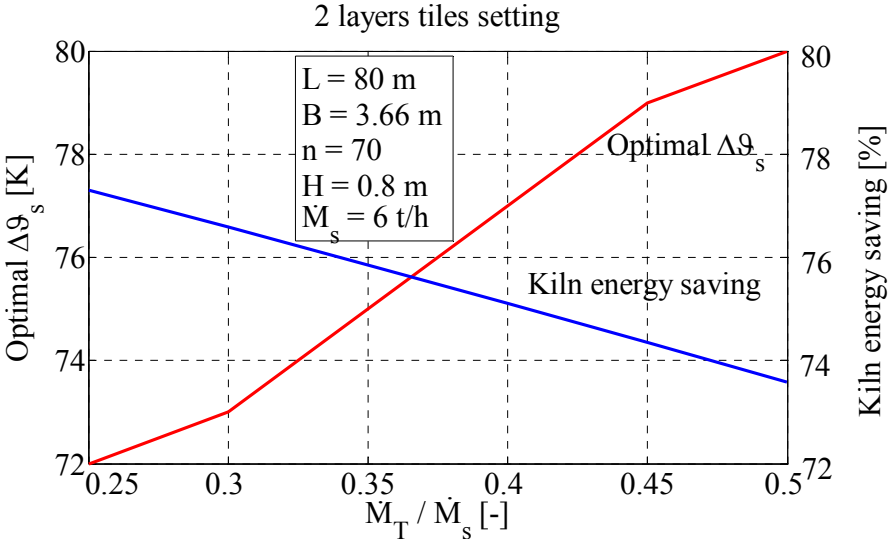


Figure 5.25:  Results for 2 layer tiles setting

## 5.5.3 Influence of the pressure drop of perforated plates

As shown in Table 5.2, the pressure drop coefficient $\xi_6$ for a perforated plate changes with a change in hole shape and arrangement. The results shown above are based on the value of $\xi_6$ being equal to 1. Therefore the influence of $\xi_6$ should be discussed. Fig. 5.26 shows this influence, which is shown to be relatively small.
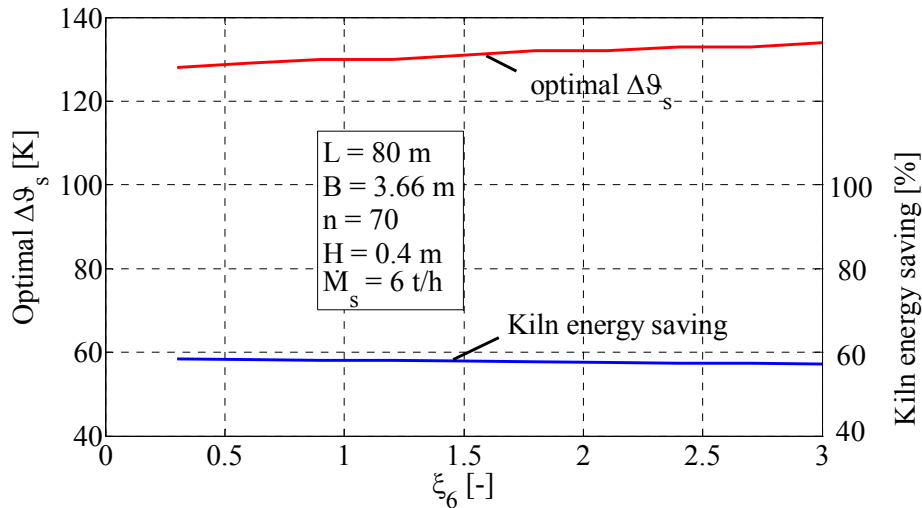
Figure 5.26: Influence of the pressure drop coefficient of the perforated plates

## 5.6 Summary

The production process for roof tile in a counter-travelling tunnel kiln was investigated in this chapter. At the beginning, the tiles' settings on the kiln furniture were described. For the new kiln process, tiles are set vertically on the kiln furniture, so that the gas recirculation in the cross section is possible.

Next, the modifications used to fit the simplified model for the brick kilns to the process of the tile kiln were discussed. The mass of the kiln furniture takes the same mass as the tile, and the heat transfer surface for each gap becomes smaller due to the discontinuous tile setting.

The ventilator power and heat transfer mechanism for the tile kiln were investigated. The specific energy consumption of the ventilator and the fossil fuel required were investigated, allowing the total specific energy requirement to be determined. The total specific energy was shown depending on the tiles' temperature difference between both sides. It was revealed that there is a minimum total energy requirement value, occurring when the temperature difference between both sides is 130 K. It was pointed out that an energy savings of 60%, when compared to the traditional tunnel kiln, can be obtained.

The simulation for the tile kiln revealed that although there is a lot of kiln furniture in the kiln, the energy requirement of the tile kiln is smaller. The reason for this is the relatively higher effective heat transfer coefficient due to the smaller tile thickness and the relatively larger heat transfer surface.

Finally, the influence of the kiln furniture, tile layers and pressure drop through the perforated plate on the energy saving were discussed.

131

# 6. Conclusion

The new tunnel kiln concept with solid-solid recuperation will further be evaluated from the point of view of energy consumption in more details. Here, the energy consumption is compared with a traditional tunnel kiln.

## 6.1 Energy comparison

In the Table 6.1 the energy consumptions of traditional tunnel kilns and the new tunnel kiln process are compared. Here the values for the clinker bricks without holes are taken. The total energy consumption is divided into different parts. The mean specific energy consumption of the traditional process for the clinker brick is 2.3 MJ/kg brick [19, 32]. This is divided into 1.05 MJ/kg for the drying process and 1.25 MJ/kg for the kiln process [32]. The drying energy is around 60% water condensation enthalpy (0.62 MJ/kg) and 40% flue gas enthalpy of drying (0.43 MJ/kg).

Table 6.1:     Comparison of energy saving of the both kiln processes

| Item | | Traditional tunnel kiln | | Counter-travelling tunnel kiln | | | | | |
| --- | --- | --- | --- | --- | --- | --- | --- | --- | --- |
| | | | | s = 60mm | | | s = 20mm | | |
| | | Energy Consu. [MJ/kg] | Energy Consu. [MJ/kg] | Energy Consu. [MJ/kg] | Energy Consu. [MJ/kg] | Energy Saving [%] | Energy Consu. [MJ/kg] | Energy Consu. [MJ/kg] | Energy Saving [%] |
| dryer | 25% water vaporization | 0.62 | 1.05 | 0.62 | 0.84 | 20% | 0.62 | 0.84 | 20% |
| | Flue gas, enthalpy change of bricks | 0.43 | | 0.22 | | | 0.22 | | |
| Kiln | Driving loss from bricks | 0.22 | 1.25 | 0.18 | 0.47 | 62% | 0.159 | 0.43 | 66% |
| | Driving loss from kiln car Ca. 33% of bricks | 0.08 | | 0.06 | | | 0.052 | | |
| | Insulation loss | 0.1 | | 0.1 | | | 0.1 | | |
| | Flue gas loss | 0.85 | | 0.10 | | | 0.093 | | |
| | Electrical energy for blowers (primary) | 0 | | 0.034 | | | 0.028 | | |
| Whole process | | 2.3 | 2.3 | 1.31 | 1.31 | 43% | 1.28 | 1.27 | 45% |

The energy consumption of the kiln process consists of the following items: the driving out loss for the hot brick is 0.22 MJ/kg, which corresponds to a mean temperature of 260°C.

The driving out loss for the kiln car is measured as 33% of the loss from the hot brick. The heat loss from the kiln wall is 0.1 MJ/kg. The heat loss of the flue gas is approximately 0.85 MJ/kg. This by-product energy loss of the process is in fact the largest proportion of energy consumption in the process. This phenomenon can be explained by the higher heat capacity flow of flue gas in comparison to that of brick. This is also the main motivation to replace solid-gas-recuperation by solid-solid-recuperation.

These energy values are compared with the values of the new tunnel kiln concept of solid-solid-recuperation. Here, two cases for different brick piles settings are discussed. In the first case, the gap thickness is 60 mm, the practical distance. In the second case, the gap thickness is set to only 20 mm, which represents the gap thickness requiring the minimum ventilator power.

The drying process of the new kiln concept is decoupled, that is the dryer and kiln can be operated independently. This has a lot of advantages. For example, the dryer can be operated according to different shifts and different seasons. Here, only the advantages from the point of view of energy are taken into consideration.

If the dryer works independently, the drying process can be obviously optimized. This optimization is for instance explained in [15] and was the object of the previous projects of the German Federation of Industrial Research Associations (AiF). For example, the supplied air temperature can be raised more than right now, when the cooling gas is sucked from the cooling zone of the kiln. Therefore, the mass flow of the air required for cooling and the flue gas loss of the dryer are obviously reduced. The flue gas loss in an independently operating dryer is 0.22 MJ/kg, which is only 50% of the flue gas loss in the current dryer. The water condensation enthalpy is a theoretical minimum value for the drying, which cannot be lowered beyond that of the traditional drying process. Therefore, by using the new concept for the tunnel kiln, altogether approximately 20% energy can be saved in the drying process.

Currently, research shows that through free air drying, one part of the condensation enthalpy is able to be saved. This is possible only with an independent dryer. Because free air drying is not state-of-the-art yet, its energy consumption is not considered.

In the new kiln process, the mean driving out temperatures are 215°C to 195°C, which is the temperature difference of both sides $\Delta\vartheta_s$ plus 25°C, the temperature of the driving-in bricks. These temperatures are below those of traditional kilns, which can be explained by the fact that the new concept has better heat transfer under the work of ventilators. Therefore, the driving out losses from the brick and kiln cars are lower. The heat losses from the kiln wall are held constant for all kilns. The most significant difference between the old and new kiln processes is the flue gas loss. In the new kiln process, this is just 0.1 MJ/kg, around 11% of the traditional process. For the new kiln, however, the energy for the ventilator has to be

included. Here, the electrical energy is converted to primary energy by a power station efficiency of 35% [31].

In conclusion, it is evident that for the kiln process itself, 62% to 66% energy can be saved. For the total process, 43% to 45% energy can be saved.

The energy savings are obvious. However, the saved energy opposes the problem of high investment costs. High investment costs consist specifically of rebuilding the traditional kilns to fit the new process. Lower investments costs are expected for refitting an existing kiln than if a new kiln is built. Such investment costs are not able to be estimated, and therefore are beyond the scope of this research project

## 6.2 Investment cost for ventilators

The new kiln process requires a series of ventilators. The number and arrangement of the ventilators are investigated in the following. From this investigation, the ventilator investment is able to be estimated.

There are different ventilator designs from different manufacturing companies. Only one kind of ventilator is investigated here: the ventilators produced by the company Brackemeier. These ventilators have already been implemented in some tunnel kilns and therefore will be more common in this industry field in the near future. The design of this ventilator is connected with the technical and process data of the kiln. The design of this ventilator is now included in the kiln cross section. This ventilator has a power of 1 kW. The price of this ventilators is approximately 30 000 EUR.

In Fig. 6.1, the arrangement of the ventilators along the kiln length required to generate the necessary recirculation flow is shown. The amount of recirculation air flow depends on the temperature, which was explained in Chapter 2. The higher the temperature, the higher the specific ventilator power is. Therefore, the higher the temperature, the closer the ventilators are to each other. Fig. 6.1 shows that further away from the end of the kiln or closer to the firing zone, the ventilators must be installed more densely. As it is shown in Fig. 6.1, when gap thickness is 60 mm, 10 ventilators are needed for each side, while when the gap thickness is 20 mm, only 9 ventilators per side are required. Therefore, a total of 20 or 18 ventilators are required for the two gap thickness setting cases respectively.  It can be seen that the ventilator number difference for these two cases is relatively small.
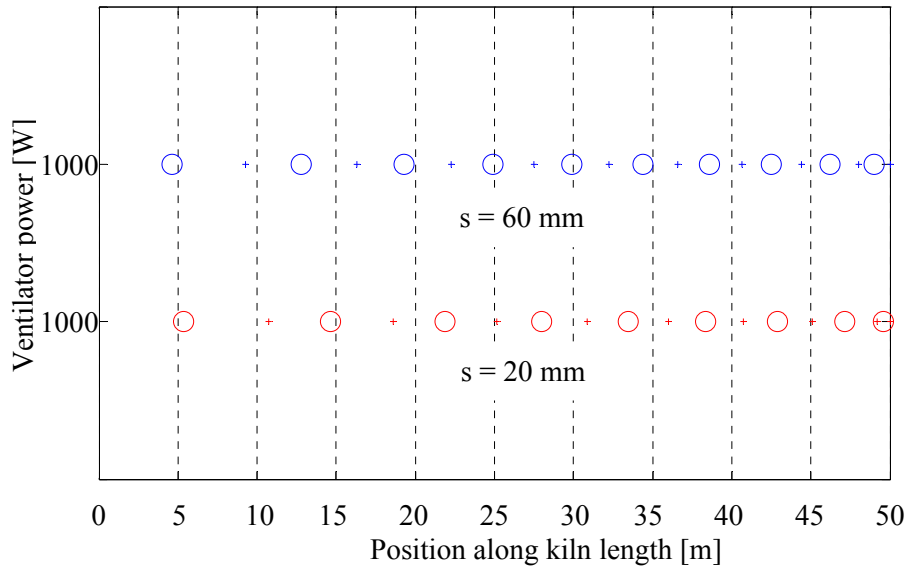
Figure 6.1:     Arrangement of ventilators

In Table 6.2, a rough estimation of amortization time for the ventilators is carried out. Monetary values are estimated from a natural gas price of 4 cent/kWh. At the gap thickness of 60 mm, the energy savings in the kiln is shown to be 62% in Table 5.1, which corresponds to 775 kJ/kg brick. At a throughput of 8 t/h, 15 million kWh/year energy can be saved, which corresponds to 600,000 EUR/year. The price for 20 ventilators is about 600,000 EUR. Therefore, the amortization time is approximately one year. It is also illustrated that when the gap thickness is 20 mm, the amortization time is slightly lower than 1 year.

Table 6.2:     Estimation of the amortization time for the ventilators

|  | Unit | s = 60 mm | s = 20 mm |
|---|---|---|---|
| Energy saving in kiln | % | 62 | 66 |
| Energy saving in kiln | kJ/kg | 775 | 813 |
| Energy saving in kiln | kW·h/year | $15 \cdot 10^6$ | $16 \cdot 10^6$ |
| Saving of natural gas | Euro/year | 600 000 | 640 000 |
| Number of ventilators | - | 20 | 18 |
| Ventilator investment | Euro | 600 000 | 540 000 |
| Amortization time | year | 1 | 0.84 |

# 6.3  Energy saving of roof tiles

As a comparison with the brick kiln, the roof tile kiln was also investigated. The specific energy consumption of the roof tiles for each term have be determined, which are shown in Fig. 5.18, and those values are summarized in Table 6.3.

Table 6.3:        Specific energy consumption for roof tiles

|  | Unit | Value |
|---|---|---|
| Optimal temperature difference between both sides | K | 130 |
| Driving out loss from tiles | MJ/kg | 0.13 |
| Driving out loss from kiln furniture | MJ/kg | 0.13 |
| Insulation loss | MJ/kg | 0.1 |
| Flue gas loss | MJ/kg | 0.11 |
| Electrical energy for blowers (primary) | MJ/kg | 0.056 |
| SUM | MJ/kg | 0.526 |

The exact energy savings of this kiln is difficult to estimate, since the specific energy consumption for the roof tiles with the traditional tunnel kiln varies greatly within a large range. If 1.34 MJ/kg of tile [32] is taken as a benchmark value for the specific energy consumption of a traditional kiln, an energy savings of about 60 % for the new kiln process can be reached for roof tile production. This value is almost the same as the energy savings for brick production, which is 62%, as shown in Table 6.1.

# 6.4  Outlook

1. The two kiln processes have different technical conditions regarding investment.  For example, the new kiln process requires a much more complicated rail system. However, the cost for flue gas treatment is significantly less. An exact cost cannot be estimated. A detailed comparison of the investment costs of both systems must be performed in further studies. In that further work, it must also be considered whether the renovation of an existing tunnel kiln would be worthwhile.

2. The energy consumption for clinker bricks and roof tiles is simulated in this work. However, there are other ceramic products as discussed in chapter 1. The production process for other products should be examined, and the energy savings should be investigated.

3. As discussed in Chapter 3, the gas flow in each gap in the cross section is not absolutely homogenous in the ventilator side, even when distribution walls are installed. Although this flow condition is improved in comparison to the traditional tunnel kiln, uneven heat transfer still exists in each gap. Therefore, further works for the cross sectional flow optimization should be carried out.

4. More numerical calculations and CFD simulations with other software besides FLUENT should be carried out as well. Verification of the models used in this work should be continued, and more advanced mathematical models should be further developed.

5. The counter-travelling tunnel kiln has a symmetric temperature profile for the preheating and cooling zone. It is impossible to implement this kiln in all ceramic production processes, especially processes which contain high sulphur dioxide or carbon dioxide. Therefore it is meaningful to investigate and enumerate what product range this new kiln concept is suitable for.

# Reference

[1]  European commission, Institute for prospective technology studies: Integrated Pollution Prevention and Control Reference Document on Best Available Techniques in the Ceramic Manufacturing Industry, 2006, Sevilla, Spain.

[2]  UBA, Exemplary Investigation into the State of Practical Realisation of Integrated Environmental Protection within the Ceramics Industry under Observance of the IPPC-Directive and the Development of BAT Reference Documents, 2001.

[3]  W. Bender: Vom Ziegelgott zum Indutrieelektroniker, Geschichte der Ziegelherstellung von den Anfängern bis Heute, 2004, Bundesverband der Deutschen Ziegelindustrie e.V., Bonn, Germany, ISBN 3-9807595-1-2

[4]  Academic dictionaries and encyclopedias
http://de.academic.ru/dic.nsf/dewiki/127980

[5]  Hurias, Alfred: Feldbrand von Ziegeln in Südafrika, Ziegelindustrie International Nr. 12/1988, p.676-681

[6]  www.takasago-inc.co.jp/eg/sk1/shuttle1.htm

[7]  Energy bulletin
http://www.energybulletin.net/node/50715

[8]  M. Chmielowski: Modellierung der unter- und oberseitigen Wärmeübertragung an plattenförmiges Gut in Rollenöfen, Ph.D. Thesis, Otto-von-Guericke-Universität, Magdeburg, Germany, 2005.

[9]  N.A. Pratten, P.M. Guilford, Energy technology in the ceramics industry sector - a thermie programme action, ETSU, CEC,1993.

[10] G. Sumer, S. Rozak, P. Gallimore, P. Green, J. Tordoff, G. Kos, G. Dahlman, Proper selection of kiln furniture, Am. Ceram. Sec. Bull. 74 (7) (1995) p.54-65.

[11] C. Agrafiotis, T. Tsoutsos, Energy saving technologies in the European ceramic sector: a systematic review, Appl. Therm. Eng. 21 (2001) p.1231-1249.

[12] R. Gubbon, Tile and brick manufacture - a decade of progress, Tile Brick Int. 10 (3) (1994) p.155-158.

[13] R. Sladek, Successful kilns for structural ceramics, Tile Brick Int. 9(4) (1993) p.209-211.

[14] J. Merienne, Energy saving in the brick-making industry with the addition of heat-producing waste, Tile Brick Int. 11(2) (1995) p.112-115.

[15] K. Junge; U. Telljohann; D. Deppe; Entkopplung des Ofen- und Trocknerbetriebes; ZI-Jahresbuch 2004; p. 20 ff.; Bauverlag Gütersloh

[16] U. Ketels; Die Untersuchung des Schwelgasaustreibungsverhaltens von Ziegelrohstoffen; Ziegelindustrie int. 1991, 10, p.537-543.

[17] K. Junge; Verminderung von Schwefelemissionen im Heißreaktor; ZI-Jahrbuch 1992, p.32-46, Bauverlag Wiesbaden.

[18] R. Riedel, Der Gegenlaufenofen, Sprechsaal 1978,1.

[19] S. Kaya, K. Küçükada, E. Mançuhan, Model-based optimization of heat recovery in the cooling zone of a tunnel kiln, Applied Thermal Engineering 28 (2008) 633-641.

[20] S. Prasertsan, T. Theppaza, G. Prateepchaikul, P. Kirirat, Development of an energy-efficient brick kiln, International Journal of energy research, Vol. 21 (1997) p.1363-1383.

[21] Riedel et al.: Der Gegenlaufofen - Funktionsprinzip, Entwicklung, Aufbau, Ergebnisse, Ziegelindustrie Int. 9/1985, p. 517-524.

[22] K. Junge, K. Jeschar, Mathematisches Modell zur Projektierung und Optimierung von Tunnelofenprozessen der Ziegelindustriel, Ziegeleitechnisches Jahrbuch 1984, Bauverlag Wiesbaden.

[23] E. Rimpel; Ziegelbrand im Gegenlaufofen, Ziegeleitechnisches Jahrbuch 1995, p.38-58.

[24] R. Jeschar, K. Junge, Gemeinsame Darstellung der Wärmeübertragung in Gegenstromöfen, Gaswärme Int. 29 (1980)5, p.243-251.

[25] E. Rimpel, Strömungs- und wärmetechnische Untersuchungen zur Optimierung in Trocknern und Öfen der Ziegelindutrie, ZI-Jahrbuch 1999, p. 76-92.

[26] K. Junge, U. Telljohann, Brennen von energetisch hochbefrachteten Leicht-hochlochziegeln, ZI-Jahrbuch 2003, p. 69-87.

[27] DeWitt, Bergman, Lavine (2007). Fundamentals of Heat and Mass Transfer (6th edition ed.). John Wiley & Sons. pp. 260–261. ISBN 978-0-471-45728-2.

[28] J. H. Ferziger, M. Peric, Computational Method for Fluid Dynamics, 3rd Edition, Sringer-Verlag Berlin Heidelberg New York, 2002, ISBN 3-540-42074-6

[29] VDI-Wärmeatlas 10. Auflage 2006, Springer-Verlag Berlin Heidelberg, 2006.

[30] Müller, R.: Die Annäherung der Temperaturabhängigkeit der Transportkoeffizienten von Gasen durch einen Potenzansatz. Chemie-Ing.-Techn. 40 (1968) p.344-349.

[31] Wikipedia
http://en.wikipedia.org/wiki/Fossil_fuel_power_station

[32] K. Junge, Energiebedarf zur Ziegelherstellung, Ziegelindustrie Int. 4/2002

[33] ANSYS, FLUENT 6.3 User's Guide, Fluent Inc, 2006

[34] ANSYS, FLUENT 6.3 Getting Started Guide, FLUENT User Services Centre. FLUENT Inc.(2006).

[35] D. B. Launder, B. E. and Spalding, Mathematical Models of Turbulence. Academic Press, London, 1972.

[36] ANSYS, FLUENT 6.3 Tutorial Guide, Fluent Inc, 2006.

[37] Y. Jaluria, K. E. Torrance, Computational heat transfer, 2nd Edition, Taylor & Francis, London, 2003, ISBN 1-56032-477-5

[38] R.C.Sachdeva, Fundamentals of Engineering heat and mass transfer, 2nd Edition, Delhi: New Age international (P) Limited, 2003.

[39] M. A. Crisfield, Non-linear Finite Element Analysis of Solids and Structures, Vol.1: Essentials. New York: John Wiley & Sons,1991.

[40] E. Fermi, L. Fermi, Thermodynamics, ISBN 486-60361-X, Dover Publications, Inc, USA, 1937.

[41] H. Reh, Tableware and sanitaryware plants follow developments in the tile industry, Ceram. Eng. Sci. Proc. 16 (1) (1995) 103-106.

# Curriculum Vitae

## Personal

**Surname:** Meng      **First name:** Ping      **Gender:** Male
**Date of Birth:** Sep 6, 1979      **Place of Birth:** Beijing      **Nationality:** China
**E-mail:** herrmeng@hotmail.com

## Education

| | | |
|---|---|---|
| 1986.9-1992.7 | **Beijing Nanxiange Primary School** | Primary School Diploma |
| 1992.9-1995.7 | **Beijing No.60 Middle School** | Junior Middle School Diploma |
| 1995.9-1998.7 | **Beijing Yucai School** | Senior High School Diploma |
| 1998.9-2002.7 | **Capital University of Economics and Business** | |
| | Bachelor of Engineering | |
| | Major: Industrial Engineering | |
| 2003.10-2005.4 | **University of Applied Sciences Berlin** | |
| | Master of Science | |
| | Major: International Technology Transfer Management | |
| 2006.10-2007.10 | **Otto von Guericke University Magdeburg** | |
| | Master of Science | |
| | Major: Quality, Safety and Environment | |
| 2007.11-today | **Otto von Guericke University Magdeburg** | |
| | Institute for Fluid Mechanics and Thermodynamics | |
| | Ph.D. student | |

## Awards

2000 Excellent student leader of Capital University of Economics and Business
2000 Excellent student of Capital University of Economics and Business
2001 Panasonic Scholarship awarded by China Friendship Peace Development Foundation
2001 Excellent Student of Beijing
2002 Excellent Graduate of Beijing